Downloaded from orbit.dtu.dk on: Apr 29, 2024

DTU Library

Advanced meteorological modelling across scales

Imberger, Marc

Link to article, DOI:
10.11581/dtu:00000091

Publication date:
2020

Document Version
Publisher's PDF, also known as Version of record

Link back to DTU Orbit

Citation (APA):
Imberger, M. (2020). *Advanced meteorological modelling across scales*. DTU Wind Energy. DTU Wind Energy PhD No. 0104(EN) https://doi.org/10.11581/dtu:00000091

General rights
Copyright and moral rights for the publications made accessible in the public portal are retained by the authors and/or other copyright owners and it is a condition of accessing publications that users recognise and abide by the legal requirements associated with these rights.

- Users may download and print one copy of any publication from the public portal for the purpose of private study or research.
- You may not further distribute the material or use it for any profit-making activity or commercial gain
- You may freely distribute the URL identifying the publication in the public portal

If you believe that this document breaches copyright please contact us providing details, and we will remove access to the work immediately and investigate your claim.

Advanced meteorological modelling across scales

Department of
Wind Energy
PhD Report 2020

Marc Imberger

DTU Wind Energy PhD-0104(EN)
DOI number: : https://doi.org/10.11581/dtu:00000091

September 2020

Authors: Marc Imberger
Title: Advanced meteorological modelling across scales
Department: Wind Energy

2020

Project Period:
15 September 2017 – 14 September 2020

Education:
PhD

Supervisor:
Xiaoli Guo Larsén, Senior researcher
DTU Wind Energy
Co-supervisor:
Neil Davis, Technical Lead for Wind Resource Assessment Application
DTU Wind Energy

DTU Wind Energy is a department of the Technical University of Denmark with a unique integration of research, education, innovation and public/private sector consulting in the field of wind energy. Our activities develop new opportunities and technology for the global and Danish exploitation of wind energy. Research focuses on key technical-scientific fields, which are central for the development, innovation and use of wind energy and provides the basis for advanced education.

DTU Wind Energy has a staff of approximately 240 and a further 35 PhD-students, spread across 38 different nationalities. The variety of research, education, innovation, testing and consultancy is reflected in the employment profile which includes faculty with research and teaching responsibilities, researchers and technical academic staff, highly skilled technicians and administrative staff.

Our facilities are situated at DTU Risø Campus and at DTU Lyngby Campus. Furthermore the department is running the national test stations in Høvsøre and Østerild.

Technical University of Denmark
Department of Wind Energy
Frederiksborgvej 399
Building 118
4000 Roskilde
Denmark

www.vindenergi.dtu.dk

DTU Wind Energy
Department of Wind Energy

Ph.D. Thesis

Advanced meteorological modelling across scales

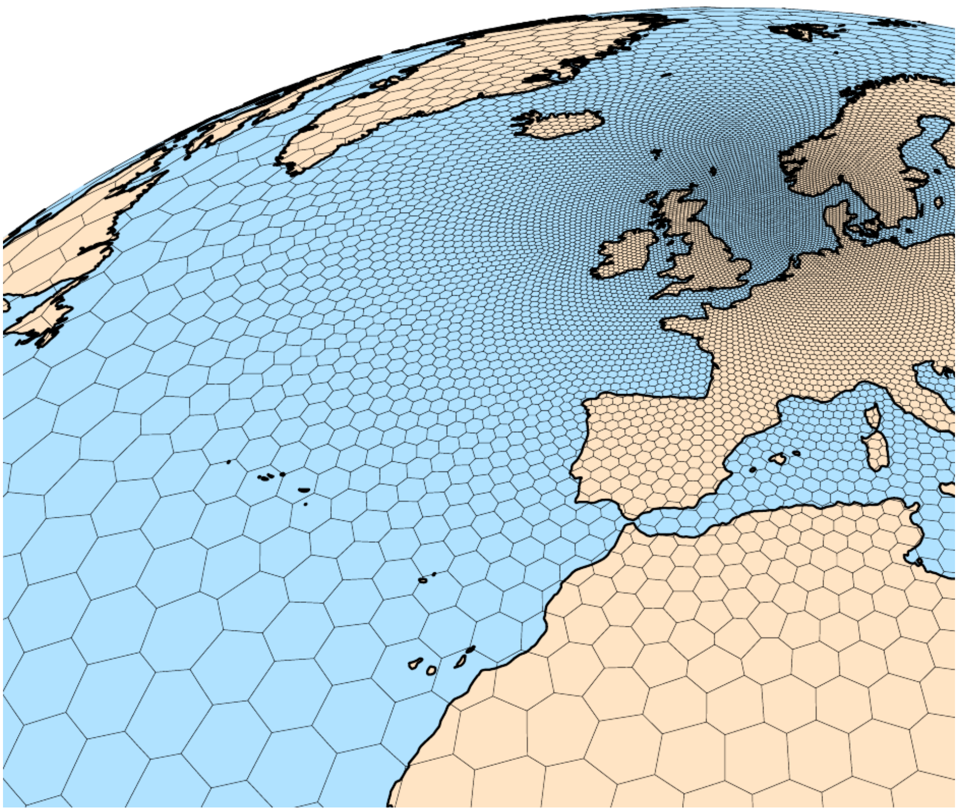

Marc Imberger

DTU Wind Energy (Risø Campus),
Roskilde, Denmark, 2020

Technical University of Denmark
DTU Wind Energy
Department of Wind Energy

DTU Risø Campus
Frederiksborgvej 399, Building 125
4000 Roskilde, Denmark
www.vindenergi.dtu.dk

Abstract

Wind farms are affected by a variety of atmospheric flow phenomena across spatial and temporal scales ranging from the macroscale and mesoscale to the microscale. This PhD project focuses on simulating a few of these phenomena using the atmospheric component of the Model For Prediction Across Scales (MPAS) to investigate its capabilities for wind energy applications. MPAS is a global model that utilizes a subset of the physics schemes from the limited-area Weather Research and Forecasting (WRF) model. It has an unstructured mesh discretization (Spherical Centroidal Voronoi Tessellations) that enables quasi-uniform and variable-resolution simulations with smooth transition zones, allowing for regional refinement of the model simulations.

In this thesis, the strengths and challenges of a global modeling approach with regional refinement, using MPAS, are examined and compared with measurements and traditional modeling, using WRF. Three different application areas are explored. The first area focuses on difficulties related with simulating a mid-latitude cyclone at medium resolution, using both WRF and MPAS. The WRF simulations have challenges due to the lateral boundaries, but with different setups a reasonable forecast can be produced. MPAS is able to improve storm intensity compared to WRF, but deviations in the model forecast increased time shifts between simulated and observed local minimum sea level pressure. The second application focuses on an episode of open cellular convection over the North Sea, allowing the investigation of MPAS' capabilities for simulating mesoscale wind variability. Given sufficiently high horizontal resolution and an adequate model initialization time, MPAS represents the increased spatial and temporal wind variability quite well, compared to point measurements and satellite derived observations. The third application area explores MPAS to study the impact of wind farms on the atmosphere. For this purpose, the 'Explicit Wake Parametrisation' scheme, previously implemented in WRF, is implemented in MPAS. After verifying the implementation in MPAS, a short-term case study is simulated, for two wind farms in the southern North Sea. During the implementation, issues with model divergence due to pressure field dependent random number generation were found and fixed, but the additional presence and impact of the propagation of small scale numerical noise requires further investigations.

Across all the studies, it was found that the lack of lateral boundary conditions in MPAS, which help constrain the model simulations in WRF, allows for more significant model deviations from the real atmospheric state in case studies. This requires further exploration of data assimilation techniques to prevent the simulation drift.

Dansk Resumé

Vindparker påvirkes af en række forskellige atmosfæriske luftstrømningsfænomener på tværs af rumlige og tidslige skalaer, fra makroskala over mesoskala til mikroskala niveau. Dette Ph.d. projekt fokuserer på at simulere nogle af disse fænomener ved brug af den atmosfæriske komponent af Model for Prediction Across Scales (MPAS) for at undersøge modellens anvendelsesmuligheder til vindenergi formål. MPAS er en global model der gør brug af en række parametriseringer fra den regionale Weather Research and Forecasting (WRF) model til at repræsentere finskala (uopløste) atmosfæredynamik aspekter. MPAS anvender ustruktureret gitter diskretisering (sfæriske, centroidale Voronoi tessellationer) der muliggør simulering med både quasi-uniformt grid og med variabel opløsning med glidende overgang mellem høj- og lavopløste regioner i modellen.

I denne afhandling undersøges styrker og udfordringer ved en fremgangsmåde hvor en global model med mulighed for regional detaljeringsgrad, MPAS, anvendes i en vindenergi kontekst, baseret på sammenligning med målinger og simuleringsresultater fra den mere traditionelt anvendte WRF model. Tre forskellige anvendelsesområder undersøges. Det første fokuserer på genvordighederne i forbindelse med simulering af en ekstratropiske cyklon ved medium opløsning ved brug af både WRF og MPAS. WRF simuleringerne har udfordringer på grund af de laterale grænsebetingelser, men med forskellige opsætninger kan der produceres en rimelig prognose. MPAS er i stand til at forbedre stormintensiteten sammenlignet med WRF, men afvigelser i modelprognosen øgede tidsforskydning mellem simuleret og observeret minimum af trykket ved havniveau. Det andet anvendelsområde fokuserer på et tilfælde af åben cellulær konvektion over Nordsøen, hvilket udnyttes til at studere MPAS' evne til at simulere mesoskala vindvariation. Med høj modelopløsning og tilstrækkelig lang modelinitialisering kan MPAS udmærket simulere den øgede vindvariation i tid og rum, holdt op imod punktmålinger og satellit-afledte observationer. Det tredje anvendelsesområde udforsker anvendelse af MPAS til at undersøge vindmølleparkernes indvirkning på atmosfæren. Til dette formål implementeres 'Explicit Wake Parametrisation' (EWP) modellen, allerede implementeret i WRF, nu også i MPAS. Efter validering at MPAS implementeringen af EWP, simuleres et kortsigtet studie for to vindmølleparker i den sydlige del af Nordsøen. Under implementeringen ledte problemer med modeldivergens til afdækningen af trykafhængighed i genereringen af tilfældige tal, hvilket blev rettet, men derudover observeres småskala numerisk støj, hvis effekt på simuleringer kræver yderliger studier.

Alle tre studier peger i retning af at fraværet af påtrykte laterale grænsebetingelser i MPAS fører til betydelige modelafvigelser fra observationer. Dette problem må adresseres i fremtidige studier af forskellige teknikker til data assimilering for, under MPAS simuleringer, løbende at reducere modelafvigelser fra atmosfærens reelle tilstand.

Preface

This thesis was prepared at the Department of Wind Energy at the Technical University of Denmark (DTU Risø Campus) as partial fulfillment for acquiring a PhD degree.

The funding for the PhD program came from internal funds with additional financial support from the ForskEL/EUDP project "OffshoreWake" (PSO-12521).

The three year PhD program included an external stay for four months (April - July 2018) at the Mesoscale & Microscale Meteorology (MMM) Laboratory at the National Center for Atmospheric Research (NCAR) in Boulder, Colorado, US.

DTU Wind Energy (Risø Campus), Roskilde, Denmark,
14. September 2020

M. Imberger

Marc Imberger

Acknowledgements

First and foremost, I would like to thank my principal supervisor Xiaoli Guo Larsén and my co-supervisor Neil Davis for their support, their patient guidance, and the valuable discussions and the feedback during the course of this PhD project. It was a pleasure to have you as supervisors! I also would like to thank Jianting Du, who brought me into the field of wind resource assessment and the RAM section in the first place. I am glad that I followed this track.

At the same time, I would like to thank William C. Skamarock, who kindly hosted my stay at NCAR and provided support during my external stay. Special thanks goes also to Michael Duda from NCAR. Michael Duda provided me not only with the MPAS-A mesh generation code base, which I am very grateful for, but he also shared his invaluable experience and knowledge about MPAS and the art of generating MPAS meshes. Thanks for the scientific help and the common lunch breaks during my time at NCAR! I would also like to thank my office-mates at NCAR, Arianna Valmassoi and Ian Dragaud for the great time we had at NCAR and in Boulder in general!

At DTU, I would like to thank my colleagues from the RAM section for providing such a great working atmosphere within the section. Special thanks goes to Antariksh Chandrashekhar Dicholkar for the numerous and valuable discussions over coffee as well as to Martin Haubjerg Rosgaard for his support in HPC related questions and the translation of the abstract. Thanks for that!

In addition, I want to thank my friends and family for their support. Lastly, I am grateful for the invaluable emotional support from my girlfried Xueqian Zhang who has been by my side since the beginning of the PhD.

Contents

CHAPTER 1

Introduction

1.1 Atmospheric Scales of Motion in the Context of Wind Energy

The Earth's atmospheric motion is characterized by a vast range of spatial and temporal scales (e.g. Orlanski 1975). Scales range from several months and years and thousands of kilometers at the planetary scale to sub-hourly time scales and sub-kilometer length scales at the microscale (Orlanski 1975; Spera 2009; Lackmann 2012). Table 1.1 presents a possible classification of different atmospheric scales based on Lackmann (2012) while Figure 1.1 shows the variance distribution of the horizontal wind speed over a range of temporal scales. Figure 1.1 indicates regions of high variance in the synoptic and mesoscale region (time scales larger than approximately 1 hour) and the microscale region with sub-hourly time scales. The two regions are separated by the so called 'spectral gap' region, which has low wind variation and occurs at the intermediate time scales around one cycle/hour (Van der Hoven 1957; Stull 1988; Larsén et al. 2016). All investigations performed within this study focus on the atmospheric scales of motions in the mesoscale and larger (cf. Table 1.1), not crossing the spectral gap region to the microscale (cf. Figure 1.1).

The multi-scale characteristic of the atmosphere will naturally influence wind turbines, wind energy resources and wind energy utilization over different scales (e.g. Spera 2009; Porté-Agel et al. 2020). Planetary scale features like the Arctic and Antarctic Oscillation have been shown to influence low-frequency wind variability in observations over Minnesota (Klink 2007) and in reanalysis data over South Africa (Bianchi et al. 2017). Synoptic scale phenomena like extratropical cyclones can affect, among others, electrical grid performance and safety (e.g. Artipoli and Durante 2014) and can cause shut-downs of wind farms (e.g. Cutululis et al. 2012). Observational data used as input for an aeroelastic simulator for wind turbines suggest that mesoscale low-level jets can affect static and mechanical wind turbine loads (Gutierrez et al. 2016). Furthermore, mesoscale convective systems like open cellular convection have been found to increase the intra-hourly wind variability, which impacts wind power generation (Vincent 2010; Vincent and Trombe 2017).

Not only are wind turbines affected by the atmosphere, but, in return, wind turbines and wind farms also affect the local atmospheric conditions across different scales. Apart from causing a downwind reduction of wind speed, they can cause vertical mixing (Baidya Roy and Traiteur 2010) and nighttime warming (Baidya Roy and Traiteur 2010; Rajewski et al. 2013). Large Eddy Simulation and limited-area mesoscale modeling of wind farms also suggest that turbines can deflect a low-level jet over the wind

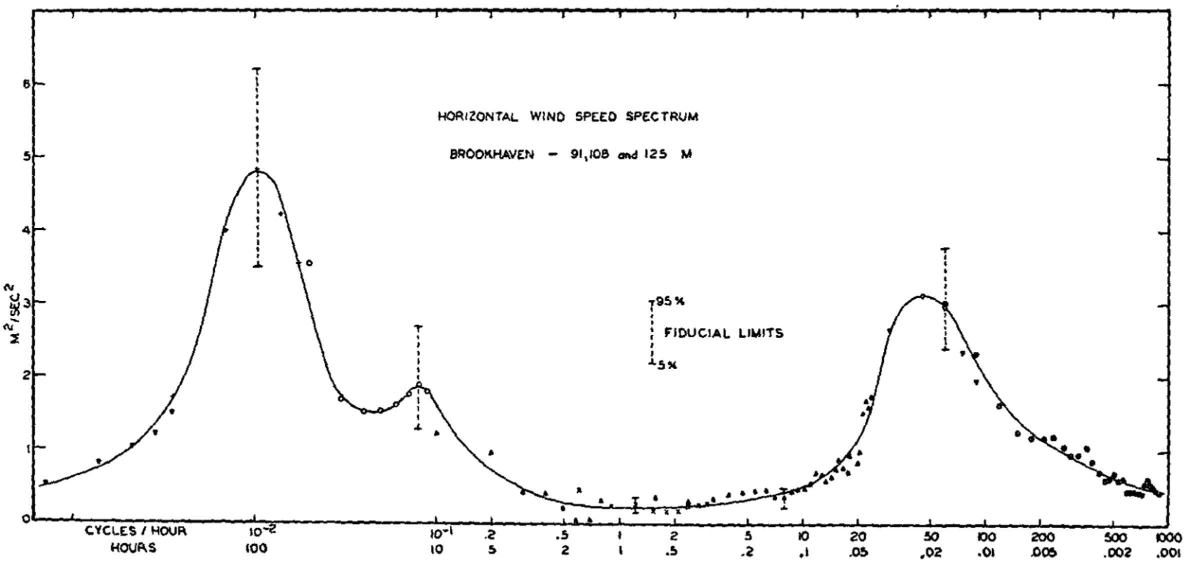

Figure 1.1: Frequency spectrum $fS(f)$ of horizontal wind speed at the Brookhaven National Laboratory as a function of frequency f. Values are obtained at around 100 m height. Reproduced with permission from Van der Hoven (1957).

farm (Abkar et al. 2016), or significantly weaken them at rotor height due to the energy extraction of the wind farm (Fitch et al. 2013a). Numerical investigations with hypothetical wind farms and global atmospheric models suggest that excessive wind farm deployment over large areas has the potential to influence the near-surface climate (Kirk-Davidoff and Keith 2008; Wang and Prinn 2010).

Despite the popularity of grouping atmospheric flows into different classes (e.g. Orlanski 1975; Fujita 1981; Lackmann 2012), sharp separations or abrupt transitions are not common in the atmospheric dynamics, due to the various interactions between different scales of motion (Eliassen 1976). From a modeling perspective, this scale-spanning nature of atmospheric motion and their interactions, set high demands on the adequate and consistent representation of the atmosphere across scales also within the field of wind energy.

Scale Classification	Spatial length scales	Time scales	Examples
Planetary scale	> 6000 km	> week	Trade winds, polar front jet stream, tidal waves
Synoptic scale	1000-6000 km	days to week	Upper-level troughs, cyclones
Mesoscale	1-1000 km	hours to day	Land-sea breezes, nocturnal low-level jets, thunderstorms
Microscale	< 1 km	< 1 h	Turbulence, planetary boundary layer

Table 1.1: Classification of different atmospheric scales of motion based on Lackmann (2012) with additional examples from Orlanski (1975) and Landberg (2015). Classifications marked in **bold** highlight the atmospheric scales focused on in the scope of this work.

1.2 Traditional Modeling Approach Within the Field of Wind Energy

To simulate atmospheric motion over a range of atmospheric scales, including small-scale features, model resolution needs to be high enough to adequately resolve the smaller-scale features (Skamarock 2004), and model domains need to be large enough to ensure the proper representation of the large-scale background flow. The increase in computational power over the last decades has allowed for the development of high-resolution models with global spatial coverage. For example, global operational forecasts are now reaching horizontal grid spacing on the order of 10 km (Neumann et al. 2019).

However, this grid spacing is still insufficient for a direct application to wind resource assessment studies, which require an adequate representation of local atmospheric features, orography and land-sea masks (Sempreviva et al. 2008). For example, the investigation of mesoscale wind variability, introduced by open cellular convection, presented in this study, relies on horizontal grid spacing as small as 2 km to provide an adequate representation of that atmospheric feature (see Chapter 5). Furthermore, the temporal availability of reanalysis and forecast products is also relatively low (Sempreviva et al. 2008).

One commonly used approach to increase model resolution is dynamical downscaling of coarser model simulations using limited-area models (LAMs) like the Weather Research and Forecasting (WRF, Skamarock et al. 2008) model. In WRF, dynamical downscaling is achieved by nesting higher resolution model grids (domains) into parent domains with coarser resolution (Skamarock et al. 2008). This method is known as grid nesting. The individual domains have a structured grid with uniform grid spacing, and the lateral boundary conditions (LBCs) for each nest are interpolated from their corresponding parent domain (Skamarock et al. 2008). The outermost LAM domain receives its LBCs from the externally provided model.

WRF grid nesting is extensively applied within the field of wind energy. It has been used, for example,

- as part of the model tool chain for the generation of wind atlases (Global Wind Atlas[1], New European Wind Atlas[2]),
- for case studies of severe weather events and their impact on wind power production (e.g. Christakos et al. 2016),
- for investigations of spatial and temporal wind variability over different regions and time scales (e.g. studies by Vincent 2010 and Santos-Alamillos et al. 2014),
- for wind speed and power forecasting (e.g. Deppe et al. 2013; Zhao et al. 2017) and
- for numerical studies of wind farm impacts on regional atmosphere and climate (e.g. Fitch et al. 2013b; Vautard et al. 2014; Siedersleben et al. 2018; Tomaszewski and Lundquist 2020; Pryor et al. 2020).

Using limited area models with grid nesting is popular, because the method makes it possible to run high-resolution simulations over a limited area of interest for a fraction of the costs of a global model with similar grid spacing. However, the usage of such models also has disadvantages when modeling across large ranges of the atmospheric scales of motion, which will be discussed below.

One of the main challenges in using limited-area models is the introduction of LBCs. As described in Warner et al. (1997), LBCs introduce boundary errors due to the inevitable differences between the forcing data and LAM results. Additional errors are introduced due to the required spatial and temporal interpolation of the coarser model data and due to the inability for the LAM results to feedback to the forcing model. Interpolation errors can cause distortions and misinterpretations of large-scale structures, like extra-tropical cyclones, when such features are introduced via the LBCs (Gustafsson 1990; Gustafsson et al. 1998; Termonia 2003; Termonia et al. 2009). Differences in the formulations of model physics can also introduce additional inconsistencies between the LAM and the forcing model (Warner et al. 1997).

Another challenge, when using a LAM, is the need to spatially spin-up atmospheric features at scales that are not present in the LBCs due to coarse resolution (Leduc and Laprise 2009), namely spatial spin-up. Leduc et al. (2011) and Matte et al. (2017) have shown that the distance from the LBCs needed to spin-up such features, depends on the size of the resolution jump between the coarse and fine grid, the flow speed, and season. Since discrete and sudden resolution jumps are inherent to the grid nesting approach (Park et al. 2014), spatial spin-up cannot be avoided and can result in regions of insufficiently resolved structures inside the LAM (Leduc and Laprise 2009; Leduc et al. 2011; Matte et al. 2017).

A more detailed discussion of challenges related to LBCs and dynamical downscaling with limited-area models can be found in Davies (2014), Hong and Kanamitsu (2014), and Davies (2017).

These challenges are particularly important for modeling across scales, which helps

[1] available at `https://globalwindatlas.info`, last accessed: August 2020
[2] available at `https://map.neweuropeanwindatlas.eu/`, last accessed: August 2020

to motivate the investigation of alternative strategies. Promising candidates for this purpose are global models with variable-resolution. They avoid the challenges associated with LBCs, while still allowing high resolution in the area of interest (e.g. Fox-Rabinovitz et al. 2008; Sakaguchi et al. 2015). The lack of artificial boundaries also allows for the consistent application of model physics and permits consistent interactions across atmospheric scales of motion (e.g. Fox-Rabinovitz et al. 2008; Sakaguchi et al. 2015).

1.3 Atmospheric Modeling Across Scales with Global Variable-resolution Models

There are a variety of global models that employ a variable-resolution approach, using a variety of model discretization techniques that allow for variable-resolution (see examples in Fox-Rabinovitz et al. 2008 and Ullrich et al. 2017). One such model, is the Model for Prediction Across Scales (MPAS, more details in Chapter 2).

MPAS is based on an unstructured grid based on Spherical Centroidal Voronoi Tessellations (SCVTs) that allow flexible mesh configurations with smooth mesh refinement (Ju et al. 2011). In contrast to other mesh refinement strategies like grid-stretching (e.g. Fox-Rabinovitz et al. 2008 and references therein), the unstructured MPAS mesh allows multiple refinement regions and refinement without simultaneously decreasing grid spacing in other regions (Ringler et al. 2011). Furthermore, MPAS' SCVT discretization also avoids other problems like mesh singularities and resolution clustering seen for instance in full latitude-longitude grids or cubed-sphere grids (Staniforth and Thuburn 2012).

The impact of MPAS' variable-resolution mesh on atmospheric flows has been explored using its atmospheric component (MPAS-A, Skamarock et al. 2012) in a range of idealized (e.g. Skamarock et al. 2012; Park et al. 2013; Park et al. 2014; Martini et al. 2015) and real case applications in hydrostatic scales (e.g. Heinzeller et al. 2016; Hashimoto et al. 2016; Michaelis et al. 2019; Michaelis and Lackmann 2019). More recently, MPAS-A has also been explored in convection-permitting scales for a broad range of applications, some of which are summarized below.

Fowler et al. (2016), implemented and investigated the behavior of the scale-aware Grell-Freitas convection scheme (Grell and Freitas 2014) on a 50 km mesh with regional refinement down to 3 km over South America. The authors performed four-day forecasts and looked, among others, on the partitioning of convective and grid-scale precipitation. They showed that the gradual refinement provides a smooth transition in the composition of convective and grid-scale precipitation also in scales associated with the gray-zone within the transition region.

Pilon et al. (2016) investigated the impact of deep and shallow convection parameterizations on the hind-cast of a Madden-Julian oscillation (MJO) event. The authors analyzed different cumulus scheme configurations on a 60 km mesh, a 15 km mesh and on a regionally refined 50-3 km mesh over the Indian Ocean and compared the results with sounding observations. The authors found that the reproduction of two intense rain events traveling eastwards substantially depends on the representation of deep convection. In the case of the scale-aware Grell-Freitas scheme, only a simulation with mesh refinement down to 3 km was able to reproduce the event due to explicitly resolved deep convection.

Promising results with MPAS-A mesh refinement have also been shown in Kramer et al. (2018). They used local refinement over the European continent to analyze three different weather events: a synoptic gale event, a föhn effect and an extreme hail event. The authors investigated three regionally refined meshes with 3 km cell spacing (60-3 km, 30-3 km and 15-3 km mesh) and one quasi-uniform 3 km mesh. They found that the MPAS-A meshes with local refinement show a comparable forecast accuracy to the most expensive global 3 km mesh. However, they also point out that the performance of the individual mesh configurations differ from case to case.

Huang et al. (2019) used a multi-refined 60-15-3 km approach to investigate track deflections of Typhoon 'Netsat' and found better agreement with respect to the northward deflection compared to regional area simulations with nested domains in WRF.

However, MPAS-A has not been explored within the field of wind energy and this knowledge gap has motivated the theme and the research questions that define scope of this PhD study.

1.4 Research Questions and Thesis Framework

The leading theme of this PhD project is the investigation of the global MPAS-A model for potential applications within the field of wind energy, with a focus on exploring the regional mesh refinement. The following research questions guided the framework of the project:

1. Where and to what extent can MPAS-A improve the traditional modeling strategy (limited-area modeling with grid nesting)?
2. What are the limitations and challenges faced in the application of the global MPAS-A compared to the traditional modeling strategy?

Driven by the above mentioned leading questions, MPAS-A has been investigated in three major case studies relevant for wind energy applications. The investigations of two of the case studies (**Chapter 4** and **Chapter 5**) expand on two peer-reviewed journal publications that will be further referred to as *P1* and *P2*:

P1 Imberger, M., Larsén, X. G., Du, J., Davis, N. **Approaches toward improving the modelling of midlatitude cyclones entering at the lateral boundary corner in the limited area WRF model (2020)**. *Quarterly Journal of the Royal Meteorological Society.* DOI:10.1002/qj.3843 (accepted/in press)

P2 Imberger, M., Larsén, X. G., Davis, N. **Investigation of Spatial and Temporal Wind Variability during Open Cellular Convection with the Model For Prediction Across Scales (MPAS) in Comparison with Measurements**. *Boundary-Layer Meteorology (accepted with minor revisions)*

They are briefly introduced in their corresponding chapter and pre-prints are attached in Appendix A and Appendix B for further reading. A complete list of dissemination activities and publications during the PhD project that are not directly part of this report can be found in Appendix C.

The detailed outline of the thesis is as follow:

An introduction to the MPAS modeling framework and its mesh discretization is presented in **Chapter 2** while **Chapter 3** presents key findings from the MPAS mesh generation phase performed as part of this project. The mesh generation process is a crucial element for an efficient and successful application of MPAS-A. The next three chapters focus on wind energy related case studies.

Chapter 4 deals with the simulation of a mid-latitude cyclone and elaborates on the effect of LBCs in the traditional modeling strategy on key simulation results, like storm intensity and location. Paper *P1* is introduced in this chapter, and parallel investigations using MPAS-A and WRF are presented and compared.

Chapter 5 presents results of a case study of open cellular convection (OCC) over the North Sea and discusses to what extent MPAS-A is able to represent the spatial and temporal wind speed variability associated with the OCC. This chapter also introduces Paper *P2*.

Chapter 6 looks deeper into the potential application of MPAS-A for wind farm impact studies on the atmosphere and elaborates on some of the modeling challenges faced during the investigation.

The thesis finalizes with concluding remarks and a general outlook regarding MPAS-A for wind energy purposes in **Chapter 7**.

CHAPTER 2
The Model For Prediction Across Scales (MPAS)

This chapter aims to provide a general introduction to MPAS and its atmospheric component MPAS-A. It describes the concept of Spherical Centroidal Voronoi Tessellations and other key features which distinguish the model from limited-area modeling with WRF or are seen crucial for the understanding of the investigations presented in Chapter 3 to Chapter 6.

2.1 Background

MPAS consists of a collection of independent modeling environments (also called MPAS *cores*) for different parts of Earth's physical systems like atmosphere, ocean, land or land/sea ice, which are developed under a large collaborative project between the Los Alamos National Laboratory and the National Center for Atmospheric Research (Skamarock et al. 2012). The independent environments are build around a commonly shared MPAS *framework*. The framework contains components that deal with parallel input/output, timekeeping, and memory parallelization, as well as other common model tasks. A more complete description of the MPAS *cores* and *framework* can be found in Turner et al. (2018) and Duda et al. (2019).

Within the scope of the PhD, only the atmospheric component of the global Model For Prediction Across Scales (MPAS-A, Skamarock et al. 2012) is used. For the sake of simplicity, all further references to MPAS refer to the atmospheric component and shared framework only.

2.2 Dynamical Core and Mesh Discretization

MPAS is a finite volume, non-hydrostatic and fully compressible model (Skamarock et al. 2012), that solves the underlying governing equations on a mesh discretization based on Spherical Centroidal Voronoi Tessellation (SCVTs, Du et al. 1999; Du et al. 2003a).

Fundamentally, SCVTs are based on ordinary Voronoi tessellations. Given an initial set of n points (or Voronoi generators) on a surface, a Voronoi tessellation divides the surface into n sub-regions (also known as Voronoi regions or Voronoi cells) with the following characteristic: each Voronoi region, belonging to a particular generator, encloses all points on the surface that are closest to that generator (e.g. Du et al. 1999; Ju et al. 2011). Figure 2.1a shows an example of a Voronoi tessellation for a given number of generators on a 2D-plane. In 2D, the Voronoi regions create polygonal regions. The dual graph to the Voronoi tessellation is called a Delaunay tessellation, which consists of triangles in 2D (e.g. Du et al. 1999; Ju et al. 2011). The dual Delaunay tessellation is, for example, used in the bisection routine and the determination of the local mesh regularity in the mesh generation algorithm (further details in Section 3.1.2). A more comprehensive definition of Voronoi and Delaunay tessellations can be found in Du et al. (1999) or Okabe et al. (2000).

Centroidal Voronoi tessellations add a requirement that the initial set of Voronoi generators are also identical to the centroids (or center of mass) of each Voronoi region with respect to a mesh density function ρ (e.g. Ju et al. 2011). The mesh density functions used in this project are described in Section 3.1.1. An example of a Centroidal Voronoi tessellation is given in Figure 2.1b. SCVTs describe a generalized version of Centroidal Voronoi tessellations on a sphere (Okabe et al. 2000; Du et al. 2003a), and belong to the category of unstructured meshes (Ringler et al. 2010).

One of the major advantages of SCVTs is, that they allow both quasi-uniform meshes and meshes with regional refinements (e.g. Du et al. 2003a; Skamarock et al. 2012). Figure 2.2a shows an example of a quasi-uniform SCVT, while Figure 2.2b depicts an example of an SCVT with regional refinement over Europe. More details about the definition of refinement regions and the generation of SCVTs will be presented in Section 3.1.1 and Section 3.1.2.

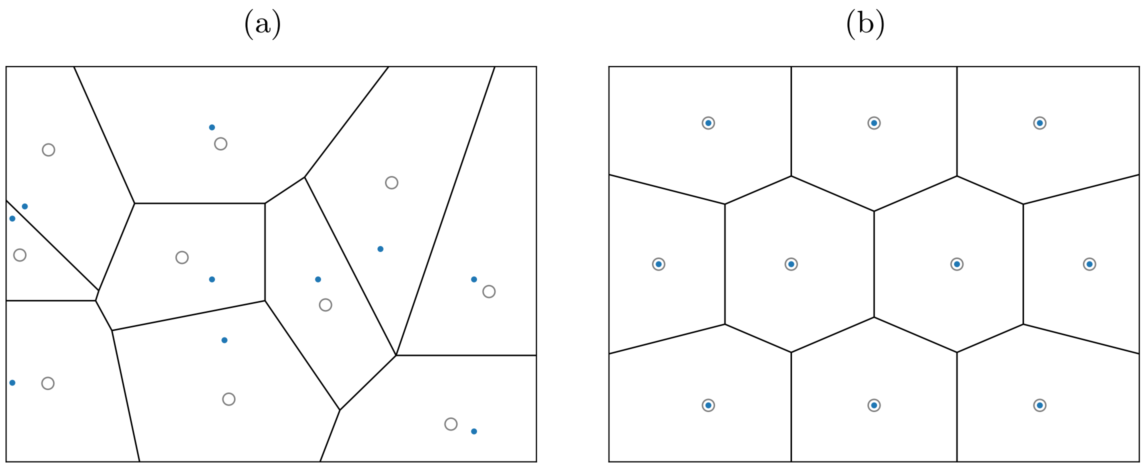

Figure 2.1: Conceptual sketch of (a) an ordinary Voronoi tessellation where the center of mass (gray circles) and Voronoi generators (blue dots) do not necessarily coincide and (b) a Centroidal Voronoi tessellation, where center of mass (gray circles) and Voronoi generators (blue dots) are identical. The density function ρ is assumed to be constant. Figure inspired from Du et al. (1999).

In MPAS, the staggering of model state variables on the SCVT follows an unstructured C-grid staggering method following Thuburn et al. (2009) and Ringler et al. (2010). The method is illustrated in Figure 2.3. In this staggering method, scalar variables (like potential temperature, pressure) are defined at the cell centers, while velocities are de-

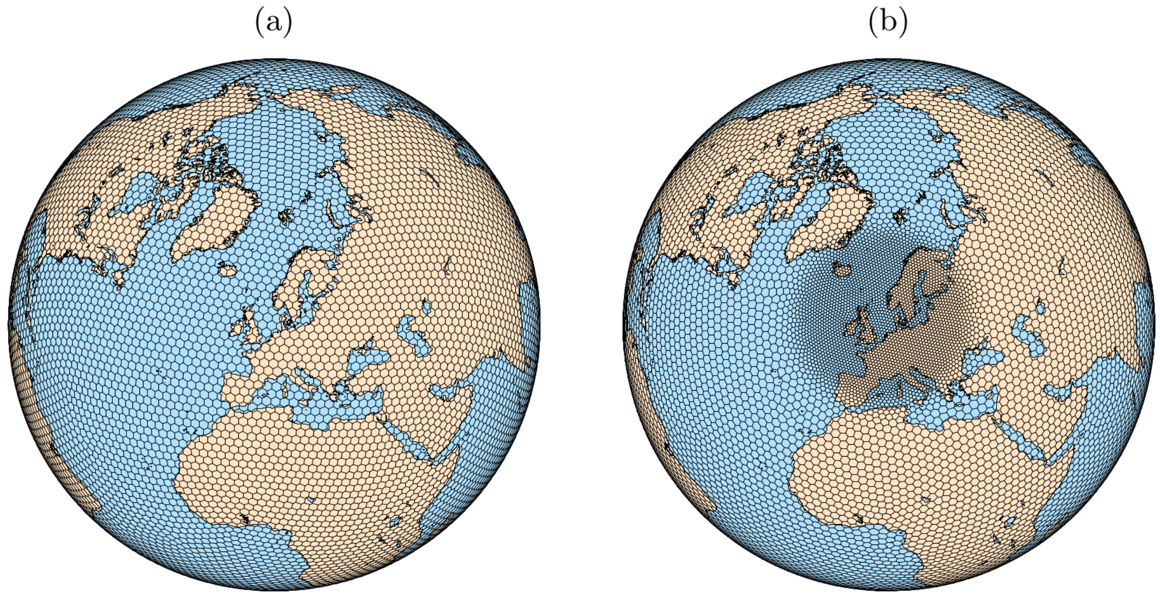

Figure 2.2: Examples of Spherical Centroidal Voronoi Tessellations suitable for MPAS: (a) quasi-uniform SCVT, (b) SCVT with gradual refinement over Europe.

fined as normal velocities on the cell faces. Vorticity (absolute and relative) is defined on cell vertices (orange dots in Figure 2.3, Thuburn et al. 2009; Skamarock et al. 2012). Figure 2.3 also highlights the dual graph to the underlying Voronoi tessellation, the Delaunay tessellation (e.g. Engwirda 2017). The cell centers of the Voronoi tessellation coincide with the cell vertices of the dual Delaunay tessellation and the cell vertices of the Voronoi tessellation coincide with the cell centers of the dual Delaunay tessellation (Thuburn et al. 2009).

In the vertical, MPAS uses a generalized hybrid coordinate system (or smoothed terrain following coordinate, see Klemp (2011)). It is formulated in (geometric) height-based coordinates, in contrast to the pressure-based formulations used in WRF (Skamarock et al. 2008). The height of vertical levels $z(x, y, \zeta)$ at a certain location is defined in Klemp (2011) as follows:

$$z(x, y, \zeta) = \zeta + A(\zeta)h_s(x, y, \zeta), \tag{2.1}$$

ζ is the terrain-independent height between 0 m (surface) and model top z_t, $A(\zeta)$ is a control parameter of the total terrain influence and $h_s(x, y, \zeta)$ is a smoothed representation of the model terrain $h(x, y)$ with $h_s(x, y, 0) = h(x, y)$. $h_s(x, y, \zeta)$ controls the removal rate of small-scale terrain effects at higher levels by smoothing the terrain representation $h_s(x, y, \zeta)$ with increasing height. $A(\zeta)$ is used to control the relaxation of the vertical levels from purely terrain following levels at the surface to levels of constant height (Klemp 2011). For further details about the method and details about terrain smoothing algorithms and proposed $A(\zeta)$ profiles, the reader is referred to Klemp (2011).

The governing equations in MPAS are formulated in flux form with the following prognostic variables: dry-air density ρ_d, horizontal and vertical momentum (ρ_du and

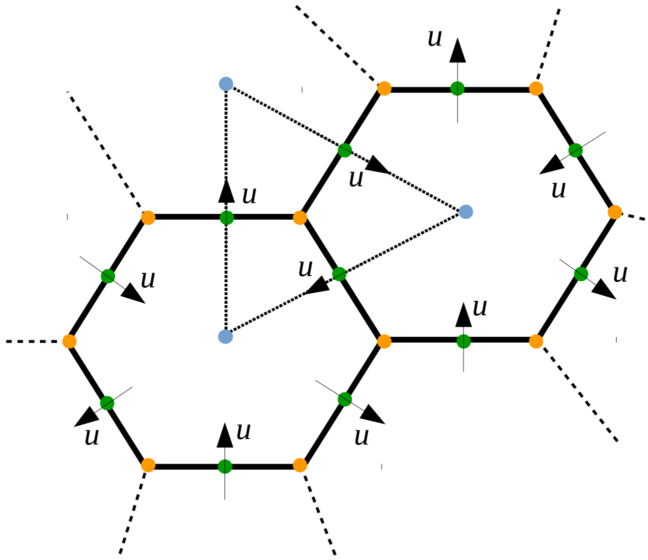

Figure 2.3: Location of C-grid staggered variables on the SCVT: cell centers (blue), cell vertices (orange) and cell faces (green). Horizontal velocities are defined as normal velocities at cell faces (black arrows). The dotted lines outline one region of the Delaunay triangulation dual graph.

ρ_dw, respectively), the coupled form of the modified potential temperature ($\rho_d\theta_m$) and the coupled form of the mixing ratios of the different water species ($\rho_d q_c$, $\rho_d q_v$,...). More details can be found in Skamarock et al. (2012) and Klemp et al. (2007)

2.3 Model Physics

MPAS' physic schemes are a subset of the physics schemes in the Advanced Research WRF model (Duda et al. 2019). With the release of MPAS V4.0, the concept of physics *'suites'* was introduced. Physics suites provide a bundle of individual physic schemes that have been successfully tested together (Duda et al. 2019). In MPAS V7.0, which is the version used within this project, three suites are available (Duda et al. 2019):

- The *'mesoscale_reference'* suite, which is designed for mesh grid spacing of 10 km and larger.
- The *'convection_permitting'* suite that allows applications in convection-permitting scales (grid spacing below 10 km). This suite contains the scale-aware Grell-Freitas cumulus scheme (Grell and Freitas 2014; Fowler et al. 2016) that transits from a deep convection scheme at hydrostatic scales to a shallow convection scheme at non-hydrostatc scales (Fowler et al. 2016).
- The *'none'* suite, which disables all physics schemes for idealized simulations.

Table 2.1 provides an overview of model physics within the *'convection_permitting'* and *'mesoscale_reference'* suite. In addition to the suites, a limited list of additional physics schemes are available as well. This includes, for example, the Kain-Fritsch cumulus parameterization scheme (Kain 2004) or the radiation scheme of the NCAR Community Atmosphere Model (Collins et al. 2004). A complete list of available physics schemes in MPAS V7.0 can be found in Duda et al. (2019).

Table 2.1: List of model physics within the *'convection_permitting'* and the *'mesoscale_reference'* suite. Used abbreviations: GF: Scale-aware Grell-Freitas (Grell and Freitas 2014), NT: New Tiedtke (Zhang et al. 2011; Zhang and Wang 2017), TMS: Thompson non-aerosol aware (Thompson et al. 2008), WSM6: WRF Single-Moment 6-Class (Hong and Lim 2006), MYNN: Mellor–Yamada–Nakanishi–Niino (Nakanishi and Niino 2009), YSU: Yonsei University Scheme (Hong et al. 2006), MM5: Revised MM5 similarity scheme (Jiménez et al. 2012), RRTMG: Rapid Radiative Transfer Model for General Circulation Models (Iacono et al. 2008).

Physics	*'convection_permitting'*	*'mesoscale_reference'*
Cumulus	GF	NT
Microphysics	TMS	WSM6
Land surface	Noah†	Noah
Boundary layer	MYNN	YSU
Surface layer	MYNN	MM5
Long-/shortwave radiation	RRTMG	RRTMG

† Niu et al. (2011) and Yang et al. (2011)

CHAPTER 3
MPAS Mesh Design and Performance

As mentioned in Section 1.4, the work within this PhD project is centered around the Model for Prediction Across Scales and one key element when designing studies that utilize the great potential of MPAS is the identification or generation of a suitable mesh for a given application.

Within the scope of this project, a full mesh assessment has been carried out, which includes the mesh design stage, the mesh generation stage, and the mesh characterization and quality assessment stage. This chapter summarizes some of the key findings during this process and the outline of the chapter is as follow: Section 3.1 gives an overview over the used methodology. Section 3.2 states the key findings from the the mesh design stage, mesh generation stage and mesh characterization and quality assessment stage of the project. The chapter finalizes with a summary of concluding remarks in Section 3.3.

3.1 Methods

3.1.1 Design of Mesh Density Function

As mentioned in Chapter 2, the mesh density function ρ is one of the key parameters for the design of SCVTs. It describes the local spacing of Voronoi generators/regions over the sphere (Ringler et al. 2011). A constant mesh density function (e.g. $\rho = 1$) results in a quasi-uniform SCVT with an approximately equal distribution of Voronoi regions over the sphere. A location dependent mesh density function results in an SCVT with more Voronoi regions in the locations of higher mesh density. The mesh density function can take many forms, depending on the application, with the main requirement being that it is positive-definite ($\rho > 0$, Du et al. 1999).

The most commonly used MPAS mesh refinements are circular refinement regions as depicted in Figure 2.2b. They have been widely explored in both idealized configurations (e.g. Ringler et al. 2011; Rauscher et al. 2013; Zhao et al. 2016; Rauscher and Ringler 2014), and have also shown good performance in real world applications (e.g. Fowler et al. 2016; Wong and Skamarock 2016; Kramer et al. 2018).

Non-circular refinement regions are also found in literature, including tropical refinement channels (Martini et al. 2015), double-refinement regions with an intermediate mesh density plateau (Huang et al. 2019), and different resolutions on each Hemisphere (Michaelis et al. 2019; Michaelis and Lackmann 2019). Within the scope of this project, only circular mesh refinements have been explored.

In the case of circular refinement regions, the mesh density $\rho(x)$ at a location x depends on the spherical distance $\|x_c - x\|$ from the center of the refinement region x_c. Park et al. (2014) proposed an analytical mesh density function based on the hyperbolic tangent function with three parameters (notation follows Park et al. 2014):

$$\rho(x) = \frac{1-\gamma}{2}\left[\tanh\left(\frac{\beta - \|x_c - x\|}{\alpha}\right) + 1\right] + \gamma, \tag{3.1}$$

where α represents the width of the transition zone between the high resolution and coarse resolution regions, β describes the scale of the refinement region and $\gamma > 0$ describes the minimum mesh density. ρ is limited between 1 (high resolution region) and γ (coarse resolution region). Since the relative resolution of the SCVTs is of higher interest than the actual underlying density function, the minimum density as free parameter is relatively impractical. One way to estimate a suitable value for the minimum mesh density can be obtained from the approximate relation in Du et al. 2003b. It relates the relative mesh resolution with the mesh density at two locations i and j as follows:

$$\frac{h_i}{h_j} \approx \left(\frac{\rho(x_j)}{\rho(x_i)}\right)^{\frac{1}{4}}. \tag{3.2}$$

By defining r as the refinement factor between the mesh resolution in the coarse resolution region (i.e. $\rho(x_i) \approx \gamma$) and the high resolution region (i.e. $\rho(x_j) \approx 1$), Equation 3.2 can be written as:

$$r = \frac{h_{\text{coarse}}}{h_{\text{fine}}} \approx \left(\frac{1}{\gamma}\right)^{\frac{1}{4}} \tag{3.3}$$

or:

$$\gamma \approx \left(\frac{1}{r}\right)^{4} \tag{3.4}$$

Within this project, Park et al. (2014)'s mesh density function (Equation 3.1) and Equation 3.4 were used to generate a variety of mesh density configurations. Table 3.1 summarizes the parameter settings for α, β, and γ that were selected in this study for the different mesh configurations.

The selection of the transition zone widths $\alpha = 0.04$ and $\alpha = 0.16$ was inspired by the two mesh configurations MPAS-TRW and MPAS-TRN used in Park et al. (2014), which showed good performance, without apparent wave distortions or reflections in an idealized configuration (Park et al. 2014). The values for γ were defined by the desired refinement factors of approximately three and 30 for the investigations in Chapter 4 and Chapter 5, respectively. The values for the refinement zone width β were selected based on a compromise between the required spatial extend of the refinement zone and the associated computational costs of large refined areas.

Figure 3.1 shows the density functions of the variable-resolution mesh configurations presented in Table 3.1. Figure 3.1 illustrates the main characteristics of circular refined variable-resolution meshes:

- the presence of two plateaus at $\rho \approx 1$ and $\rho \approx \gamma$, which define the the fine and coarse resolution region respectively, and

Name of mesh density function	α [.]	β [.]	γ [.]
ρ_{x30}	0.04	0.105	$(1/30)^4$
$\rho_{\mathrm{x30,sm}}$	0.16	0.05	$(1/30)^4$
ρ_{x3}	0.04	0.314	$(1/3)^4$
MPAS-TRW (Park et al. 2014)	0.148	0.784	$(1/3)^4$
MPAS-TRN (Park et al. 2014)	0.038	0.717	$(1/3)^4$

Table 3.1: Parameter settings for mesh density functions ρ_{x30}, $\rho_{\mathrm{x30,sm}}$ and ρ_{x3} designed in this study and the settings of the two mesh configurations used in Park et al. (2014) (MPAS-TRW and MPAS-TRN): Transition zone width α, width of the refined region β and minimum mesh density parameter γ.

- a gradual change in mesh density between the two plateaus, resulting in a transition region between the coarse and fine scale resolution.

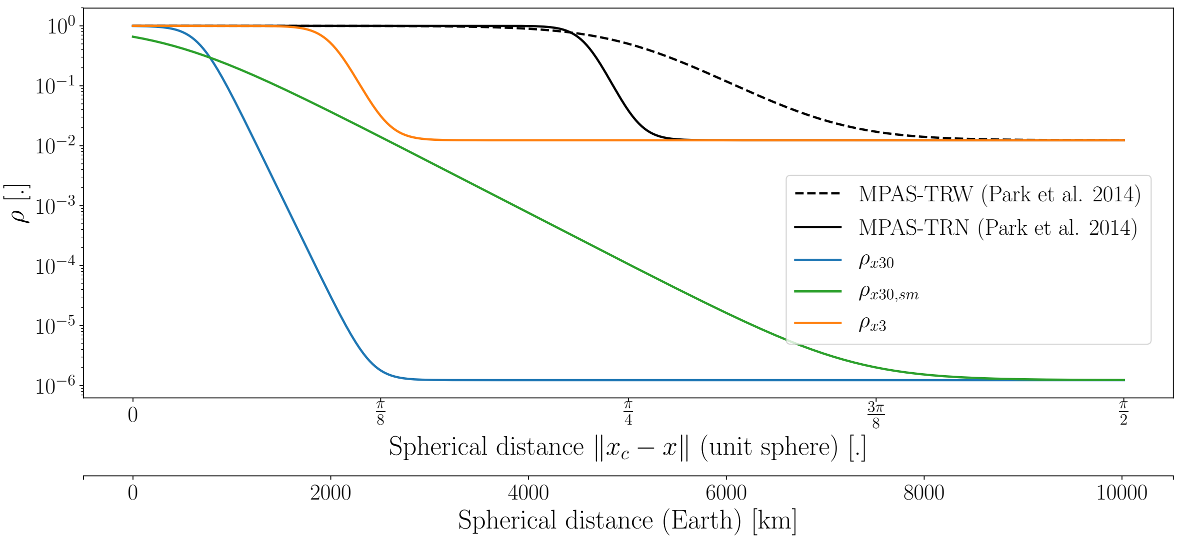

Figure 3.1: Mesh density functions of the variable-resolution mesh configurations from Equation 3.1 with the parameters for α, β, and γ from Table 3.1.

In comparison to the mesh configurations in Park et al. (2014), the generated meshes within this study have a much smaller refined region (in all cases). In the case of ρ_{x30}, the circular refinement region has a radius of approximately 140 km and a transition zone width of approximately 1800 km, while ρ_{x3} has a refinement region radius of approximately 1400 km and a transition zone width of approximately 2800 km (Figure 3.1). In the case of $\rho_{\mathrm{x30,sm}}$, there is no clear refinement region defined (no density plateau where $\rho \approx 1$) and the very wide transition zone width extends to about 9000-9500 km. The density function $\rho_{\mathrm{x30,sm}}$ was used for the testing of the mesh generation routine and was not applied to any real case application.

The design of the mesh density function will indirectly affect the computational efforts associated with the MPAS mesh, since the formulation defines the relative ratio between the coarse resolution region (computationally cheap) and the fine scale region (computationally expensive), and how wide/narrow the transition zone will be.

3.1.2 Mesh Generation Utility

This subsection introduces the mesh generation algorithm that has been applied for all SCVT generations performed this project. The implementation is based on a slightly modified version of the currently unpublished[1] MPAS-A mesh generation utility developed at the National Center for Atmospheric Research (see also Acknowledgments section). It performs the calculation of the SCVTs on the unit sphere, and uses the STRIPACK (Renka 1997) software package to calculate the Voronoi and Delaunay tessellations.

The underlying algorithm for the SCVT generation is *Lloyd's Method* (Lloyd 1982; Du et al. 1999; Du et al. 2003b) which consists of the following steps:

Lloyd's Method

---

1. Chose an initial set of k points as Voronoi generators $\{\mathbf{z_i}\}_{i=1}^{k}$ on the domain Ω
2. Construct the Voronoi tessellation of Ω associated with $\{\mathbf{z_i}\}_{i=1}^{k}$
3. Determine for each Voronoi region $\{V_i\}_{i=1}^{k}$ the mass centroids $\{\mathbf{m_i}\}_{i=1}^{k}$
4. Use $\{\mathbf{m_i}\}_{i=1}^{k}$ as $\{\mathbf{z_i}\}_{i=1}^{k}$
5. Repeat Step 2-4 until a certain termination criteria is reached

---

The termination criteria used for *Lloyd's Method* (Step 5) is based on the average euclidean distance $\bar{d}$ between the estimated mass centroids at iteration $l-1$ and l and is formulated as follows:

$$\bar{d} = \frac{1}{n}\sum_{i=1}^{n}\sqrt{\left(m_{i_x}^{l-1} - m_{i_x}^{l}\right)^2 + \left(m_{i_y}^{l-1} - m_{i_y}^{l}\right)^2 + \left(m_{i_z}^{l-1} - m_{i_z}^{l}\right)^2} < \epsilon \tag{3.5}$$

A threshold value of $\epsilon = 1.0 \times 10^{-10}$ is selected for all SCVTs which was found to be an appropriate choice for convergence threshold (Michael Duda, NCAR, personal communication).

While it is possible to directly apply *Lloyd's Method* to create a SCVT with an arbitrary number of Voronoi generators, experience (MPAS Tutorial 2019) has shown that an incremental production of the SCVT, in a recursive process, results in the faster generation of higher quality. The initial SCVT to start the recursion (M_0) is obtained from the direct application of *Lloyd's Method* on a very small set of Voronoi generators (on the order of 100), which is computed quickly due to the low number of generators. For the subsequent steps in the recursive process, the initial set of points in Step 1 of *Lloyd's Method*, for a mesh M_{k+1}, are deliberately chosen from a bisected version of

[1]as of June 2020

the previously produced SCVT M_k (Du et al. 2003b). Due to the bisection, the newly generated SCVT M_{k+1} will automatically have twice the absolute resolution of M_k and $4n-6$ Voronoi generators/cells, where n is the number of Voronoi generators on the M_k mesh.

In addition to the convergence criteria, the SCVTs must fulfill a second criteria to be usable in MPAS: It is required that the corresponding Delaunay dual mesh of the generated SCVT is completely free of obtuse triangles. This is required, because the presence of obtuse triangles breaks down the reconstruction of the discrete vorticity variable, which requires that each Voronoi vertex is located inside their parent Delaunay triangle (Engwirda 2017).

In this study, the mesh generation utility was slightly modified, such that it would regularly output the number and geographic location of obtuse triangles during the iteration process. This was beneficial for sorting out or modifying mesh configurations during an early stage. Obtuse triangle were mainly found in configurations where the refinement zone was too narrow in comparison to the number of Voronoi generators used (highly distorted Voronoi regions).

Figure 3.2 shows an example of the convergence graph for one of the smaller generated meshes. It can be seen that the average euclidean distance between mass centroids does not decrease monotonously, but is characterized by occasional spikes. The spikes indicate major graph reorganizations for example, the creation/destruction of cell edges during the iteration process.

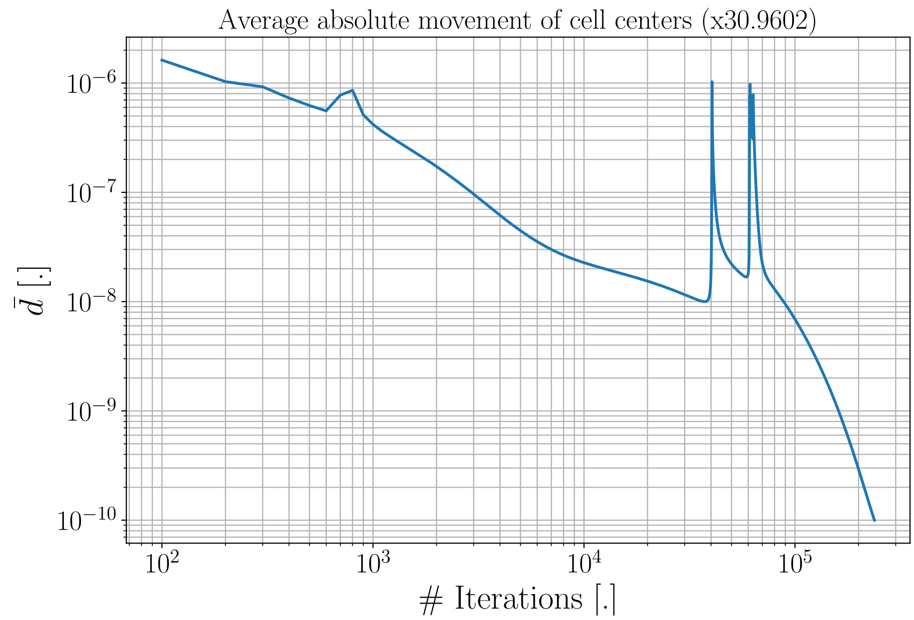

Figure 3.2: Global average absolute movement of cell centers during the iterative creation process of a SCVT exemplified for the mesh with density function $\rho_{\mathrm{x30,sm}}$ and 9602 Voronoi generators. The spikes seen around 8×10^2, 4×10^4 and 6×10^4 iterations indicate major mesh reorganizations during the generation process.

This emphasizes the importance that the threshold value ϵ needs to be set such that any necessary mesh reorganizations can occur.

3.1.3 Local Uniformity Index

For the quantification of local uniformity, the Voronoi cell quality measure or σ as described in Ringler et al. (2008) is used in this study. It is further referred to as the Local Uniformity Index (LUI). For each Voronoi region V_i, $\sigma(V_i)$ is defined as the ratio between the minimum and maximum distance from the Voronoi generator $\mathbf{x}_i$ to the Voronoi generators $\mathbf{x}_j$ of all of its neighbor regions V_j:

$$\sigma(V_i) = \frac{\min_j \|\mathbf{x}_i - \mathbf{x}_j\|}{\max_j \|\mathbf{x}_i - \mathbf{x}_j\|} \leq 1 \tag{3.6}$$

$\sigma(V_i) = 1$ indicates equilateral polygons (all distances have the same length) while $\sigma(V_i) \ll 1$ indicates highly skewed polygons.

3.1.4 Idealized Test Cases

Two idealized simulation setups (I1 and I2) are used in this study to assess the quality of a given generated mesh before further application.

I1 describes the Jablonowski and Williamson 2006 baroclinic wave test version without initially perturbed initial conditions (balanced initial flow field). While the test was originally developed to test dynamical core configurations, it can also be applied to investigate the models capability of maintaining the steady-state initial conditions (Jablonowski and Williamson 2006). Degradation of the initial state is caused by gravity waves, numerical round-off, and truncation errors (Jablonowski and Williamson 2006). The latter effect is enhanced around regions with strong local mesh distortion (Ringler et al. 2011), making this test well suited for the detection of unacceptable local mesh distortions.

I2 is an extended version of the Jablonowski and Williamson (2006) baroclinic wave test version with initial zonal wind perturbation, further described in Park et al. (2013) and Park et al. (2014). In I2, the originally unbalanced initial perturbation in Jablonowski and Williamson (2006) is replaced by a perturbation in the zonal wind field at zonal wavenumber 9 (Park et al. 2013). This test suite is well suited for the detection of deviations in the model solutions caused by the variable-resolution region (Park et al. 2014). It is also useful for the detection of wave reflections and distortions (Park et al. 2014), and could therefore help identify improper mesh designs.

For both I1 and I2, all generated SCVTs are rotated in such a way that the center point of the fine scale resolution region is located at 45°N 0°E prior to application.

3.2 Results and Discussion

3.2.1 Effect of Density Function and Voronoi Generators on Grid Cell Distances

Figure 3.3 depicts the relative distribution of grid distances for three of the meshes generated in this study. They are based on the same mesh density function (Figure 3.1, orange line), but have different numbers of Voronoi generators. It can be seen that the relative distribution of grid distances looks similar in all three realizations, while the absolute values of the grid distance statistics (minimum, maximum, mean, median) change. Around 15,000 Voronoi generators are enough to produce a variable-resolution mesh with a median grid distance distribution of around 212 km for the given mesh density function, but more than 60,000 Voronoi generators are needed to reduce the median by a factor of 2. Additionally, it can be seen that an increase in the number of Voronoi generators reduces the grid distances in all regions of the mesh (the refined region, the transition zone, and the coarse resolution region). These results highlight the importance of the mesh density function, which fixes the relative grid distance of the underlying SCVTs, while the number of Voronoi generators/regions can only influence the absolute grid distances of the SCVTs.

Figure 3.4 shows the histogram of a mesh configuration based on ρ_{x30} (Figure 3.1, blue line) and 901123 Voronoi generators. In contrast to the mesh configurations depicted in Figure 3.3, this mesh configuration is dominated by the number of cells within the refinement region. 50% of the cells in this configurations have a cell spacing of 3 km and smaller.

The absolute number of Voronoi generators has a direct influence on the computational requirements associated with the MPAS mesh, both through the number of computational cells, and the maximum model time step, which is limited by the Courant-Friedrichs-Lewy (CFL) condition.

This limitation to a single time step will also affect the computational efficiency of the solver, especially for mesh configurations where most of the grid cells are not inside the refinement zone (Park et al. 2013). In the case of the mesh configuration in Figure 3.3a, the time step is set by the smallest grid distance of around 60 km, while more than 50% of the cells have a cell spacing of around 210 km and larger (factor of 3.5). This results in a computationally unnecessary short time step for most of the cells. If the majority of the grid cells are however located within in the refinement zone (e.g. the configuration depicted in Figure 3.4), the effect of the fixed time step is reduced (distance between minimum grid distance and median grid distance is smaller).

Figure 3.3 and Figure 3.4 show that both the refined and the coarse scale region actually consist of a range of grid distances even though the mesh density varies little in those regions (cf. Figure 3.1). This illustrates the high sensitivity of the overall structure of the cell center distance distribution on the mesh density formulation.

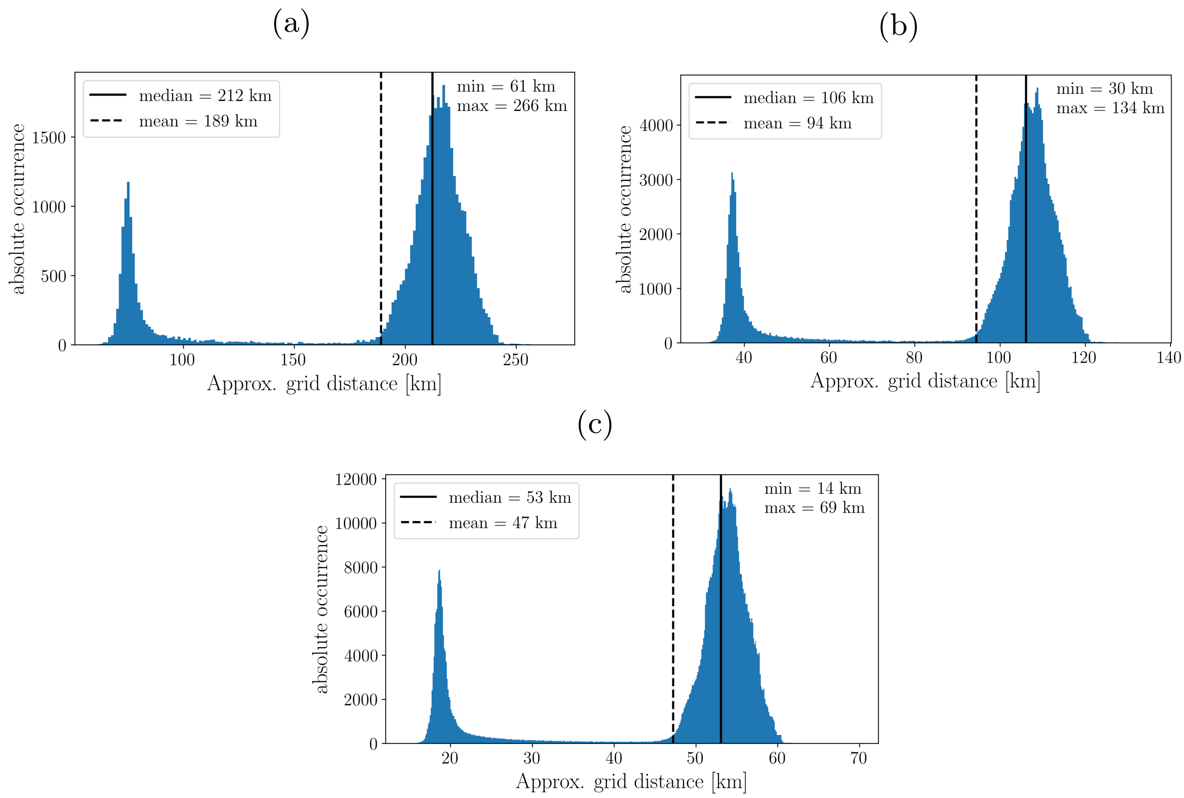

Figure 3.3: Histogram of cell center distances of three SCVTs with identical mesh density function but with (a) 15362, (b) 61442 and (c) 245762 Voronoi generators. Be aware of the different scales in the x-axis and y-axis of the plots.

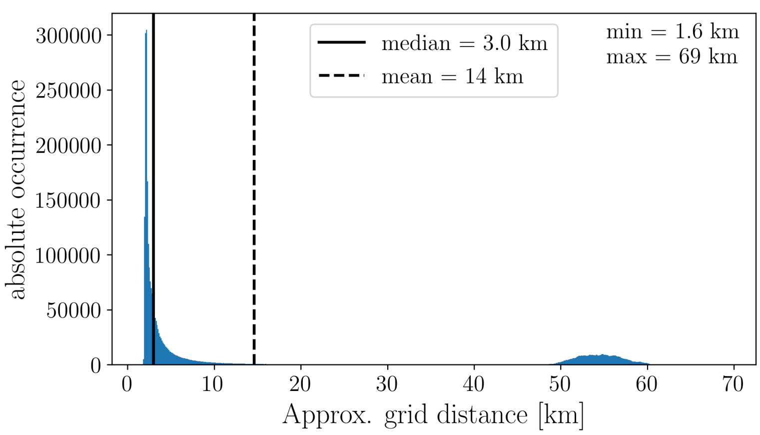

Figure 3.4: Histogram of cell center distances of mesh configuration with mesh density function ρ_{x30} (Figure 3.1, blue line) and 901123 Voronoi generators

3.2.2 Mesh Generation Performance

As part of the setup of the MPAS model on the *JESS* High Performance Computer (HPC) at DTU, a performance analysis of the mesh generation utility (Section 3.1.2) was carried out. The calculation is limited to being carried out on a single computational node, since the parallelization is only available through shared memory via OpenMP. All mesh generation runs in this study are executed with 25 OMP threads, which makes partial use of the Intel hyper-threading capabilities of the Intel® Xeon® Processor E5-2680 v2 on *JESS*, which has 20 CPU cores. This setup was found to be the most efficient based on a sensitivity study involving an SCVT generation with 38402 initial Voronoi generators. Figure 3.5 summarizes some of the key findings of the performance investigation. It can be seen that the mesh generation is computationally very heavy, especially if a large number of Voronoi generators is involved. While small to medium sized meshes, below 1×10^5, are obtained rather quickly, the generation of SCVTs with very high absolute resolution require months to reach convergence. The near-linear relationship in the log-log scale indicates power law behavior between Voronoi generators and required walltime. This imposes limitations on the generation of high-resolution meshes and mesh sensitivity studies.

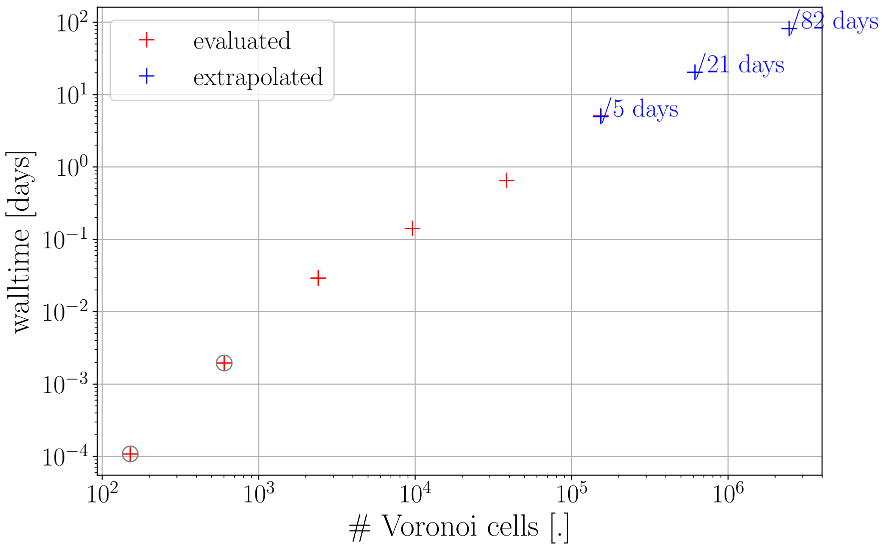

Figure 3.5: Measured (red) and estimated (blue) computational time for the creation of meshes using the mesh density function $\rho_{x30,sm}$ with different number of Voronoi generators using the standard setup (single node, 25 OMP threads, convergence threshold $\epsilon = 1 \times 10^{-10}$). Gray circles indicate data points where $\bar{d}$ leveled off before reaching ϵ (calculation was terminated by maximum number of iterations).

3.2.3 Mesh Quality Assessment of Generated Meshes

Within this study, a mesh quality assessment based on the idealized cases I1 and I2 (cf. Section 3.1.4) is performed. Three different mesh configurations that provide the foundation for the real case applications in Chapter 4 and Chapter 5 are investigated: a quasi-uniform SCVT with 204,802 Voronoi generators ("54 km mesh"), a variable-resolution mesh with density function ρ_{x3} and 245,762 Voronoi generators ("54-18 km" mesh) and a variable-resolution mesh with density function ρ_{x30} and 901,123 Voronoi generators ("55-2 km" mesh). Their properties are summarized in Table 3.2.

Name of mesh	# Voronoi cells	ρ	α [.]	β [.]	γ [.]
54 km	204802	quasi-uniform ($\rho = 1$)			
54-18 km	245762	ρ_{x3}	0.04	0.314	$(1/30)^4$
55-2 km	901123	ρ_{x30}	0.04	0.105	$(1/3)^4$

Table 3.2: Properties of three mesh configurations investigated in this section: name, number of Voronoi generators/cells and properties of the underlying mesh density function. The naming of the mesh density function ρ follows the naming in Figure 3.1 and Table 3.1.

Local Uniformity of Resulting Meshes

Figure 3.6 shows the spatial distribution and histogram of the LUI (cf. Section 3.1.3) for the three investigated meshes. The LUI ranges in all three meshes between 0.7 and 1.0 (right column, Figure 3.6). The variable-resolution meshes have a higher share of moderately skewed Voronoi cells, with a LUI less than 0.8, which are mostly located in the transition area between the coarse and fine scale regions (cf. Figure 3.6c,e). This is expected, since the transition zone is affected most by local non-uniformity due to differences in the mesh density function. It is worth noting that the LUI distribution of the 55-2 km mesh (Figure 3.6f) does not differ largely from the LUI distribution of the 54-18 km mesh (Figure 3.6d), despite having a 10 times larger refinement factor and the same transition zone width (cf. Table 3.2). One reason for this might be the much higher number of Voronoi generators (901,123 compared to 245,762), which keep the changes in mesh density between neighboring cells relatively small. Regions with moderately skewed Voronoi cells can also be found in regions outside the transition region (e.g. over Mongolia in the 54-18 km mesh, Figure 3.6c and Alaska in the 55-2 km mesh, Figure 3.6e).

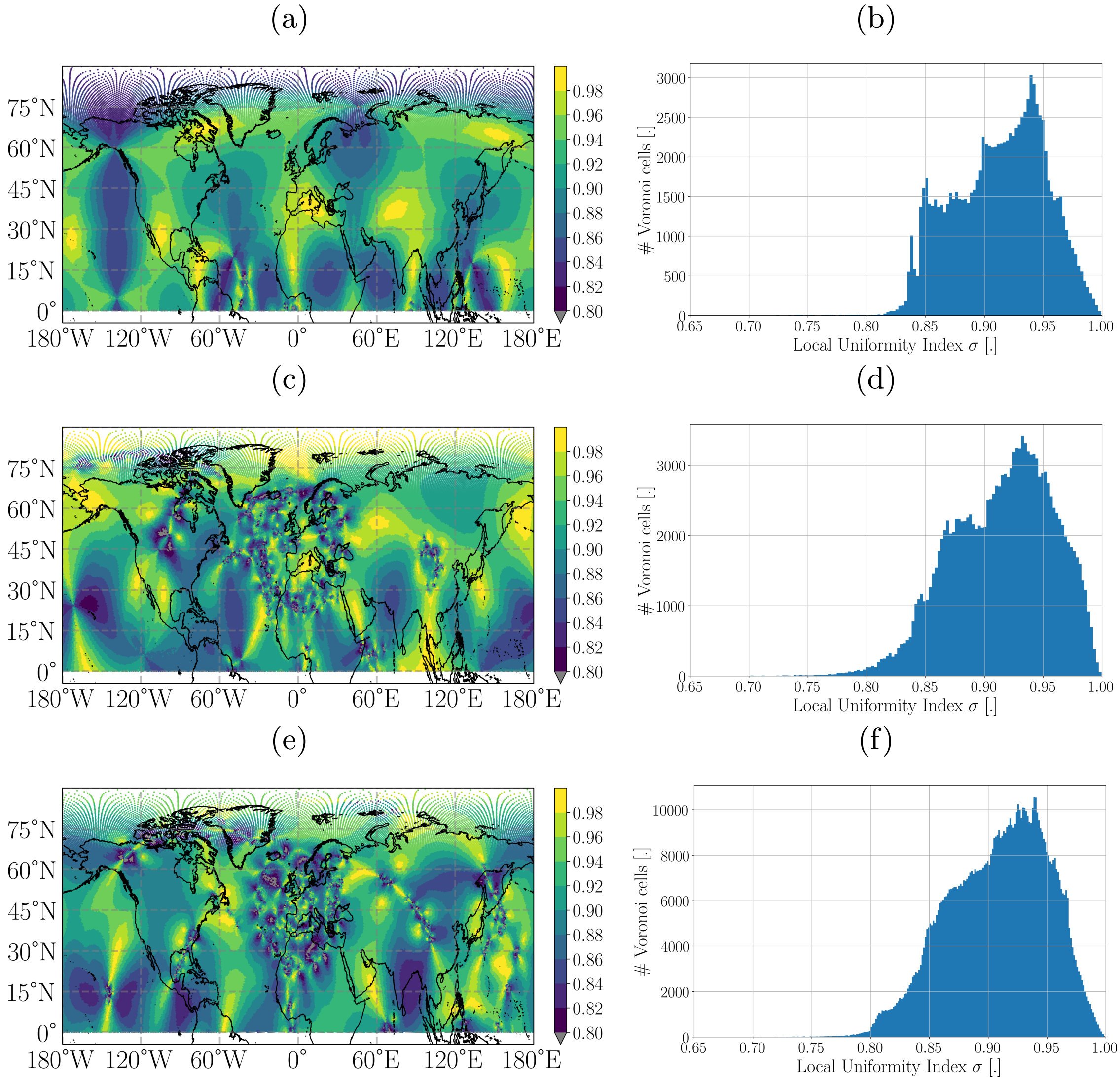

Figure 3.6: Spatial distribution (left column) and histogram (right column) of Local Uniformity Index over the northern hemisphere for the 54 km quasi-uniform mesh (top row), the 54-18 km variable-resolution mesh (middle row) and the 55-2 km variable-resolution mesh (bottom row).

Maintenance of Initially Balanced Jet

The results from the I1 idealized mesh test suite is depicted in Figure 3.7. The variable-resolution meshes display surface pressure perturbations due to the excitement of unstable modes (Skamarock et al. 2012) at around day 5 (Figure 3.7e,h), which are not yet seen in the quasi-uniform mesh configuration (Figure 3.7b). One of the reasons for the degradation of the initial state are gravity waves and errors due to numerical round-off and truncation (Jablonowski and Williamson 2006). In MPAS, truncation errors are largest around pentagons (Skamarock et al. 2012) and in locations with strong local mesh distortions (Ringler et al. 2011), which in turn impacts the local accuracy. While the quasi-uniform mesh has only 20 pentagons within the Northern Hemisphere, the 55-2 km and 54-18 km have 391 pentagons and 138 pentagons, respectively. This might have an impact on the truncation error. In addition, both variable-resolution meshes have lower mean LUIs than the quasi-uniform mesh, which also contributes to a larger truncation error, exciting the unstable modes more quickly (Ringler et al. 2011; Skamarock et al. 2012).

At day 8, the magnitude of the fluctuations in the surface pressure field in the 55-2 km variable mesh (Figure 3.7i) is larger than observed in 54-18 km mesh (Figure 3.7f), and the quasi-uniform mesh also shows signs of surface pressure perturbations.

The results from this test case emphasize the importance of the local grid uniformity and how it can affect the development of an initially balanced flow field, which should be taken into account in the mesh design.

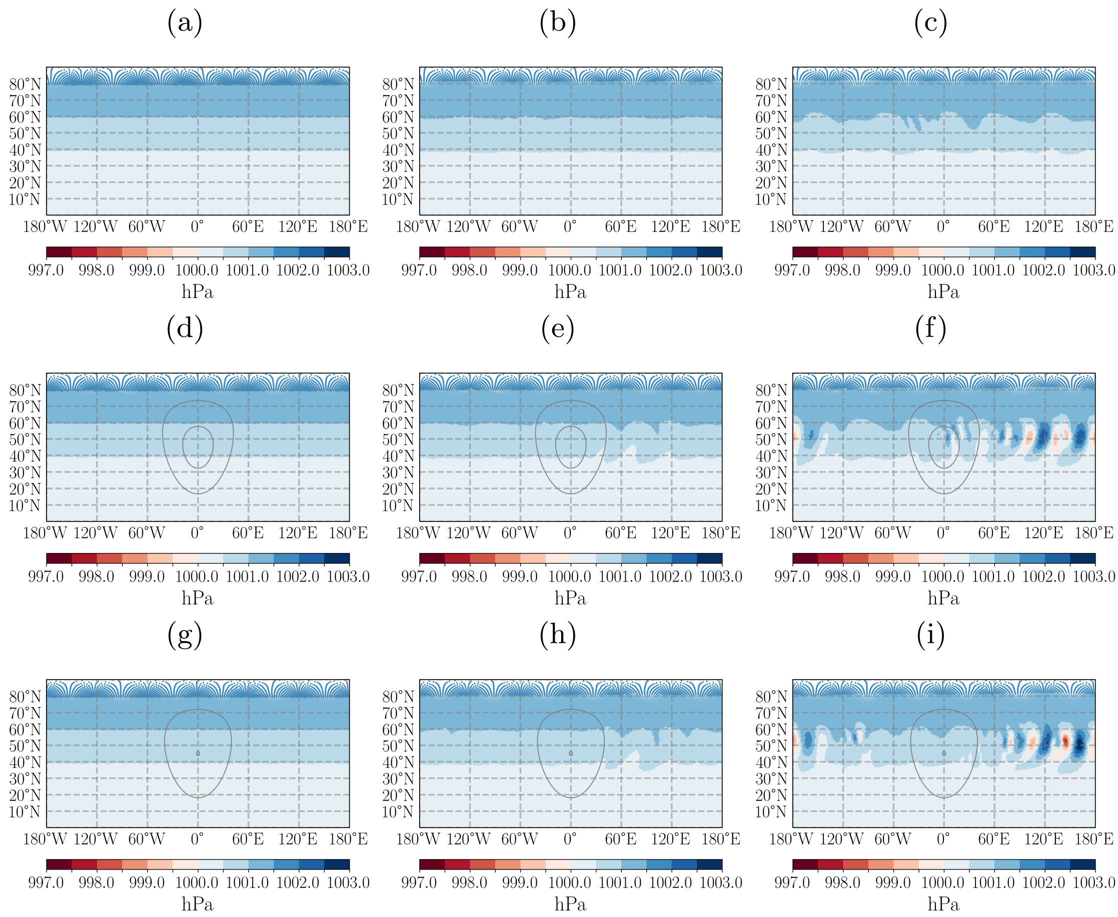

Figure 3.7: Jablonowski and Williamson (2006) baroclinic wave test without initial perturbation at day 0 (left column), day 5 (middle column) and day 8 (right column) for the 54 km quasi-uniform mesh (top row), the 54-18 km variable-resolution mesh (middle row) and the 55-2 km variable-resolution mesh (bottom row). The transition regions in the variable-resolution meshes are indicated in gray based on 1.01 $\times$ min(ρ) (inner contour) and 0.99 $\times$ max(ρ) (outer contour) respectively.

Wave Reflection and Distortion

Another aspect related with the mesh quality is the reflection and distortion of waves due to the variable-resolution region. This is tested for the generated meshes using the extended Jablonowski and Williamson (2006) baroclinic wave test, with normal mode initialization as described in Park et al. (2013) and Park et al. (2014). Figure 3.8 shows the vertical wind speed at the 850 hPa level for days 5 and 7 of the model integration. The very consistent vertical wind speed patterns before, inside, and after the mesh refinement region suggest that the larger scale structure of the wave train is not negatively influenced by the refinement region(cf. Figure 3.8c-f). Major wave reflections or distortions are not detected. However, isolated local noise in the vertical wind speed is visible in the variable-resolution mesh. Similar noise effects were also observed in Park et al. (2014).

A comparison with the spatial distribution of Voronoi cell quality index in Figure 3.6 shows that the noisy regions coincide with mesh regions with large gradients in LUI (e.g. the region between 100°E - 120°E in the 54-18 km mesh, Figure 3.8c or around 160°E in Figure 3.8f). This could indicate potential local misinterpretation or breakdown of assumptions in the reconstruction of the vertical wind speed in skewed Voronoi regions. It must be noted that the local noise does not seem to influence the vertical wind speed outside of the critical regions.

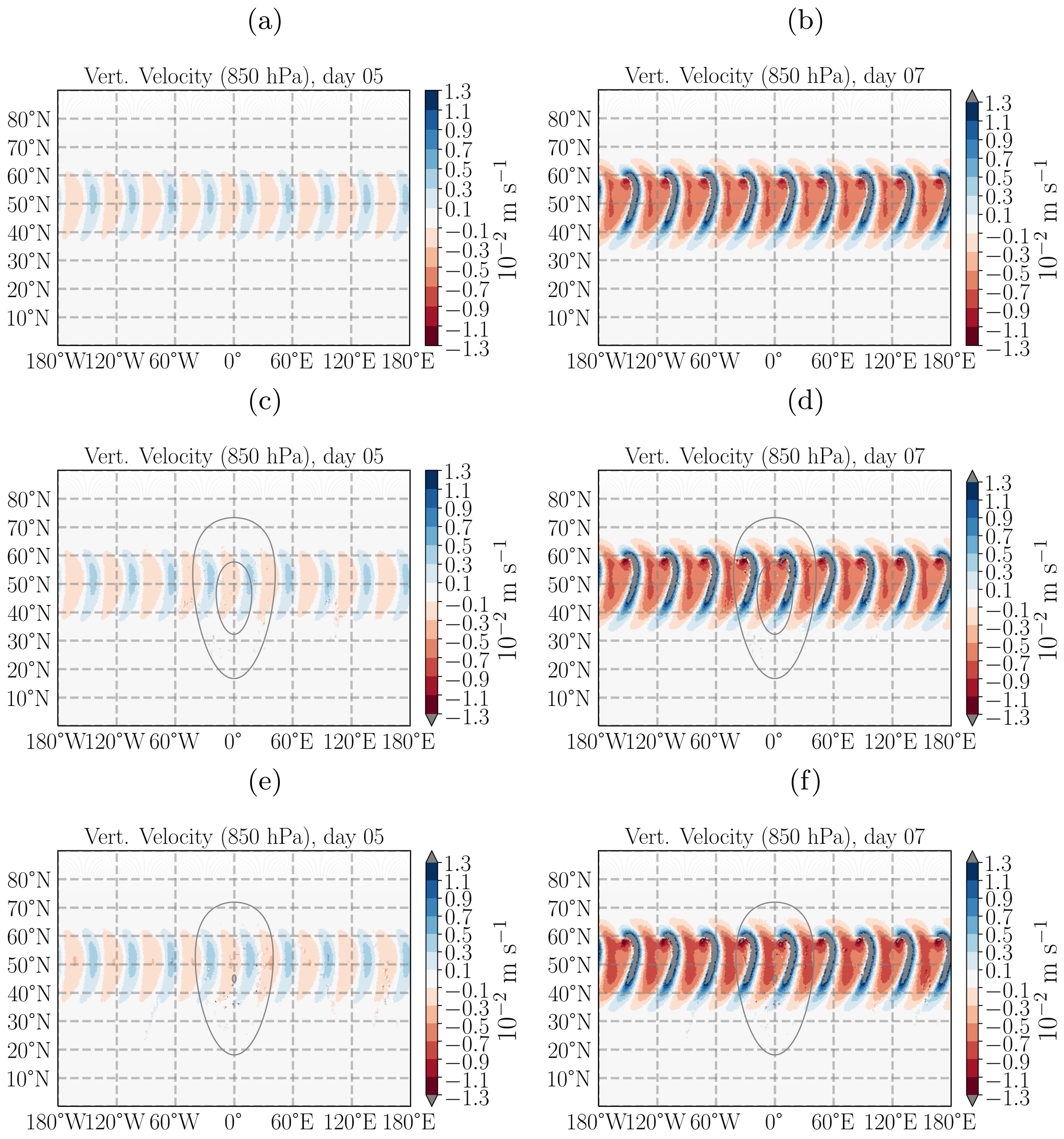

Figure 3.8: Vertical wind speed at 850 hPa level at day 5 (left column) and day 7 (right column) for the 54 km mesh (top row), the 54-18 km mesh (middle row) and the 55-2 km (bottom row). The transition regions in the variable-resolution meshes are indicated in gray based on 1.01 × min(ρ) (inner contour) and 0.99 × max(ρ) (outer contour) respectively.

3.3 Concluding remarks for SCVT design

Based on the findings in Section 3.2, several challenges and constraints were found that need to be taken into account when designing an SCVT:

- The design of the mesh density function is a crucial element since its defines the relative grid resolution. Therefore, it affects not only the smoothness between regions of different absolute resolution, but also the share of resources attributed to certain areas of the mesh (refinement region, transition region, coarse resolution region). In the ideal setup, a very wide and gradual transition minimizes resolution jumps between the different resolution regions and reduces the associated negative effects mentioned in Section 1.2. However, this impact must be weighted against the additional computational costs associated with very wide transition zones, which can become especially expensive in high-resolution configurations.
- The number of Voronoi generators determines the absolute resolution of the SCVT and is also the main driver influencing the computation time during the SCVT generation. While grid generation is a one-time investment, the current calculation time is not negligible. Investigations that require highly resolved refinement regions (i.e. large numbers of Voronoi generators) are especially affected by this. This includes, for example, the investigation of wind speed fluctuations during open cellular convection in Chapter 5 and the investigations related to wind farm wakes (Chapter 6). Domain sensitivity studies, which would require the sets of meshes are hardly feasible with the current setup. In addition to the mesh generation itself, the absolute number of Voronoi generators also influences the computational time for the MPAS model runs themselves, due to the increased number of model cell columns and the necessary reduction of the simulation time step due to increased spatial resolution, which needs to be taken into account as well.
- Sufficiently high local uniformity is required to guarantee a high-quality SCVT. Overly skewed Voronoi cells ($\sigma << 1$) are already prevented by the mesh generation tool itself, due to the prohibition of obtuse triangles. However, mesh regions with moderately skewed Voronoi regions and large gradients in the LUI can introduce local noise effects that impact the local accuracy of the model simulation (cf. Figure 3.8). It must be noted that these regions are not only found near the transition zones (Figure 3.6c,e) and are also found in quasi-uniform meshes (Figure 3.6a). This stresses the need for high local uniformity, which can be achieved by sufficiently small and smooth changes in the mesh density, or by having a sufficiently high number of Voronoi generators (Gersho 1979; Ringler et al. 2011).

On the basis of the mesh quality assessment performed in Section 3.2, both the quasi-uniform and the variable resolution meshes show reasonable performance. Their relatively high LUI values, sufficiently long maintenance of the initially balanced jet solution, and absence of wave reflections or distortions give confidence for their usage for real case application.

CHAPTER 4
Mid-latitude Storm Modeling - Case Study of Storm "Christian"

This chapter focuses on the results of a case study of the mid-latitude storm "Christian", extending upon the work performed in Paper *P1* (Appendix A). Paper *P1* investigated the challenges of modeling storm "Christian" in WRF, due to the storm entering at the corner of the model domain. Here, it is looked at how the storm is modeled using MPAS in comparison with the WRF results.

Section 4.1 provides the motivation and background for the study, while Sections 4.2 and 4.3 present findings from the two different modeling perspectives (limited-area model WRF and global MPAS model, respectively). The chapter finishes with a discussion of the results and conclusions in Section 4.4 and future work in Section 4.5.

4.1 Background and Motivation

Mid-latitude storms (also called extra-tropical cyclones) are large-scale weather phenomena that have a large influence on the weather in the mid-latitudes (e.g. Catto et al. 2019). They are connected with extreme precipitation (e.g. Pfahl and Wernli 2012), wind gusts, and high surface winds (e.g. Collier et al. 1994; Browning 2004; Earl et al. 2017).

The high wind speeds associated with the mid-latitude storms can affect grid performance and safety (e.g. Artipoli and Durante 2014) and can cause the shutdown of wind farms due to the exceedance of wind turbine cut-out criteria (e.g. Cutululis et al. 2012). An investigation of day-ahead wind power forecasts for Germany between 2012 and 2014 found that extra-tropical cyclones located over the North Sea, Baltic sea or Germany can be linked to 38% of the days with largest day-ahead power forecast errors (Steiner et al. 2017). From a modeling perspective, extra-tropical cyclones are characterized by a range of spatial scales and require sufficiently high spatial resolution to adequately represent the system.

Traditional methods of downscaling, with limited area models using both single and nested domains have been applied for individual case studies (e.g. Christakos et al. 2016; Larsén et al. 2017a), storm catalogs (e.g. Roberts et al. 2014), and storm climatologies (e.g. Larsén et al. 2017b).

While the results are generally satisfactory, problems arise when the large-scale storm structures are not initialized inside the LAM, but need to be introduced via the LBCs (Termonia et al. 2009). Insufficient coupling intervals and corruption of the LBC information due to spatial and temporal interpolation at the LAM boundaries can deteriorate model performance (Gustafsson 1990; Gustafsson et al. 1998; Termonia 2003; Termonia et al. 2009). A case study by Gustafsson (1990) revealed structural damage in the small scales of an upper-air trough in the relaxation zone when the LBCs were not updated frequently enough. Termonia (2003) observed reduced storm deepening in a case study of storm Lothar with the ALADIN LAM. The weaker storm was attributed to the use of temporal interpolation due to infrequent forcing data updates. A reduced pressure drop was also observed in another storm investigated in Termonia et al. (2009), which was attributed to the same cause.

The problem of introducing large-scale storm structures into LAMs is examined further within the scope of this project. Here, a especially challenging special case has been investigated in Paper *P1*, namely the introduction of large-scale storm features close to the lateral boundary corner in WRF. Results of Paper *P1* will be introduced in Section 4.2.

Some of issues mentioned in Gustafsson (1990), Gustafsson et al. (1998), Termonia (2003), Termonia et al. (2009) and Paper *P1* can be reduced or avoided by sophisticated simulation design, with respect to domain size and the location of the lateral boundaries. However, this is not always possible, for example for long-term storm climatologies or operational forecasts, that cannot change their domains for all possible cases. For such scenarios, the global model MPAS, with local refinement could be beneficial, as it avoids the above mentioned LBCs challenges completely, including the issues related to spatial and temporal interpolation. Furthermore, the gradual refinement also avoids sudden resolution jumps. The lack of regularly updated LBCs, however, removes the external control on the simulation and might affect the general forecast capabilities.

As part of this PhD project, MPAS' performance is investigated with respect to the same mid-latitude case study (storm "Christian") as presented in *P1*. The study aims to extend the investigation performed in Paper *P1* and tries to investigate if, and to what extent, MPAS can improve the determination of relevant storm parameters like the storm intensity, storm duration, and forecast timings in comparison to WRF and observations.

4.2 Storm "Christian" from WRF Perspective - Introduction to Paper *P1* (Appendix A)

Paper *P1* "Approaches toward improving the modelling of midlatitude cyclones entering at the lateral boundary corner in the limited area WRF model" investigated the introduction of large-scale storm structures via the lateral boundaries and the especially critical lateral boundary corner in the limited area model WRF. The paper focuses on a case study of storm "Christian", which has shown a lack of storm deepening and a displacement of the large-scale structure when introduced close to the lateral boundary corner.

The study investigated different commonly used approaches to improve the introduction of the storm to the LAM and analyzed their ability to improve key storm parameters. The investigated approaches were model domain displacement to avoid the corner issue, adjustments to the relaxation zone width, spectral nudging techniques, and different update frequencies of the LBCs. All scenarios were analyzed with respect to their impact on the storm structure and location, storm intensity (based on minimum sea level pressure), and the wind speed at 850 hPa.

It was found that spectral nudging could be beneficial for reducing spatial distortions, but that the additional spatial smoothing due to the nudging also prevented the storm structure from deepening properly. An increase of the LBC update frequency from every six hours to an hourly update provided the largest improvements for storm intensity. The increased update frequency avoided additional spatial smoothing and reduced the effects due to temporal interpolation. Relaxation zone adjustments or spectral nudging were not able to counterbalance the lack of high update frequencies at the lateral boundaries. It was also shown that the different modeling strategies affected mainly the sea level pressure in the vicinity of the storm structure, with limited impact on the sea level pressure beyond approximately 400 km away from the storm center.

4.3 Storm "Christian" from MPAS Perspective

4.3.1 MPAS Setup

Two different mesh configurations were used to simulate storm "Christian" using MPAS, a quasi-uniform 54 km mesh (x1.204802) and a 54 km mesh with local refinement to 18 km over Europe with 245,762 Voronoi generators (x3.245762). The mesh density of x3.245762 follows ρ_{x3} introduced in Chapter 3 (Figure 3.1). The coarse resolution region was chosen based on the 0.5° × 0.5° resolution of the Climate Forecast System Version 2 (CFSv2, Saha et al. 2011; Saha et al. 2014) initial and boundary conditions used in Paper *P1*. The resolution of the refinement zone in x3.245762 of around 18 km is inspired by the WRF domain resolution in Paper *P1*. Figure 4.1a depicts the histogram of horizontal cell spacing in x1.204802 and x3.245762. Figure 4.1b indicates the spatial distribution of the horizontal cell distances in the refinement region of the 54-18 km mesh around the critical lateral boundary corner region of the WRF domain used in Paper *P1*.

All MPAS configurations have 55 vertical levels with a model top at 30 km, which follows the standard model configuration (Duda et al. 2019).

Each mesh configuration was run with three different model physics configurations. The first setting applies a selection of model physics that is most similar to the WRF configuration in Paper *P1*, which has been shown good performance in simulating mid-latitude storms (Larsén et al. 2017b) using WRF. It is further references as "CPKF". "CPKF" differs from MPAS' '*convection_permitting*' physics suite (cf. Table 2.1) only in the choice of the cumulus paramterization scheme. "CPKF" uses Kain-Fritsch (Kain 2004) instead of the scale-aware Grell-Freitas scheme (Grell and Freitas 2014). The coarseness of the MPAS configuration (refinement zone has a cell spacing of only 18 km) allows the usage of the Kain-Fritsch scheme.

To investigate MPAS' sensitivity to model physics, investigations with the pre-defined physics suites '*convection_permitting*' and '*mesoscale_reference*' (cf. Table 2.1) are

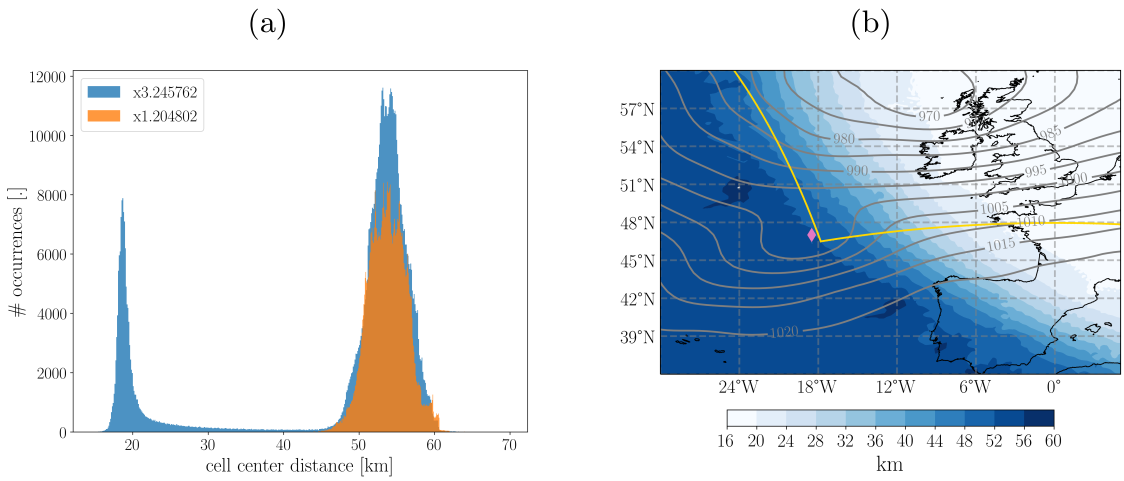

Figure 4.1: (a) Histogram of horizontal cell center distances of the quasi-uniform 54 km mesh (x1.204802, orange) and the 54 km mesh with local refinement to 18 km (x3.245762, blue). (b) Contours (blue-white) of average cell center distances between a Voronoi region and its neighbors in x3.245762. The yellow frame shows the critical lateral boundary corner region of the WRF domain used in Paper *P1*. The gray contours in (b) depict the mean sea level pressure field obtained from the CFSv2 6-hourly forecast at 27 October 2013, 1200 UTC. The pink diamond in (b) indicates the location of the local minimum sea level pressure of the CFSv2 6-hourly forecast at 27 October 2013, 1200 UTC.

performed as well. They will be further refered to as "CP" and "MESO", respectively.

The model is initialized from the CFSv2 6-hourly forecast product from 26 October 2013, 1200 UTC and is run for three days with the first 12 hours discarded due to model spin-up, leaving 2.5 days for analysis. Sea surface temperature and sea ice are not updated during the integration period.

The native MPAS model output is interpolated to a $0.5° \times 0.5°$ regular latitude/longitude grid via barycentric interpolation using the Earth System Modeling Framework (ESMF, Hill et al. 2004, Version 6.3.0r). This is done to allow comparison with the CFSv2 data set. To allow comparisons between the two sets of MPAS meshes, the native MPAS model outputs are interpolated to a $0.1° \times 0.1°$ regular latitude/longitude grid with the same method.

4.3.2 Sea Level Pressure Buoy Observations for Model Evaluation

Time series of sea level pressure (SLP) observations from six buoys are used for the evaluation of the MPAS model performance. The buoy observations are from the European Marine Observation and Data Network (EMODnet) - Physics System[1] (Novellino et al. 2015) and their spatial locations are depicted in Figure 4.2. Table 4.1 provides more information about the specific locations, data availability and the SLP upper limit

[1] `https://www.emodnet-physics.eu/Portal`, last accessed: Nov. 2018

thresholds used for the storm duration analysis (cf. Section 4.3.3). Results from station #17, #34, #10 and #19 are also used in Paper *P1*. The two easternmost stations #8 and #9 are added here to examine the model performance as the storm moves further east.

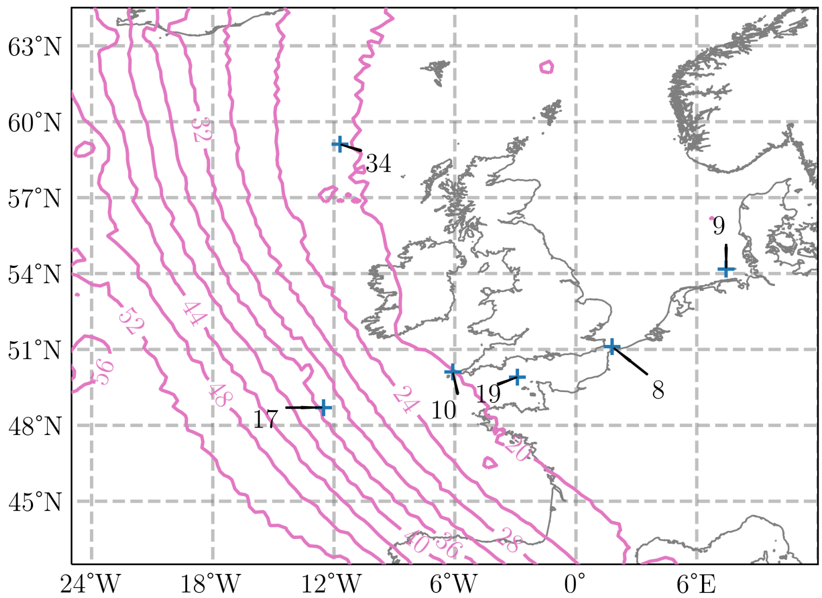

Figure 4.2: Spatial distribution of the six buoys (blue plus) with their identifiers described in Table 4.1. Pink contours: average distance between Voronoi cell centers in the transition zone of the x3.245762 mesh configuration.

Table 4.1: Station number, platform code, location, and data availability rate within the period of interest (27 October 2013, 0000 UTC - 29 October 2013, 12000 UTC) of the six buoy locations. The corresponding SLP thresholds p_t used for the storm duration time analysis (details in Section 4.3.3) are also stated. Stations are listed from west to east.

Station identifier	platform code	location	Availability rate (coverage)	p_t [hPa]
17	62029	48.7°N 12.5°W	every 60 min (100%)	1000.1
34	64045	59.1°N 11.7°W	every 60 min (100%)	-†
10	62107	50.1°N 6.1°W	every 60 min (100%)	992.4
19	62103	49.9°N 2.9°W	every 60 min (98.4%)	995.2
8	62304	51.1°N 1.8°E	every 60 min (100%)	995.1
9	'UFSDeutscheBucht'	54.17°N 7.45°E	every 60 min (100%)	986.8

† not included in storm duration time analysis

4.3.3 Storm Characterization

The following three parameters are used to characterize the storm and to evaluate the model performance:

- **Storm intensity**: the storm intensity can be defined in various ways (Roberts et al. 2014), here the magnitude of the local minimum sea level pressure (LMSLP) is used. This measure does not include the effect of time shifts, and different simulations might see their highest storm intensity at different times.
- **Storm arrival time**: The storm arrival time is defined as the time when the modeled or observed SLP time series, at a particular point, sees its LMSLP. The difference between arrival times is used to define time shifts in the storm forecast.
- **Storm duration time**: The storm duration time is defined as the number of hours for which the SLP remains below an SLP threshold p_t at a certain location. The p_t thresholds are defined as LMSLP + 10 hPa and are summarized in Table 4.1. To exclude SLP effects that are not related to the passing of storm "Christian", only the period between 27 October 2013, 0900 UTC and the end of the simulation (28 October 2013, 1200 UTC) are considered for the storm duration time.

Due to its remote location from the storm track, station #34 is excluded from the storm characterization analysis and only used to estimate the models performance further away from the storm track.

4.3.4 Results

Spatial SLP Field: Comparison between MPAS with "CPKF" physics and CFSv2

MPAS is compared with CFSv2 to get an overview of MPAS' performance on synoptic scales. Since CFSv2 is the driving data for the WRF simulations in Paper *P1*, emerging differences in the synoptic scale can help to understand differences between the WRF and MPAS performance.

Figure 4.3 depicts the SLP field determined from the CFSv2 forecast and the MPAS runs with "CPKF" physics configuration 24 hours after MPAS model initialization (27 October 2013, 1200 UTC). At that moment, the storm is outside of the refinement region. MPAS places the low-pressure system associated with "Christian" further to the west (Figure 4.3b,c) than the CFSv2 forecast (Figure 4.3a). This displacement is seen in both the quasi-uniform (further referred to as x1.204802-CPKF) and the variable-resolution (further referred to as x3.245762-CPKF) MPAS configurations (Figure 4.3e,f), with only marginal differences between x1.204802-CPKF and x3.245762-CPKF (Figure 4.3d). This suggests that the storm displacement is not caused by effects of the refinement region on the coarse region, but instead influenced by the model's dynamics and physics.

After 48 hours into the simulation (28 October 2013, 1200 UTC, Figure 4.4), "Christian" has entered the refinement region in the 54-18 km mesh. Differences in the SLP field between the x1.204802-CPKF and x3.245762-CPKF become visible on the south-west side of the storm structure with reduced SLP in x3.245762-CPKF (east of the UK, Figure 4.4d). Model differences further away from the storm structure emerge as well (e.g. in the west of Ireland and north of the UK). Marginal differences in the MPAS storm intensities (967.7 hPa in x3.245762-CPKF and 968.0 hPa in x1.204802-CPKF) at that time suggest that the differences are mostly due to deviations in the spatial structure and location of the storm, and not due to an increased storm intensity. This also provides evidence that the storm structure was modified when passing through the transition zone, and into the refinement region. When compared with the CFSv2, both MPAS configurations show a slightly south-west/north-east stretched low-pressure system (Figure 4.4b,c) compared to the more uniformly shaped system in CFSv2 (Figure 4.4a). Both MPAS configurations show similar performance with highly reduced SLP over most of the investigated domain (Figure 4.4e,f) in comparison with CFSv2.

SLP Time Series Analysis: Comparison between MPAS with "CPKF" physics, WRF and CFSv2

Figure 4.5 depicts the modeled SLP time series of x1.204802-CPKF and x3.245762-CPKF together with the buoy observations, modeled SLP from the CFSv2 6-hour forecasts and the seven WRF configurations presented in Paper *P1*. The model integration time of the WRF simulations performed in Paper *P1* was extended by 36 hours until 29 October 2013, 1200 UTC to fully cover the storm development at all six buoy stations. Both the quasi-uniform (x1.204802-CPKF) and the variable-resolution (x3.245762-CPKF) MPAS configurations show decent agreement with respect to the general trends in the time series. At all stations except station #17, MPAS is able to realistically reproduce the storm intensity based on the absolute values of the LMSLP. This can be seen more clearly in Figure 4.6a, which depicts the difference in storm intensity between the models (MPAS and WRF) and the observations.

At station #8 and station #9, MPAS outperforms the WRF simulations with respect to the storm intensity. At those locations, the CFSv2 performance is also quite poor (Figure 4.5e,f). At station #10, only the WRF configurations with increased LBC update frequency and the southward shifted domain show better performance than MPAS (Figure 4.5a). At station #17, MPAS simulates a significantly lower LMSLP compared

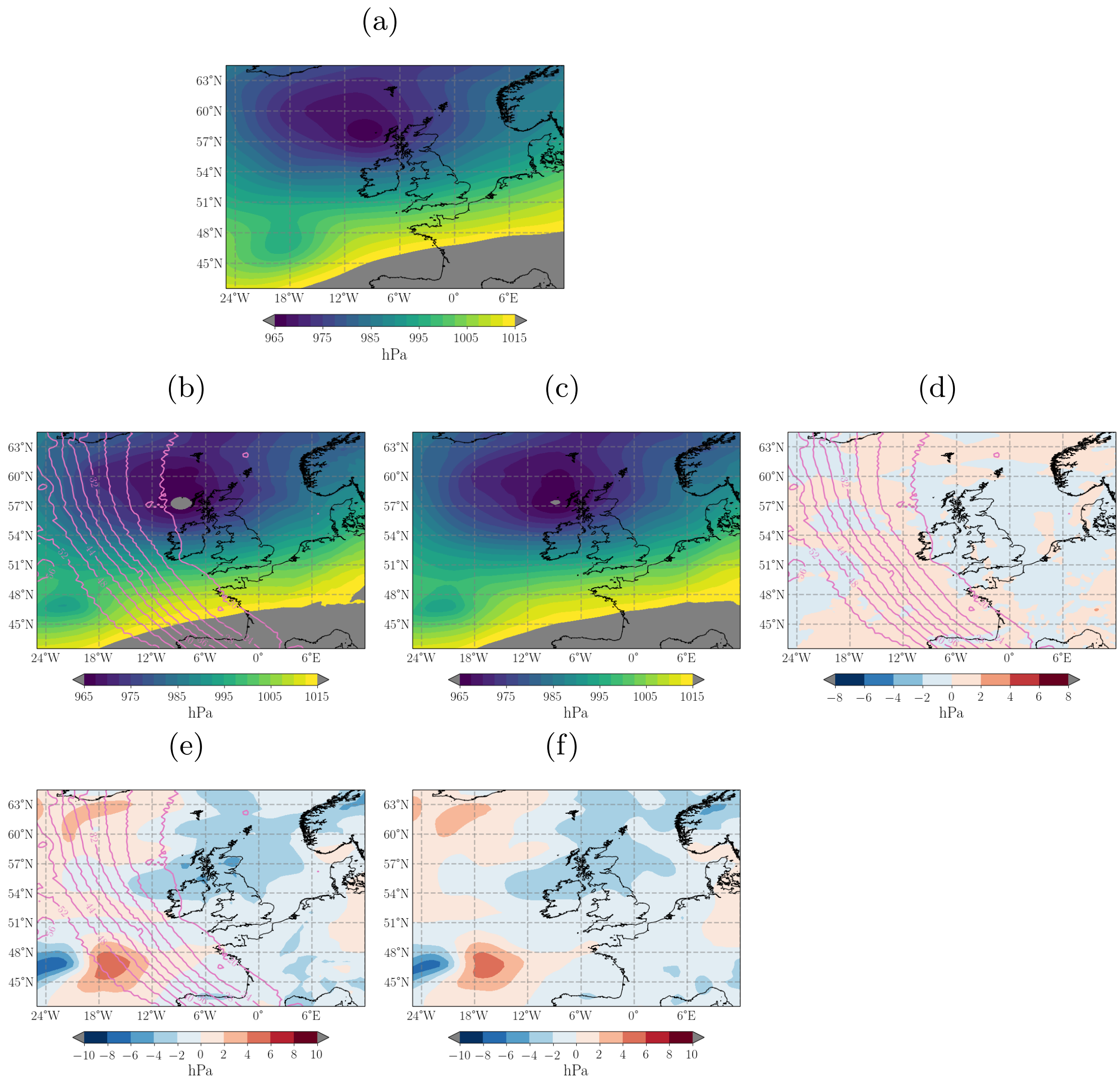

Figure 4.3: Contours of SLP at 27 October 2013, 1200 UTC (24 hours after MPAS model initialization): (a) CFSv2, (b) variable-resolution 54-18 km MPAS with "CPKF" physics configuration (x3.245762-CPKF), (c) quasi-uniform 54-km MPAS with "CPKF" physics configuration (x1.204802-CPKF), (d) SLP difference between x3.245762-CPKF and x1.204802-CPKF. Positive values indicate higher SLP in x3.245762-CPKF. (e) SLP difference between x3.245762-CPKF and CFSv2. Positive values indicate higher SLP in x3.245762-CPKF. (f) SLP difference between x1.204802-CPKF and CFSv2. Positive values indicate higher SLP in x1.204802-CPKF. Values outside the given limits are depicted in gray. The pink contour lines in (b), (d) and (e) show the average cell center distance in x3.245762-CPKF. Attention is drawn on the different scales in (e) and (f) compared to (d).

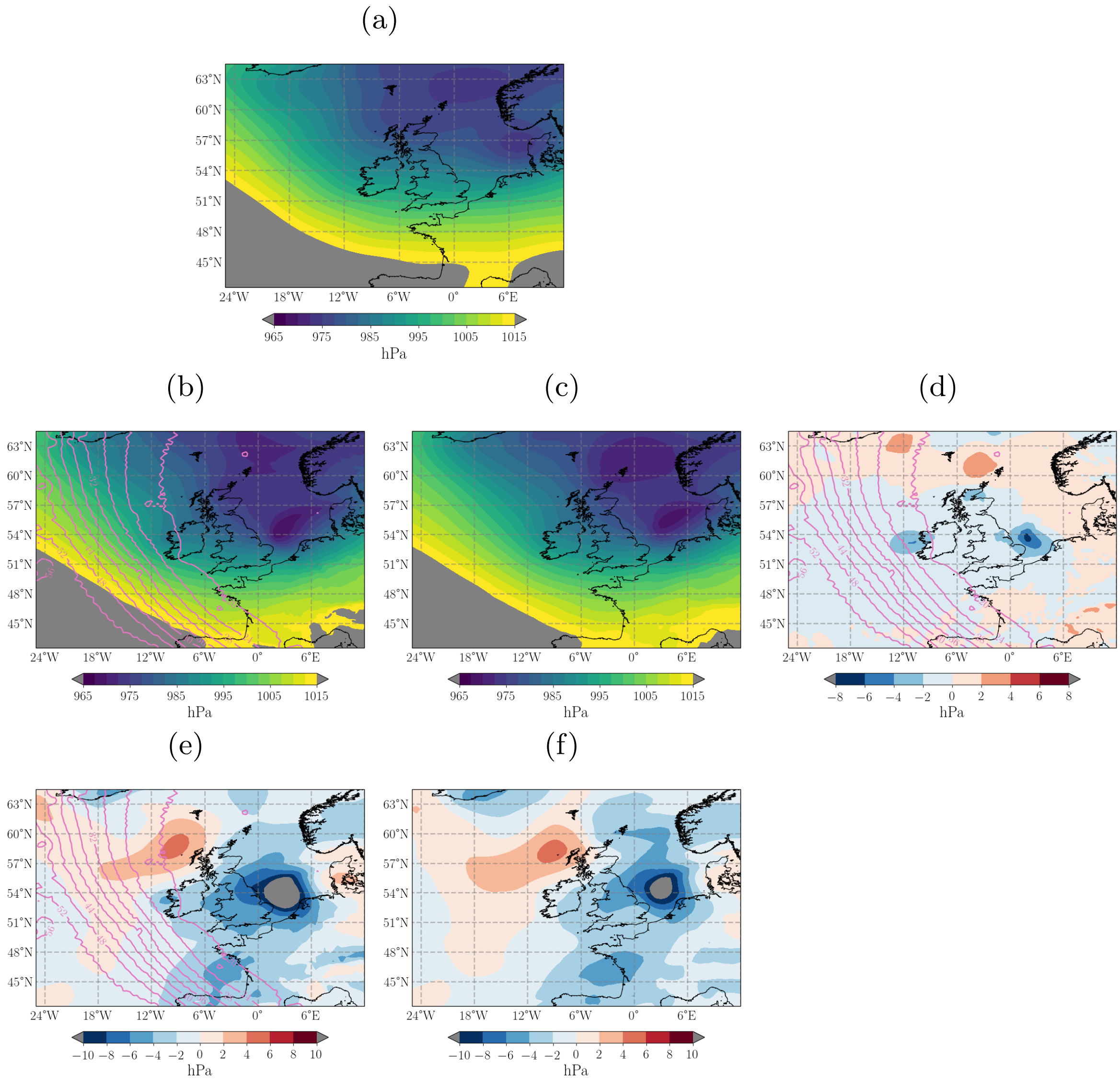

Figure 4.4: Same as Figure 4.3 but for 28 October 2013, 1200 UTC (48 hours after model initialization).

to the observations while WRF and CFSv2 perform better. The behavior at station #17 is seen in both x3.245762-CPKF and x1.204802-CPKF, which suggests that the bias is not related to station #17 being located within the transition zone of the 54-18 km mesh (cf. Figure 4.2).

The WRF simulations follow the large scale trend dictated by the CFSv2 forcing data. This is not surprising, since the WRF domain is relatively small and therefore, is constrained by the LBCs (Leduc and Laprise 2009). The beneficial effects of this steering are observed at locations far away from the storm center (e.g. station #34, Figure 4.5b), and for periods long before and after the storm passes by a station (Figure 4.5a,c-f). However, the impact of the LBCs on WRF seems to limit the intensification of the storm as seen in poor performance of both the CFSv2 forcing data and WRF at stations #10, #19, #8, and #9 (Figure 4.6a). An increased LBC update interval did improve the performance at station #10 (cf. WRF configurations "CFSv2-3h" and "CFSv2-1h" in Figure 4.6a).

In the WRF simulations, the negative effects of the linear temporal interpolation, between subsequent lateral boundary condition updates, are detectable. This is especially visible at station #19 (Figure 4.5d), where the CFSv2 data only provides information before and after the local minimum in SLP. This has the consequence that the resulting forcing from the boundary conditions imposes an increase in the SLP to the LAM before the minimum is reached. Therefore, the actual pressure drop associated with the LMSLP is missed completely.

With respect to the storm arrival time, x1.204802-CPKF determines the storm arrival time too late at all stations except for station #9 ,while x3.245762-CPKF determines the time too late at all stations. This results in a positive time shift compared to the measurements (Figure 4.6b). Prior to the storm arrival time, MPAS follows the trends in the observed SLP reasonably well (Figure 4.5). The later storm arrival time is partly attributed to the westward shift of the storm structure in the MPAS runs, which was seen when compared with the CFSv2 simulation (Figure 4.3). The time shifts in x3.245762-CPKF are similar or higher when compared to the quasi-uniform x1.204802-CPKF configuration. This effect is more or less independent from the stations that are directly affected by the storm (Figure 4.5a,c-f).

The WRF simulations have the opposite response, as they generally simulate the storm arrival time too early compared to the measurements (Figure 4.6b). A positive time shift is only observed in the WRF configurations with a high degree of spectral nudging (NUD100km) and the extended relaxation zone (2xRelaxZone) at station #8 and #17. The CFSv2 forecasts estimate the storm arrival times quite well (Figure 4.5).

With respect to the storm duration, the performance of the different WRF configurations depends on the station. Combined with the discrete nature of the measure, quantitative statements about the performance are limited. The comparison of the two MPAS configurations shows that x3.245762-CPKF results have longer storm durations than the observations, with differences of two hours at station #8, #9, #10 and #19 (Figure 4.6c). This prolonged duration is mostly the result of the modeled SLP not recovering quickly enough after the storms passage. At station #17, both MPAS simulations perform similarly well.

All in all, the introduction of a transition zone did not show systematic improvements in the simulation of storm "Christian", with respect to storm intensity, storm arrival time, or storm duration time. Conversely, at most locations, it slightly deteriorated the performance of the simulation.

Impact of MPAS Physics Configuration on SLP Time Series and Storm Characteristics

Due to observed positive biases in time shift and storm duration in both MPAS mesh configurations with the "CPKF" physics scheme, two other physics configurations "CP" and "MESO" are explored in this study. This is done to examine the impact of the model physics on observed deviations from the measurements. Figure 4.7 compares the impact of the chosen model physics on the simulation of the SLP time series. It can be seen that the differences between the simulations with different model physics configurations are mostly limited to the period around the storm arrival time and within 24 hours afterwards. Deviations are especially visible at station #10, #19, #8 and #9. At station #34, none of the MPAS configurations is able to predict the changing trend in SLP between 0000 UTC and 1200 UTC on 28 October 2013. This deviation from the observations seems to be uninfluenced by the different model physics. The variable-resolution configuration with the "CP" physics is the only configuration that is able to predict the high storm intensity at station #9 (Figure 4.7).

However, the MPAS configurations with "CPKF" physics perform best for estimating the storm arrival time. This is shown in the reduced time shifts compared to the "CP" and "MESO" physics configurations given the same MPAS mesh configuration (variable-resolution or quasi-uniform, Figure 4.8b). Independent of the chosen physics scheme, the time shifts remain similar or are larger in the simulations with variable-resolution meshes compared to their quasi-uniform counterparts. Identical time shifts and identical storm duration between quasi-uniform simulations of one set of physics and variable-resolution simulations of another set of physics are observed (Figure 4.8b,c). However, the phenomenon is likely an artifact of the discrete nature of the measures, which cover only full hours.

Based on an overall assessment of the SLP time series (Figure 4.7) and the MPAS performances with respect to storm intensity, storm arrival time and storm duration (Figure 4.8), the quasi-uniform mesh configuration with the "CPKF" physics configuration (x1.204802-CPKF) shows the best overall performance. The detected variations in the storm characteristics across the different physics configurations suggest some sensitivity of the storm structure to physics parameterizations.

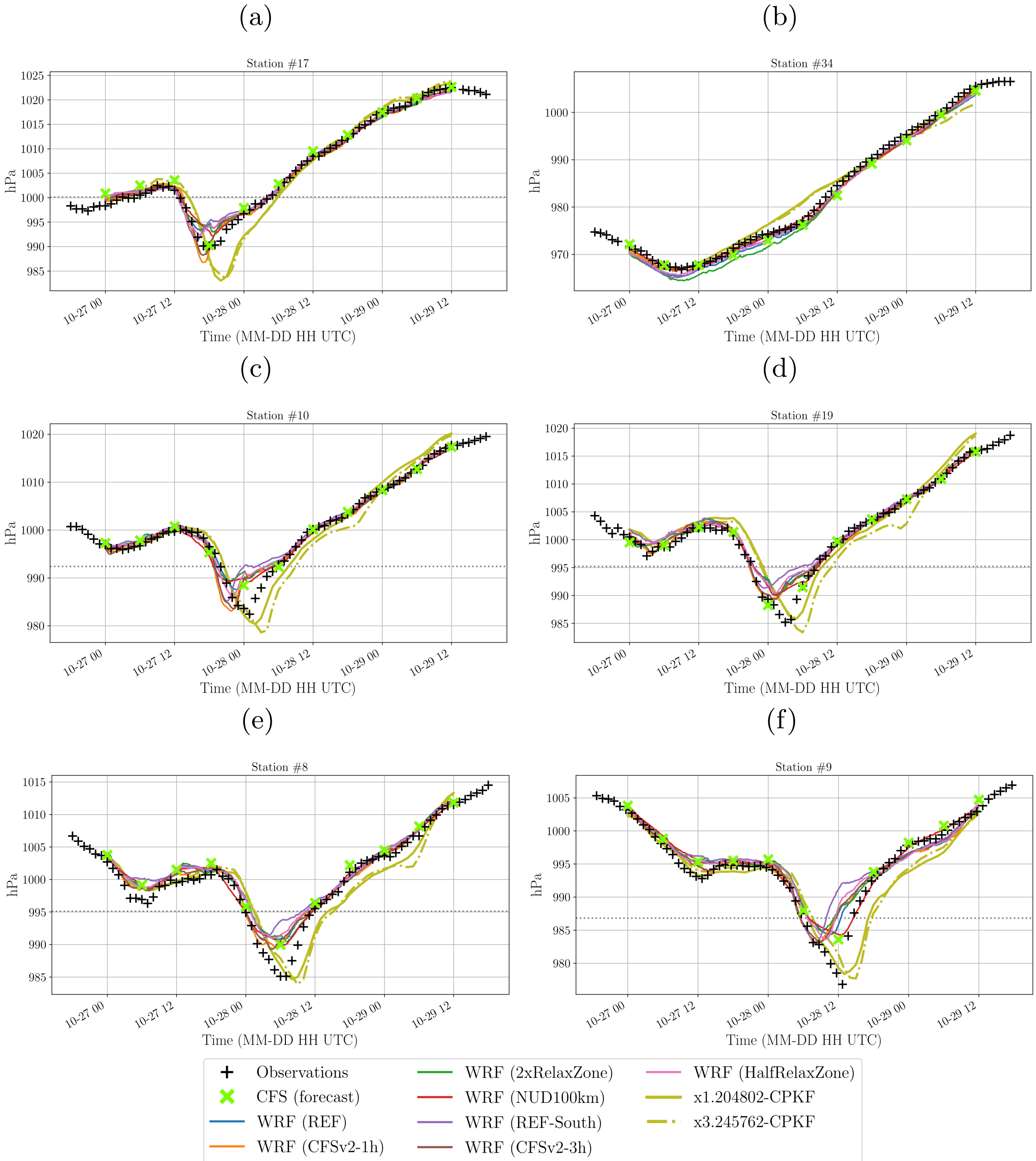

Figure 4.5: Modeled and observed time series of SLP at (a) station #17, (b) station #34, (c) station #10, (d) station #19, (e) station #8 and (f) station #9. Black plus: Buoy observations, green 'x': SLP from CFSv2 6-hour forecast. Yellow lines: quasi-uniform (solid) and variable-resolution (dashdotted) MPAS runs with "CPKF" physics configuration. Thin solid lines: Results from extended WRF simulations presented in Paper *P1*. The naming convention of the WRF simulations follows Table 2 in Paper *P1* (see Appendix A). Dotted black line: SLP thresholds p_t used for the storm duration time analysis.

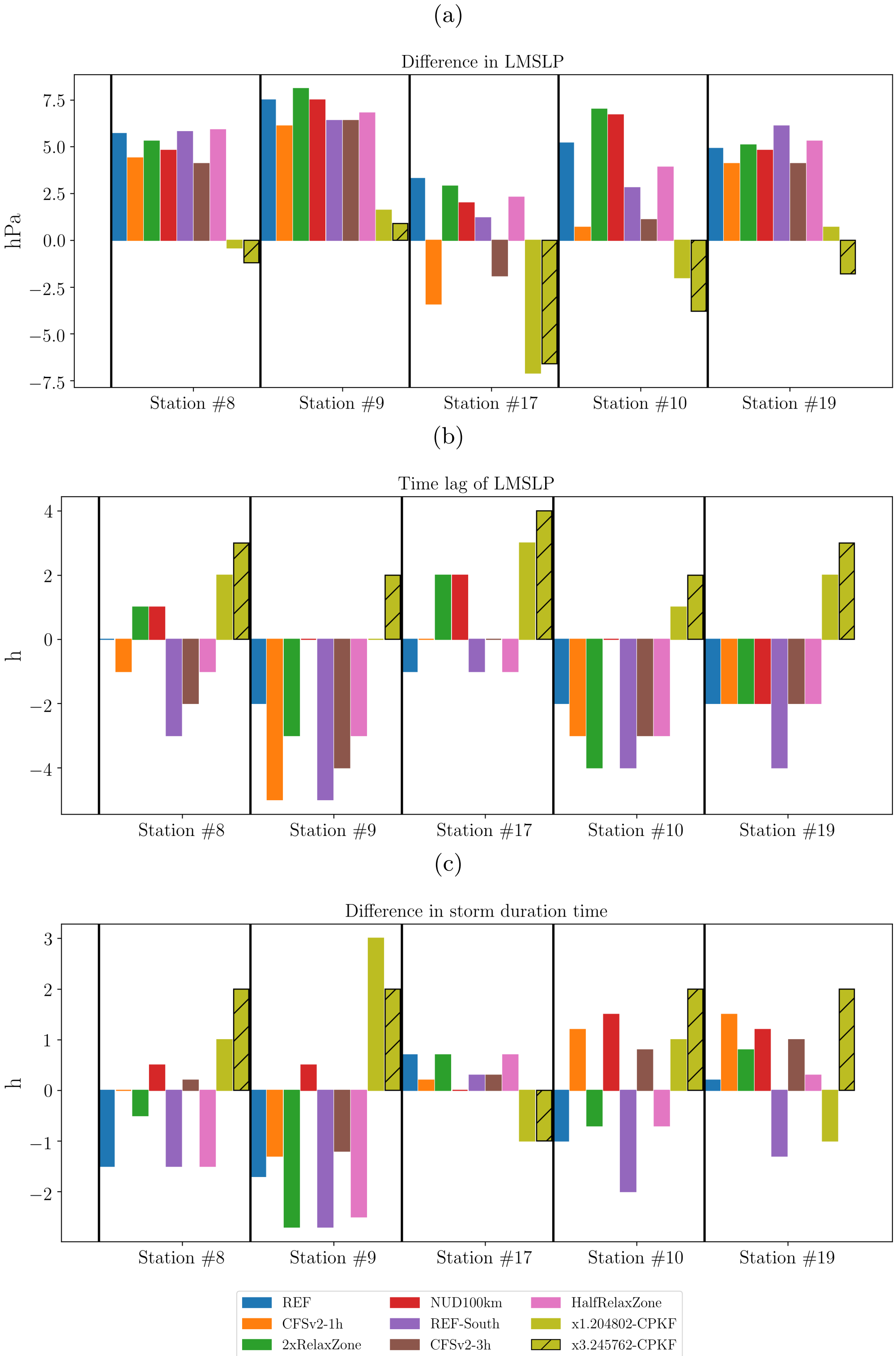

Figure 4.6: (a) Difference between modeled and observed LMSLP. Positive differences indicate a higher LMSLP in the model. (b) Time difference between modeled and observed storm arrival time. Positive time differences indicate a later storm arrival time in the modeled time series. (c) Difference between modeled and observed storm duration. Positive differences indicate a longer storm duration in the modeled data. The naming convention of the WRF simulations follows Table 2 in Paper *P1* (see Appendix A).

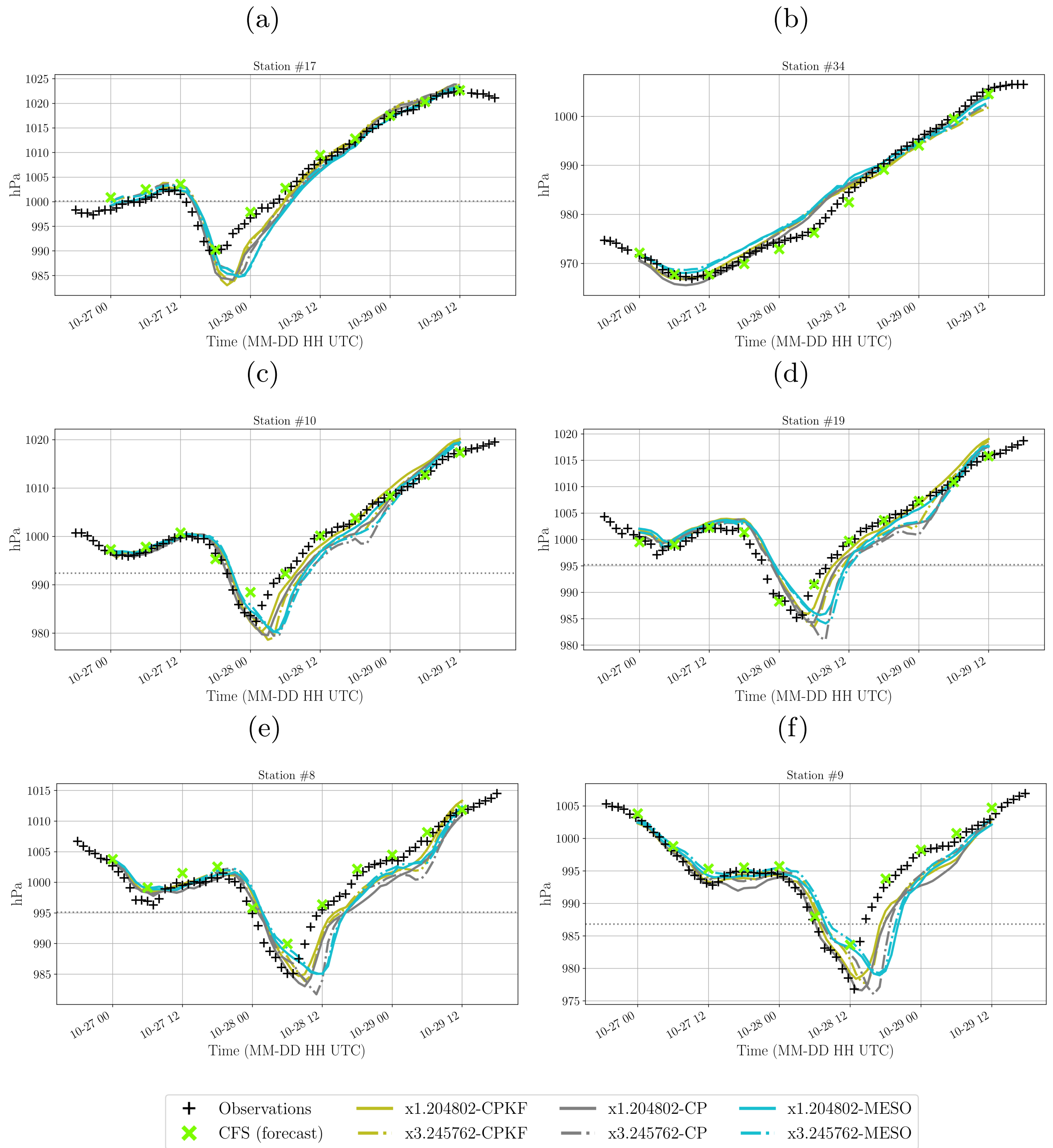

Figure 4.7: MPAS modeled SLP time series obtained from the quasi-uniform (solid lines) and variable-resolution (dashdotted lines) mesh with different physics configurations (indicated by the suffix "CPKF", "CP" and "MESO" in legend): (a) station #17, (b) station #34, (c) station #10, (d) station #19, (e) station #8 and (f) station #9. Black plus: Buoy observations, green 'x': SLP from CFSv2 6-hour forecast.

(a)

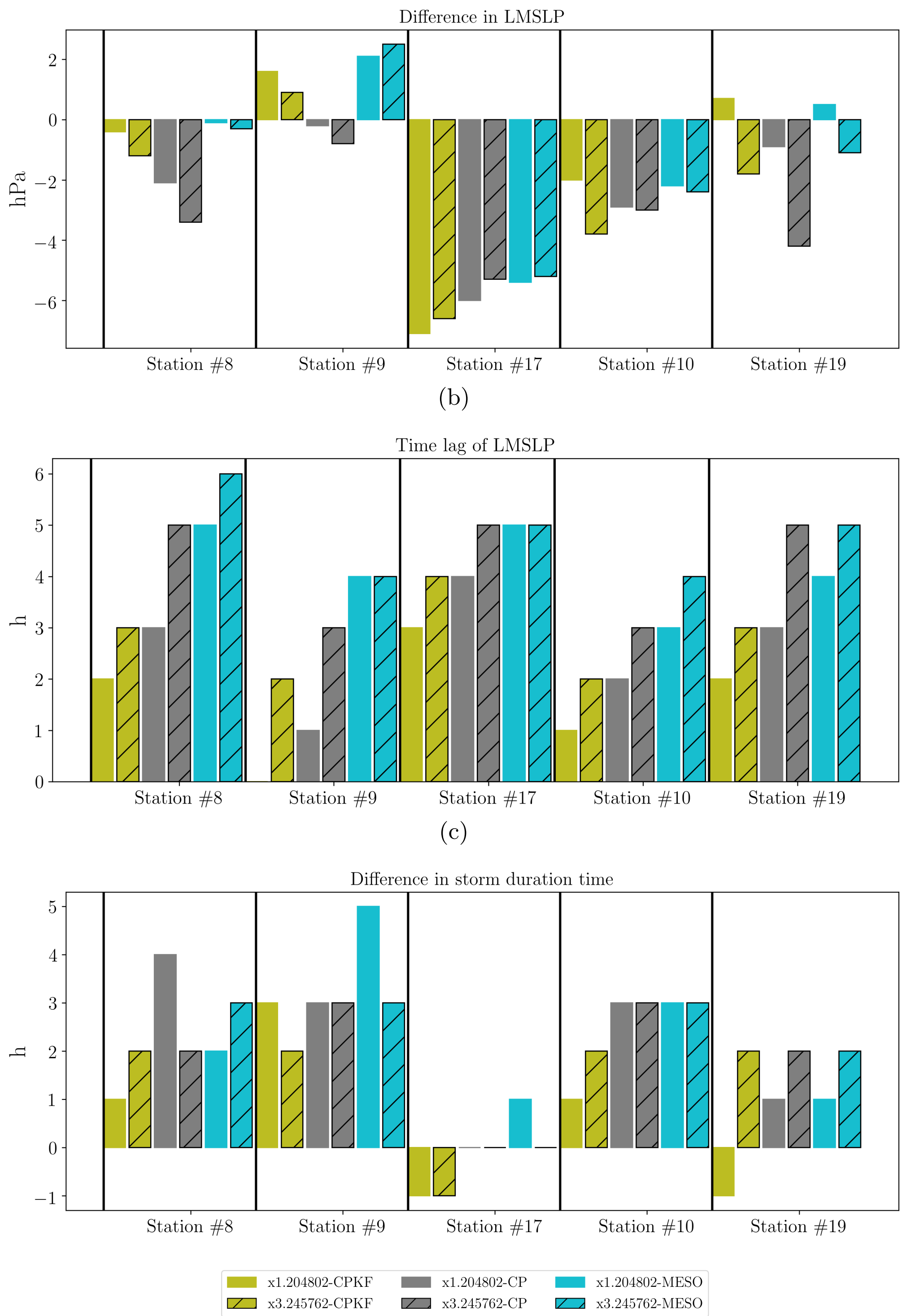

Figure 4.8: Comparison between observed and simulated storm characteristics from MPAS with different physics configurations: (a) Difference between modeled and observed LMSLP. Positive differences indicate a higher LMSLP in the model. (b) Difference between modeled and observed storm arrival time. Positive differences indicates a later storm arrival time in the modeled time series. (c) Difference between modeled and observed storm duration. Positive differences indicate a longer storm duration in the modeled data.

4.4 Discussion and Conclusion

Overall, this study shows that MPAS is able to adequately simulate the episode of storm "Christian" with respect to the larger-scale trends. Significant improvements in the determination of the storm intensity are found compared to CFSv2 and WRF. However, positive biases in the storm arrival time and prolonged storm duration (as defined in Section 4.3.3) are detected compared to observations. While the current investigation focused only on the sea level pressure and derived quantities (storm duration and time shifts), the analysis does reveal some of the key characteristics in MPAS for simulating a mid-latitude storm case study. This study especially highlights the impact of regularly updated lateral boundary conditions, or the lack thereof, on the storm characteristics.

The independence of the MPAS model integration from external forcing data (after model initialization) enabled the model to freely develop the storm structure. This results in storm intensities that are in better agreement with the observations at most stations (Figure 4.6a, Figure 4.5) in comparison with CFSv2 or WRF. The CFSv2 forecast was not able to develop a sufficiently deep storm (e.g. Figure 4.5c,e,f). As a direct consequence, the performance of the WRF downscaling was unavoidably deteriorated due to the large influence of the CFSv2 from the lateral boundaries. Even though WRF provides a variety of methods to control the impact of the lateral boundary conditions (nudging techniques, domain displacement, relaxation zone adjustments, LBC update frequency), they can influence the large scale steering only to a limited extent. This effect is enhanced by the relatively small size of the WRF domain, which limits the space for development of higher resolution features.

Further away from the storm structure, with respect to time and space, the positive benefits of the regular LBC updates become visible. Before and after the critical local storm arrival time (approximately plus/minus six hours depending on the station), the CFSv2 forecast is in good agreement with the observations. In turn, the WRF simulations are also close to the observations during those times. The MPAS simulations, on the other hand, are free of external factors once they are initialized. Therefore, deviations during the MPAS model integration, like the emerging westwards shift of the storm in the MPAS forecasts (cf. Figure 4.3e,f and Figure 4.4e,f), are not influenced or corrected. Both the quasi-uniform and variable-resolution meshes are affected similarly by this (cf. minor differences in SLP in Figure 4.3d). This synoptic flow deviation from the real atmospheric state also partly explains the observed positive time shifts compared to the measurements (Figure 4.6b, Figure 4.6b).

While a deviation in the predicted storm arrival time is an important factor in forecasting, its importance might be of lower concern for studies that focus on time-independent evaluations and statistics. Such studies include investigations of the cumulative sum of hours with wind speeds above a certain threshold as presented in Christakos et al. (2016) or the creation of windstorm footprints as presented in Roberts et al. (2014).

Larger-scale trends in the spatial and temporal evolution of the SLP are similar in the quasi-uniform and variable-resolution simulations. However, the introduction of the mesh refinement showed signs that the transition region can affect the storm structure. In the case of x3.245762-CPKF, an excessive deepening of a small area in the south-western area of the storm (cf. snapshots in Figure 4.4b-d) caused a further westward shift in the location of the LMSLP compared to its quasi-uniform counterpart. This is superimposed on the already existing westward-shift of the whole storm structure due to the initial deviations in the MPAS forecast. Consequently, x3.245762-CPKF systematically simulates a later storm arrival time at stations within the refinement region and in the vicinity of the storm track (station #10, #19, #8 and #9 in Figure 4.5c-f) when compared to x1.204802-CPKF. This behavior is also more or less independent from the chosen model physics (Figure 4.8b). In general, the choice of model physics has a varied impact on the storm intensity, storm arrival time, and storm duration. For some locations and storm indicators (e.g. storm intensity at station #8 and #9), the impact of the model physics has a bigger impact than the mesh configuration (quasi-uniform or variable-resolution).

It must be noted that the presented investigation provides only a limited view on the impact of the transition zone and refinement region on the mid-latitude cyclone being studied, due to its focus on the large-scale SLP field. Nevertheless, the analysis does indicate that the transition of complex structures like mid-latitude storms from coarse to fine scale regions still remains challenging also in the case of gradual transition zones. Major drawbacks due to external LBCs (sudden resolution jump and spatial and temporal interpolation and physics inconsistencies) are avoided, but distortions of the storm structure are not avoided completely.

4.5 Future Work

The assessment of the MPAS model performance on the case study of storm "Christian" revealed several areas that require and motivate further investigations:

- **Expansion beyond SLP analysis**: The current investigation provides a narrow view on the potential benefits of the refinement zone, due to the focus on SLP, which represents a large-scale storm feature (Hoskins and Hodges 2002). A more detailed analysis including, for example the 850 hPa wind speed and vorticity field, is needed to obtain a clearer picture of the potential benefits of the refinement zone, and to help explain the changes in storm structure that were observed in this study. Both fields contain more information about the smaller-scale storm features (Hoskins and Hodges 2002) and can provide a deeper insight into the impact of model refinement.
- **Mesh sensitivity analysis**: The current study investigated only a single variable-resolution mesh configuration with circular refinement. For fast traveling structures like mid-latitude storms, the initial variable-resolution setup might have a too narrow transition zone. This could have negative affect the storm development. Further tests, especially with respect to the transition zone width, are required to get a better understanding of the impact of the transition zone width on the storm structures. In combination with the simulation of further case studies, the sensitivity analysis could help to improve the MPAS setup for mid-latitude storm simulations over the North Sea area.

- **Exploration of data assimilation techniques**: The inclusion of regular updates of the atmospheric conditions could help to constrain the MPAS simulations and avoid large deviations from the actual atmospheric state in the large scales. For this purpose, continuous data assimilation techniques might be worth exploring. Bullock Jr. et al. (2018) proposed a continuous data assimilation implementation strategy for analysis nudging in MPAS. The methodology follows the concept by Stauffer and Seaman (1990) which is also used in WRF (Skamarock et al. 2008). This approach could help to constrain model deviations provided that the underlying analysis performs satisfactorily with respect to observations. This would require a thorough study of the performance of the nudged fields. Furthermore, additional adjustments might need to be considered to avoid too aggressive nudging in the vicinity of the storm.

CHAPTER 5
Modeling Open Cellular Convection

This chapter describes the second case study of MPAS for wind energy applications performed in this PhD project, and deals with the simulation of an episode of open cellular convection (OCC) over the North Sea and its associated impact on spatial and temporal wind variability. As with the storm "Christian" case study in Chapter 4, the OCC episode has been investigated with both MPAS and WRF. Background information and motivation for the OCC case study is presented in Section 5.1 and a description of the used MPAS and WRF model setups is provided in Section 5.2.

A large part of the results from this case study are reported in "Investigation of Spatial and Temporal Wind Variability during Open Cellular Convection with the Model For Prediction Across Scales (MPAS) in Comparison with Measurements" (Paper *P2*), which is summarized in Section 5.3. In addition, key findings from two additional investigations are presented in Section 5.4 and Section 5.5. Section 5.4 presents results from a MPAS sensitivity study that focused on the impact of the model initialization time on the modeled offshore wind speed and wind direction time series. Section 5.5 focuses on the spatial development of OCC structures in MPAS, compared to the traditional WRF nesting approach. The chapter finalizes with a discussion in Section 5.6.

5.1 Background and Motivation

[This Section 5.1 is based to a large extent on Section 1 and Section 2.1 of Paper *P2*]

Open cellular convection (OCC) describes an atmospheric phenomenon that is characterized by organized convective cellular structures (or open cells) over the marine boundary layer (Agee 1987). Open cells typically develop in situations where colder air masses are advected over warmer sea surfaces behind a cold front, for example, during cold-air outbreaks (Agee et al. 1973). They are characterized by cloudy cell borders with thin updraft regions that surround cloud free regions with broader downdraft regions in the cell center (Atkinson and Zhang 1996). The individual cellular structures have a spatial extension on the order of 20 to 50 km (Bakan and Schwarz 1992) and the moving OCC structures are accompanied by large temporal and spatial wind variability over the sea (Vincent 2010; Larsén et al. 2017a). OCCs have large impacts on offshore wind farm power production due to the high spatial correlation of wind speed fluctuations, especially over regions with high spatial concentration of turbines, like the North Sea area (Akhmatov et al. 2007; Vincent and Trombe 2017; Göçmen et al. 2020). This is especial critical in the North Sea area, because it is not only the main region for offshore wind energy development in Europe (WindEurope 2020), but also frequently experiences OCC conditions (Bakan and Schwarz 1992; Larsén et al. 2017b).

From a modeling perspective, the simulation of a cold-air outbreak with OCC provides an interesting use case for the MPAS model. The proper simulation of OCC and the associated spatial and temporal wind variability involves a broad range of atmospheric scales. The timing and location of the frontal zone needs to be captured to adequately represent the sudden change in wind direction. In addition, a high model resolution is required to realistically reproduce the mesoscale cellular structures and their associated wind fluctuations. In an investigation with WRF, Vincent (2010) found that a model grid distance on the order of 2 km is required to adequately represent OCC wind variability.

This chapter presents the simulation of a cold-air outbreak from December 2010, which was accompanied by an episode of OCC over the North Sea area. On 16 December 2010, arctic cold air moved south/southeastwards across the UK and North Sea region. An episode of OCC was observed behind the cold front and persisted until approximately 17 December 2010, 0000 UTC. Figure 5.1a shows the surface analysis chart at 16 December 2010, 0000 UTC while Figure 5.1b depicts a cloud picture of the open cell structures at 16 December 2010, 1830 UTC.

(a)

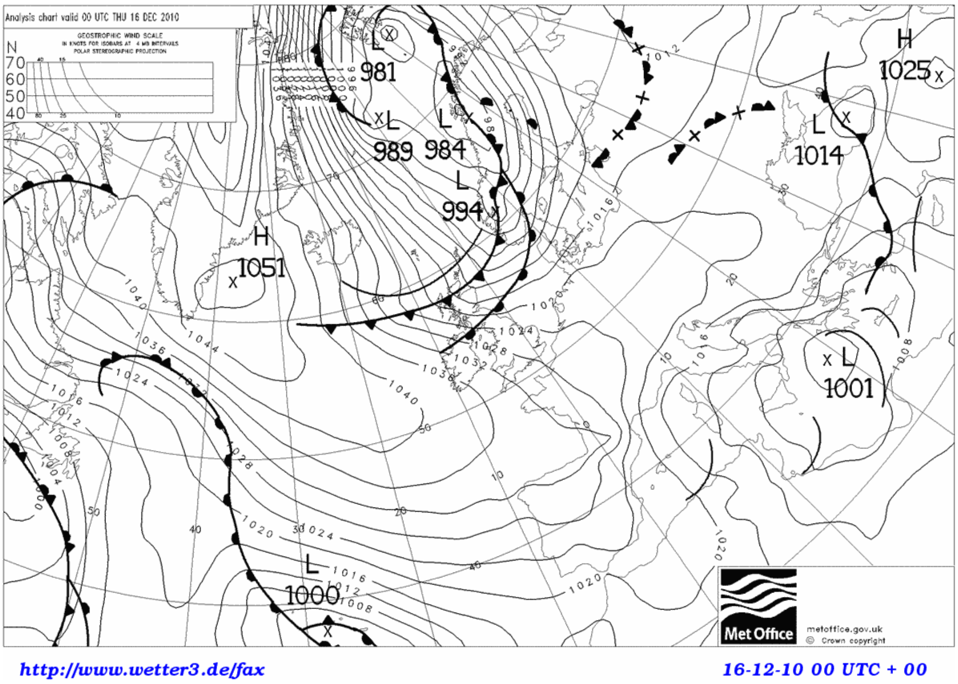

(b)

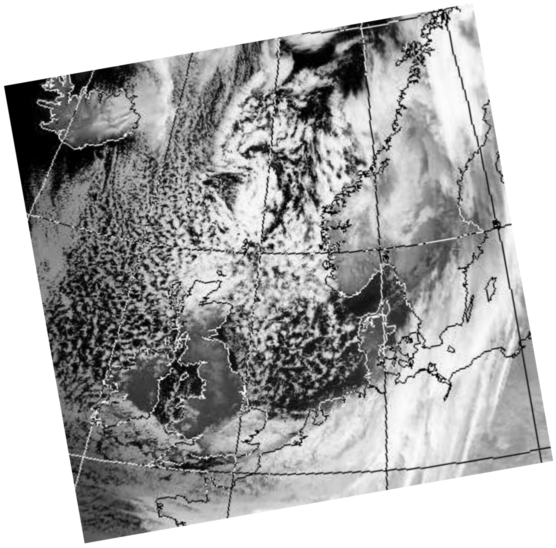

Figure 5.1: (a) Surface analysis chart valid at 16 December 2010, 0000 UTC from UK's Met Office ©Crown Copyright 2010 - Met Office. Archived analysis chart obtained from `http://www1.wetter3.de/archiv_ukmet_dt.html` (last accessed: Feb. 2020), (b) NOAA-19 Weather satellite image (channel 5) from 16 December 2010, 1830 UTC (clipped to northern Europe). Source: NERC Satellite Receiving Station, University of Dundee, `http://www.sat.dundee.ac.uk/abin/piccygridhtml/avhrr/2010/12/16/1244+19/ch5.jpg` (last accessed: Aug. 2019).

5.2 Methods

5.2.1 MPAS Model Setup

To assess MPAS's capabilities to capture the temporal and spatial wind variability associated with OCC, a variable-resolution mesh configuration with circular refinement has been designed in this project. The mesh cell distances range from approximately 55 km in the coarse scale region to approximately 2 km in the refined region, which is located over the North Sea area (Figure 5.2). The generated mesh, with its 901,123 Voronoi generators, follows the mesh density function ρ_{x30} introduced in Chapter 3 and has been tested in idealized mode (cf. Section 3.2.3). This configuration balances the high requirements on small model grid distances with the overall computational costs.

Fifty-five model levels are used in the vertical and the model physics follow the *'convection_permitting'* physics suite (cf. Table 2.1). The CFSR 6-h forecast data product (Saha et al. 2010) provides the initial conditions (at 0.5° spatial resolution), and the input for the sea surface temperature and sea ice updates (at 0.3° spatial resolution). The sea surface temperature and sea ice are updated every six hours. Three different model initialization times have been investigated: 15 December 2010, 0000 UTC (further referred to as MPAS-15UTC00 configuration), 15 December 2010, 1800 UTC (further referred to as MPAS-15UTC18) and 16 December 2010, 0000 UTC (MPAS-16UTC00). Each model configuration is integrated until 17 December 2010, 0000 UTC.

5.2.2 WRF Model Setup

A WRF (Version 3.7.1) configuration, with one-way nesting, is run as part of this study to compare with the MPAS simulation. The configuration consists of an outermost domain of 18 km horizontal grid spacing and two nests with a horizontal grid spacing of 6 km and 2 km, respectively, and 52 model levels in the vertical. The location of the three domains are depicted in Figure 5.2a.

The initialization time, for the WRF simulation, is set to 15 December 2010, 0000 UTC, which is identical to the MPAS-15UTC00 configuration (cf. Section 5.2.1). The model is integrated for 48 hours with a 6-hourly update of the LBCs and the sea surface temperature. The initial and boundary conditions are provided from the same external data set (CFSR 6-h forecast data product) used for the MPAS simulations.

The WRF model physics were selected to be similar to the MPAS *'convection_permitting'* suite (cf. Table 2.1) and are summarized in Table 5.1. This includes the selection of the scale-aware Grell-Freitas cumulus scheme, which is activated in all three WRF domains to act similar to MPAS, where the scale-aware scheme is activated over the whole globe. The scale-aware Grell-Freitas scheme is designed to effectively turn off deep convection and to act as shallow convection scheme when horizontal grid spacing is decreasing (Grell and Freitas 2014).

Table 5.1: Summary of the WRF physics configuration used in this investigation. Used abbreviations: MYNN: Mellor–Yamada–Nakanishi–Niino, RRTMG: Rapid Radiative Transfer Model for General Circulation Models.

Physics	Parameterization scheme
Cumulus	Scale-aware Grell-Freitas (Grell and Freitas 2014)
Microphysics	Thompson (Thompson et al. 2008)
Land surface	Noah (Tewari et al. 2004)
Boundary layer	MYNN (Nakanishi and Niino 2009)
Surface layer	MYNN (Nakanishi and Niino 2009)
Long-/shortwave radiation	RRTMG (Iacono et al. 2008)

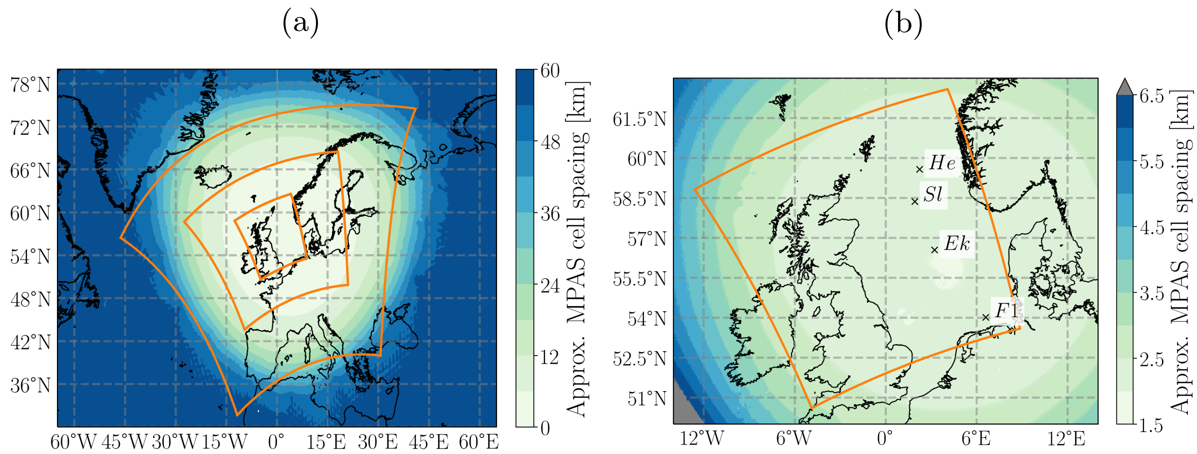

Figure 5.2: (a) Approximate MPAS cell spacing between a Voronoi cell center and its neighbors over Europe (green-blue contours). Orange frames: Location of the WRF outermost domain and its two nests. (b) Zoomed version of (a) with focus on the North Sea region. The orange frame in (b) indicates the location of the innermost WRF domain. The black 'x'-markers in (b) depict the location of the four measuring locations 'Heimdal' (He), 'Sleipner-A' (Sl), 'Ekofisk' (Ek) and Fino 1 (F1) used in the time series analysis in Section 5.4. Note the different scaling of the colorbars in (a) and (b).

5.3 Investigation of Wind Variability during OCC Conditions with MPAS - Introduction to Paper *P2* (Appendix B)

Paper *P2* "Investigation of Spatial and Temporal Wind Variability during Open Cellular Convection with the Model For Prediction Across Scales (MPAS) in Comparison with Measurements" investigates the capabilities of MPAS to represent the temporal and spatial wind variability associated with OCC in the southern North Sea area. The analysis is based on the MPAS-16UTC00 scenario described in Section 5.2.1. Model results are compared with satellite retrieved wind speeds, four ground based measurement sites and one sounding location. The ground based measurement sites are distributed over the

North Sea area.

It was found that MPAS is able to represent spatial and temporal wind variability in a realistic way given the constrains of the model's effective resolution. The wind speed variability connected with the OCC was isolated by means of high-pass filtering in the time domain. The model and the measurements agree well with respect to the standard deviation of the filtered wind speed at three of the four ground based stations. The differences are bounded within 0.1 m s^{-1} when deviations due to data availability rate are considered as well. Furthermore, the observed increase in 10-minute wind speed step changes under OCC conditions was also captured in the model, while OCC unaffected sites in the model follow the expected normal climatological conditions determined by Mehrens et al. (2016).

With respect to the spatial wind variability, decent agreement between modeled spatial power spectrum and the spectrum from satellite retrieved winds is found for wavelengths larger than the model's effective resolution.

It was also observed that the gradual development of small scale atmospheric movements due to the smooth transition zone allowed the creation of OCC structures as soon as the model resolution becomes high enough, without the need of additional spatial model spin-up observed in limited area models (Vincent 2010, further investigation in Section 5.5).

Overall, MPAS was able to

- satisfactorily capture the temporal wind speed variability,
- properly represent the OCC related increase of the 10-minute wind speed step changes,
- adequately model the additional energy in the spatial wind speed power spectrum within the limits imposed by the effective resolution, and
- develop OCC structures as soon as the model resolution allows without additionally required spatial spin-up.

5.4 Influence of Model Initialization On Wind Speed Time Series

Figure 5.3 depicts the modeled and observed wind speed time series at four measuring locations in the north sea (Heimdal, Sleipner-A, Ekofisk and Fino 1). It is observed that the MPAS simulation initialized at 0000 UTC on 15 December 2010 (scenario MPAS-15UTC00) results in a significant overestimation of the wind speed magnitude in the later stages of the simulation, after 1800 UTC, when the OCC should be present (cf. satellite image in Figure 5.1b).

While the generally observed decreasing tendency of mean wind speed after 16 December 2010, 0600 UTC is maintained at Heimdal, the modeled wind speed magnitude at Sleipner-A, Ekofisk and Fino 1 do not follow this trend. The misinterpretation of the wind speed trend is not visible in the limited-area simulation in WRF, and also vanishes in the MPAS simulations initialized later (18 hours and 24 hours, respectively,

Figure 5.3). This suggests a model drift from the real atmospheric state in the large-scales in MPAS-15UTC00, rather than an impact of the model physics or the mesh configuration on the wind speed time series. MPAS-16UTC00 and WRF show decent agreement with the measurements. MPAS-15UTC18 also starts diverging towards the end of the simulation period from the observed wind speed trend at the two northern measuring sites (Heimdal and Sleipner-A).

Further analysis shows that the deviations originate from the displacement of a low-pressure system over Scandinavia for simulations with early initialization times. In MPAS-15UTC00, the system is shifted to the south (Figure 5.4a) compared to the MPAS-16UTC00 and WRF simulations (Figure 5.4b and Figure 5.4c, respectively). The displacement results in a weather regime shift in the North Sea area in MPAS-15UTC00. Instead of the north/northwesterly flow with OCC, the low-pressure system suppresses and replaces the development of OCC in the eastern North Sea area. The wind speed magnitude increases and the north/northwesterly flow turns to a more southward direction in the northern North Sea area due to the influence of the counterclockwise flow rotation around the low pressure system. This causes the wind field in the later stages of the simulation to be dominated by the low-pressure system instead of the OCC (Figure 5.5a and Figure 5.5b-c, respectively).

This is different than during the earlier modeling period (15 October 2013, 0000 UTC to approximately 15 October 2013, 0000 UTC), where the WRF and MPAS-15UTC00 performance remains highly comparable at the measuring sites. This includes not only the wind speed trends (Figure 5.3), but also the magnitude and changes in wind direction (Figure 5.6). The close agreement suggests that there is no deviation in the large-scale atmospheric features that potentially affect the North Sea area (location of synoptic pressure systems and frontal zones) during that period. For instance, the timing of the passing warm front (cf. Figure 5.1a) and its associated flow direction change is captured very well at Fino 1 (Figure 5.6d at approximately 15 December 2010, 2000 UTC) by MPAS-15UTC00 and WRF.

The first major differences between MPAS-15UTC00 and WRF occur in the timing of the sudden change in wind direction from westerly to northerly flow (Figure 5.6). This change is associated with the passing of the cold front over the measuring sites (cf. Figure 5.1a). MPAS-15UTC00 simulates the cold front earlier than WRF, with differences on the order of 30 minutes (Ekofisk) to 1 hour (Heimdal). As expected, the MPAS simulations initialized later, MPAS-15UTC18 and MPAS-16UTC00, provide a better estimation of the timing of the cold frontal passage.

(a)

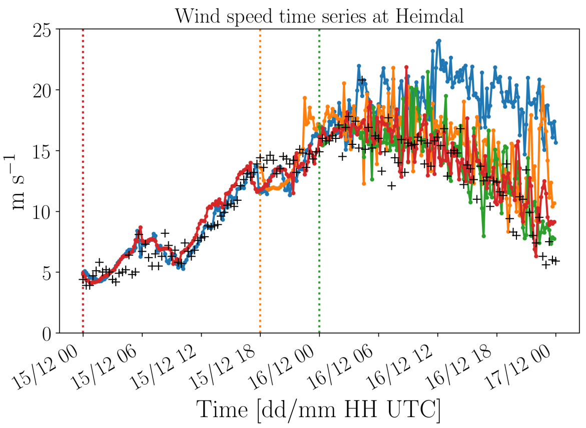

(b)

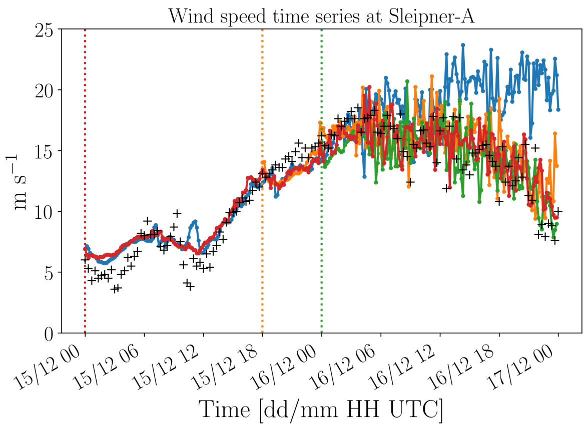

(c)

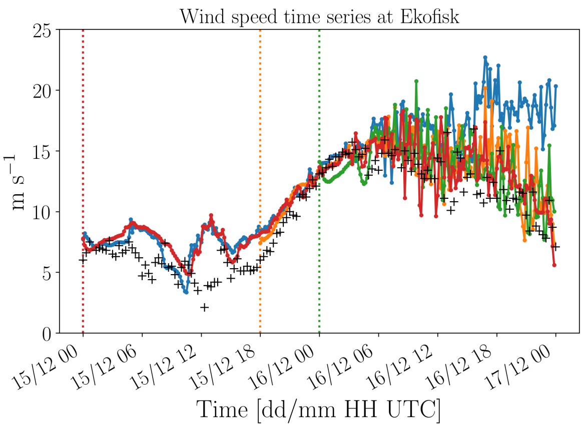

(d)

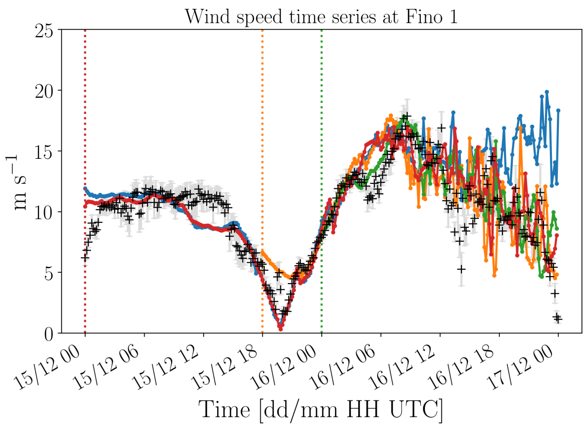

Figure 5.3: Modelled (colored lines) and observed (black plus) wind speed at (a) Heimdal (10 m above ground), (b) Sleipner-A (10 m above ground), (c) Ekofisk (10 m above ground) and (d) Fino 1 (71 m above ground). Blue: MPAS initialized at 15 December 2010, 0000 UTC, orange: MPAS initialized at 15 December 2010, 1800 UTC, green: MPAS initialized at 16 December 2010, 0000 UTC, red: WRF initialized at 15 December 2010, 0000 UTC. The vertical dashed lines highlight the initialization time of the different model configurations. The gray bars in (d) show mean wind speed (10-minutes) plus/minus one standard deviation.

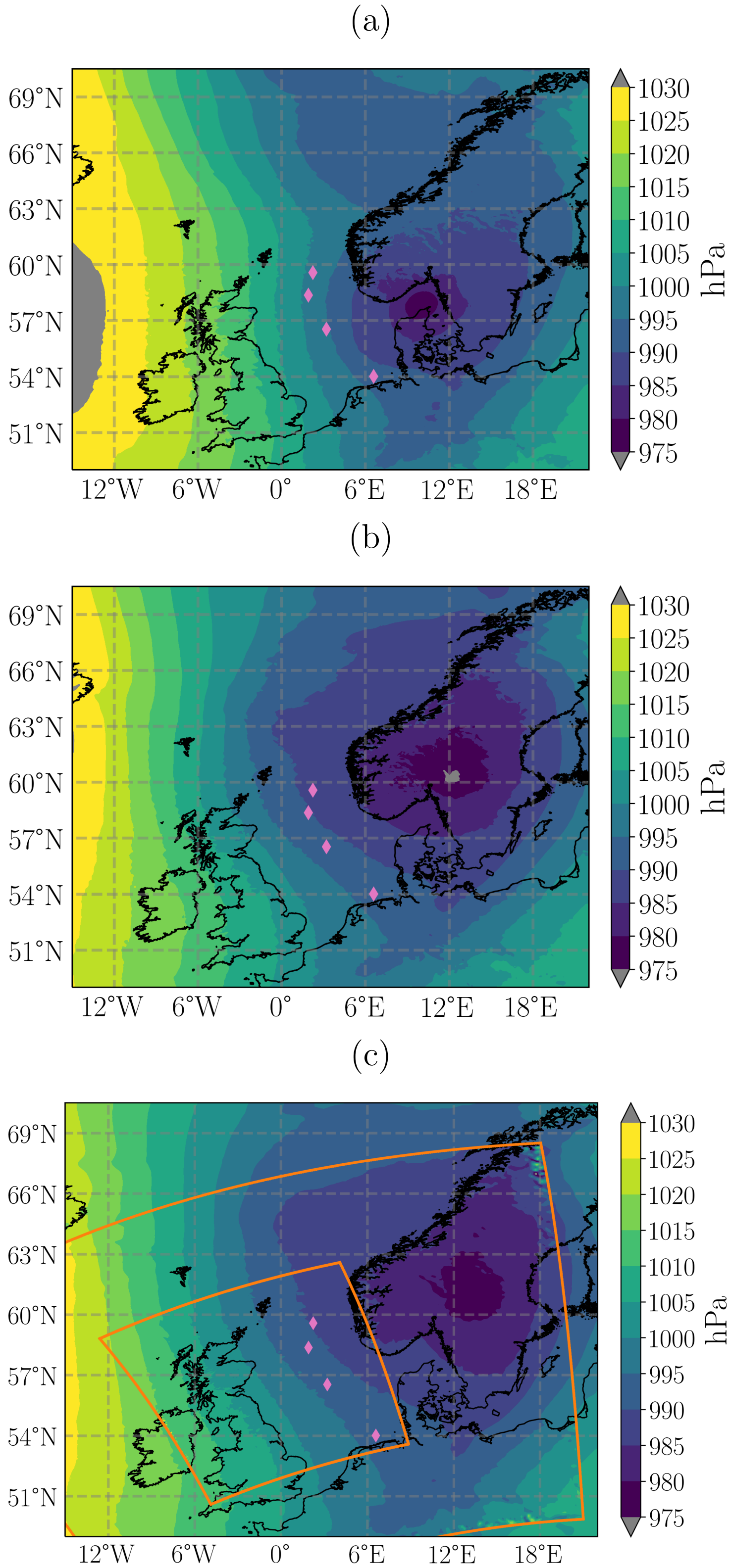

Figure 5.4: Snapshot of the modeled mean sea level pressure (MSLP) at 16 December 2010, 1830 UTC for different simulation scenarios: (a) MPAS-15UTC00, (b) MPAS-16UTC00 (c) WRF. Pink diamonds: measuring locations Heimdal, Sleipner-A, Ekofisk, Fino 1 (from north to south). The orange frames in (c) indicate the border of the second and third WRF domain depicted in Figure 5.2a. Results in (c) are obtained by using the WRF model output with highest spatial resolution available for a particular region.

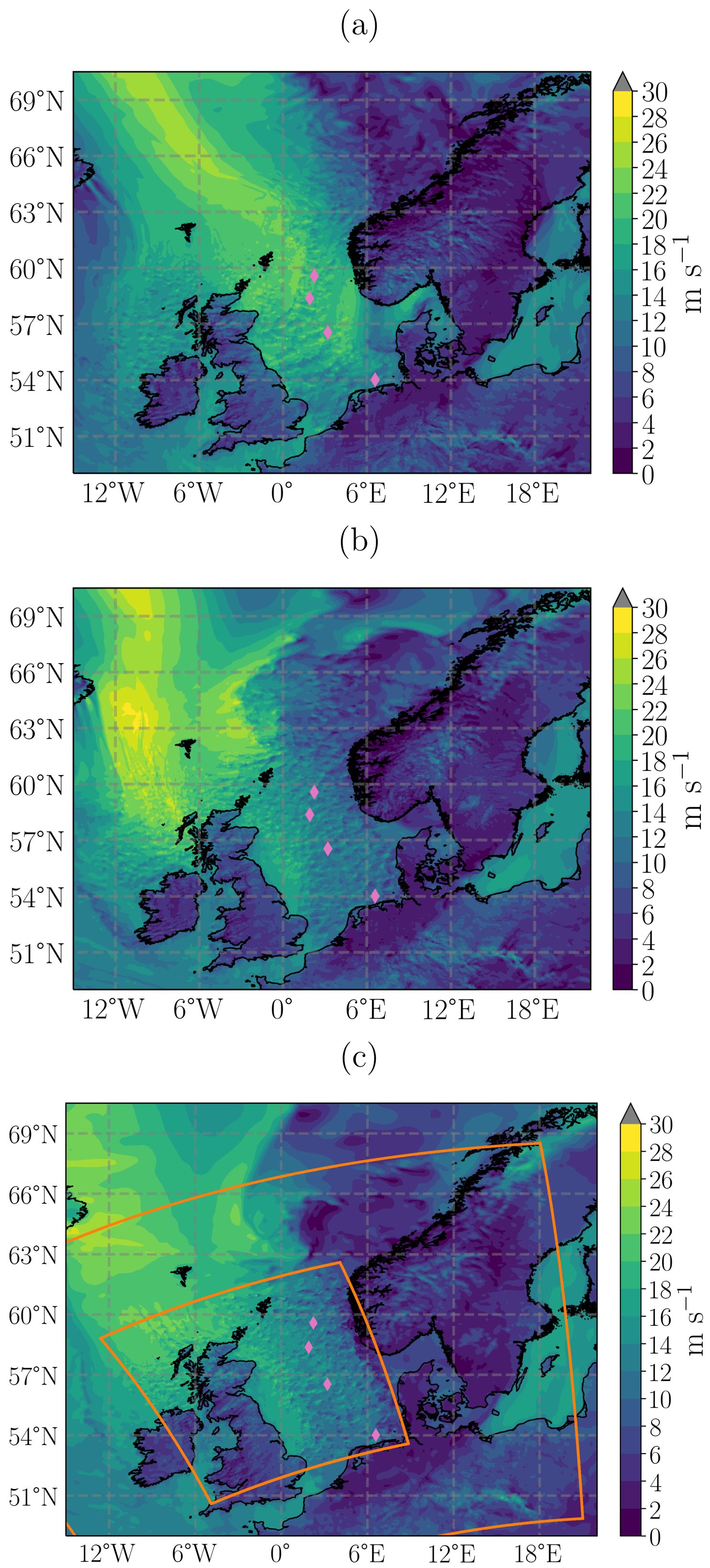

Figure 5.5: Same as Figure 5.4 but for absolute wind speed (10 m).

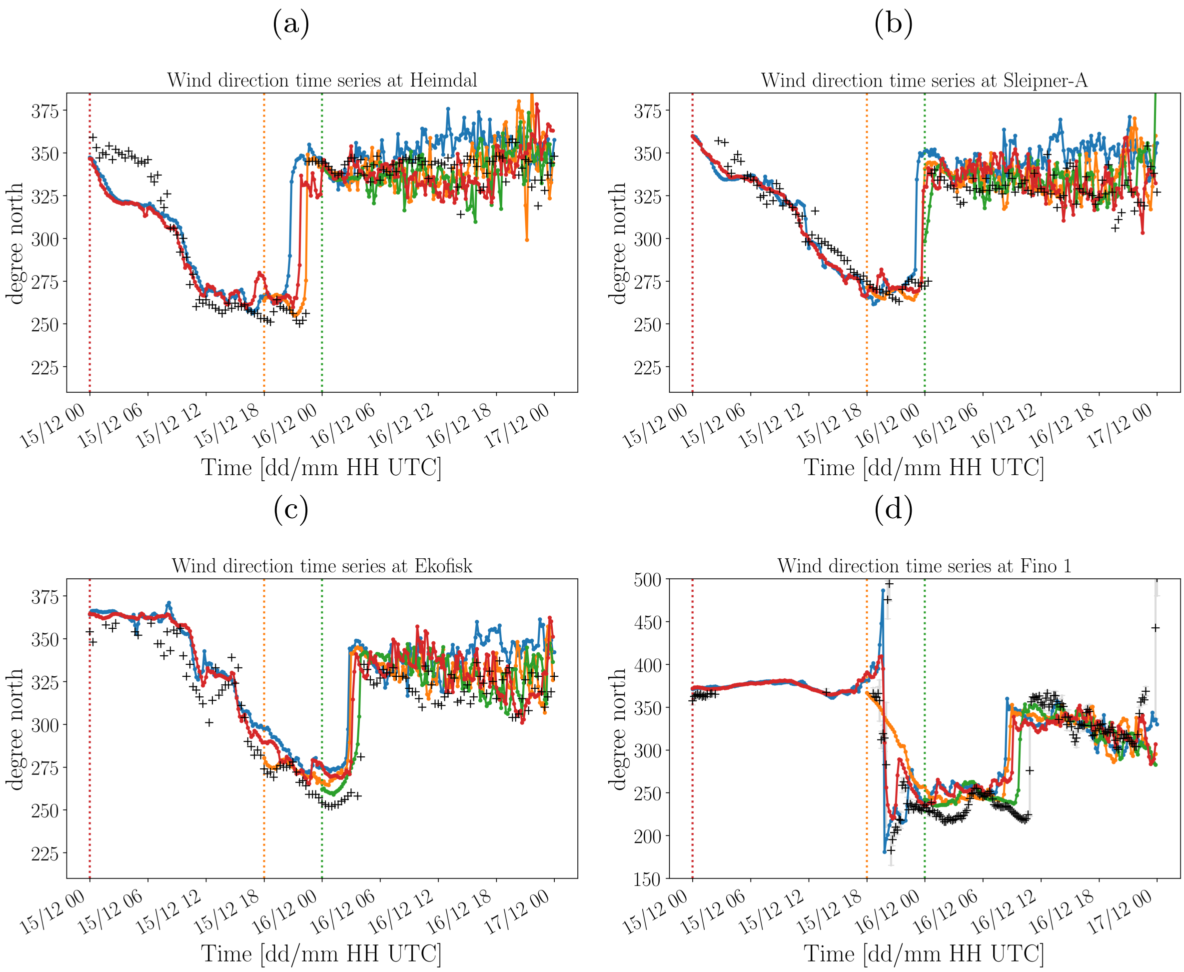

Figure 5.6: Same as Figure 5.3 but for wind direction. To enhance readability and avoid large jumps in the graph due to the dominating wind direction from the north, a constant value of 360° has been added to all wind directions smaller than 180°. Be aware of the different range of the y-axis in Figure 5.6d.

5.5 Impact of WRF Nesting on Spatial OCC Development

While MPAS' smooth transition zone allows the gradual build-up up of the smaller scales of atmospheric features, WRF's grid spacing changes suddenly at the domain boundaries. This influences the build-up of small-scale features like OCC close to inflow border of the WRF domain. This can be seen in the vertical velocity at the model level closest to 100 m (Figure 5.7a). In comparison to the MPAS results (scenario MPAS-16UTC00, Figure 5.7b), the cell structures in WRF are missing or are only insufficiently build up, close to the north-eastern inflow boundary. This is seen more clearly when examining the time-averaged mean of the vertical velocity along each WRF grid column from the southwest to the northeast (Figure 5.8). The characteristic up- and downdrafts associated with the OCC are only seen after 60-65 grid cells or 120-130 km away from the north-western inflow boundary. This needs to be taken into account during the initial domain design to avoid negative impacts due to the insufficient build-up of the cellular structures. It must be noted that the measuring sites used in this project were located sufficiently far away from affected domain region that they were not impacted by this (cf. Figure 5.8).

At the outflow of the innermost WRF domain, major inconsistencies in the vertical velocity are observed at the border of the innermost (third) and the second domain. This can be seen, for example, in the region between the UK and the Netherlands in Figure 5.7. This is expected, because the second WRF domain with its $\Delta x = 6$ km grid spacing can only fully resolve features with wavelengths of around 42 km and above (based on the effective resolution of $7\Delta x$ of WRF, Skamarock 2004). Features with wavelengths between 12 km (Nyquist-frequency) and 42 km are only insufficiently resolved and OCC with their diameters in the order of 20-50 km (Bakan and Schwarz 1992) fall into this category. Therefore, the development of mesoscale cellular structures is suppressed outside the innermost WRF domain. Since the current WRF configuration is one-way nested, the OCC developed in the innermost nest does not feed back to the results of the second domain. Further investigations with a two-way nested WRF configuration would be needed to find potential impacts on the model results in the second domain.

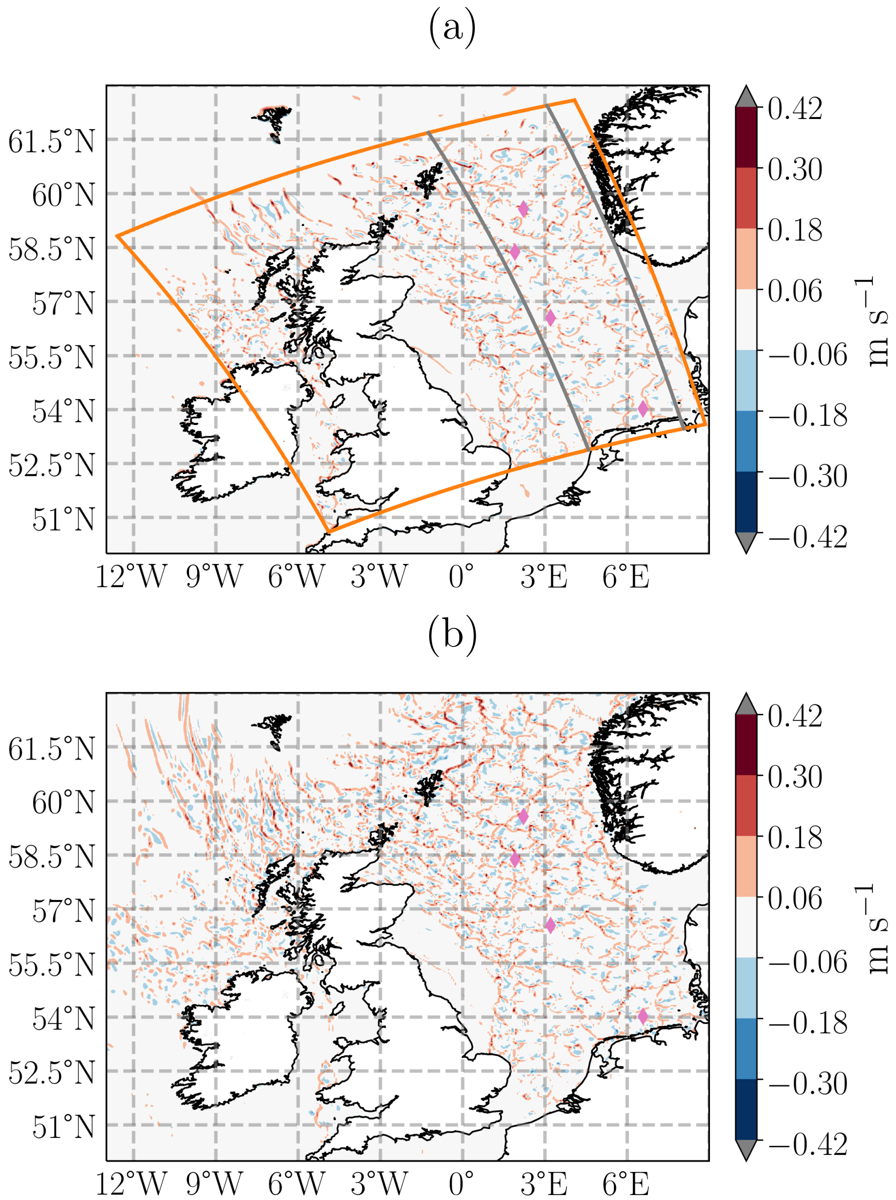

Figure 5.7: Snapshot of vertical wind speed at model level closest to 100 m at 16 December 2010, 1830 UTC determined by (a) WRF and (b) MPAS-16UTC00. The orange frame in (a) depicts the innermost WRF model domain. The gray lines in (a) mark the south-western and north-eastern border for the spatial averaging of the mean vertical up- and downdraft depicted in Figure 5.8. The pink diamonds in (a) and (b) depict the four measuring sites Heimdal, Sleipner-A, Ekofisk and Fino 1 (from north to south).

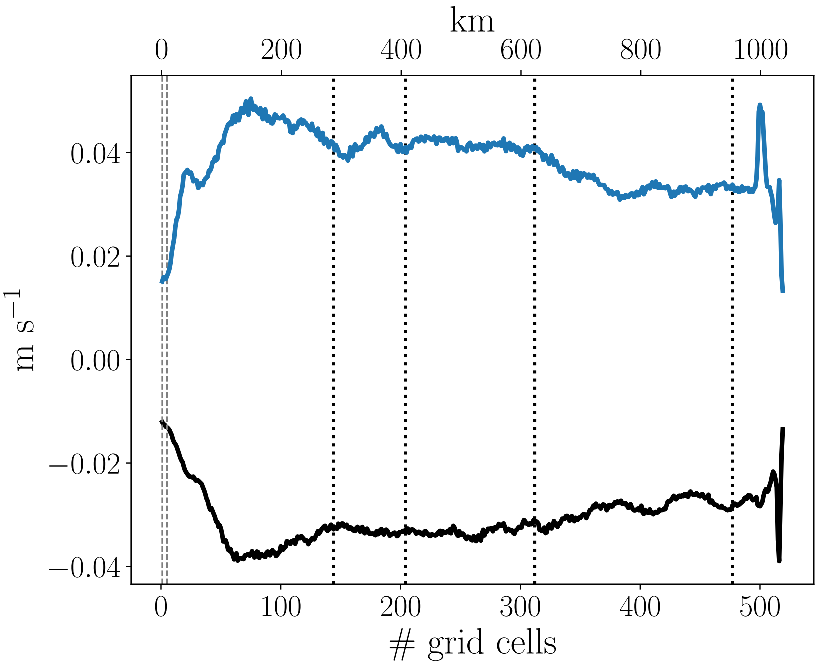

Figure 5.8: Mean vertical updraft (blue) and downdraft (black) in the innermost WRF domain at model level closest to 100 m as a function of the distance from the north-western inflow border. The dashed gray lines enclose the WRF relaxation zone. The vertical dashed black lines indicate the distance of Heimdal, Sleipner-A, Ekofisk and Fino 1 (from left to right) from the inflow border. The up- and downdrafts are time averaged between 16 December 2010, 1400 UTC and 17 December 2010, 0000 UTC and averaged in south-west/north-east direction between the gray lines depicted in Figure 5.7a.

5.6 Discussion

The results in Section 5.3 and Section 5.4 show that MPAS is able to properly represent the wind variability in time and space associated with OCC. This remains valid within the limits set by the model's effective resolution and under the condition that the model is initialized close enough to the OCC event of interest. If initialized too early, large-scale model deviations from the real atmospheric can change the relevant synoptic features and alter the expected OCC development. While the relatively high sensitivity to the initial conditions in MPAS is not surprising, due to the lack of external steering from LBC updates, it is worth noting that MPAS needs to be initialized significantly closer to the actual OCC event than what experience from WRF would suggest. Since open cellular convection is a relatively small-scale atmospheric phenomenon, the forecast requires a sufficiently long period of model spin-up to build-up the necessary small scale structures that are not present in the coarse initial conditions (Warner 2010; Davies 2014). In combination with the close initialization time, this can restrict the period available for a statistically meaningful analysis of the OCC episode. While simulations with WRF also suffer from this effect, the potential of earlier model initialization can mitigate the effect away from the actual period of interest. For OCC induced spatial and temporal wind variability within the lower part of the boundary layer, Paper *P2* showed that 6 hours of model spin-up is already sufficient for studying the impact on the flow field, given the mesh configuration and initial conditions. However, if other aspects of OCC are investigated (cloud and precipitation properties), the required model spin-up time might be different.

From a spatial perspective, the gradual mesh refinement in MPAS results in an overall smoother and more consistent representation of the development of the OCC structures and wind field compared to WRF (cf. Figure 5.7, Figure 5.5b,c). This could be especially beneficial when the detailed spatial build-up and decay of the OCC structures plays a significant role in the analysis, since the spatial distortions due to sudden resolution jumps in WRF are avoided.

However, this benefit is rather small for the investigation of temporal wind variability over a small area as performed in this project. A properly designed WRF configuration, which takes into account the inherent challenges of the sudden model resolution jump, like the additional required spatial spin-up, showed similar performance for the modeled wind speed time series at Heimdal, Sleipner-A, Ekofisk and Fino 1 (Section 5.4). One potential reason for the comparatively good performance of the one-way nested WRF approach could be the relative shallowness of the modeled phenomena. OCC are strongly driven by large scale phenomena like the air-sea temperature difference and the advection of cold air (Atkinson and Zhang 1996), with potentially limited influence on the driving scales. For this reason, the lack of feedback to the larger scale, due to the use of one-way nesting in WRF, seems to be of minor importance for the wind speed and wind direction time series.

CHAPTER 6
Modeling of Offshore Mesoscale Wind Farm Wakes

This chapter presents a study related to the potential application of MPAS for performing wind farm impact studies on the atmosphere. The motivation and the background are given in Section 6.1 and an overview of the observational data sets, the wind farm parameterization scheme and MPAS model setups are explained in Section 6.2. Key challenges and findings are presented in Section 6.3 and the chapter ends with a collection of general implications and the future outlook for wind farm impact studies with MPAS (Section 6.4).

6.1 Background & Motivation

As mentioned in Section 1.1, wind farms and wind farm clusters are not only affected by a variety of atmospheric flows across scales, but also alter the atmospheric flow themselves. A variety of methods have been developed to include wind farm effects in mesoscale LAMs and global models. They range from relatively simple representations via increased model surface roughness and/or modifications of displacements heights (e.g. Keith et al. 2004; Barrie and Kirk-Davidoff 2010; Wang and Prinn 2010) to more complex descriptions as elevated momentum sinks (e.g. Boettcher et al. 2015; Volker et al. 2015) and additional sources of TKE (e.g. Baidya Roy et al. 2004; Adams and Keith 2007; Fitch et al. 2012). Depending on the parameterization scheme, sub-grid scale processes like wake expansion in the vertical (Volker et al. 2015) or, to some degree, wind farm layout awareness (e.g. Abkar and Porté-Agel 2015) are considered.

Driven by computational constrains, previous numerical modeling studies of wind farm effects on global scales in general circulation models (Keith et al. 2004; Kirk-Davidoff and Keith 2008; Barrie and Kirk-Davidoff 2010; Wang and Prinn 2010; Wang and Prinn 2011) were performed on very coarse horizontal grids (on the order of 200-300 km), with simple wind farm representation via increased surface roughness. While this method is computationally efficient, and therefore well suited for global long-term climatological studies, the wind farm effects can only be captured to a limited extent. Furthermore, Fitch et al. (2013b)'s numerical study of wind farm effects during a strong diurnal cycle suggests that the atmospheric impacts of wind farms represented by increased surface roughness can result in unrealistic atmospheric feedback. Fitch et al. (2013b) detected unrealistically high sensible heat fluxes during the daytime in scenarios where wind farms are represented as increased surface roughness. They also found that surface roughness based wakes developed the strongest wakes during the day, while more detailed parameterization, which include an elevated momentum sink and TKE source, show the strongest wakes to occur during the night. The surface roughness approach was also accompanied by large amounts of TKE during daytime, which have not been observed to this extent in observational studies.

One of the reasons that the surface roughness models have been used in global studies is that more advanced wind farm paramterization models (WFPs) require higher spatial resolution than is typically used. Tomaszewski and Lundquist (2020) found in a sensitivity study using WRF that horizontal grid spacing of 3 km within the wind farm region is needed to adequately simulate the surface temperature impacts and wind deficits of wind farms in Iowa. Global studies on a uniform mesh with such a grid cell spacing (around 3 km), are currently not feasible due to the immense computational costs.

MPAS with its ability to use variable-resolution meshes can meet the high demands on horizontal resolution around the wind farms in the refinement zone, while the transitioning to coarser cell spacing outside of the area of interest keep the computational costs low compared to quasi-uniform simulations. Furthermore, the lack of boundary conditions in MPAS provides the opportunity to investigate the potential up-scaling of of large wind farm or wind farm cluster effects to larger scales. To the best knowledge of the author, MPAS has not yet been used for investigations of wind farm impacts on the atmosphere, and its capabilities for applications in this area are therefore unknown. Thus, a more detailed investigation is needed.

Within the scope of this Project, the 'Explicit Wake Parametrisation' (EWP, Volker et al. 2015) has been implemented and tested in MPAS in a initial case study. However, the initial case study revealed some unrealistic model deviations between the simulation with and without wind farm parameterization and this chapter presents the results from the initial case study and the major steps taken to trace back the origin of the model deviations.

The outline of this chapter is as follow: Section 6.2 provides a full description of the methods connected with the initial case study and the follow-up investigations (Analysis I - Analysis III). Results are presented in Section 6.3. Section 6.3.1 describes the results and observed challenges in the initial case study on a variable-resolution 60-3 km mesh configuration. It also presents results from Analysis I in which the complex EWP formulation is replaced with a simple increased surface roughness approach with minor impacts on the unrealistic model deviations. Analysis II (Section 6.3.2) presents the results of a physics sensitivity analysis on a coarse, quasi-uniform 240 km mesh configuration, which revealed inconsistent treatment of pseudo-randomness in the RRTMG radiation scheme. Analysis III (Section 6.3.3) investigates perturbation pressure differences on quasi-uniform mesh configurations with a minimal set of physics to inspect model deviations caused by "chaos seeding" (Ancell et al. 2018). The chapter finalizes with general implications and a future outlook in Section 6.4.

6.2 Methods

6.2.1 Observational Data and Simulation Period

Within the scope of the initial case study, a scenario with two existing wind farms in the Danish North Sea is chosen. Figure 6.1 depicts the spatial location of the two wind farms Sandbank and DanTysk together with the two met masts Fino 1 and Fino 3. Fino 1 is located relatively far from the wind farms, while Fino 3 is located between the two wind farms, to the west of DanTysk. Therefore, Fino 3 is highly impacted by both wind farms. More details about the two wind farms are given in Table 6.1, and details about the two met masts Fino 1 and Fino 3 are provided in Table 6.2.

A 2-day period from 17 February 2017, 0000 UTC to 19 February 2017, 0000 UTC (including 12 hours of model spin-up) was found to be suitable for the initial investigation of wind farm impacts on the atmosphere, for the following reasons:

1. **Atmospheric stability**: the simulation period contains an episode of relatively neutral and stable atmospheric conditions, where wind farm wakes are often more pronounced (e.g. Westerhellweg et al. 2014). Atmospheric stability is determined from the Bulk-Richardson number at Fino 3 based on wind speed and temperature measurements from the water surface and approximately 30 m above sea level.
2. **Absolute wind speed**: the wind speed at 91 m (Fino 3) is larger than the cut-in wind speed of the turbines of 4 m/s over the whole period.
3. **Data coverage**: the period is covered by met mast data from Fino 1 and Fino 3 with an availability rate of at least 95% for the wind speed and wind direction.

The search space was restricted to the year 2017 and 2018 for which additional wind speed, wind direction and power production data of Sandbank and DanTysk was made available. However, the wind farm data was not used within the scope of this study.

Table 6.1: Properties of the two wind farms Sandbank and DanTysk. Data are obtained from *The Wind Power* database, available at `https://www.thewindpower.net/`, last accessed: July 2020.

	Sandbank	DanTysk
installed capacity [MW]	288	288
number of turbines [.]	72	80
turbine type	Siemens SWT-4.0-130	Siemens SWT-3.6-120
turbine hub-height [m]	95	88
rotor diameter [m]	130	120

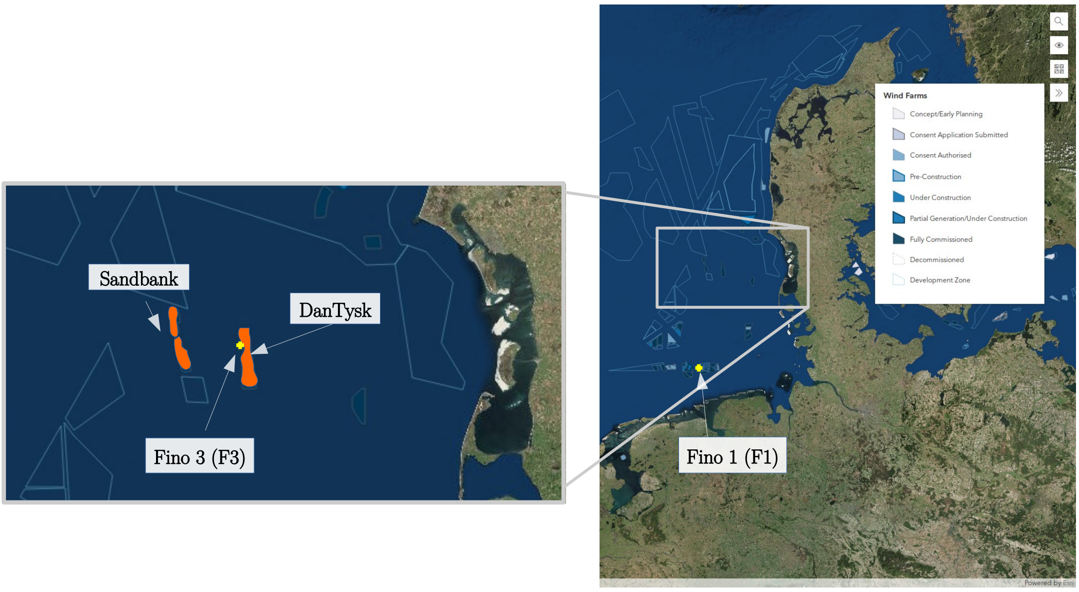

Figure 6.1: Depiction of the two wind farms Sandbank and DanTysk and the two met masts Fino 1 and Fino 3 in the southern North Sea. Figure inspired from Imberger et al. 2019 with modifications. Background map derived from: 4Coffshore, Global Offshore Renewable Map, available at `https://www.4coffshore.com/offshorewind/`, last accessed: July 2020.

Table 6.2: Name, geographic location and selected measurements from the two met masts Fino 1 and Fino 3. Measuring height and data availability rate within the period of interest (17 February 2017, 1200 UTC to 19 February 2017, 0000 UTC) are stated in brackets behind each variable. The following abbreviations are used: WS: Wind speed, WD: Wind direction, T: Air temperature, SST: Sea surface temperature. The measurements are obtained from the *Federal Maritime and Hydrographic Agency FINO database* (`http://fino.bsh.de`, last accessed: July 2020)

	Fino 1	Fino 3
geographic location	54.0149°N 6.5876°E	55.1950 °N 7.1583°E
selected measurements	WS (91 m, every 10 min)	WS (31 m† and 91 m, every 10 min)
	WD (91 m, every 10 min)	WD (101 m, every 10 min)
		SST† (water surface, every 30 min)
		T† (29 m, every 10 min)

† used for calculation of Bulk-Richardson Number

6.2.2 Wind Farm Paramterization

'Explicit Wake Parametrisation' Scheme

As mentioned in Section 6.1, a variety of schemes have been developed, in recent years, to parameterize wind farms in mesoscale models. Within the scope of this project and the initial case study, the 'Explicit Wake Parametrisation' (EWP) scheme by Volker et al. (2015) is implemented to investigate MPAS' capabilities for wind farm impact studies. The scheme was selected for the following reasons:

1. It is an established method that has already been used in a range of applications with the WRF model (e.g. Hasager et al. 2017; Pryor et al. 2020)
2. Personal familiarity with the scheme and experience[1] in applying EWP for wind farm impact studies in WRF
3. Extensive documentation on the implementation of the scheme in WRF that originates from the in-house development of the scheme.

In brief, the drag forces induced by the wind turbines are expressed in the EWP scheme as grid-cell averaged forces on the flow (Volker et al. 2015). The additional grid-cell averaged turbulence due to the presence of the wind turbines is managed via an explicit sub-grid scale turbulence diffusion formulation (Volker et al. 2015) that causes vertical expansion of the velocity deficit within the grid cell (Volker et al. 2015). Additional TKE, due to the presence of the wind farms, is solely produced from the wind shear in the vertical caused by the velocity deficit, i.e. no explicit TKE source term is added to the TKE equation in the PBL-scheme.

The scheme interacts with the MPAS model via the modification of the velocity tendencies of the PBL scheme by applying a grid-cell averaged acceleration $\bar{f}_d(k)$ to the flow (Volker et al. 2015). $\bar{f}_d(k)$ is derived from the total effective thrust force associated with a single turbine and is calculated as:

$$\bar{f}_d(k) = -\sqrt{\frac{\pi}{8}} \frac{c_t r_0^2 \bar{u}_0^2}{A\sigma_e} \exp\left[-\frac{1}{2}\left(\frac{z(k)-h}{\sigma_e}\right)^2\right] \tag{6.1}$$

with c_t being the wind turbine thrust coefficient for a given upstream velocity $\bar{u}_0$, r_0 being the turbine rotor diameter, $z(k)$ being the height above ground at model level k and h being the hub-height of the wind turbine. The variable A describes the area of the MPAS grid cell in which the wind turbine is located. The decomposition of $\bar{f}_d(k)$ in its zonal and meridional component is done based on the local wind direction $\phi(k)$ (Volker et al. 2015).

The mesh cell size dependent effective length scale σ_e is defined as:

$$\sigma_e = \frac{\bar{u}_0}{3KL}\left[\left(\frac{2K}{\bar{u}_0}L + {\sigma_0}^2\right)^{3/2} - \sigma_0^3\right] \tag{6.2}$$

[1]Personal contributions to entries *J1* (journal article in preparation) and *R1* (non peer-reviewed report) listed in the publication list in Appendix C, which were conducted during the PhD program, but are not part of this thesis report.

with K being the turbulence diffusion coefficient, L being the mesh cell size dependent downstream distance and $\sigma_0 = \alpha r_0$ being the initial length scale for the near-wake expansion.

The turbulence diffusion coefficient K is provided by the PBL scheme while the empirical scaling factor α needs to be specified via the MPAS namelist. In this study, a scaling factor of $\alpha = 1.5$ based on the selection in Volker (2014) is used. The downstream distance L, which is defined as half a grid cell distance in WRF, is replaced by half the cell distance between two Voronoi cell centers in the MPAS version.

As in WRF, all turbines are assumed to be located in the center of their corresponding mesh cell and the total trust force is calculated as a superposition of all individual thrust forces within a grid cell (in case of multiple turbines). A more complete description of EWP scheme, including a detailed derivation of Equation 6.1 and Equation 6.2, is provided in Volker et al. (2015).

Within the scope of this chapter, EWP is applied in the initial case study and in Analysis II.

Wind Farm as Increased Surface Roughness

In the implicit scheme, wind farms are parameterized as constant increased surface roughness. The scheme is merely used for the qualitative assessment of model deviations in Analysis I to Analysis III. This is done to investigate the reaction of MPAS to simple changes in surface roughness, without introducing the complexity of the EWP scheme at the same time. Since the wind farms are located offshore, an increased surface roughness was achieved by replacing Charnock's relation for surface roughness over water in the MYNN surface layer scheme. It is replaced by the identity $z_0 = 0.5$ m for cells containing wind farms. The magnitude was inspired by the model settings in Frandsen et al. (2009)'s investigation of large offshore wind farms with the mesoscale model KAMM.

6.2.3 MPAS Scenarios and Mesh Configurations

Within the scope of this chapter, thirteen different scenarios, with different configurations of physics schemes, mesh configuration, and wind farm representations, were designed. A summary of the mentioned scenarios is provided in Table 6.3. They are categorized according to the investigation where they first appear (initial case study or the follow-up investigations Analysis I to Analysis III).

In general, each scenario consists of simulations both with and without activated WFPs. Both simulations are initialized from the same initialization file. For each model output time step, results from the reference simulation are subtracted from the simulations with activated WFP and the difference between the two simulations is examined.

In total, three different MPAS mesh configurations are used: one variable-resolution (60-3 km cell spacing) and two quasi-uniform meshes (240 km and 60 km cell spacing). All described MPAS configurations share a standard model configuration with 55 vertical levels and a model top of 30 km. They also share the initialization time at 17 February 2017, 0000 UTC with reanalysis data from the 0.5° Global Forecast System. GFS

Scenario	MPAS mesh	Model time step (in s)	WFP	Con-vection	Micro-physics	Land surface	physics Radiation (longwave)	Radiation (shortwave)	Cloud fraction
Initial case study:									
EWP60-3KISS	60-3 km	12	EWP	GF	TMS	Noah[a]	RRTMG	RRTMG	Xu-R
Analysis I: Surface roughness approach:									
Z060-3KISS	60-3 km	12	Z0	GF	TMS	Noah	RRTMG	RRTMG	Xu-R
Analysis II: Physics sensitivity study:									
Z0240-GTN	240 km	1200	Z0	GF	TMS	Noah			
Z0240-R-Xu	240 km	1200	Z0	GF	TMS	Noah	RRTMG		Xu-R
Z0240-R-bin	240 km	1200	Z0	GF	TMS	Noah	RRTMG		binary[c]
Z0240-CAM	240 km	1200	Z0	GF	TMS	Noah	CAM		Xu-R
Z0240-KISS	240 km	1200	Z0	GF	TMS	Noah	RRTMG	RRTMG	Xu-R
Z0240-MT	240 km	1200	Z0	GF	TMS	Noah	RRTMG-MT[b]	RRTMG-MT	Xu-R
EWP60-3MT	60-3 km	12	EWP	GF	TMS	Noah	RRTMG-MT	RRTMG-MT	Xu-R
Z060-3MT	60-3 km	12	Z0	GF	TMS	Noah	RRTMG-MT	RRTMG-MT	Xu-R
Analysis III: Minimized physics setting:									
Z0240-MYNN	240 km	1200	Z0		(only MYNN surface and boundary layer scheme)				
Z0240-MYNN-DT300	240 km	300	Z0		(only MYNN surface and boundary layer scheme)				
Z060-MYNN	60 km	300	Z0		(only MYNN surface and boundary layer scheme)				

[a] Niu et al. 2011; Yang et al. 2011
[c] binary: cloud area fraction either 0 (completely cloud free) or 1 (completely cloud covered)
[b] RRTMG-MT: RRTMG with Mersenne-Twister random number generator (RNG) instead of KISSVEC RNG.

Table 6.3: Summary of sensitivity studies within the context of the wind farm verification process. All scenarios use the Mellor–Yamada–Nakanishi–Niino (MYNN, Nakanishi and Niino 2009) scheme for the parameterization of the surface layer and boundary layer. Used abbreviations: WFP: Wind farm parameterization, EWP: Explicit Wake Parametrisation, Z0: Surface roughness length paramterization, GF: Scale-aware Grell-Freitas (Grell and Freitas 2014), TMS: Thompson microphysics (Thompson et al. 2008), RRTMG: Rapid Radiative Transfer Model for General Circulation Models (Iacono et al. 2008), CAM: Radiation scheme of the NCAR Community Atmosphere Model (Collins et al. 2004), Xu-R: Xu and Randall 1996's semi-empirical cloud parameterization.

is downloaded from the *National Oceanic and Atmospheric Administration's National Centers for Environmental Information (NCEI)* database[2].

The 60-3 km mesh was obtained from the *MPAS-Atmosphere mesh repository*[3] and consists of 835,586 Voronoi cells (further referred to as x20.835586). The original mesh was rotated so that the refinement region is centered over the southern North Sea region. Figure 6.2a depicts the approximate grid distance in the refinement region. Figure 6.2b shows the representation of Sandbank and DanTysk on the x20.835586 mesh and the cell locations where time series data for the comparison with Fino 1 and Fino 3 are extracted for the initial case study. This mesh is used for the initial case study and in Analysis I and Analysis II.

Two quasi-uniform mesh configurations with approximate resolutions of 240 km and 60 km, respectively were used for an additional sensitivity study of wind farm effects with reduced complexity (follow-up studies Analysis II and Analysis III). They are combined with the increased surface roughness length approach (Section 6.2.2). This means that the wind farms are reduced to a single all-water cell that is closest to the wind farms (see example for the 240 km mesh in Figure 6.2c). The 240 km and 60 km mesh consist of 10,242 and 163,842 Voronoi cells, respectively. Both meshes were obtained from the MPAS-Atmosphere mesh repository[3].

[2] `https://www.ncdc.noaa.gov/data-access/model-data/model-datasets/global-forcast-system-gfs`, last accessed: July 2020

[3] `https://mpas-dev.github.io/atmosphere/atmosphere_meshes.html`, last accessed: July 2020

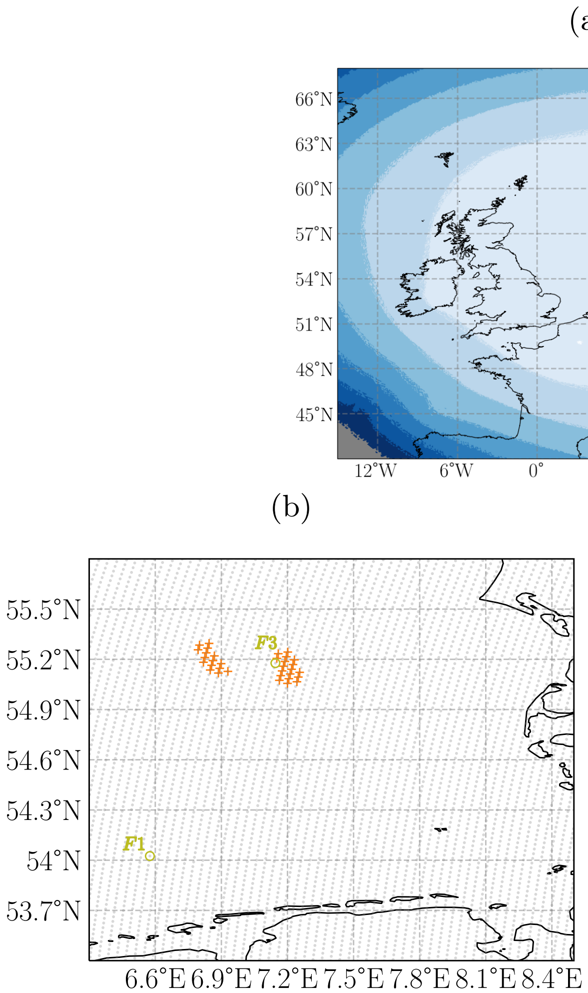

Figure 6.2: (a) Cell-average distance between a Voronoi cell center and its neighbors within the refinement region. Values outside the specified limits are depicted in gray. (b) Representation of the two wind farms Sandbank and DanTysk (orange pluses) on the 60-3 km mesh. The gray dots represent the Voronoi cell centers of the x20.835586 mesh. Cell centers used for comparisons with Fino 1 (F1) and Fino 3 (F3) are indicated with a yellow circle. (c) Representation of wind farms (orange plus) on 240 km mesh. The gray dots represent the Voronoi cell centers.

6.3 Results and Discussion

6.3.1 Initial Case Study and Results from Analysis I

Figure 6.3a-d depicts the modeled wind speed and wind direction of the default MPAS simulation (initial case study, Scenario EWP60-3KISS) runs, with activated EWP (further referred to as MPAS-EWP) and without EWP (further referred to as MPAS-REF). Results are depicted together with wind speed and wind direction measurements from Fino 1 and Fino 3. With respect to the overall quality of the reference simulation, MPAS-REF performs quite well, and is able to capture the large-scale trends in the wind speed observed at Fino 1 and Fino 3. While the large-scale trends in the wind direction at Fino 3 are also captured well, there are significant differences in the wind direction between the simulation and the measurements at Fino 1.

Based on the comparisons at Fino 1 and Fino 3, MPAS-EWP performs as expected and shows major deviations from MPAS-REF only in situations where the atmospheric conditions and wind farm geometry suggest wind farm impacts. This includes for example the observed reduction of the wind speed at Fino 3 between 18 February 2017, 0000 UTC and 18 February 2017, 1400 UTC (Figure 6.3c). During this period, Fino 3 is affected by the wake of Sanbank due to atmospheric flow from westerly directions (Figure 6.3a). Figure 6.3e illustrates this impact using a snapshot of the spatial wind speed differences between MPAS-EWP and MPAS-REF at 18 February 2017, 0200 UTC.

Due to the lack of north-northeasterly winds in the analyzed period, Fino 1 should not be affected by wind farm wakes. This this confirmed by the nearly identical wind speed results of MPAS-REF and MPAS-EWP at Fino 1 (Figure 6.3d). Minor deviations are attributed to emerging deviations in the background flow between the two simulation (cf. snapshot of modeled spatial wind speed differences at 18 February 2017, 1800 UTC in Figure 6.3f). Those deviations start appearing towards the end of the simulation period, which suggests an emerging divergence of the two simulation.

While the focus on regional spatial scales on a short temporal time scale indicates promising results, a closer look at the larger scales revealed nonphysical model deviations far away from the wind farms. This is shown in Figure 6.4a, which depicts model differences in wind speed between MPAS-EWP and MPAS-REF at the second model level (approximately 76 m above ground) six hours after model initialization as a function of the distance from the wind farm. Model differences are seen far beyond the area of influence at that point in time (i.e. right of the green line in Figure 6.4a) even under an assumed physical propagation speed of information from the installed wind farm of approximately 343 m s^{-1} (the speed of sound). Similar effects are visible in the pressure field as well (Figure 6.4b). It must be noted that the wind speed magnitudes are relatively low in absolute terms, but can reach values slightly below the magnitude of the wind farm wake wind speed deficit itself (Figure 6.4a). In the case of the pressure fluctuations in Figure 6.4b, the magnitude exceeds the observed effects seen at the wind farms.

To rule out that the nonphysical model deviations originate from the EWP formulation itself, the complex EWP parameterization is replaced by the simple increased surface roughness approach in Analysis I (Scenarios Z060-3KISS). The very similar results with the increased surface roughness approach (Figure 6.4c,d) suggest that the origin is not the EWP implementation. Other causes could be related to the MPAS dynamics, numerical artifacts, or impacts of model physics configuration.

To further narrow down the origin, the impact of model physics is investigated via a variety of configurations. Due to the relatively long computational time on the 60-3 km mesh, the physics sensitivity study was performed on a 240 km quasi-uniform mesh and with the simplified surface roughness representation. This is justifiable, since the overall characteristics of the nonphysical behavior has been seen in both EWP and the simplified approach.

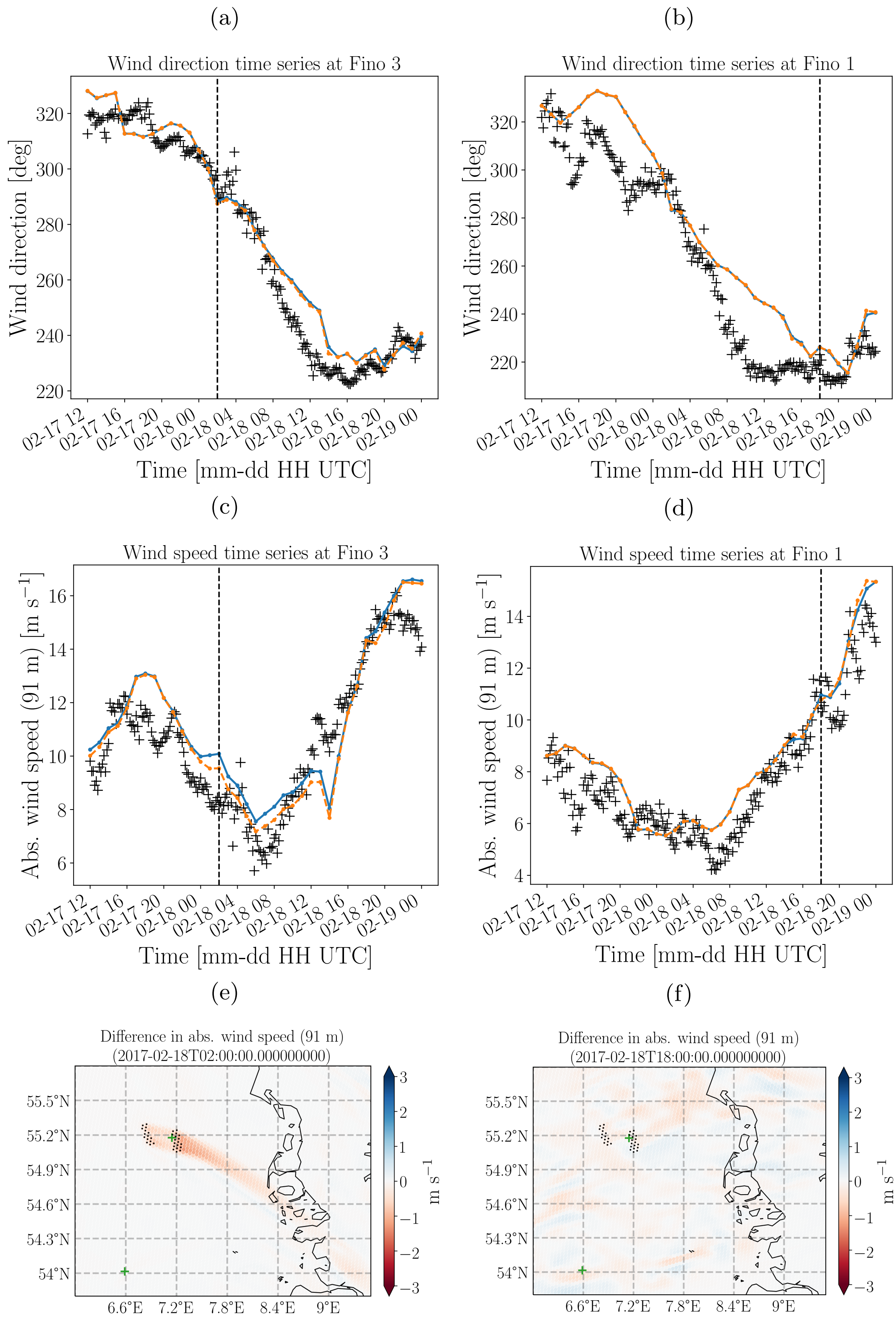

Figure 6.3: Comparsion between MPAS-REF (blue) and MPAS-EWP (orange) with measurements (black plus signs): (a) wind direction at Fino 3, (b) wind direction at Fino 1, (c) wind speed at Fino 3, (d) wind speed at Fino 1. (e) Difference in absolute wind speed between MPAS-EWP and MPAS-REF on 18 February 2017, 0200 UTC at 91 m. Positive differences indicate higher wind speeds in MPAS-EWP. (f) same as (e) but for 18 Feb. 2017, 1800 UTC. The vertical dashed lines in (a),(c) and (b),(d) correspond to the time step of (e) and (f), respectively.

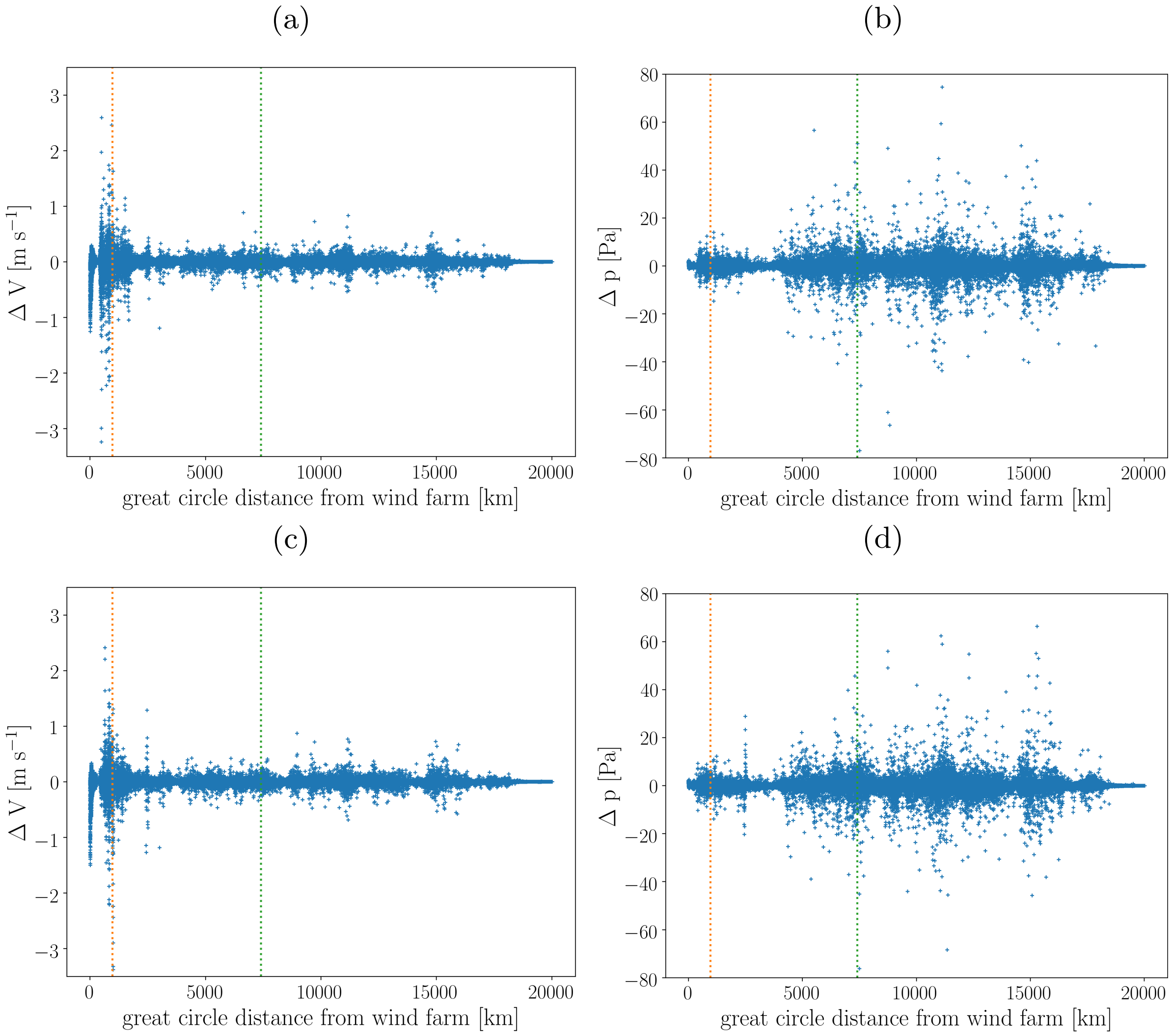

Figure 6.4: Difference between simulations with and without activated WFP at model level 2 at 17 February 2017, 0600 UTC (six hours after initialization) on the 60-3 km mesh: (a) wind speed differences for Scenario EWP60-3KISS, (b) pressure differences for Scenario EWP60-3KISS, (c) wind speed differences for Scenario Z060-3KISS, (d) pressure differences for Scenario Z060-3KISS. For orientation, the orange and green line highlight the maximum travel distance of a signal that originated from the wind farm in the North Sea area and would propagate radially with an average propagation speed of 45 m s^{-1} and 343 m s^{-1}, respectively.

6.3.2 Origin of Model Deviations with and without WFP - Model State Dependent Pseudo-Randomness (Analysis II)

The physics sensitivity study on the 240 km mesh revealed a strong relationship between large deviations in the WFP analysis and the RRTMG radiation scheme. This is especially clear in the comparison between Scenario Z0240-GTN and Scenario Z0240-R-Xu (cf. Table 6.3). Here, the inclusion of the longwave RRTMG scheme in Scenario Z0240-R-Xu significantly increased the model deviations (cf. Figure 6.5a,b). Such large deviations are not observed when the longwave RRTMG scheme is combined with a binary cloud fraction scheme (Scenario Z0240-R-bin, Figure 6.5c), only when combined with Xu and Randall (1996)'s cloud fraction scheme (Scenario Z0240-R-Xu, Figure 6.5b). This suggests that the deviations are related to the treatment of cloud fractions in the RRTMG scheme. This is further confirmed by the lack of deviations in Scenario Z0240-CAM (cf. Table 6.3), where Xu and Randall (1996)'s cloud fraction scheme is combined with the radiation scheme of the NCAR Community Atmosphere Model (Figure 6.5d).

An in-depth analysis of the treatment of cloud fractions in the RRTMG scheme revealed that differences in the treatment originate from the choice of the pseudorandom number generator (PRNG) for the stochastic cloud generator in the RRTMG scheme. The basic idea, of the stochastic cloud generator, is that the complex cloud structure within each model column can be approximated by a series of stochastically created sub-columns (Räisänen and Barker 2004) with homogeneous layers (i.e. binary cloud fractions and uniform concentrations). In sum, the individual sub-columns fulfill the constrains given by the cloud fraction and cloud overlapping assumptions in the vertical (Pincus et al. 2006). In order to create the sub-columns in a stochastic manner, while maintaining reproducibility, a PRNG with reproducible initial seeds is required. Within the RRTMG schemes in MPAS (both longwave and shortwave), the default way of determining the seeds for the PRNG is based on the absolute value of the pressure at the four lowest model levels (KISSVEC approach, cf. Listing 6.1).

While this method guarantees reproducibility for each individual model simulation, any modification that affects the pressure in the lowest four levels, such as the modification of the surface roughness, naturally produces a different model state and therefore a different seed value. Due to the formulation of the KISSVEC seed generator (Listing 6.1), pressure differences as small as 10^{-9} Pa in either of the four levels will result in a different set of seeds in the simulations with and without WFP. The resulting seed differences for the PRNG trigger a chain reaction resulting in different sub-columns in the stochastic cloud generator, which in turn affect the calculation of radiation fluxes and heating rates (Pincus et al. 2006). Due to the strong interactions in the atmosphere, differences in the fluxes and heating rates will then influence other atmospheric parameters.

It must be noted that the difference in sub-column sampling is mainly an issue when non-binary cloud fractions are used, which also explains the observed negligible pressure differences in Scenario Z0240-R-bin (Figure 6.5c). The complete independence of the two model integrations after model initialization and the potential triggering of non-

```fortran

! ----- Create seed  --------

! Advance randum number generator by changeseed values
      if (irng.eq.0) then
! For kissvec, create a seed that depends on the state of the columns. Maybe not the best way, but it works.
! Must use pmid from bottom four layers.
         do i=1,ncol
            if (pmid(i,1).lt.pmid(i,2)) then
               stop 'MCICA_SUBCOL: KISSVEC SEED GENERATOR REQUIRES PMID FROM BOTTOM FOUR LAYERS.'
            endif
            seed1(i) = (pmid(i,1) - int(pmid(i,1)))  * 1000000000_im
            seed2(i) = (pmid(i,2) - int(pmid(i,2)))  * 1000000000_im
            seed3(i) = (pmid(i,3) - int(pmid(i,3)))  * 1000000000_im
            seed4(i) = (pmid(i,4) - int(pmid(i,4)))  * 1000000000_im
          enddo
         do i=1,changeSeed
            call kissvec(seed1, seed2, seed3, seed4, rand_num)
         enddo
      elseif (irng.eq.1) then
         randomNumbers = new_RandomNumberSequence(seed = changeSeed)
      endif
```

Listing 6.1: Extract of the PRNG seed generation method within the implementation of the RRTMG scheme in MPAS (l. 2382 - 2402 of *module_ra_rrtmg_lw.F*). The complete source code is available at `https://github.com/MPAS-Dev/MPAS-Model`, last accessed: July 2020

linear feedbacks due to the small differences within each model run intensifies the model divergence. While both model runs are valid by themselves, one-to-one comparisons of time snapshots from the different model runs are negatively affected by this treatment of pseudorandomness.

The default PRNG can be relatively easily replaced with the Mersenne Twister (MT) PRNG formulation in the RRTMG scheme, which does not depend on the model state, because the seeding is based on a single integer ("changeSeed" variable, cf. Listing 6.1). However, this does require changes to the routines themselves and recompilation. Full-physics runs with the modified RRTMG scheme on the 240 km mesh (Scenario Z0240-MT) show that the use of the MT PRNG clearly reduces the model differences (compare Figure 6.6c,d with Figure 6.6a,b).

While the change in PRNG showed significant improvements in the wind speed field for the quasi-uniform simulation on the 240 km mesh, only moderate improvements are found when applied to simulations on the 60-3 km mesh. A re-run of the initial case study (Scenario EWP60-3KISS) with the modified PRNG in the RRTMG scheme (Scenario EWP60-3MT) still exhibits the nonphysical deviations (Figure 6.7a,b). They also remain more or less independent from the WFP (Figure 6.7a,b in comparison with Figure 6.7c,d). This suggests that the PRNG is not the driving force of the significant model deviations and that the driver of the observed effects is more likely related to a numerical artifact known as "chaos seeding" (Ancell et al. 2018), which will be elaborated further in the following section.

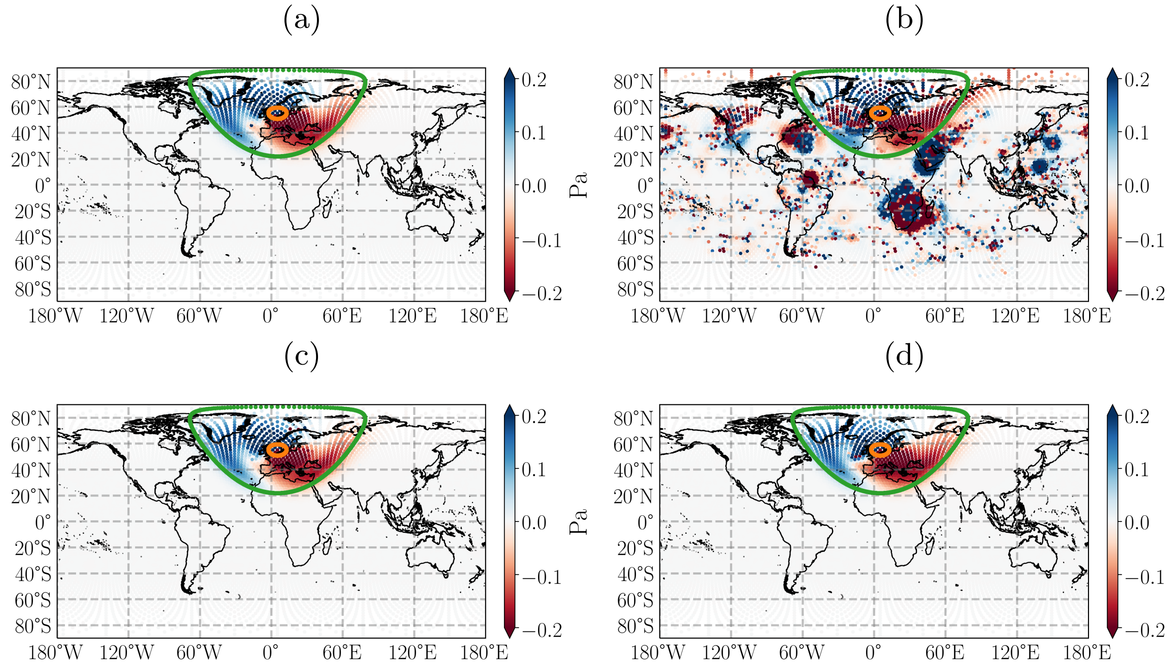

Figure 6.5: Pressure difference at model level 2 between MPAS with surface roughness WFP and MPAS without WFP at 17 February 2017, 0300 UTC (three hours after initialization) for (a) Scenario Z0240-GTN, (b) Scenario Z0240-R-Xu, (c) Scenario Z0240-R-bin and (e) Scenario Z0240-CAM. Scenario naming follows Table 6.3. For orientation, the orange and green line highlight the maximum travel distance of a signal that originated from the wind farm in the North Sea area and would propagate radially with an average propagation speed of 45 m s^{-1} and 343 m s^{-1}, respectively.

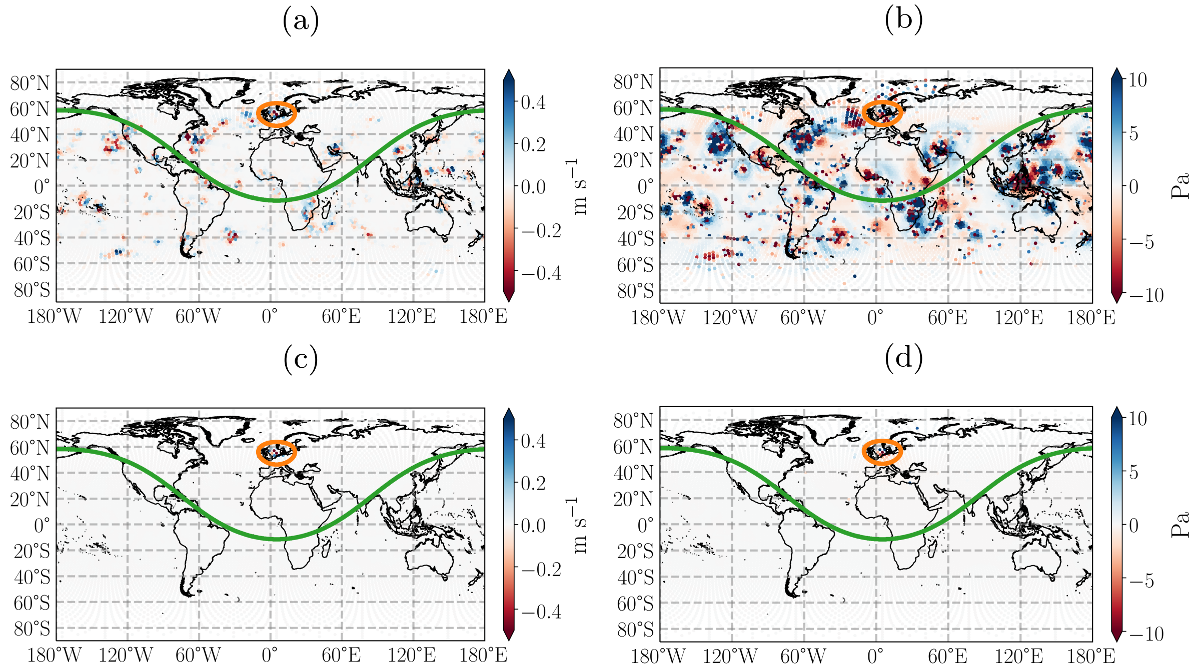

Figure 6.6: Difference between simulations with and without activated WFP at model level 2 at 17 February 2017, 0600 UTC (six hours after initialization) on the 240 km mesh: (a) wind speed differences for Scenario Z0240-KISS, (b) pressure differences for Scenario Z0240-KISS, (c) wind speed differences for Scenario Z0240-MT, (d) pressure differences for Scenario Z0240-MT. For orientation, the orange and green line highlight the maximum travel distance of a signal that originated from the wind farm in the North Sea area and would propagate radially with an average propagation speed of 45 m s^{-1} and 343 m s^{-1}, respectively. Scenario names follow Table 6.3.

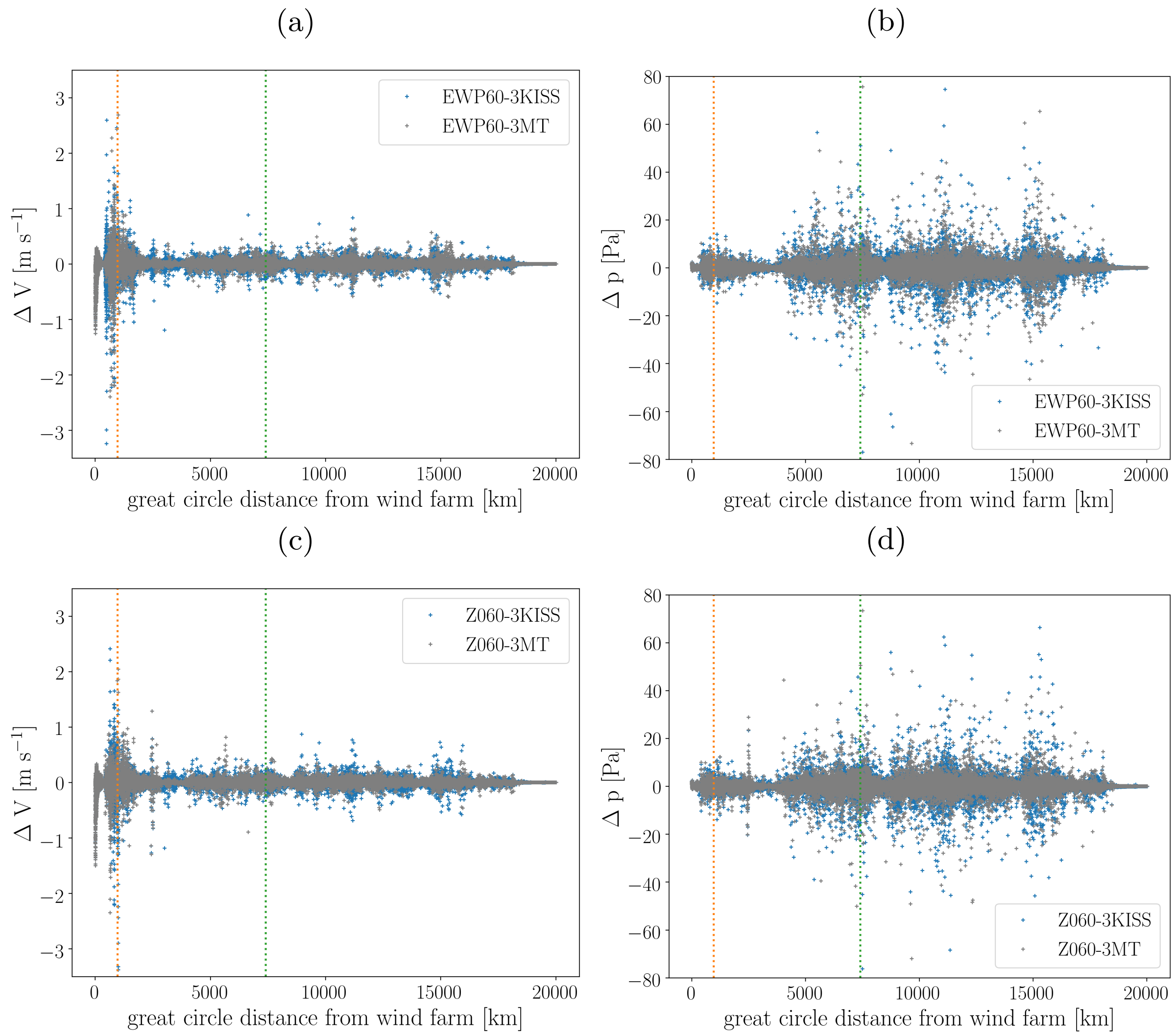

Figure 6.7: Difference between simulations with and without activated WFP at model level 2 at 17 February 2017, 0600 UTC (six hours after initialization) on the 60-3 km mesh: (a) wind speed differences for Scenario EWP60-3KISS and Scenario EWP60-3MT, (b) pressure differences Scenario EWP60-3KISS and Scenario EWP60-3MT, (c) wind speed differences for Scenario Z060-3KISS and Scenario Z060-3MT, (d) pressure differences for Scenario Z060-3KISS and Scenario Z060-3MT. For orientation, the orange and green line highlight the maximum travel distance of a signal that originated from the wind farm in the North Sea area and would propagate radially with an average propagation speed of 45 m s^{-1} and 343 m s^{-1}, respectively. Scenario names follow Table 6.3.

6.3.3 Origin of Model Deviations with and without WFP - Effects due to "chaos seeding" (Analysis III)

The model state dependent PRNG explains the reasons for some of the significant model deviations due to tiny pressure differences between two MPAS simulations, but not their spread in the first place. The spread can be explained by "chaos seeding", which is defined by Ancell et al. (2018) as the fast and unrealistic spread of numerical noise due to local initial perturbations of model prognostic variables.

In their study with the limited-area model WRF, Ancell et al. (2018) observed the unrealistic propagation of small perturbations with a propagation speed of about 1000 m s^{-1}, from an initial local soil moisture perturbation. This is approximately three times faster than the speed of sound. The authors attribute this propagation speed to the spatial finite-difference scheme and the way the initial perturbation is communicated. In WRF, Ancell et al. (2018) determined the observed perturbation travel speed to be $5\Delta x$ per time step. They define the speed based on the behavior of the fifth-order finite difference approximation in combination with the grid staggering method and the diffusive nature of the approximation (Ancell et al. 2018). While MPAS' model discretization is fundamentally different (finite-volume discretization instead of finite difference, unstructured SCVT instead of structured grid, Skamarock et al. 2012), similar noise propagation is likely.

To investigate this further, a sensitivity study with three different quasi-uniform mesh configurations with minimal physics settings (Scenario Z0240-MYNN, Scenario Z0240-MYNN-DT300 and Scenario Z060-MYNN) is performed. Scenario Z0240-MYNN uses the 240 km mesh with a model time step of 1200 s while Scenario Z0240-MYNN-DT300 applies the same mesh with a model time step of 300 s. Scenario Z060-MYNN uses the 60 km mesh and a model time step of 300 s. The three configurations confirmed the presence of similar deviations in the perturbation pressure field already after one hour into the simulation (Figure 6.8). Perturbations are visible far beyond the threshold expected by sound propagation speed (dashed black line, Figure 6.8). The perturbation magnitudes also include values larger than 10^{-9} Pa, which would lead to further perturbations by impacting the model state dependent KISSVEC PRNG (cf. analysis in Section 6.3.2). The perturbation expansion generally follows a radial expansion from the original source. The absolute value of the difference tends towards machine precision with high variability (Figure 6.8).

The sensitivity study also emphasizes the dependency of the propagation speed on the model time step and model grid spacing. Given the model grid spacing of 240 km, the size of the propagation zone increases when the model time step is decreased from 1200 s to 300 s. On the other hand, the expansion rate is reduced, when the model grid spacing is decreased 240 km to 60 km, given the same model time step of 300 s. This relationship likely becomes more complicated in variable-resolution meshes, where the ratio between the model time step (constant) and mesh grid distance can vary largely over the global domain. This makes it difficult to isolate the effect on variable resolution meshes.

The study revealed that the effects due to chaos seeding might be an important factor

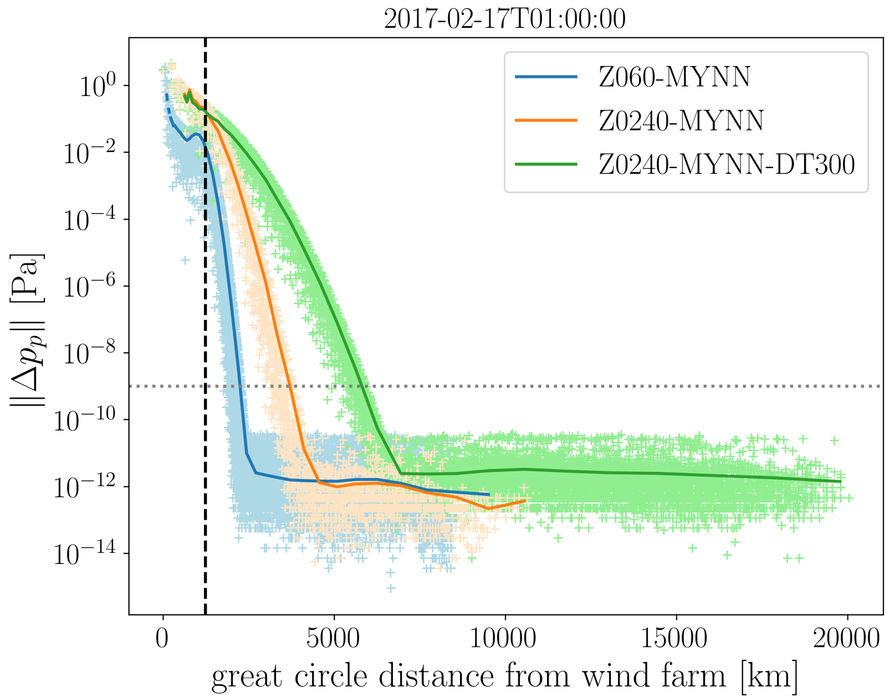

Figure 6.8: Absolute difference in perturbation pressure (p_p) between the simulations with and without WFP schemes for Scenario Z0240-MYNN, Scenario Z0240-MYNN-DT300 and Scenario Z060-MYNN after one hour of model integration. The solid lines are obtained by log-smoothed data averaging with 22 points per grid-distance decade. The vertical dashed black line highlights the maximum travel distance of a signal that originated from the wind farm in the North Sea area and would propagate radially with an average propagation speed of 343 m s^{-1} (speed of sound). The horizontal dashed gray line at 10^{-9} Pa indicates the lower limit above which MPAS cells would be affected by the model state dependent KISSVEC PRNG. Scenario names follow Table 6.3.

for the significant model deviations seen in the early stages of the simulation. This is in line with the results found in Ancell et al. (2018)'s wind farm impact study in WRF where the authors compared two simulations with and without WFP on a vast 4-km domain, which covered nearly the entity of the continental United States. They found significant differences in the surface pressure unrealistically far way from the introduced wind farm. The authors attribute the deviations to areas of precipitation triggered by the propagating signal due to chaos seeding.

In WRF, wind farm studies are typically performed on smaller domains than the domain presented in Ancell et al. (2018) (cf. model setup in Fitch et al. 2013b; Siedersleben et al. 2018; Tomaszewski and Lundquist 2020). In such small domains, the effects of chaos seeding are barely detectable, since the anticipated, valid, model deviations due to wind farm impacts propagate and fill the small domains so quickly that it becomes challenging to clearly separate the wind farm impacts from the background noise by a simple one-to-one comparison of snapshots between the simulation with WFP and without WFP. This also holds for other numerical effects like the revealed model state dependent PRNG seeding in the RRTMG scheme[4]. In MPAS on the other hand, the unbounded spatial extent of the model domain allows remote perturbations to build up to non-negligible magnitudes due to the non-linear feedbacks of the atmosphere. This can happen before valid flow deviations from the wind farms reach the affected regions. If they reach the affected area, they start interacting with the artificially created model deviations, reducing the ability to interpret the results from the simulations.

6.4 General Implications and Future Outlook for Wind Farm Studies with MPAS

The findings from Section 6.3.1 to Section 6.3.3 suggest that modeling with the global MPAS demands a different strategy compared to limited-area modeling when it comes to the study of wind farms and their impact on the atmosphere. While the initial study in Section 6.3.1 has shown that MPAS with an enabled EWP scheme does perform decently for shorter runs (i.e. focus on regional impacts within one or two days), difficulties arise for long-term simulations and one-to-one comparisons. Significant model deviations between the simulations with and without WFP are observed that can partly be attributed to the relatively free model integration without steering, and to the high sensitivity to numerical artifacts like the chaos seeding effect (cf. Section 6.3.3).

This model divergence makes it difficult to apply MPAS for relatively short case studies. Limited-area applications like WRF might be more suited in these cases where the frequent LBC updates and other techniques like spectral nudging can limit model divergence, with the potential caveat of restricting the propagation of the wind farm impacts to larger scales. For long-term statistical analyses, however, the drift of the two simulations in the time-domain might be of minor importance and MPAS could potentially add value due to upscaling effects. This needs however a much longer simulation periods (cf. outlook in Chapter 7).

The sensitivity to the chaos seeding effect and the build-up of noise to a similar magnitude as the investigated wind farm wake phenomenon itself, strongly suggests the use of alternative evaluation methods to the classical one-to-one model comparison. This is needed to detach the actual wind farm impacts from the numerical artifacts in the analysis. Ancell et al. (2018) proposed two evaluation methods that can be used to reduce misinterpretations caused by the chaos seeding effect, namely the Ensemble Sensitivity Approach (ESA, see e.g. Ancell and Hakim 2007) and Empirical Orthogonal Function Analysis (EOF, e.g. Navarra and Simoncini 2010; Wilks 2019). This motivates further exploration of those techniques for wind farm impact studies with MPAS.

It must be noted that both methods have been already explored in other contexts within the field of wind energy. ESA, for example, has been used for the short-term prediction of wind ramps (Smith and Ancell 2017) and short-term wind speed forecasting (Zack et al. 2010a; Zack et al. 2010b; Zack et al. 2010c). EOF Analysis has been used

[4]The model state dependent KISSVEC PRNG in the RRTMG scheme is also the default (hard-coded) configuration in WRF, cf. WRF GitHub page, `https://github.com/wrf-model/WRF`, last accessed: July 2020

for prediction of wind power fluctuations (Ellis et al. 2015) and an investigation of spatio-temporal variability of wind energy resources (Santos-Alamillos et al. 2014).

Ancell et al. (2018) also proposed switching to numerical simulations with double precision to reduce the impact of the chaos seeding effect. The results in Section 6.3.3, however, suggest that a shift towards double precision simulations (default configuration in MPAS, Duda et al. 2019) does not suppress the numerical effects sufficiently enough to prevent significant imprints on the model solution for wind farm studies (cf. Figure 6.7) with MPAS.

A strong limitation of the current investigation is the relatively short simulation period in the MPAS simulations, which is partly associated with the relatively high computational cost of MPAS configurations with the required high spatial resolution of 3 km. Much longer simulation periods are required to be able to examine long-term statistics (e.g. climatological averages) or large-scale upscaling effects. Thus, an obvious continuation of the current study is the setup and exploration of longer-term MPAS simulations together with evaluation techniques like EOF. MPAS with the integrated EWP scheme and a mesh configuration similar to Figure 6.2a could be used to investigate potential impacts of wind farms in the North Sea area on the larger scales without the limitations imposed by the fixed lateral boundary conditions in limited area models. Investigations like these could be relevant with regard to future scenarios of installed onshore and offshore wind farm capacities, which are expected to significantly increase not only in the North Sea area, but across the world (IRENA 2019). A good starting point for a wind farm impact study with MPAS could be the wind farm scenarios described in Vautard et al. 2014 (European installations for 2020) or Agora Energiewende et al. 2020 (Installations in the German Bight for 2050), since both have already been evaluated with traditional methods (nested limited-area model).

CHAPTER 7

Concluding Remarks & General Outlook - MPAS for Wind Energy Applications

Within the scope of this PhD project, the global MPAS model, with regional mesh refinement has been explored with respect to its potential for several wind energy related applications. The investigations were driven by two questions: where and to what extent can the model improve the traditional modeling approaches (limited area modeling and nesting) and what are the main considerations that need to be taken into account when MPAS is used for wind energy applications.

Key contributions from this PhD project are:

- Evaluation of the previously unexplored strengths and limitations of MPAS for wind energy applications, based on three characteristic and challenging case studies: a mid-latitude storm, open cellular convection, and a study of offshore wind farm wakes.
- The investigation of the impact of boundary corners on cyclone introduction to WRF in Paper *P1* expands the ongoing research on LBC impacts on LAMs and the improvement of large-scale information introduction via the lateral boundaries.
- MPAS with variable-resolution mesh configuration has been successfully applied for the simulation of the organizes atmospheric structures of open cellular convection (OCC) for the first time. The analysis of OCC associated wind variability in MPAS in Paper *P2* and its satisfactory results contribute to the ongoing exploration of the potential of global MPAS with mesh refinement.
- The 'Explicit Wake Parametrisation' has been implemented in MPAS, thus introducing wind farm wake calculation to MPAS for the first time. It has been tested in a short episode over two offshore wind farms in the North Sea and numerical challenges related to "chaos seeding" in MPAS and the treatment of pseudorandomness have been revealed, analyzed, and documented.

The large freedom in the mesh design (Chapter 3) and the three case studies in Chapter 4 to Chapter 6 revealed some great opportunities, but they also highlighted challenges that need to be considered.

One of the major differences in applying MPAS vs WRF is the absense of lateral boundary conditions and the resulting direct and indirect consequences for modeling case studies. On the one hand, the absence of LBCs avoids (by design) challenges related to introduction of large scale atmospheric phenomena into the interior, high resolution model region, as discussed in Section 4.2 (Paper *P1*). On the other hand, the lack of boundary conditions in MPAS increases the importance of the model initialization. It also introduces a strong weather forecasting component, in addition to the downscaling of atmospheric features. This naturally adds forecasting challenges like atmospheric predictability into the modeling, which are not as dominant in the WRF grid nesting approach, when performing case studies. As discussed in Chapter 4, events like mid-latitude storms, which are difficult to predict well (Warner 2010), can be highly affected by model deviations from the real atmospheric state. This negatively impacts key parameters like storm locations.

The strong weather forecasting component also sets certain limitations on the model initialization time, which is less of a concern in the WRF grid nesting approach. As seen in the OCC investigation in Chapter 5, model deviations due to too early model initialization can significantly alter the atmospheric state, which can distort or suppress the development of the small-scale phenomena of interest. However, initializing the model too close to the period of interest can also be problematic, especially when long temporal model spin-up times are needed to allow the smaller atmospheric scales to develop. Especially in the current setup, where MPAS is initialized from relatively coarse initial conditions. However, spatial model spin-up is significantly reduced compared to WRF grid nesting. The smooth transition region allows for a gradual build-up of atmospheric scales of motion and increased spatial consistency of atmospheric structures (Chapter 4).

Another consequence of the high degree of freedom in MPAS is its sensitive behavior to small perturbations. As shown in Chapter 6, small perturbations do not necessarily need to be of physical origin or of large amplitude to influence model comparisons in the time domain. The global model character makes it possible for small-scale noise or numerical inconsistencies (like the treatment of pseudorandomness, Chapter 6) to pop up, grow in magnitude, and propagate. For relatively weak signals from a global perspective (e.g. wind farm wakes of a small wind farm cluster), the resulting model deviations can even overgrow the actual phenomena of interest within the order of hours (Chapter 6). A direct model comparison in the time domain (that is comparisons of modeled variables from simulations with WFP and without WFP at the same point in time), is therefore rather difficult to apply. For studies with the WRF grid nesting approach, this is a commonly used method (e.g recent investigations by Siedersleben et al. 2018 or Tomaszewski and Lundquist 2020). Alternative methods like empirical orthogonal functions might be more suited in this case (see discussion in Section 6.4).

The above mentioned points clearly emphasize the need of an external control mechanisms for case studies in MPAS. This is needed to limit model divergence from the real atmospheric state in the larger-scales as observed in Chapter 4 and Chapter 5. This could be potentially done by means of continuous data assimilation strategies like observation or analysis nudging under the constraints already mentioned in Section 4.5. Further investigations in this direction are required. It must be noted, that the current official MPAS release does support neither observational nor analysis nudging (Duda et al. 2019).

The studies performed in this PhD project have also shown that most observed limitations in MPAS are bound to challenges related to weather prediction. MPAS' capabilities in representing small-scale atmospheric features like open cellular convection (Chapter 5) has been quite satisfactory. This suggests that long-term climatological studies, with focus on statistical representation of the atmosphere might be more suitable for global MPAS simulations. For those studies, model initialization and forecasting of time and location of individual events is less important.

Long-term global simulation runs, however, require a significant amount of computational resources and disk space. This holds especially for meshes like the 55-2 km mesh (Chapter 5) and the 60-3 km mesh in Chapter 6 that have a significant number of Voronoi centers and small model time step. Due to the constraints imposed by the available HPC infrastructure, efficient performance of long-term MPAS runs was relatively limited, but is expected to improve with the very recently acquired new HPC infrastructure at the department.

As shown in Chapter 3, the generation of high-quality SCVTs is also connected with significant computational efforts (cf. Section 3.2.2) compared to the generation of WRF model domains. While this is partly associated with the higher complexity of generating SCVTs, the mesh generation utility used in this work only supports parallelization via OpenMP. More recently, efficient algorithms for SCVT generation like JIGSAW-GEO (Engwirda 2017) were developed. It was very recently evaluated for mesh generation in the MPAS-Ocean model (Hoch et al. 2020) with promising results. Highly efficient algorithms could significantly improve mesh generation and would allow for more advanced testing of refinement strategies for different applications.

Bibliography

Abkar, Mahdi and Fernando Porté-Agel (2015). “A new wind-farm parameterization for large-scale atmospheric models”. In: *Journal of Renewable and Sustainable Energy* 7.1. ISSN: 19417012. DOI: 10.1063/1.4907600.

Abkar, Mahdi, Ahmad Sharifi, and Fernando Porté-Agel (2016). “Wake flow in a wind farm during a diurnal cycle”. In: *Journal of Turbulence* 17.4, pp. 420–441. ISSN: 14685248. DOI: 10.1080/14685248.2015.1127379. URL: https://doi.org/10.1080/14685248.2015.1127379.

Adams, Manda S and David W Keith (2007). “A wind farm parametrization for WRF”. In: *8th WRF Users Workshop*. URL: https://www2.mmm.ucar.edu/wrf/users/workshops/WS2007/abstracts/5-5_Adams.pdf.

Agee, E. M. (1987). “Mesoscale cellular convection over the oceans”. In: *Dynamics of Atmospheres and Oceans* 10.4, pp. 317–341. ISSN: 03770265. DOI: 10.1016/0377-0265(87)90023-6.

Agee, E. M., T. S. Chen, and K. E. Dowell (1973). “A Review of Mesoscale Cellular Convection”. In: *Bulletin of the American Meteorological Society* 54.10, pp. 1004–1012. ISSN: 0003-0007. DOI: 10.1175/1520-0477(1973)054<1004:aromcc>2.0.co;2.

Agora Energiewende, Agora Verkehrswende, Technical University of Denmark, and Max-Planck-Ins- titute for Biogeochemistry (2020). “Making the Most of Offshore Wind: Re-Evaluating the Potential of Offshore Wind in the German North Sea.” In: *Agora Energiewende, Agora Verkehrswende, Technical University of Denmark and Max-Planck-Ins- titute for Biogeochemistry (2020): Making the Most of Offshore Wind: Re-Evaluating the Potential of Offshore Wind in the German North Sea.* Study commissioned by Agora Energiewende and Agora Verkehrswende. URL: https://www.agora-energiewende.de/fileadmin2/Projekte/2019/Offshore_Potentials/176_A-EW_A-VW_Offshore-Potentials_Publication_WEB.pdf.

Akhmatov, Vladislav, Carsten Rasmussen, Peter Børre Eriksen, and Jens Pedersen (2007). “Technical aspects of status and expected future trends for wind power in Denmark”. In: *Wind Energy* 10.1, pp. 31–49. ISSN: 10954244. DOI: 10.1002/we.206.

Ancell, Brian C., Allison Bogusz, Matthew J. Lauridsen, and Christian J. Nauert (2018). "Seeding chaos: The dire consequences of numerical noise in NWP perturbation experiments". In: *Bulletin of the American Meteorological Society* 99.3, pp. 615–628. DOI: 10.1175/BAMS-D-17-0129.1.

Ancell, Brian and Gregory J. Hakim (2007). "Comparing adjoint- and ensemble-sensitivity analysis with applications to observation targeting". In: *Monthly Weather Review* 135.12, pp. 4117–4134. DOI: 10.1175/2007MWR1904.1.

Artipoli, G and F Durante (2014). "Physical Modeling in Wind Energy Forecasting". In: *Dewi Magazin* 44, pp. 10–15. URL: https://pdfs.semanticscholar.org/baaa/0abdb12157ebe381ec4ffc1d1621b15b3a3f.pdf.

Atkinson, B. W. and J. Wu Zhang (1996). "Mesoscale shallow convection in the atmosphere". In: *Reviews of Geophysics* 34.4, pp. 403–431. DOI: 10.1029/96RG02623.

Baidya Roy, S., S. W. Pacala, and R. L. Walko (2004). "Can large wind farms affect local meteorology?" In: *Journal of Geophysical Research D: Atmospheres* 109.19, pp. 1–6. DOI: 10.1029/2004JD004763.

Baidya Roy, S. and Justin J. Traiteur (2010). "Impacts of wind farms on surface air temperatures". In: *Proceedings of the National Academy of Sciences* 107.42, pp. 17899–17904. ISSN: 0027-8424. DOI: 10.1073/pnas.1000493107.

Bakan, S. and E. Schwarz (1992). "Cellular convection over the north-eastern Atlantic". In: *International Journal of Climatology* 12.4, pp. 353–367. ISSN: 10970088. DOI: 10.1002/joc.3370120404.

Barrie, D B and D B Kirk-Davidoff (2010). "Weather response to a large wind turbine array". In: *Atmospheric Chemistry and Physics* 10.2, pp. 769–775. ISSN: 1680-7324. DOI: 10.5194/acp-10-769-2010.

Bianchi, Emilio, Andrés Solarte, and Tomás Manuel Guozden (2017). "Large scale climate drivers for wind resource in Southern South America". In: *Renewable Energy* 114, pp. 708–715. ISSN: 18790682. DOI: 10.1016/j.renene.2017.07.075.

Boettcher, Marita, Peter Hoffmann, Hermann J. Lenhart, K. Heinke Schlunzen, and Robert Schoetter (2015). "Influence of large offshore wind farms on North German climate". In: *Meteorologische Zeitschrift* 24.5, pp. 465–480. DOI: 10.1127/metz/2015/0652.

Browning, K. A. (2004). "The sting at the end of the tail: Damaging winds associated with extratropical cyclones". In: *Quarterly Journal of the Royal Meteorological Society* 130.597, pp. 375–399. ISSN: 00359009. DOI: 10.1256/qj.02.143.

Bullock Jr., Orren Russell, Hosein Foroutan, Robert C. Gilliam, and Jerold A. Herwehe (2018). “Adding four-dimensional data assimilation by analysis nudging to the Model for Prediction Across Scales – Atmosphere (version 4.0)”. In: *Geoscientific Model Development* 11.7, pp. 2897–2922. ISSN: 1991-9603. DOI: 10.5194/gmd-11-2897-2018.

Catto, Jennifer L., Duncan Ackerley, James F. Booth, Adrian J. Champion, Brian A. Colle, Stephan Pfahl, Joaquim G. Pinto, Julian F. Quinting, and Christian Seiler (2019). “The Future of Midlatitude Cyclones”. In: *Current Climate Change Reports* 5.4, pp. 407–420. ISSN: 2198-6061. DOI: 10.1007/s40641-019-00149-4.

Christakos, Konstantinos, Ioannis Cheliotis, George Varlas, and Gert-Jan Steeneveld (2016). “Offshore Wind Energy Analysis of Cyclone Xaver over North Europe”. In: *Energy Procedia* 94.1876, pp. 37–44. ISSN: 18766102. DOI: 10.1016/j.egypro.2016.09.187.

Collier, C.G., J. Dixon, M.S.J. Harrison, J.C.R. Hunt, J.F.B. Mitchell, and D.S. Richardson (1994). “Extreme surface winds in mid-latitude storms: forecasting and changes in climatology”. In: *Journal of Wind Engineering and Industrial Aerodynamics* 52.C, pp. 1–27. DOI: 10.1016/0167-6105(94)90036-1.

Collins, William D. et al. (2004). *Description of the NCAR Community Atmosphere Model (CAM 3.0).* Tech. rep. June. Boulder, CO, USA: National Center For Atmospheric Research, p. 214. URL: https://www2.mmm.ucar.edu/wrf/users/phys_refs/SW_LW/CAM.pdf.

Cutululis, Nicolaos A., Marisciel Litong-Palima, and Poul Sørensen (2012). “Offshore wind power production in critical weather conditions”. In: *Proceedings of EWEA 2012 - European Wind Energy Conference & Exhibition.* Vol. 1, pp. 74–81. ISBN: 9781627482912.

Davies, Terry (2014). “Lateral boundary conditions for limited area models”. In: *Quarterly Journal of the Royal Meteorological Society* 140.678, pp. 185–196. ISSN: 00359009. DOI: 10.1002/qj.2127. URL: http://doi.wiley.com/10.1002/qj.2127.

— (2017). “Dynamical downscaling and variable resolution in limited-area models”. In: *Quarterly Journal of the Royal Meteorological Society* 143.702, pp. 209–222. DOI: 10.1002/qj.2913.

Deppe, Adam J., William A. Gallus, and Eugene S. Takle (2013). “A WRF ensemble for improved wind speed forecasts at turbine height”. In: *Weather and Forecasting* 28.1, pp. 212–228. DOI: 10.1175/WAF-D-11-00112.1.

Du, Qiang, Vance Faber, and Max Gunzburger (1999). "Centroidal Voronoi Tessellations: Applications and Algorithms". In: *SIAM Review* 41.4, pp. 637–676. ISSN: 0036-1445. DOI: 10.1137/S0036144599352836.

Du, Qiang, Max D. Gunzburger, and Lili Ju (2003a). "Constrained Centroidal Voronoi Tessellations for Surfaces". In: *SIAM Journal on Scientific Computing* 24.5, pp. 1488–1506. ISSN: 1064-8275. DOI: 10.1137/S1064827501391576. URL: http://epubs.siam.org/doi/10.1137/S1064827501391576.

— (2003b). "Voronoi-based finite volume methods, optimal Voronoi meshes, and PDEs on the sphere". In: *Computer Methods in Applied Mechanics and Engineering* 192.35-36, pp. 3933–3957. ISSN: 00457825. DOI: 10.1016/S0045-7825(03)00394-3.

Duda, Michael, Laura Fowler, Bill Skamarock, Conrad Roesch, Doug Jacobsen, and Todd Ringler (2019). *MPAS-Atmosphere Model User's Guide Version 7.0*. Available under https://www2.mmm.ucar.edu/projects/mpas/mpas_atmosphere_users_guide_7.0.pdf, last accessed: Apr. 2020.

Earl, N., S. Dorling, M. Starks, and R. Finch (2017). "Subsynoptic-scale features associated with extreme surface gusts in UK extratropical cyclone events". In: *Geophysical Research Letters* 44.8, pp. 3932–3940. ISSN: 00948276. DOI: 10.1002/2017GL073124.

Eliassen, A. (1976). "Atmospheric motions of different scales and their transport capacities". In: *Optical and Quantum Electronics* 8.2, pp. 105–115. DOI: 10.1007/BF00619438.

Ellis, Nick, Robert Davy, and Alberto Troccoli (2015). "Predicting wind power variability events using different statistical methods driven by regional atmospheric model output". In: *Wind Energy* 18.9, pp. 1611–1628. DOI: 10.1002/we.1779. URL: http://doi.wiley.com/10.1002/we.1779.

Engwirda, Darren (2017). "JIGSAW-GEO (1.0): locally orthogonal staggered unstructured grid generation for general circulation modelling on the sphere". In: *Geoscientific Model Development* 10.6, pp. 2117–2140. ISSN: 1991-9603. DOI: 10.5194/gmd-10-2117-2017.

Fitch, Anna C., Julie K. Lundquist, and Joseph B. Olson (2013a). "Mesoscale influences of wind farms throughout a diurnal cycle". In: *Monthly Weather Review* 141.7, pp. 2173–2198. ISSN: 00270644. DOI: 10.1175/MWR-D-12-00185.1.

Fitch, Anna C., Joseph B. Olson, and Julie K. Lundquist (2013b). "Parameterization of wind farms in climate models". In: *Journal of Climate* 26.17, pp. 6439–6458. ISSN: 08948755. DOI: 10.1175/JCLI-D-12-00376.1.

Fitch, Anna C., Joseph B. Olson, Julie K. Lundquist, Jimy Dudhia, Alok K. Gupta, John Michalakes, and Idar Barstad (2012). "Local and Mesoscale Impacts of Wind Farms as Parameterized in a Mesoscale NWP Model". In: *Monthly Weather Review* 140.9, pp. 3017–3038. DOI: 10.1175/MWR-D-11-00352.1.

Fowler, Laura D., William C. Skamarock, Georg A. Grell, Saulo R. Freitas, and Michael G. Duda (2016). "Analyzing the Grell–Freitas Convection Scheme from Hydrostatic to Nonhydrostatic Scales within a Global Model". In: *Monthly Weather Review* 144.6, pp. 2285–2306. ISSN: 0027-0644. DOI: 10.1175/MWR-D-15-0311.1.

Fox-Rabinovitz, Michael, J. Côté, B. Dugas, M. Déqué, J. L. McGregor, and A. Belochitski (2008). "Stretched-grid Model Intercomparison Project: Decadal regional climate simulations with enhanced variable and uniform-resolution GCMs". In: *Meteorology and Atmospheric Physics* 100.1-4, pp. 159–178. DOI: 10.1007/s00703-008-0301-z.

Frandsen, Sten T. et al. (2009). "The making of a second-generation wind farm efficiency model complex". In: *Wind Energy* 12.5, pp. 445–458. DOI: 10.1002/we.351. URL: http://doi.wiley.com/10.1002/we.351.

Fujita, T. Theodore (1981). "Tornadoes and Downbursts in the Context of Generalized Planetary Scales". In: *Journal of the Atmospheric Sciences* 38.8, pp. 1511–1534. ISSN: 0022-4928. DOI: 10.1175/1520-0469(1981)038<1511:TADITC>2.0.CO;2.

Gersho, Allen (1979). "Asymptotically Optimal Block Quantization". In: *IEEE Transactions on Information Theory* 25.4, pp. 373–380. ISSN: 15579654. DOI: 10.1109/TIT.1979.1056067.

Göçmen, Tuhfe, Xiaoli Guo Larsén, and Marc Imberger (2020). "The effects of Open Cellular Convection on Wind Farm Operation and Wakes". In: *Journal of Physics: Conference Series* n/a.n/a. (in press).

Grell, G. A. and S. R. Freitas (2014). "A scale and aerosol aware stochastic convective parameterization for weather and air quality modeling". In: *Atmospheric Chemistry and Physics* 14.10, pp. 5233–5250. DOI: 10.5194/acp-14-5233-2014.

Gustafsson, Nils (1990). "Sensitivity of limited area model data assimilation to lateral boundary condition fields". In: *Tellus A: Dynamic Meteorology and Oceanography* 42.1, pp. 109–115. ISSN: 1600-0870. DOI: 10.3402/tellusa.v42i1.11864.

Gustafsson, Nils, Erland Källén, and Sigurdur Thorsteinsson (1998). "Sensitivity of forecast errors to initial and lateral boundary conditions". In: *Tellus A: Dynamic Meteorology and Oceanography* 50.2, pp. 167–185. ISSN: 1600-0870. DOI: 10.3402/tellusa.v50i2.14519.

Gutierrez, W., G. Araya, P. Kiliyanpilakkil, A. Ruiz-Columbie, M. Tutkun, and L. Castillo (2016). "Structural impact assessment of low level jets over wind turbines". In: *Journal of Renewable and Sustainable Energy* 8.2. ISSN: 19417012. DOI: 10.1063/1.4945359.

Hasager, Charlotte Bay, Nicolai Gayle Nygaard, Patrick J.H. Volker, Ioanna Karagali, Søren Juhl Andersen, and Jake Badger (2017). "Wind farm wake: The 2016 Horns Rev photo case". In: *Energies* 10.3. ISSN: 19961073. DOI: 10.3390/en10030317.

Hashimoto, Atsushi, James M. Done, Laura D. Fowler, and Cindy L. Bruyère (2016). "Tropical cyclone activity in nested regional and global grid-refined simulations". In: *Climate Dynamics* 47, pp. 497–508. ISSN: 0930-7575. DOI: 10.1007/s00382-015-2852-2.

Heinzeller, D., M. G. Duda, and H. Kunstmann (2016). "Towards convection-resolving, global atmospheric simulations with the Model for Prediction Across Scales (MPAS) v3.1: An extreme scaling experiment". In: *Geoscientific Model Development* 9.1, pp. 77–110. DOI: 10.5194/gmd-9-77-2016.

Hill, C., C. DeLuca, Balaji, M. Suarez, and A. Da Silva (2004). "The architecture of the earth system modeling framework". In: *Computing in Science & Engineering* 6.1, pp. 18–28. DOI: 10.1109/MCISE.2004.1255817.

Hoch, Kristin E., Mark R. Petersen, Steven R. Brus, Darren Engwirda, Andrew F. Roberts, Kevin L. Rosa, and Phillip J. Wolfram (2020). "MPAS-Ocean Simulation Quality for Variable-Resolution North American Coastal Meshes". In: *Journal of Advances in Modeling Earth Systems* 12.3, pp. 1–23. DOI: 10.1029/2019MS001848.

Hong, S.-Y. and J.-O. J. Lim (2006). "The WRF single-moment 6-class microphysics scheme (WSM6)". In: *Journal of the Korean Meteorological Society* 42.2, pp. 129–151. URL: http://www.mmm.ucar.edu/wrf/users/docs/WSM6-hong_and_lim_JKMS.pdf.

Hong, Song-You and Masao Kanamitsu (2014). "Dynamical downscaling: Fundamental issues from an NWP point of view and recommendations". In: *Asia-Pacific Journal of Atmospheric Sciences* 50.1, pp. 83–104. DOI: 10.1007/s13143-014-0029-2.

Hong, Song-You, Yign Noh, and Jimy Dudhia (2006). "A New Vertical Diffusion Package with an Explicit Treatment of Entrainment Processes". In: *Monthly Weather Review* 134.9, pp. 2318–2341. DOI: 10.1175/MWR3199.1.

Hoskins, Brian J. and Kevin I. Hodges (2002). "New perspectives on the Northern Hemisphere winter storm tracks". In: *Journal of the Atmospheric Sciences* 59.6, pp. 1041–1061. DOI: 10.1175/1520-0469(2002)059<1041:NPOTNH>2.0.CO;2.

Huang, Ching-Yuang, Chien-Hsiang Huang, and William C. Skamarock (2019). “Track Deflection of Typhoon Nesat (2017) as Realized by Multiresolution Simulations of a Global Model”. In: *Monthly Weather Review* 147.5, pp. 1593–1613. ISSN: 0027-0644. DOI: 10.1175/MWR-D-18-0275.1.

Iacono, Michael J., Jennifer S. Delamere, Eli J. Mlawer, Mark W. Shephard, Shepard A. Clough, and William D. Collins (2008). “Radiative forcing by long-lived greenhouse gases: Calculations with the AER radiative transfer models”. In: *Journal of Geophysical Research: Atmospheres* 113.D13. DOI: 10.1029/2008JD009944.

Imberger, Marc, Xiaoli Guo Larsén, and Neil Davis (2019). “Offshore wind farm wakes in global circulation model MPAS compared with WRF and measurements [Presentation Slides]”. In: *EGU General Assembly 2019*. Vienna, Austria. URL: https://presentations.copernicus.org/EGU2019/EGU2019-506_presentation.pdf.

IRENA (2019). *Future of Wind: Deployment, investment, technology, grid integration and socio-economic aspects (A Global Energy Transformation paper)*. last accessed: August 2020. Abu Dhabi: International Renewable Energy Agency (IRENA), pp. 1–88. ISBN: 9789292601553. URL: https://www.irena.org/documentdownloads/publications/re_technologies_cost_analysis-hydropower.pdf.

Jablonowski, Christiane and David L Williamson (2006). “A baroclinic instability test case for atmospheric model dynamical cores”. In: *Quarterly Journal of the Royal Meteorological Society* 132.621C, pp. 2943–2975. DOI: 10.1256/qj.06.12. URL: http://doi.wiley.com/10.1256/qj.06.12.

Jiménez, Pedro A., Jimy Dudhia, J. Fidel González-Rouco, Jorge Navarro, Juan P. Montávez, and Elena García-Bustamante (2012). “A Revised Scheme for the WRF Surface Layer Formulation”. In: *Monthly Weather Review* 140.3, pp. 898–918. ISSN: 0027-0644. DOI: 10.1175/MWR-D-11-00056.1.

Ju, Lili, Todd Ringler, and Max Gunzburger (2011). “Voronoi Tessellations and Their Application to Climate and Global Modeling”. In: *Lecture Notes in Computational Science and Engineering*. Vol. 80, pp. 313–342. ISBN: 978-3-642-11639-1. DOI: 10.1007/978-3-642-11640-7_10.

Kain, John S. (2004). “The Kain–Fritsch Convective Parameterization: An Update”. In: *Journal of Applied Meteorology* 43.1, pp. 170–181. ISSN: 0894-8763. DOI: 10.1175/1520-0450(2004)043<0170:TKCPAU>2.0.CO;2.

Keith, David W., Joseph F. DeCarolis, David C. Denkenberger, Donald H. Lenschow, Sergey L. Malyshev, Stephen Pacala, and Philip J. Rasch (2004). “The influence of large-scale wind power on global climate”. In: *Proceedings of the National Academy of Sciences* 101.46, pp. 16115–16120. ISSN: 0027-8424. DOI: 10.1073/pnas.0406930101.

Kirk-Davidoff, Daniel B. and David W. Keith (2008). “On the Climate Impact of Surface Roughness Anomalies”. In: *Journal of the Atmospheric Sciences* 65.7, pp. 2215–2234. ISSN: 1520-0469. DOI: 10.1175/2007JAS2509.1.

Klemp, J. B. (2011). “A Terrain-Following Coordinate with Smoothed Coordinate Surfaces”. In: *Monthly Weather Review* 139.7, pp. 2163–2169. ISSN: 0027-0644. DOI: 10.1175/MWR-D-10-05046.1.

Klemp, Joseph B., W. C. Skamarock, and J. Dudhia (2007). “Conservative split-explicit time integration methods for the compressible nonhydrostatic equations”. In: *Monthly Weather Review* 135.8, pp. 2897–2913. DOI: 10.1175/MWR3440.1.

Klink, Katherine (2007). “Atmospheric circulation effects on wind speed variability at turbine height”. In: *Journal of Applied Meteorology and Climatology* 46.4, pp. 445–456. ISSN: 15588424. DOI: 10.1175/JAM2466.1.

Kramer, Matthijs, Dominikus Heinzeller, Hugo Hartmann, Wim van den Berg, and Gert-Jan Steeneveld (2018). “Assessment of MPAS variable resolution simulations in the grey-zone of convection against WRF model results and observations”. In: *Climate Dynamics*, pp. 1–14. ISSN: 0930-7575. DOI: 10.1007/s00382-018-4562-z.

Lackmann, Gary M. (2012). *Midlatitude synoptic meteorology: Dynamics, analysis, and forecasting*. Boston, United States: Americal Meteorological Society, 45 Beacon Street, Boston, Massachusetts 02108, p. 388. ISBN: 9781878220103.

Landberg, Lars (2015). *Meteorology for Wind Energy*. Ed. by Lars Landberg. Chichester, UK: John Wiley & Sons, Ltd. ISBN: 9781118913451. DOI: 10.1002/9781118913451.

Larsén, Xiaoli G., Søren E. Larsen, and Erik L. Petersen (2016). “Full-Scale Spectrum of Boundary-Layer Winds”. In: *Boundary-Layer Meteorology* 159.2, pp. 349–371. ISSN: 15731472. DOI: 10.1007/s10546-016-0129-x.

Larsén, Xiaoli Guo, Jianting Du, Rodolfo Bolaños, and Søren Larsen (2017a). “On the impact of wind on the development of wave field during storm Britta”. In: *Ocean Dynamics* 67.11, pp. 1407–1427. ISSN: 16167228. DOI: 10.1007/s10236-017-1100-1.

Larsén, Xiaoli et al. (2017b). *Extreme winds and waves for offshore turbines: Coupling atmosphere and wave modeling for design and operation in coastal zones*. Tech. rep. October. Roskilde, Denmark: Wind Energy Department, Technical University of Denmark. URL: https://backend.orbit.dtu.dk/ws/portalfiles/portal/139272513/FinalReport_PSO12020_XWiWa_20171031.pdf.

Leduc, Martin and René Laprise (2009). "Regional climate model sensitivity to domain size". In: *Climate Dynamics* 32.6, pp. 833–854. ISSN: 0930-7575. DOI: 10.1007/s00382-008-0400-z.

Leduc, Martin, René Laprise, Mathieu Moretti-Poisson, and Jean Philippe Morin (2011). "Sensitivity to domain size of mid-latitude summer simulations with a regional climate model". In: *Climate Dynamics* 37.1, pp. 343–356. DOI: 10.1007/s00382-011-1008-2.

Lloyd, S. (1982). "Least squares quantization in PCM". In: *IEEE Transactions on Information Theory* 28.2, pp. 129–137. ISSN: 0018-9448. DOI: 10.1109/TIT.1982.1056489. URL: http://ieeexplore.ieee.org/document/1056489/.

Martini, Matus N., William I. Gustafson, Travis A. O'Brien, and Po-Lun Ma (2015). "Evaluation of tropical channel refinement using MPAS-A aquaplanet simulations". In: *Journal of Advances in Modeling Earth Systems* 7.3, pp. 1351–1367. ISSN: 19422466. DOI: 10.1002/2015MS000470.

Matte, Dominic, René Laprise, Julie M. Thériault, and Philippe Lucas-Picher (2017). "Spatial spin-up of fine scales in a regional climate model simulation driven by low-resolution boundary conditions". In: *Climate Dynamics* 49.1-2, pp. 563–574. ISSN: 0930-7575. DOI: 10.1007/s00382-016-3358-2.

Mehrens, Anna R., Andrea N. Hahmann, Xiaoli G. Larsén, and Lueder von Bremen (2016). "Correlation and coherence of mesoscale wind speeds over the sea". In: *Quarterly Journal of the Royal Meteorological Society* 142.701, pp. 3186–3194. ISSN: 1477870X. DOI: 10.1002/qj.2900.

Michaelis, Allison C. and Gary M. Lackmann (2019). "Climatological Changes in the Extratropical Transition of Tropical Cyclones in High-Resolution Global Simulations". In: *Journal of Climate* 32.24, pp. 8733–8753. ISSN: 0894-8755. DOI: 10.1175/JCLI-D-19-0259.1.

Michaelis, Allison C., Gary M. Lackmann, and Walter A. Robinson (2019). "Evaluation of a unique approach to high-resolution climate modeling using the Model for Prediction Across Scales – Atmosphere (MPAS-A) version 5.1". In: *Geoscientific Model Development* 12.8, pp. 3725–3743. ISSN: 1991-9603. DOI: 10.5194/gmd-12-3725-2019. URL: https://www.geosci-model-dev.net/12/3725/2019/.

MPAS Tutorial (2019). *Generating Meshes For MPAS [Presentation Slides]*. Available under https://www2.mmm.ucar.edu/projects/mpas/tutorial/Boulder2019/slides/15.mesh_generation.pdf, last accessed: June 2020.

Nakanishi, Mikio and Hiroshi Niino (2009). "Development of an Improved Turbulence Closure Model for the Atmospheric Boundary Layer". In: *Journal of the Meteorological Society of Japan. Ser. II* 87.5, pp. 895–912. DOI: 10.2151/jmsj.87.895.

Navarra, Antonio and Valeria Simoncini (2010). *A Guide to Empirical Orthogonal Functions for Climate Data Analysis*. Vol. (5)2. 2. Dordrecht: Springer Netherlands, pp. 285–299. DOI: 10.1007/978-90-481-3702-2. URL: http://link.springer.com/10.1007/978-90-481-3702-2.

Neumann, Philipp et al. (2019). "Assessing the scales in numerical weather and climate predictions: Will exascale be the rescue?" In: *Philosophical Transactions of the Royal Society A: Mathematical, Physical and Engineering Sciences* 377.2142. DOI: 10.1098/rsta.2018.0148.

Niu, Guo-Yue et al. (2011). "The community Noah land surface model with multiparameterization options (Noah-MP): 1. Model description and evaluation with local-scale measurements". In: *Journal of Geophysical Research: Atmospheres* 116.D12. DOI: 10.1029/2010JD015139.

Novellino, Antonio, Paolo D'Angelo, Giacomo Benedetti, Giuseppe Manzella, Patrick Gorringe, Dick Schaap, Sylvie Pouliquen, and Lesley Rickards (2015). "European marine observation data network - EMODnet physics". In: *OCEANS 2015 - Genova*. IEEE, pp. 1–6. ISBN: 978-1-4799-8736-8. DOI: 10.1109/OCEANS-Genova.2015.7271548. URL: http://ieeexplore.ieee.org/document/7271548/.

Okabe, Atsuyuki, Barry Boots, Kokichi Sugihara, and Nok Chiu Sun (2000). *Spatial Tessellations: Concepts and Applications of Voronoi Diagrams*. 2nd ed. Wiley Series in Probability and Statistics. Hoboken, NJ, USA: John Wiley & Sons, Inc., p. 696. ISBN: 9780470317013. DOI: 10.1002/9780470317013.

Orlanski, Isidoro (1975). "A Rational Subdivision of Scales for Atmospheric Processes." In: *Bulletin of the American Meteorological Society* 56.5, pp. 527–530. URL: http://www.jstor.org/stable/26216020.

Park, Sang-hun, Joseph B. Klemp, and William C. Skamarock (2014). "A Comparison of Mesh Refinement in the Global MPAS-A and WRF Models Using an Idealized Normal-Mode Baroclinic Wave Simulation". In: *Monthly Weather Review* 142.10, pp. 3614–3634. DOI: 10.1175/MWR-D-14-00004.1.

Park, Sang-Hun, William C. Skamarock, Joseph B. Klemp, Laura D. Fowler, and Michael G. Duda (2013). "Evaluation of Global Atmospheric Solvers Using Extensions of the Jablonowski and Williamson Baroclinic Wave Test Case". In: *Monthly Weather Review* 141.9, pp. 3116–3129. DOI: 10.1175/MWR-D-12-00096.1.

Pfahl, Stephan and Heini Wernli (2012). “Quantifying the relevance of cyclones for precipitation extremes”. In: *Journal of Climate* 25.19, pp. 6770–6780. ISSN: 08948755. DOI: 10.1175/JCLI-D-11-00705.1.

Pilon, Romain, Chidong Zhang, and Jimy Dudhia (2016). “Roles of deep and shallow convection and microphysics in the MJO simulated by the model for prediction across scales”. In: *Journal of Geophysical Research* 121.18, pp. 10, 575–10, 600. DOI: 10.1002/2015JD024697.

Pincus, Robert, Richard Hemler, and Stephen A. Klein (2006). “Using stochastically generated subcolumns to represent cloud structure in a large-scale model”. In: *Monthly Weather Review* 134.12, pp. 3644–3656. ISSN: 00270644. DOI: 10.1175/MWR3257.1.

Porté-Agel, Fernando, Majid Bastankhah, and Sina Shamsoddin (2020). “Wind-Turbine and Wind-Farm Flows: A Review”. In: *Boundary-Layer Meteorology* 174.1, pp. 1–59. DOI: 10.1007/s10546-019-00473-0.

Pryor, Sara C., Tristan J. Shepherd, Patrick J.H. Volker, Andrea N. Hahmann, and Rebecca J. Barthelmie (2020). “"Wind Theft" from onshore wind turbine arrays: Sensitivity to wind farm parameterization and resolution”. In: *Journal of Applied Meteorology and Climatology* 59.1, pp. 153–174. ISSN: 15588432. DOI: 10.1175/JAMC-D-19-0235.1.

Räisänen, Petri and Howard W. Barker (2004). “Evaluation and optimization of sampling errors for the Monte Carlo Independent Column Approximation”. In: *Quarterly Journal of the Royal Meteorological Society* 130.601, pp. 2069–2085. ISSN: 00359009. DOI: 10.1256/qj.03.215.

Rajewski, Daniel A. et al. (2013). “Crop wind energy experiment (CWEX): Observations of surface-layer, boundary layer, and mesoscale interactions with a wind farm”. In: *Bulletin of the American Meteorological Society* 94.5, pp. 655–672. DOI: 10.1175/BAMS-D-11-00240.1.

Rauscher, Sara A. and Todd D. Ringler (2014). “Impact of Variable-Resolution Meshes on Midlatitude Baroclinic Eddies Using CAM-MPAS-A”. In: *Monthly Weather Review* 142.11, pp. 4256–4268. DOI: 10.1175/MWR-D-13-00366.1.

Rauscher, Sara A., Todd D. Ringler, William C. Skamarock, and Arthur A. Mirin (2013). “Exploring a Global Multiresolution Modeling Approach Using Aquaplanet Simulations”. In: *Journal of Climate* 26.8, pp. 2432–2452. ISSN: 0894-8755. DOI: 10.1175/JCLI-D-12-00154.1.

Renka, Robert J. (1997). “Algorithm 772: STRIPACK: Delaunay Triangulation and Voronoi Diagram on the Surface of a Sphere”. In: *ACM Trans. Math. Softw.* 23.3, pp. 416–434. ISSN: 0098-3500. DOI: 10.1145/275323.275329. URL: https://doi.org/10.1145/275323.275329.

Ringler, Todd D., Doug Jacobsen, Max Gunzburger, Lili Ju, Michael Duda, and William Skamarock (2011). "Exploring a multiresolution modeling approach within the shallow-water equations". In: *Monthly Weather Review* 139.11, pp. 3348–3368. DOI: 10.1175/MWR-D-10-05049.1.

Ringler, Todd D., J. Thuburn, J.B. Klemp, and W.C. Skamarock (2010). "A unified approach to energy conservation and potential vorticity dynamics for arbitrarily-structured C-grids". In: *Journal of Computational Physics* 229.9, pp. 3065–3090. ISSN: 00219991. DOI: 10.1016/j.jcp.2009.12.007.

Ringler, Todd, Lili Ju, and Max Gunzburger (2008). "A multiresolution method for climate system modeling: application of spherical centroidal Voronoi tessellations". In: *Ocean Dynamics* 58.5-6, pp. 475–498. ISSN: 1616-7341. DOI: 10.1007/s10236-008-0157-2.

Roberts, J. F., A. J. Champion, L. C. Dawkins, K. I. Hodges, L. C. Shaffrey, D. B. Stephenson, M. A. Stringer, H. E. Thornton, and B. D. Youngman (2014). "The XWS open access catalogue of extreme European windstorms from 1979 to 2012". In: *Natural Hazards and Earth System Sciences* 14.9, pp. 2487–2501. DOI: 10.5194/nhess-14-2487-2014.

Saha, Suranjana et al. (2010). *NCEP Climate Forecast System Reanalysis (CFSR) 6-hourly Products, January 1979 to December 2010*. Research Data Archive at the National Center for Atmospheric Research, Computational and Information Systems Laboratory. URL: https://doi.org/10.5065/D69K487J. last accessed: 06 July 2018.

Saha, Suranjana et al. (2011). *NCEP Climate Forecast System Version 2 (CFSv2) 6-hourly Products*. Research Data Archive at the National Center for Atmospheric Research, Computational and Information Systems Laboratory. URL: https://doi.org/10.5065/D61C1TXF. last accessed: 20 January 2017.

— (2014). "The NCEP Climate Forecast System Version 2". In: *Journal of Climate* 27.6, pp. 2185–2208. DOI: 10.1175/JCLI-D-12-00823.1.

Sakaguchi, Koichi et al. (2015). "Exploring a Multiresolution Approach Using AMIP Simulations". In: *Journal of Climate* 28.14, pp. 5549–5574. ISSN: 0894-8755. DOI: 10.1175/JCLI-D-14-00729.1.

Santos-Alamillos, F. J., D. Pozo-Vázquez, J. A. Ruiz-Arias, V. Lara-Fanego, and J. Tovar-Pescador (2014). "A methodology for evaluating the spatial variability of wind energy resources: Application to assess the potential contribution of wind energy to baseload power". In: *Renewable Energy* 69, pp. 147–156. DOI: 10.1016/j.renene.2014.03.006.

Sempreviva, A. M., R. J. Barthelmie, and S. C. Pryor (2008). "Review of methodologies for offshore wind resource assessment in European seas". In: *Surveys in Geophysics* 29.6, pp. 471–497. DOI: 10.1007/s10712-008-9050-2.

Siedersleben, S. K., J. K. Lundquist, A. Platis, J. Bange, K. Bärfuss, A. Lampert, B. Cañadillas, T. Neumann, and S. Emeis (2018). "Micrometeorological impacts of offshore wind farms as seen in observations and simulations". In: *Environmental Research Letters* 13.12. DOI: 10.1088/1748-9326/aaea0b.

Skamarock, W.C., J.B. Klemp, J. Dudhi, D.O. Gill, D.M. Barker, M.G. Duda, X.-Y. Huang, Wei Wang, and J.G. Powers (2008). *A Description of the Advanced Research WRF Version 3*. Tech. rep. June. Tech. Note NCAR/TN-475+STR, p. 113. DOI: 10.5065/D68S4MVH. URL: http://dx.doi.org/10.5065/D68S4MVH.

Skamarock, William C. (2004). "Evaluating Mesoscale NWP Models Using Kinetic Energy Spectra". In: *Monthly Weather Review* 132.12, pp. 3019–3032. DOI: 10.1175/MWR2830.1. URL: http://journals.ametsoc.org/doi/abs/10.1175/MWR2830.1.

Skamarock, William C., Joseph B. Klemp, Michael G. Duda, Laura D. Fowler, Sang-Hun Park, and Todd D. Ringler (2012). "A Multiscale Nonhydrostatic Atmospheric Model Using Centroidal Voronoi Tesselations and C-grid Staggering". In: *Monthly Weather Review* 140.9, pp. 3090–3105. ISSN: 00270644. DOI: 10.1175/MWR-D-11-00215.1.

Smith, Nicholas H. and Brian C. Ancell (2017). "Ensemble sensitivity analysis of wind ramp events with applications to observation targeting". In: *Monthly Weather Review* 145.7, pp. 2505–2522. ISSN: 15200493. DOI: 10.1175/MWR-D-16-0306.1.

Spera, David A. (2009). *Wind Turbine Technology: Fundamental Concepts of Wind Turbine Engineering*. Ed. by David A. Spera. 2nd ed. ASME Press, p. 835. ISBN: 9780791802601.

Staniforth, Andrew and John Thuburn (2012). "Horizontal grids for global weather and climate prediction models: A review". In: *Quarterly Journal of the Royal Meteorological Society* 138.662, pp. 1–26. DOI: 10.1002/qj.958.

Stauffer, David R. and Nelson L. Seaman (1990). "Use of Four-Dimensional Data Assimilation in a Limited-Area Mesoscale Model. Part I: Experiments with Synoptic-Scale Data". In: *Monthly Weather Review* 118.6, pp. 1250–1277. ISSN: 0027-0644. DOI: 10.1175/1520-0493(1990)118<1250:UOFDDA>2.0.CO;2.

Steiner, Andrea, Carmen Köhler, Isabel Metzinger, Axel Braun, Mathias Zirkelbach, Dominique Ernst, Peter Tran, and Bodo Ritter (2017). "Critical weather situations for renewable energies – Part A: Cyclone detection for wind power". In: *Renewable Energy* 101, pp. 41–50. ISSN: 09601481. DOI: 10.1016/j.renene.2016.08.013.

Stull, R. B. (1988). *An introduction to boundary layer meteorology*. Kluwer Academic Publishers. DOI: 10.1007/978-94-009-3027-8.

Termonia, Piet (2003). "Monitoring and Improving the Temporal Interpolation of Lateral-Boundary Coupling Data for Limited-Area Models". In: *Monthly Weather Review* 131.10, pp. 2450–2463. ISSN: 0027-0644. DOI: 10.1175/1520-0493(2003)131<2450:MAITTI>2.0.CO;2.

Termonia, Piet, Alex Deckmyn, and Rafiq Hamdi (2009). "Study of the Lateral Boundary Condition Temporal Resolution Problem and a Proposed Solution by Means of Boundary Error Restarts". In: *Monthly Weather Review* 137.10, pp. 3551–3566. ISSN: 0027-0644. DOI: 10.1175/2009MWR2964.1.

Tewari, M et al. (2004). "Implementation and Verification of the Unified NOAH Land Surface Model in the WRF Model. 20th Conference on Weather Analysis and Forecasting/16th Conference on Numerical Weather Prediction". In: *16th Conference on Numerical Weather Prediction, Seattle, WA, Jan*, pp. 10–15.

Thompson, Gregory, Paul R. Field, Roy M. Rasmussen, and William D. Hall (2008). "Explicit Forecasts of Winter Precipitation Using an Improved Bulk Microphysics Scheme. Part II: Implementation of a New Snow Parameterization". In: *Monthly Weather Review* 136.12, pp. 5095–5115. DOI: 10.1175/2008MWR2387.1.

Thuburn, J., T.D. Ringler, W.C. Skamarock, and J.B. Klemp (2009). "Numerical representation of geostrophic modes on arbitrarily structured C-grids". In: *Journal of Computational Physics* 228.22, pp. 8321–8335. ISSN: 00219991. DOI: 10.1016/j.jcp.2009.08.006.

Tomaszewski, Jessica M. and Julie K. Lundquist (2020). "Simulated wind farm wake sensitivity to configuration choices in the Weather Research and Forecasting model version 3.8.1". In: *Geoscientific Model Development* 13.6, pp. 2645–2662. DOI: 10.5194/gmd-13-2645-2020.

Turner, Adrian K, William H Lipscomb, Elizabeth C Hunke, Douglas W Jacobsen, Todd D Ringler, and Jonathan D Wolfe (2018). *MPAS-Seaice Model User's Guide*. DOI: 10.5281/zenodo.1227325.

Ullrich, Paul A. et al. (2017). “DCMIP2016: A review of non-hydrostatic dynamical core design and intercomparison of participating models”. In: *Geoscientific Model Development* 10.12, pp. 4477–4509. DOI: 10.5194/gmd-10-4477-2017.

Van der Hoven, Isaac (1957). “POWER SPECTRUM OF HORIZONTAL WIND SPEED IN THE FREQUENCY RANGE FROM 0.0007 TO 900 CYCLES PER HOUR”. In: *Journal of Meteorology* 14.2, pp. 160–164. ISSN: 0095-9634. DOI: 10.1175/1520-0469(1957)014<0160:PSOHWS>2.0.CO;2.

Vautard, Robert, Françoise Thais, Isabelle Tobin, François Marie Bréon, Jean Guy Devezeaux De Lavergne, Augustin Colette, Pascal Yiou, and Paolo Michele Ruti (2014). “Regional climate model simulations indicate limited climatic impacts by operational and planned European wind farms”. In: *Nature Communications* 5, pp. 1–9. DOI: 10.1038/ncomms4196.

Vincent, Claire L. and Pierre Julien Trombe (2017). *Forecasting intrahourly variability of wind generation.* Elsevier Ltd, pp. 219–233. ISBN: 9780081005057. DOI: 10.1016/B978-0-08-100504-0.00008-1. URL: http://dx.doi.org/10.1016/B978-0-08-100504-0.00008-1.

Vincent, Claire Louise (2010). “Mesoscale wind fluctuations over Danish waters”. Risø-PhD. Technical University of Denmark. Risø National Laboratory for Sustainable Energy. ISBN: 9788755038646. URL: https://backend.orbit.dtu.dk/ws/files/5578190/ris-phd-70.pdf.

Volker, P (2014). “Wake effects of large offshore wind farms - a study of mesoscale atmosphere and ocean feedbacks”. No. 0035(EN). Technical University of Denmark. URL: https://backend.orbit.dtu.dk/ws/portalfiles/portal/97913080/Wake_Effects_of_Large_Offshore_Wind_Farms.pdf.

Volker, P. J. H., J. Badger, A. N. Hahmann, and S. Ott (2015). “The Explicit Wake Parametrisation V1.0: a wind farm parametrisation in the mesoscale model WRF”. In: *Geoscientific Model Development* 8.11, pp. 3715–3731. DOI: 10.5194/gmd-8-3715-2015.

Wang, C. and R. G. Prinn (2010). “Potential climatic impacts and reliability of very large-scale wind farms”. In: *Atmospheric Chemistry and Physics* 10.4, pp. 2053–2061. DOI: 10.5194/acp-10-2053-2010.

Wang, Chien and Ronald G. Prinn (2011). “Potential climatic impacts and reliability of large-scale offshore wind farms”. In: *Environmental Research Letters* 6.2, p. 025101. DOI: 10.1088/1748-9326/6/2/025101.

Warner, Thomas T., Ralph A. Peterson, and Russell E. Treadon (1997). "A Tutorial on Lateral Boundary Conditions as a Basic and Potentially Serious Limitation to Regional Numerical Weather Prediction". In: *Bulletin of the American Meteorological Society* 78.11, pp. 2599–2617. ISSN: 00030007. DOI: 10.1175/1520-0477(1997)078<2599:ATOLBC>2.0.CO;2.

Warner, Thomas Tomkins (2010). *Numerical weather and climate prediction.* Vol. 9780521513890. Cambridge University Press, pp. 1–526. DOI: 10.1017/CBO9780511763243.

Westerhellweg, Annette, Beatriz Cañadillas, Friederike Kinder, and Tom Neumann (2014). "Wake measurements at alpha ventus - Dependency on stability and turbulence intensity". In: *Journal of Physics: Conference Series* 555.1. ISSN: 17426596. DOI: 10.1088/1742-6596/555/1/012106.

Wilks, Daniel S. (2019). *Statistical Methods in the Atmospheric Sciences.* 4th ed. Elsevier, p. 818. ISBN: 978-0-12-815823-4.

WindEurope (2020). *Offshore Wind in Europe - Key trends and statistics 2019.* Tech. rep. Retrieved from: https://windeurope.org/wp-content/uploads/files/about-wind/statistics/WindEurope-Annual-Offshore-Statistics-2019.pdf. WindEurope asbl/vzw, Brussels, Belgium.

Wong, May and William C. Skamarock (2016). "Spectral Characteristics of Convective-Scale Precipitation Observations and Forecasts". In: *Monthly Weather Review* 144.11, pp. 4183–4196. ISSN: 0027-0644. DOI: 10.1175/MWR-D-16-0183.1.

Xu, Kuan-Man and David A. Randall (1996). "A Semiempirical Cloudiness Parameterization for Use in Climate Models". In: *Journal of the Atmospheric Sciences* 53.21, pp. 3084–3102. DOI: 10.1175/1520-0469(1996)053<3084:ASCPFU>2.0.CO;2.

Yang, Zong-Liang et al. (2011). "The community Noah land surface model with multiparameterization options (Noah-MP): 2. Evaluation over global river basins". In: *Journal of Geophysical Research: Atmospheres* 116.D12. DOI: 10.1029/2010JD015140.

Zack, J, E Natenberg, S Young, G Van Knowe, K Waight, J Manobainco, and C Kamath (2010a). *Application of ensemble sensitivity analysis to observation targeting for short-term wind speed forecasting in the Tehachapi region winter season.* Tech. rep. Lawrence Livermore National Laboratory. URL: https://computing.llnl.gov/projects/starsapphire-data-driven-modeling-analysis/LLNL-TR-460956.pdf.

— (2010b). *Application of Ensemble Sensitivity Analysis to Observation Targeting for Short-term Wind Speed Forecasting in the Washington-Oregon Region.* Tech. rep. Lawrence Livermore National Laboratory. URL: https://computing.llnl.gov/

projects/starsapphire-data-driven-modeling-analysis/LLNL-TR-458086.pdf.

Zack, J, E Natenberg, S Young, J Manobainco, and C Kamath (2010c). *Application of Ensemble Sensitivity Analysis to Observation Targeting for Short-term Wind Speed Forecasting*. Tech. rep. Lawrence Livermore National Laboratory. URL: https://computing.llnl.gov/projects/starsapphire-data-driven-modeling-analysis/LLNL-TR-424442.pdf.

Zhang, Chunxi and Yuqing Wang (2017). "Projected Future Changes of Tropical Cyclone Activity over the Western North and South Pacific in a 20-km-Mesh Regional Climate Model". In: *Journal of Climate* 30.15, pp. 5923–5941. ISSN: 0894-8755. DOI: 10.1175/JCLI-D-16-0597.1.

Zhang, Chunxi, Yuqing Wang, and Kevin Hamilton (2011). "Improved Representation of Boundary Layer Clouds over the Southeast Pacific in ARW-WRF Using a Modified Tiedtke Cumulus Parameterization Scheme*". In: *Monthly Weather Review* 139.11, pp. 3489–3513. ISSN: 0027-0644. DOI: 10.1175/MWR-D-10-05091.1.

Zhao, Chun et al. (2016). "Exploring the impacts of physics and resolution on aqua-planet simulations from a nonhydrostatic global variable-resolution modeling framework". In: *Journal of Advances in Modeling Earth Systems* 8.4, pp. 1751–1768. DOI: 10.1002/2016MS000727.

Zhao, Jing, Yanling Guo, Xia Xiao, Jianzhou Wang, Dezhong Chi, and Zhenhai Guo (2017). "Multi-step wind speed and power forecasts based on a WRF simulation and an optimized association method". In: *Applied Energy* 197, pp. 183–202. DOI: 10.1016/j.apenergy.2017.04.017.

APPENDIX A
Approaches toward improving the modelling of midlatitude cyclones entering at the lateral boundary corner in the limited area WRF model

The following manuscript is the pre-print version of the paper:

Imberger, M., Larsén, X. G., Davis, N., & Du, J. (Accepted/In press). **Approaches toward improving the modelling of midlatitude cyclones entering at the lateral boundary corner in the limited area WRF model.** Quarterly Journal of the Royal Meteorological Society. https://doi.org/10.1002/qj.3843

ORIGINAL ARTICLE

Approaches toward improving the modelling of mid-latitude cyclones entering at the lateral boundary corner in the limited area model WRF

Marc Imberger[1] | Xiaoli Guo Larsén[1] | Neil Davis[1] | Jianting Du[2]

[1]Wind Energy Department, Technical University of Denmark - Risø Campus, Roskilde, Denmark

[2]The First Institute of Oceanography, MNR, Qingdao, China

Correspondence
Marc Imberger, Wind Energy Department, Technical University of Denmark - Risø Campus, Roskilde, Denmark
Email: maim@dtu.dk

Funding information
DTU Wind Energy Department (internal funds) and Danish "OffshoreWake" project (PSO-12521)

ABSTRACT

Lateral boundaries can have a large effect on the introduction of external large-scale structures in limited area models. This case study of a mid-latitude cyclone using the Advanced Weather Research and Forecasting (WRF) model examines challenges in simulating the storm intensity (characterised by sea level pressure, relative vorticity and wind speed) when a storm centre enters close to the lateral boundary corner in the outermost model domain. A domain shift, nudging techniques, adjustments of the WRF relaxation layer and the influence of boundary condition update frequency are investigated as possible solutions. The update frequency of the lateral boundary conditions is found to be the most efficient in improving the storm intensity, while adjustments to the relaxation layer or nudging techniques

did not overcome the lack of insufficiently updated lateral boundary conditions. This suggests that the modelling of the storm intensification requires sufficiently high temporal resolution.

Keywords: limited area modelling, meso-scale modelling, lateral boundary conditions, mid-latitude cyclone, WRF

1 | INTRODUCTION

Regional weather and climate models are commonly used to perform high resolution simulations over limited areas of interest (see e.g. Giorgi (2019) and references therein), and are therefore, also referred to as limited area models (LAMs). LAMs allow for smaller scale features to be resolved, improving the simulation results (e.g. Denis et al. (2002), Feser (2006)), at reduced computational costs, but add lateral boundary conditions (LBCs) as an additional dependence (e.g. Laprise (2003)). However, sharp changes in resolution (horizontal and vertical), between the LBCs and the LAM, can introduce spatial inconsistencies due to the spatial interpolation (Warner et al. (1997)). Additionally, LAMs require LBCs at every integration time step, typically a few seconds or minutes, while global reanalysis and forecast products are provided with resolutions on the order of hours. This makes temporal interpolation unavoidable (Warner et al. (1997)). Warner et al. (1997) highlighted that the update frequency of LBCs is one of the largest challenges when using LAMs, noting that it is especially relevant when the update frequency is low in comparison to the timescales of the meteorological feature of interest.

Several studies using HIRLAM (HIgh Resolution Limited Area Model, Källén (1996)) have shown that the influence of LBCs on LAM model results are especially important for cases with strong external forcing, e.g. severe storm events. Gustafsson (1990) found that a higher update frequency provided better forecasts based on the 24-h forecast skill of mean sea level pressure (MSLP) during rapid cyclogenesis. When the update frequency was not high enough, structural damage to the small scale upper-air trough was found in the relaxation zone. In a follow-up study, Gustafsson et al. (1998) showed that errors in the initial and lateral boundary data could explain two February 1995 events that were poorly forecasted by the operational HIRLAM model.

The impact of LBC update times has been found in other models as well. Termonia (2003) found that the ALADIN regional model (ALADIN International Team (1997)) required an update frequency of one hour to forecast Storm Lothar[1] with similar quality to the forcing data from ALADIN-France. Termonia et al. (2009) observed that the errors introduced due to the temporal interpolation of infrequent LBC data led to a reduced pressure drop of another storm in the ALADIN model.

In addition to an increased update frequency, Chikhar and Gauthier (2017) found that the use of spectral nudging could lead to a significant reduction of the temperature bias in the fifth generation Canadian Regional Climate Model (CRCM5). They also found that neither an increased model domain nor an increased blending zone (Davies relaxation zone) were able to correct these biases. While they found significant improvement when increasing the LBC update frequency from 6-hourly to hourly, additional increase to sub-hourly resolution had limited effect.

While the earlier studies focused on how LBC interpolation can impact the forecast skill of individual storms, these effects also impact other types of investigations, for example, storm climatology studies like Larsén et al. (2017a). In studies like Larsén et al. (2019), which focuses on the estimation of extreme offshore wind speeds, correctly simulating both the intensity and location of hundreds of storms is crucial for reliable statistics. Therefore, careful design of the LAM settings is required. Larsén et al. (2017a) points out the importance of domain size, horizontal resolution, initialisation, and simulation time on model results. However, another challenge was identified, that of storms entering through the corner of the model domain rather than through an edge, which leads to a lack of storm intensification and can have large track errors. This was initially identified during a domain evaluation study using the Weather Research and Forecasting (WRF, Skamarock et al. (2008)) model in Imberger (2017), which was carried out within the framework of the above mentioned storm climatology over the North Sea (Larsén et al. (2017a)). Imberger (2017) tested different WRF domain setups and found a lack of expected storm development, in terms of both deepening and track, compared to forcing data and the best track data provided by the Extreme Wind Storms Catalogue (XWS, Roberts et al. (2014)) for a particular case, where the storm centre entered the domain very close to its south-western corner. This issue will be further referred to as the "corner issue" and described in more details in Section 2. This study builds upon and extends the initial findings in Imberger (2017) by addressing the following questions: (1) how does the "corner issue" influence large structures on the order of several hundred kilometres, such as the area of decreased

[1] Referred to as "French Christmas storm" in Termonia (2003)

sea level pressure (SLP) and the horizontal wind fields, and (2) to what extent can commonly applied methods for modifying the LBC introduction improve the LAM model results regarding storm intensity and path.

Four methods are evaluated in this study, domain displacement, nudging techniques, adjustment of the relaxation layer, and increased LBC update frequency, which will be described in more detail in Section 3. The paper is laid out as follows: A more thorough introduction to the "corner issue" is given in Section 2; The general model setup and all investigated model scenarios are presented in Section 3; Section 4 describes the evaluation methods including a description of measurements, key time-periods and the best storm track data used for validation. The results are presented in Section 5, and key findings are discussed in Section 6. The paper finalises with conclusions in Section 7.

2 | THE "CORNER ISSUE"

The "corner issue" refers to the distorted introduction of the large-scale structure of a mid-latitude storm when the storm centre is located too close to the lateral boundary corner of the LAM. One example of a domain setup suffering from the "corner issue" would be the domain setup "REF", in Figure 1, for the simulation of storm "Christian". The cyclone centre passes through the south-west corner of the boundary region and, as the model integration continues, the combination of spatial and temporal interpolation and model relaxation in the buffer zone of the LAM domain acts on the large-scale structure from two different directions. In the storm case investigated by Imberger (2017), this resulted in a lack of expected storm deepening and storm track deviation from forcing data and XWS best track data. It was also shown that shifting the domain southward, ("REF-South" in Figure 1) to avoid the "corner issue", improves the intensification of the simulated storm. The reduced pressure drop due to the "corner issue", seen with storm "Christian", was also found for two other storm cases in the XWS catalogue (storm "Ulli" and storm "Patrick", not shown). This suggests that the "corner issue" is not, in principal, related to the structure of a particular storm, but a more general issue. However, in this study, we focus on a single storm, to allow for more sensitivity studies to be performed.

"Christian" was chosen as the example, because (1) it was a failed case in the storm climatology created by Larsén et al. (2017a), which used a standard model approach (fixed domain, 6-hourly LBC update interval), and (2) it represents a typical storm within the area covered by the XWS catalogue. When compared to the full list of storms in the XWS catalogue, "Christian's" lowest minimum sea level pressure and highest maximum wind speed are quite representative for the listed storms (Figure 2), making it well suited for a case study. "Christian" was a Hurricane-force 12 European wind storm that impacted several European countries during October 2013 on its path from the North Atlantic toward the Baltic Sea. The name "Christian" follows the designation from the Free University Berlin, as all storm names in this publication do, but other names have been used by different institutions: "St. Jude" (UK MetOffice), "Simone" (Swedish Meteorological and Hydrological Institute) and "Oktoberstormen/Allan" (Danish Meteorological Institute). "Christian" originated as a secondary low to the south of the Icelandic Low "Burkhard" on 26 October. It was characterised as a rapidly moving storm with landfall in the region of Cornwall on 2200 UTC 27 October 2013 (Haeseler and Lefebvre (2013)). The highest intensity of the storm based on minimum SLP and maximum 850 hPa relative vorticity was reached on 28 October 2013 (cf. XWS Catalogue (cited 2019)). Additional information about the storm track and atmospheric parameters of "Christian" are summarised in the XWS Catalogue (cited 2019) and AIR Worldwide (cited 2018), while Hewson et al. (2014) provides a comprehensive description of its meteorological characteristics.

3 | MODEL SETUP

In this section, the model setups will be described. First in Section 3.1 the basic setup of the model, which is consistent across most of the simulations, will be introduced. Then in Section 3.2 the different sensitivity studies will be described.

3.1 | Basic Model Setup

The limited area model used in this investigation is version 3.7.1 of the non-hydrostatic Advanced Weather Research and Forecasting Model (WRF, Skamarock et al. (2008)) using the ARW core and terrain-following vertical coordinate.

Figure 1 (solid orange frame) shows the domain used for most of the simulations, "REF", which has a spatial extent of 2700 km x 1800 km and a horizontal resolution of 18 km, leading to a domain that consists of 150 x 100 grid points. No nested domains were used, since the focus was on the impact of LBCs from a global model. There are 52 levels in the vertical.

LBCs are introduced into the WRF model through a Davies relaxation zone. The relaxation zone consists of a number of grid cells inside the LAM domain where relaxation towards spatially and temporally interpolated large-scale forcing data takes place. In this zone, the update of prognostic variables is determined based on the difference between the large-scale forcing value and the LAM model value (Davies and Turner (1977)). The weight of the large-scale data decreases with the distance from the domain border. The weight is calculated using two weighting functions $F_1(n)$ and $F_2(n)$ and a 5-point horizontal smoother (see Skamarock et al. (2008) for details). The weighting functions are defined as:

$$\begin{aligned} F_1(n) &= \frac{1}{10\Delta t}\frac{1+N_r-n}{N_r-1} \\ F_2(n) &= \frac{1}{50\Delta t}\frac{1+N_r-n}{N_r-1} \\ 2 &\leq n \leq N_r, \end{aligned} \tag{1}$$

where n is the position from the border, $N_r = N_{relax} + 1$ is the total Davies relaxation zone width, N_{relax} is the pure relaxation zone width, and Δt is the integration time step, which was set to 37.5 s in this study. By default, the WRF model has $N_{relax} = 4$. Given the Davies relaxation zone, two LAM border areas can be defined, namely a "hard" and a "soft" border. The "hard" border is what we typically think of as the extent of the domain, while the "soft" border is located at the edge of the relaxation zone, where the LAM physics are fully in control of the solution.

The total simulation time, which is the same for all simulations, is set to 36 hours (1200 UTC 26 October 2013 to 0000 UTC 28 October 2013). Included in the total simulation time is a 12 hour spin-up period, which allowed a sufficient build up of the kinetic energy in higher model levels, based on the kinetic energy spectrum (not shown). The storm centre enters the WRF domain 24 hours after initialisation, allowing for the investigation of model results both before and after the introduction of the storm. If not stated otherwise, LBCs are updated every 6 hours using data from the 6 hour forecast of the previous initialisation of the Climate Forecast System Version 2 Forecast (CFSv2; see Saha et al. (2014) for the publication and Saha et al. (2011) for the data set). The 6 hour window is used by default as this is a common update frequency. The spatial resolution of CFSv2 is 0.2 degrees for surface fields and 0.5 degrees for variables provided on the vertical pressure levels. LBCs between two subsequent forcing data fields needed by the LAM are obtained by linear interpolation to the integration time step (here 37.5 s) of the model (WRF default).

Micro-physics are parameterised with the New Thompson enhanced bulk scheme (Thompson et al. (2008)) and cloud fractions for micro-physics clouds are activated and follow Xu and Randall (1996). To parameterise convective processes under this horizontal resolution, the Kain-Fritsch parameterisation scheme (Kain (2004)) is activated and the calling period is set to 5 minutes. Long- and shortwave radiation are calculated by the RRTMG scheme as described in Iacono et al. (2008) and called every 18 min, following the recommendation in Dudhia (2017). The Unified Noah land surface model (Tewari et al. (2004)) with four soil levels is chosen to represent the land surface while land usage is obtained from the U.S Geological Survey (USGS, 24 land use categories). The Level 3 Mellor-Yamada-Nakanishi-Niino (MYNN, Nakanishi and Niino (2006)) scheme is used to model surface and planetary boundary layer (PBL). This physics configuration follows the setup used in Larsén et al. (2017b) and Larsén et al. (2019), which showed good performance when simulating storms events. Sea surface temperature is not updated during the simulation. A summary of the model specifications can be found in Table 1.

3.2 | Sensitivity Studies

This section describes the different perturbations to the reference model setup described in Section 3.1 to investigate the issues related to the introduction of "Christian" into the WRF LAM domain. All methods in this study were carried out using the available capabilities of the WRF model environment, allowing for easy implementation in other studies. The simulation naming convention and a short description of case study characteristics is provided in Table 2. These studies can be sorted in four main categories:

- Displacement of the model domain (Section 3.2.1)
- The use of spectral nudging (Section 3.2.2),
- Relaxation zone adjustments of the WRF domain (Section 3.2.3),
- Adjustments of temporal update frequency of the lateral boundary conditions (Section 3.2.4).

The first method relies on a modification to the static WRF domain (shifting), but the other three investigations can be applied without changing the WRF model domain. If not stated otherwise, model parameters are identical to the parameters for the reference simulation (cf. Table 1).

3.2.1 | Domain Displacement Method

In this sensitivity study, a simple displacement of the model domain is applied, allowing the storm structure to be introduced closer to the centre of the western edge. This is shown in Figure 1 where the solid orange frame is the original domain ("REF"). The dashed line in the figure depicts an identical domain that has been shifted to the south ("REF-South").

3.2.2 | Spectral Nudging Method

Termonia (2003) showed that the worst performance for the linear interpolation of the LBCs of storms occurs when the storm is fully outside of the domain at one LBC update time-step and at the next time-step it is fully inside the domain. By adding nudging to the LAM, the information about the storm can be added to the interior of the model even though it was not added through the boundaries. For this study, the the spectral nudging technique (Waldron et al. (1996), von Storch et al. (2000)) was used. The key idea of spectral nudging is that nudging should only act on coarse scales, determined by a specified wave number threshold. Spectral nudging is widely used since it can reduce the sensitivity of the model solution to domain geometry, like the domain placement on earth (see Miguez-Macho et al. (2004)).

The implementation of spectral nudging in WRF is based on the formulation in the Regional Atmospheric Modeling System (RAMS) by Miguez-Macho et al. (2004) and can be described as stated in Equation 2 (Gómez and Miguez-Macho (2017)):

$$\frac{\partial \alpha}{\partial t} = F(\alpha, \vec{x}, t) + G_\alpha W(\vec{x}, t) V(z) \mathrm{Filt}_{xy} [(\hat{\alpha_0} - \alpha)] \tag{2}$$

The notation is based on Gómez and Miguez-Macho (2017) with the following definitions: α is a generic placeholder for any model state variable and $\hat{\alpha_0}$ describes the target value for the nudging procedure, which comes in this case from the forcing data. F describes the tendency term determined by the model at a specific time t and place $\vec{x}$ and G_α represents the nudging strength. W and V are time-dependent weight factor and vertical weight factor respectively. Filt_{xy} represents the filtering algorithm applied to $(\hat{\alpha_0} - \alpha)$. Filtering is first performed row-wise and then repeated column-wise, for each row/column in $(\hat{\alpha_0} - \alpha)$. The nudging is carried out using the following steps: (1) transformation to spectral space via Fast Fourier Transformation (FFT), (2) zeroing out signal amplitude for wavelengths smaller than the cut-off wavelength, (3) back-transformation via Inverse FFT (Gómez and Miguez-Macho (2017)). This means that wavelengths larger than the threshold will remain in the nudging data, while smaller wavelengths will be filtered out. For further details, the reader is referred to Gómez and Miguez-Macho (2017), which provides a comprehensive description of the implementation of spectral nudging in WRF.

In the current study, spectral nudging towards the forcing data for higher wavelengths was applied to the following list of governing variables: grid-relative wind components (U,V), potential temperature (θ), and geopotential height (ϕ). A constant nudging strength G_α of 0.0003 s^{-1} following the default value in Skamarock et al. (2008) is used. In the WRF model, spectral nudging is controlled by two parameters, the nudging strength and the nudging range. The nudging strength (weak/strong) defines how strongly the LAM is nudged toward the nudging data, and the nudging range (narrow/wide) defines the range of wavelengths that are affected by the nudging. Two nudging ranges were investigated in this study, corresponding to nudging waves larger than 900 km ("NUD900km") and larger than 100 km ("NUD100km"). When the cyclone enters the WRF domain (1200 UTC 27 October 2013), its west-east extension is approximately 200 km, based on the largest closed isobar in the CFSv2 data. It should be noted that the effective resolution of WRF in this study is approximately 126 km, based on the expected 7 Δx resolution of WRF (Skamarock (2004)), meaning that effectively all resolvable wave lengths in the outermost domain are affected by the spectral nudging term in the "NUD100km" study. This suggests that for "NUD100km", spectral nudging acts similarly to grid nudging (Stauffer and Seaman (1990)), which adds a nudging term to all wavelengths. For both simulations, nudging is active in the whole domain and over the whole simulation period (i.e. $W(\vec{x}, t) \equiv 1$), but only above the planetary boundary layer (i.e. $V(z) = 1$ for heights above the PBL, zero otherwise).

3.2.3 | Relaxation Zone Adjustment

The thickness of the Davies relaxation zone should have an impact on the introduction of a system such as "Christian" to the LAM. To investigate the behaviour of the storm when changing the relaxation zone width, two setups were investigated. The first reduces the relaxation zone width to $N_{relax} = 2$ grid cells ("HalfRelaxZone"), while the second uses twice the default width, i.e. $N_{relax} = 8$ grid cells ("2xRelaxZone").

3.2.4 | Increased LBC Update Frequency

Several studies have shown the impact of increased LBC update frequency on the introduction of storms into a LAM. In this study, two simulations were tested that utilised additional forecasts from the CFSv2. Both 3-hourly update ("CFSv2-3h") and hourly update ("CFSv2-1h") frequencies were examined. This is inspired by commonly investigated update frequencies (see e.g. Tudor and Termonia (2010), Matte et al. (2017)) and used intervals in operational models (e.g. Consortium for Small Scale Modeling (COSMO) (cited 2018)). Due to the unique setup of the CFSv2 simulation, where each forecast is only 6 hours long, the hourly forecast period is represented as follows, the initial fields are from the 6 hour forecast of the simulation started at 0600 UTC 26 October 2013, then the next six hours are forecast hours 1-6 of the simulation started at 1200 UTC, and continuing in six hour windows until the end of the study.

4 | TOOLS AND PRODUCTS USED FOR MODEL EVALUATION

The different simulation setups described in Section 3.2 are evaluated using comparisons with buoy observations, investigations of snap-shots at times of interest, and deviation from the Extreme Wind Storms catalogue.

4.1 | Buoy Observations

The coarse resolution of the modelled data limits a quantitative comparison of wind speed and direction using point measurements, due to the resolution mismatch. Therefore, the values of wind speed magnitude will be considered qualitatively. However, SLP is less sensitive to the resolution mismatch, and therefore, can be evaluated quantitatively. For this study, buoy measurements from the European Marine Observation and Data Network (EMODnet, cited 2018) are used to perform these evaluations, which provides observations of a collection of oceanic and meteorological variables.

Initially all relevant buoy data, inside the WRF domain and available at the top of the hour, to match the output time of WRF, within simulation time between 0000 UTC 27 October 2013 and 0000 UTC 28 October 2013 are selected, along with 6 hours before and after the WRF simulation time to study additional trends in the measurements. The data set is then filtered to remove data flagged with quality issues. This results in a collection of 12 stations used in the analysis. The locations of the buoy measurements will be shown later in Section 5.6. The model SLP is reconstructed from the WRF output parameters geopotential height, temperature, pressure, and water vapour mixing ratio, using the *wrf_slp* function, which is part of the *WRFUserARW.ncl* library in the NCAR Command Language (NCL,UCAR/NCAR/CISL/TDD (2017)). Model and observed SLP are compared by using the closest model grid point to each buoy location.

4.2 | Investigated Time Stamps

Two snap-shots were used to investigate the spatial behaviour of the storm, 1800 UTC 27 October 2013 and 0000 UTC 28 October 2013. These were selected for a few different reasons: (1) the entire storm was located inside the meso-scale model domain, (2) the model had enough time to develop its own features and (3) there are available buoy measurements over a wide spatial range, including close to the storm centre.

For temporal analyses, the entire simulation period, excluding spin-up time, (0000 UTC 27 October 2013 to 0000 UTC 28 October 2013) is used to compare the different simulations.

4.3 | Storm Track Data from Extreme Wind Storms (XWS) Catalogue

The Extreme Wind Storms (XWS) Catalogue is a database of 52 European windstorms covering the time period from 1979 to 2013 (see Roberts et al. (2014) for the article and XWS Catalogue (cited 2019) for the data set). The catalogue contains two sets of storm tracks, one based on minimum mean SLP and the other on the maximum relative vorticity at 850 hPa, and 3-second gust footprints (raw data set and re-calibrated) for each storm. The footprints are defined by the maximum 3-second gust over a 72 h period at a certain location. A detailed overview of the methodology behind the XWS data set is given in Roberts et al. (2014). Within the scope of the current investigation, the storm track data of cyclone "Christian", based on minimum SLP, is used for examining the model results. The track data provides the position of the local minimum sea level pressure (LMSLP) every 3 hours, and is obtained from a regional dynamically downscaled version of the ERA-Interim (Dee et al. (2011)) data set using the methodology described in Hoskins and Hodges (2002).

5 | RESULTS

The results are presented in six parts. First, the storm intensification and LMSLP location of each of the different simulations is presented and compared to CFSv2 and XWS in Section 5.1. Then, Section 5.2 shows the results of the simple domain shift method, while Section 5.3 to Section 5.5 show the results from domain independent methods to tackle the "corner issue". Finally, Section 5.6 presents a spatial and temporal comparison of the different simulations with buoy data. The data obtained from the forcing data CFSv2 and from "REF-South" are clipped to the reference domain.

5.1 | Storm Intensification Compared to CFSv2 and XWS

Table 3 summarises the magnitudes in LMSLP, for each of the WRF simulations, as well as, the CFSv2 forcing data and the XWS catalogue at 1800 UTC 27 October 2013 (30 hours after model initialisation) and 0000 UTC 28 October 2013 (36 hours after model initialisation). The storm intensity is quantified using the LMSLP of the storm centre. "CFSv2-1h" is the only simulation that provides LMSLP more than 3 hPa below the forcing data estimation at both 30 h and 36 h after model initialisation. "CFSv2-3h" and "REF-South" have a LMSLP value more than 3 hPa below the forcing data 36 h after initialisation. Furthermore, it can be seen that CFSv2 and XWS agree quite well in terms of the storm intensity based on minimum SLP.

Table 4 and Table 5 compare the simulated storm centre locations, and their distances to XWS and CFSv2 at 1800 UTC 27 October 2013 and 0000 UTC 28 October 2013, respectively. With respect to the storm centre location, a difference of 130 km is found between the XWS and CFSv2 location at 1800 UTC 27 October 2013 and 220 km at 0000 UTC 28 October 2013. This is comparable to the cyclones west-east extension when it enters the WRF domain (1200 UTC 27 October 2013), which is on the order of 200 km or three to four CFSv2 grid points (0.5 degree spatial resolution). The distance between the WRF storm centre and that of the CFSv2 is always less than the distance between the CFSv2 and the XWS (except for "REF" at 0000 UTC 28 October 2013). However, this value varies quite significantly depending on the simulation setup.

5.2 | Reference Case and Effect of Domain Displacement

There are major differences in the development of the storm with the default domain ("REF") and the shifted domain ("REF-South", Figure 1). Figure 3 shows the impact of the domain shift on storm intensity and position. At 0000 UTC 28 October 2013, "REF" (Figure 3d) develops a small decrease in SLP down to 986 hPa centred north of Cornwall, while "REF-South" (Figure 3f) shows a much stronger decrease in SLP of 981 hPa and a different location of the storm centre, which is over south Wales. The CFSv2 had an intensity of 984 hPa, which is actually lower than the "REF" case (cf. Table 3). This strongly indicates a misinterpretation of the forcing data at the lateral boundary corner in "REF". While a higher storm intensification is expected in the higher LAM domain resolution, the storm intensification in "REF" is not present and the LMSLP is higher than estimated by CFSv2. Furthermore, the storm centre (based on the location of the LMSLP) is displaced compared to the forcing data (compare Figure 3b). "REF-South" also simulates the storm centre much closer to the forcing data (30 km, see Table 5) than "REF" (160 km, see Table 5). The differences in the simulation are seen when the storm enters the domain approximately at 1200 UTC 27 October 2013 (left-column of Figure 3), which suggests differences in how the storm is introduced to the LAM model. A closer look at the modelled 250 hPa wind speed field at the same time (1200 UTC 27 October 2013; not shown) revealed that the jet-stream is also affected by artificial wind speed patterns at the southern border of the WRF domain which are not visible in "REF-South". The differences obtained by the simple domain shift also suggest that more general effects like potential inconsistencies between CFSv2 and WRF physics or spin-up time are not the dominant factor for the distortion, since they would be identical in both situations.

Figure 4a to Figure 4c show the wind speed at 850 hPa on 0000 UTC 28 October 2013 for CFSv2, "REF", and "REF-South". The greatest difference between the two WRF simulations is visible in the regions of low wind speeds, below $10\ \mathrm{m\ s^{-1}}$. In "REF-South" and CFSv2, this region is located near Cardiff and extending to the north-east, while in "REF" it is found off the coast of Pembrokshire to the south-west of the other simulations. Differences in the high wind speed region, above $35\ \mathrm{m\ s^{-1}}$, and large-scale flow direction are similar in all simulations. While the difference between the maximum wind speed at 850 hPa of "REF" ($V_{max,REF} = 40.2\ \mathrm{m\ s^{-1}}$) and "REF-South" ($V_{max,REF-South} = 40.5\ \mathrm{m\ s^{-1}}$) is marginal, both simulations underestimate the maximum wind speed obtained from CFSv2 by around

3 m s^{-1} ($V_{max,CFSv2}$ = 43.0 m s^{-1}). Regarding the location of the high wind speed zone, "REF" is in closer agreement with the forcing data, while "REF-South" shows an extension of the high wind speed north of 52°N over England.

5.3 | Effect of Spectral Nudging

There are large changes to the SLP field when applying the spectral nudging technique (Figure 5). In the "NUD100km" simulation, the storm centre has shifted to the north-east, when compared with "REF". Additionally, the deepening of the storm to the north of Cornwall, which was found in "REF", is not present in "NUD100km". The nudging also created blurring effects, resulting in a spreading of the low SLP field around the storm, compared to the "REF-South" and CFSv2 simulations, and a large region of moderately lower SLP than in "REF". However, "NUD100km" does a similar job of estimating the location of the storm when compared with "REF-South" and CFSv2 (see Table 5).

The higher wavelength range of "NUD900km" leads to a slightly higher SLP across most of the domain, but overall negligible differences are found in comparison with "NUD100km" (not shown). A third spectral nudging study, that extended the nudging to model layers in the PBL, did not show significant effects in the sea level pressure field either (not shown). Based on these results, spectral nudging did not improve the forecast of "Christian" as much as moving the domain did in "REF-South".

When investigating the wind speed field at 850 hPa (Figure 4d), it is easy to see the effect of the spectral nudging term on the wind speed components U and V. The regions of low and high wind speeds are close to the shape and location of the corresponding regions in the CFSv2 data set (Figure 4a). The large extension of the low wind speed region in southwest-northeast direction is maintained in the simulation while this feature is not present in "REF-South".

It must be emphasised that the wind speed components U and V are directly influenced by the spectral nudging term while SLP is not. This explains the stronger effect on the wind speed field while the SLP field is less affected.

5.4 | Effect of Relaxation Zone Adjustments

Figure 6 shows the SLP field for the simulations with adjusted Davies relaxation zone width. The relaxation zone width has a significant impact on the storm intensification in this particular case, likely due to the storm entering close to the corner of the domain. The results of "2xRelaxZone" do not show a significant decrease in SLP, but actually a strong increase in SLP over Cornwall. In "HalfRelaxZone", there is a decrease in SLP around the storm centre from CFSv2, however, the increase in the storm intensity is still smaller than in "REF-South", and the location of the storm centre is between that of "REF" and "REF-South" (cf. Table 5).

Some of the reasons for these differences can be seen by looking at the 850 hPa relative vorticity field (Figure 7). In all four simulations, an artificial pattern is visible near the south-west corner of the relaxation zone, which runs parallel to the "soft" border of the relaxation zone. While similar patterns are visible in all four simulations, the width of the relaxation zone effects how far into the domain the distortion is found. Additionally, by extending the "soft" border of the relaxation zone further into the domain, and thereby, closer to the area of interest, additional spatial blur and distortion of the horizontal fields occurs.

Tudor and Termonia (2010) found that a very wide relaxation zone could cause features to bounce back into the domain, rather than leave as they should. This issue was investigated here, but no such behaviour was found in either the SLP field or the relative vorticity field at 850 hPa (not shown).

5.5 | Effect of LBC Update Frequency

Figure 8 shows the SLP results from the "CFSv2-3h" (Figure 8a) and "CFSv2-1h" (Figure 8b) simulations at 0000 UTC 28 October 2013. The simulations with higher update frequency show a major decrease in SLP compared to "REF", which is more pronounced in "CFSv2-1h" than "CFSv2-3h". The SLP difference compared to "REF" shows the impact more clearly, with lower SLP across most of the domain in the higher frequency simulations. The largest SLP differences, between 5 hPa and 8 hPa, are located to the north-east of the CFSv2 storm centre in both "CFSv2-3h" (Figure 8c) and "CFSv2-1h" (Figure 8d). LMSLP values as low as 981 hPa ("CFSv2-3h") and 979 hPa ("CFSv2-1h") are seen.

The increased storm intensity in "CFSv2-1h" can also be seen in the 850 hPa wind speed field (Figure 4f). The highest wind speeds found in "CFSv2-1h", maximum wind speed of $V_{max,CFSv2-1h}$ = 44.5 m s^{-1}, compared to "CFSv2-3h", maximum wind speed of $V_{max,CFSv2-3h}$ = 42.8 m s^{-1}, and the original CFSv2 data ($V_{max,CFSv2}$ = 43.0 m s^{-1}) in the high wind speed region. In "CFSv2-3h" (Figure 4e), the wind speed is not increased compared to the original CFSv2 data set (Figure 4a). In the low wind region, to the north of the storm, the changes to the wind speed and large-scale flow direction are not as pronounced. The low wind region in "CFSv2-1h" is located slightly further north-east.

5.6 | Spatial and Temporal Distribution

The measured and simulated SLP are compared at the 12 buoys selected using the process described in Section 4.1 at both snap-shot times (Figure 9). The results are sorted by distance to the CFSv2 storm centre, to evaluate its relationship to model performance. We find that there is a relationship between the distance to the storm centre and the spread of the simulation results. Locations close to the CFSv2 storm centre, within approximately 400 km, show significant differences, but the results are consistent in areas further from the storm centre. Although stations #34 and #35 have large differences even though they are located far from the storm centre in all scenarios at both times.

The buoy data was also used to evaluate the performance of the different model simulations across the entire time of the simulation. The temporal dimension plays an important role in the model evaluation, as seen in the spatial plots of the SLP field across the different simulations. The SLP time-series at all 12 buoy locations were compared with the simulation, however only four locations were focused on for this report (Figure 10). The four locations were selected for the following reasons: buoy station #17 was close enough to the storm travel path to be impacted in both simulation and measurements; buoy station #34 was far from the storm track of cyclone "Christian", allowing for the investigation of model performance far from the storm; buoy station #10 was located east of the storm travel path, allowing the investigation of the front-side of the storm; and buoy station #19 was picked due to its location in the English Channel, which was identified as a region of large wind speed changes using the XWS storm footprint.

The time-series plots allow for the investigation of general SLP trends and the timing of the minimum SLP for a given location in both the simulations and measurements. At buoy station #17, both the drop in SLP due to the passing storm centre and the subsequent recovery of SLP after the storm passed the buoy is noticable clearly in both the measurements and all the models. However, while the general trend is followed in all simulations, only "CFSv2-1h" and "CFSv2-3h" capture the timing and magnitude of the SLP drop around 1700 UTC 27 October 2013. All other configurations have a time shift of around one hour. At buoy station #10, which is passed by the storm at a later time, all of the models show a phase shift of around two hours, and while "CFSv2-1h" and "CFSv2-3h" have larger pressure drops than the other models, the drop is still smaller than the observed value. This phase shift is not as obvious at buoy station #19, which is around 230 km further east than station #10, but only "CFSv2-1h" and "CFSv2-3h" capture the magnitudes of the pressure well. Further away from the storm centre, at buoy station #34, there are still significant differences in the SLP estimation across the different simulations. The simulations with high update frequencies ("CFSv2-1h", "CFSv2-3h") and the heavily nudged simulation ("NUD100km") are closer to the measurements than the other simulations especially in the region of low SLP around 0800 UTC 27 October 2013 before the storm enters the domain. This could be related to the impact of another very strong depression, referred as "Burkhard" in e.g. Haeseler and Lefebvre (2013), which was located close to buoy station #34, see also Section 2.

6 | DISCUSSION

While the proper introduction of the large-scale structures via the boundaries of a LAM is generally important, the "corner issue" reveals that boundary corners are especially vulnerable when complex large-scale structures like mid-latitude storms are involved. Shifting the domain so that the storm does not enter at the corner of the domain (i.e. avoiding the "corner issue") was found to improve the simulation of both the storm intensity and location. This highlights that the introduction at the boundary corner is a particular challenge that might not be experienced under normal conditions (i.e. introduction via the edge of the domain). Domain shift investigations of the other storm cases mentioned earlier (storm "Ulli" and storm "Patrick") revealed the same effect of improved storm intensification with respect to the sea level pressure field (not shown). This emphasises that the lack of storm intensification as a consequence of the "corner issue" is not unique to a specific storm type.

Four different methods for introducing a typical mid-latitude storm into the WRF LAM were investigated and evaluated spatially and temporally using the forcing data, external storm track data, and buoy observations with a focus on limiting the "corner issue's" impact. Of the three approaches using fixed domains, only the increased LBC update frequency improved the simulation compared to the large scale forcing data. This points out that the main driver in conserving the large-scale structures in this case is the proper import of the forcing data via LBCs which can achieved best by either a domain shift, if possible, or an increased LBC update frequency. This enables the LAM to conserve the large-scale structures and allows for the development of smaller-scale features that were not present in the forcing data, but are associated with the storm. While a direct usage of the forcing data would avoid the issue of lateral boundaries and the "corner issue" completely, the coarse resolution and lack of small scale information limits its use for studying meteorological parameters that rely on well resolved small-scale patterns, like wind speed. Changes to the introduction of the LBCs influences the storm location and size, while smoothing influences localised features, such as the intensification of the storm centre.

An inherent problem of avoiding the "corner issue" by domain shifting is the question of how much shifting is sufficient, which likely varies depending on the size of the storm. Furthermore, moving the domain is often not an option. For example, when running forecasts and climatologies, the domain needs to be fixed to ensure consistency and allow for automation of the study, i.e. not every case can be focused on as a case study. Therefore, three approaches, which do not involve moving the domain, were investigated: spectral nudging, relaxation zone adjustments, and changes to the LBC update frequency.

Spectral nudging was investigated because it constrains the LAM to maintain the large-scale information provided by the forcing data, without limiting the LAMs ability to build up the smaller scales. While it was able to correct the storm location compared to the "corner issue" affected simulation, it also introduced spatial blurring/smoothing effects which prevented the expected intensification of the storm in the WRF simulation (Figure 5). Similar effects were also found in Alexandru et al. (2009), who observed a reduction in the spectral power of the vorticity field when performing large-scale spectral nudging using the Canadian RCM (CRCM). This reduction could be associated with decreased cyclone intensities (Alexandru et al. (2009)). This highlights one difference when evaluating simulation setups for mean state investigations and for extreme events. LAM studies of mean state behaviour aim to add local information that should not significantly alter the large-scale flow, and therefore, nudging the model toward the forcing data can be beneficial. However, LAM studies of extreme events, such as storms, require the retention of small scale structures that enhance the large scale flow, which standard nudging techniques will often smooth out, by nudging towards the forcing data. This is because, nudging reinforces the mean state behaviour, which can be useful for long-term mean climate studies, but must be used with care when focusing on extreme events, such as storms. Spectral nudging seeks to limit the smoothing of small scale features through its wave-length cutoff. The cutoff wavelength should be based on the reliability of the large scale forcing data. While the CFSv2 forecast product used as forcing data is provided every 0.5 degrees, the spectral atmospheric model behind the forecast product has a triangular truncation of T126 (Saha et al. (2014)), which is equivalent to approximately 100 km (Saha et al. (2014)). Based on this estimate, sufficiently resolved scales are only expected for wavelengths larger than 100 km, which makes "NUD100km" a fringe case until which spectral nudging would be meaningful. "NUD900km" improved the storm's location compared to "REF" (without nudging), suggesting that scales larger than 900 km are crucial for improving the storm location in this case. The only marginal differences seen between "NUD900km" and "NUD100km" with respect to the storm intensification indicate that the LAM still fails to build up crucial structures responsible for the storm deepening beyond what is already present in the forcing data when faced with the "corner issue".

Since the "corner issue" is related to the passing of a feature through the boundary of the model, adjustments to the lateral boundary relaxation zone have an impact on this process. Similar to spectral nudging, the relaxation zone generates spatial smoothing, but in this case only in an area next to the lateral boundary. By increasing the relaxation zone's width, it is possible to introduce the storm structure more gradually. By reducing the relaxation zone's width, it is possible to concentrate the forcing on a small band close to the boundary. This results in less smoothing/blurring in the interior of the model domain and higher storm intensification (cf. Figure 6d, Table 3). Spatial smoothing due to the relaxation zone is especially relevant in the context of the "corner issue" because the number of relaxation zone cells in the LBC boundary corner is affected by the relaxation zone layers from both adjacent edges. A doubling of the relaxation zone width from N_{relax} = 4 (default) to N_{relax} = 8 will double the relaxation zone layers at each adjacent edge, quadrupling the number of overlapping relaxation zone cells in the corner area. This significantly increases the number of cells where model relaxation in the boundary corner can take place.

The relaxation zone sensitivity analysis highlights also another challenge in connection with the relaxation, namely the presence of non-physical features as for example seen in the relative vorticity field along the southern "soft" border (Figure 7). These features were present in all simulations, but are clearest in "2xRelaxZone". While the presence of perturbations within the relaxation zone is observed also under normal conditions (see e.g. Warner et al. (1997), Davies (2014)), structures close to the LAM corner are especially vulnerable due to relaxation of the forcing data from two sides. This suggest that both the "hard" and "soft" borders need to be taken into account when introducing large scale features close to the lateral boundary corner. These effects turned out to be most problematic in "2xRelaxZone", since the increased relaxation zone width brought the affected area closer to the area of interest.

Increasing the temporal frequency of the LBCs was found to improve the introduction of the storm, and reduce the smoothing effects. Only the "REF-South" simulation had an SLP drop of similar magnitude to "CFSv2-3h" and "CFSv2-1h", but in "REF-South", significant storm deepening did not occur until 36 hours into the simulation. Both the location of the storm centre and the storm intensity are closer to the expected results obtained from "REF-South" when using the higher frequency LBC updates. The improvement seen in simulations with increased LBC update frequency is in line with previous studies such as Gustafsson (1990), Termonia (2003) and Termonia et al. (2009). In the case of "Christian", its fast movement further favours the use of high frequency LBC updates. The travel speed of the storm, in the time period of interest, is approximately 95 km h^{-1}, based on comparing the CFSv2 LMSLP locations in Table 4 and Table 5. Using the storm locations from the XWS data set suggests a travelling speed of 80 km h^{-1}. At 95 km h^{-1}, the storm would move approximately 570 km in the 6-hours between LBC updates in the default case. This is equivalent to approximately $32\Delta x$, and approximately three times the storm size based on the estimation in Section 5.1. Accordingly, it is a challenge for the LAM to develop the necessary small-scale structures, since the system passes the model domain so quickly, not allowing the time necessary for the model to adjust to the new large-scale features.

When storm locations and distances are evaluated, the origin of the data sets must be kept in mind. Both CFSv2 products and XWS are based on simulations with coarse horizontal resolution. This makes it difficult to specify a "true" storm location. A slight difference in the location of the LMSLP can already have a significant effect on the absolute distance in kilometres. In relation to grid point distances however, the differences are rather small. The distances between LMSLP in CFSv2 and XWS as stated in Table 4 (130 km) and Table 5 (220 km) are equivalent to approximately two to four grid points.

The comparison with the buoy locations shows that the impact of the introduction of "Christian" into WRF was found to be largest for locations near the storm (Figure 9). At locations away from the storm all simulations were in agreement, and performed reasonably well, highlighting that such a small and fast moving storm has little impact far away from the storm centre.

In addition to the model setups discussed in this study, a few additional setups could be worth exploring. For example, different horizontal resolutions of the forcing data could have an impact on the introduction of the storm to the model. Matte et al. (2017) showed that the relative change in resolution between the forcing data and the LAM (in their case the Canadian RCM5) influences the spatial spin-up of features away from the LBCs. In this study, WRF has a resolution of 18 km and CFSv2 is provided every 0.5 degree, resulting in a resolution jump between J=2.5 to 3.0. This resolution jump of factor three is also one of the recommended resolution jumps used within WRF i.e. between subsequent nested domains (see e.g. best practices by Gill and Pyle (2012)) and is therefore a quite representative resolution jump. The "J3" scenario in Matte et al. (2017) had a similar resolution jump. In that scenario, they estimated that the spatial spin-up of small scale structures in the relative vorticity field at 700 hPa was between 50-60 grid cells for an hourly update frequency and 80-90 grid cells for a 6 hourly update. Their spin-up region is measured from the "hard" border, i.e. including the Davies relaxation zone. In the current study, the LAM domain is rather small (150x100 grid points). Combined with the previously discussed spin-up challenges due to the fast travel speed of "Christian", it can be assumed that the current model will not fully develop the small-scale features, especially in the cases with an update every 6 hours. While an increase of the domain size is needed to cope with the additionally required spatial spin-up, the benefits have to be weighted against the added computational costs of larger domains. However, the question of how the spatial spin-up of small-scales affects the introduction of the larger scale structures in this case remains for future work.

Overall, the results suggest that using a higher update frequency is the best approach for introducing storms into the model domain. However, that requires higher resolution data to be available, which is not always the case. When higher frequency data is not available, spectral nudging provides a method of correcting spatial distortions, but comes at the expense of spatial smoothing. Alternatively, if the model domain is relatively large and the focus area of interest is sufficiently far away from the border, targeted restarting of the simulation, as presented in Termonia et al. (2009) could be used. Instead of introducing the large-scale structure from the outside, via the LBCs, targeted restarts allow the model to be initialised with the large-scale structure already in the model domain. This however requires enough domain space and simulation time to spin up the smaller-scales that were lost due to the restart (Termonia et al. (2009)).

7 | CONCLUSION

Methods covering spatial and temporal adjustments are investigated to explore the challenge of introducing fast moving large-scale meteorological information into a limited area model. This study highlights specific challenges related to the storm passing through the lateral boundary corner. While reallocating the domains for each particular simulation is straightforward, it is of limited use for general investigations. Spectral nudging provides a useful tool to tackle spatial distortions, but needs to be be weighted against the related spatial smoothing with its negative effects on storm intensification. This emphasises that studies of extremes require a different LBC introduction strategy compared to studies of mean state investigations, where additional spatial smoothing is less influential. An increased update frequency of the lateral boundary conditions is shown to be very crucial and efficient in the situation of fast propagating systems. It reduces effects of artificially created distortions and smoothing caused by temporal interpolation and is therefore the recommended method for addressing the "corner issue" if high temporal resolution data is available.

acknowledgements

Great thanks goes to Danish ForskEL project XWiWA (PSO-12020) and OffshoreWake (PSO-12521) and the people and institutions behind the Extreme Wind Storms Catalogue providing the meteorological details of the investigated storm. Point measurements used were made available by the EMODnet Physics project, www.emodnet-physics.eu/map, funded by the European Commission Directorate General for Maritime Affairs and Fisheries. The

Climate Forecast System Version 2 Forecast Products used in this publication are downloaded from UCAR/NCAR Research Data Archive. The first author likes to thank the researchers at the Mesoscale & Microscale Meteorology Division at NCAR for their help. The fourth author acknowledges “Wave Boundary Layer Model in Typhoon Condition and its Application in Wind-Wave Coupling System, GY0219Q06". The first author thanks also the developer team behind the python packages *matplotlib* (Hunter (2007)) and *cartopy* (Met Office (2010 - 2015)). The authors have no conflict of interest to report.

references

AIR Worldwide (cited 2018) Air Loss Estimates in Real Time (ALERT) online service. URL: `http://alert.air-worldwide.com/EventSummary.aspx?e=723&tp=72&c=1`.

ALADIN International Team (1997) The ALADIN project : Mesoscale modelling seen as a basic tool for weather forecasting and atmospheric research. *WMO Bull.*, **46**, 317–324.

Alexandru, A., de Elia, R., Laprise, R., Separovic, L. and Biner, S. (2009) Sensitivity Study of Regional Climate Model Simulations to Large-Scale Nudging Parameters. *Mon. Wea. Rev.*, **137**, 1666–1686.

Chikhar, K. and Gauthier, P. (2017) Impact of Lateral Boundary Conditions on Regional Analyses. *Mon. Wea. Rev.*, **145**, 1361–1379.

Consortium for Small Scale Modeling (COSMO) (cited 2018) Operational Applications within COSMO. URL: `http://www.cosmo-model.org/content/tasks/operational/default.htm`.

Davies, H. C. and Turner, R. E. (1977) Updating prediction models by dynamical relaxation: an examination of the technique. *Quart. J. Roy. Meteor. Soc.*, **103**, 225–245.

Davies, T. (2014) Lateral boundary conditions for limited area models. *Quart. J. Roy. Meteor. Soc.*, **140**, 185–196. URL: `http://doi.wiley.com/10.1002/qj.2127`.

Dee, D. P., Uppala, S. M., Simmons, A. J., Berrisford, P., Poli, P., Kobayashi, S., Andrae, U., Balmaseda, M. A., Balsamo, G., Bauer, P., Bechtold, P., Beljaars, A. C. M., van de Berg, L., Bidlot, J., Bormann, N., Delsol, C., Dragani, R., Fuentes, M., Geer, A. J., Haimberger, L., Healy, S. B., Hersbach, H., Hólm, E. V., Isaksen, L., Kållberg, P., Köhler, M., Matricardi, M., McNally, A. P., Monge-Sanz, B. M., Morcrette, J.-J., Park, B.-K., Peubey, C., de Rosnay, P., Tavolato, C., Thépaut, J.-N. and Vitart, F. (2011)

The ERA-Interim reanalysis: configuration and performance of the data assimilation system. *Quart. J. Roy. Meteor. Soc.*, **137**, 553–597.

Denis, B., Laprise, R., Caya, D. and Côté, J. (2002) Downscaling ability of one-way nested regional climate models: The Big-Brother Experiment. *Climate Dyn.*, **18**, 627–646.

Dudhia, J. (2017) Overview of WRF physics. In *SUMMER 2017 BASIC WRF TUTORIAL*. URL: `https://www2.mmm.ucar.edu/wrf/users/tutorial/201707/physics.pdf`.

EMODnet (cited 2018) The european marine observation and data network. URL: `www.emodnet-physics.eu/Portal`.

Feser, F. (2006) Enhanced detectability of added value in limited-area model results separated into different spatial scales. *Mon. Wea. Rev.*, **134**, 2180–2190.

Gill, D. and Pyle, M. (2012) Nesting in WRF. In *JANUARY 2012 BASIC WRF TUTORIAL*. URL: `https://www2.mmm.ucar.edu/wrf/users/tutorial/201201/WRFNesting.ppt.pdf`.

Giorgi, F. (2019) Thirty Years of Regional Climate Modeling: Where Are We and Where Are We Going next? *J. Geophys. Res.*, **124**, 5696–5723.

Gómez, B. and Miguez-Macho, G. (2017) The impact of wave number selection and spin-up time in spectral nudging. *Quart. J. Roy. Meteor. Soc.*, **143**, 1772–1786.

Gustafsson, N. (1990) Sensitivity of limited area model data assimilation to lateral boundary condition fields. *Tellus*, **42**, 109–115.

Gustafsson, N., Källén, E. and Thorsteinsson, S. (1998) Sensitivity of forecast errors to initial and lateral boundary conditions. *Tellus*, **50**, 167–185.

Haeseler, S. and Lefebvre, C. (2013) Heavy storm CHRISTIAN on 28 October 2013. *Tech. Rep. October*, German Meteorological Office. URL: `https://www.dwd.de/EN/ourservices/specialevents/storms/20131028_CHRISTIAN_europe_en.pdf?__blob=publicationFile&v=7`.

Hewson, T., Magnusson, L., Breivik, O., Prates, F., Tsonevsky, I. and de Vries, H. (2014) Windstorms in northwest Europe in late 2013. In *ECMWF Newsletter* (ed. Riddaway;Bob), no. 139 in ECMWF Newsletter, chap. Meteorolog, 22–28. Reading, Berkshire RG2 9AX, UK: European Centre for Medium-Range Weather Forcaset (ECMWF).

Hoskins, B. J. and Hodges, K. I. (2002) New Perspectives on the Northern Hemisphere Winter Storm Tracks. *J. Atmos. Sci.*, **59**, 1041–1061.

Hunter, J. D. (2007) Matplotlib: A 2d graphics environment. *Comput. Sci. Eng.*, **9**, 90–95.

Iacono, M. J., Delamere, J. S., Mlawer, E. J., Shephard, M. W., Clough, S. A. and Collins, W. D. (2008) Radiative forcing by long-lived greenhouse gases: Calculations with the AER radiative transfer models. *J. Geophys. Res.*, **113**, D13103.

Imberger, M. (2017) *Modeling rough weather over the North Sea - using COAWST for offshore wind energy applications*. Master thesis report, Wind Energy Department, Technical University of Denmark, Denmark. URL: `http://production.datastore.cvt.dk/oafilestore?oid=596dea925010df6dc860f342&targetid=596dea925010df6dc860f345`.

Kain, J. S. (2004) The Kain–Fritsch Convective Parameterization: An Update. *J. Appl. Meteor.*, **43**, 170–181.

Källén, E. (1996) HIRLAM DOCUMENTATION MANUAL. *Tech. rep.*, HIRLAM Consortium. URL: `http://hirlam.org/index.php/hirlam-documentation/doc_download/1531-hirlam-documentation-system-2-5-june-1996`.

Laprise, R. (2003) Resolved Scales and Nonlinear Interactions in Limited-Area Models. *J. Atmos. Sci.*, **60**, 768–779.

Larsén, X., Rodolfo, B., Du, J., Kelly, M. C., Kofoed-Hansen, H., Larsen, S. E., Karagali, I., Badger, M., Hahmann, A. N., Imberger, M., Tornfeldt, S. J., Jackson, S., Volker, P., Svenstrup Petersen, O., Jenkins, A. and Graham, A. (2017a) Extreme winds and waves for offshore turbines: Coupling atmosphere and wave modeling for design and operation in coastal zones. *Tech. rep.*, Technical University of Denmark, Roskilde, Denmark. URL: `https://orbit.dtu.dk/ws/files/139272513/FinalReport_PSO12020_XWiWa_20171031.pdf`.

Larsén, X. G., Du, J., Bolaños, R., Imberger, M., Kelly, M. C., Badger, M. and Larsen, S. (2019) Estimation of offshore extreme wind from wind–wave coupled modeling. *Wind Energy*, **22**, 1043–1057.

Larsén, X. G., Du, J., Bolaños, R. and Larsen, S. (2017b) On the impact of wind on the development of wave field during storm Britta. *Ocean Dynam.*, **67**, 1407–1427.

Matte, D., Laprise, R., Thériault, J. M. and Lucas-Picher, P. (2017) Spatial spin-up of fine scales in a regional climate model simulation driven by low-resolution boundary conditions. *Climate Dyn.*, **49**, 563–574.

Met Office (2010 - 2015) *Cartopy: a cartographic python library with a matplotlib interface*. Exeter, Devon. URL: `http://scitools.org.uk/cartopy`.

Miguez-Macho, G., Stenchikov, G. L. and Robock, A. (2004) Spectral nudging to eliminate the effects of domain position and geometry in regional climate model simulations. *J. Geophys. Res.*, **109**, 1–15.

Nakanishi, M. and Niino, H. (2006) An improved Mellor-Yamada Level-3 model: Its numerical stability and application to a regional prediction of advection fog. *Bound.-Layer Meteorol.*, **119**, 397–407.

Roberts, J. F., Champion, A. J., Dawkins, L. C., Hodges, K. I., Shaffrey, L. C., Stephenson, D. B., Stringer, M. A., Thornton, H. E. and Youngman, B. D. (2014) The XWS open access catalogue of extreme European windstorms from 1979 to 2012. *Nat. Hazard Earth Sys.*, **14**, 2487–2501.

Saha, S., Moorthi, S., Wu, X., Wang, J., Nadiga, S., Tripp, P., Behringer, D., Hou, Y.-T., Chuang, H.-y., Iredell, M., Ek, M., Meng, J., Yang, R., Mendez, M. P., van den Dool, H., Zhang, Q., Wang, W., Chen, M. and Becker, E. (2011) Ncep climate forecast system version 2 (cfsv2) 6-hourly products. URL: `https://doi.org/10.5065/D61C1TXF`. Last accessed: 20 Januar 2017.

— (2014) The NCEP Climate Forecast System Version 2. *J. Climate*, **27**, 2185–2208.

Skamarock, W. C. (2004) Evaluating Mesoscale NWP Models Using Kinetic Energy Spectra. *Mon. Wea. Rev.*, **132**, 3019–3032.

Skamarock, W. C., Klemp, J. B., Dudhia, J., Gill, D. O., Barker, D. M., Duda, M. G., Huang, X.-Y., Wang, W. and Powers, J. (2008) A Description of the Advanced Research WRF Version 3. *Tech. rep.*, Mesoscale and Microscale Meteorology Division, National Center for Atmospheric Research, Boulder, Colorado, USA. URL: `http://dx.doi.org/10.5065/D68S4MVH`.

Stauffer, D. R. and Seaman, N. L. (1990) Use of four-dimensional data assimilation in a limited-area mesoscale model. Part I: experiments with synoptic-scale data.

von Storch, H., Langenberg, H. and Feser, F. (2000) A Spectral Nudging Technique for Dynamical Downscaling Purposes. *Mon. Wea. Rev.*, **128**, 3664–3673.

Termonia, P. (2003) Monitoring and Improving the Temporal Interpolation of Lateral-Boundary Coupling Data for Limited-Area Models. *Mon. Wea. Rev.*, **131**, 2450–2463.

Termonia, P., Deckmyn, A. and Hamdi, R. (2009) Study of the Lateral Boundary Condition Temporal Resolution Problem and a Proposed Solution by Means of Boundary Error Restarts. *Mon. Wea. Rev.*, **137**, 3551–3566.

Tewari, M., Chen, F., Wang, W., Dudhi, J., LeMone, M., Mitchell, K., Ek, M., Gayno, G., Wegiel, J. and Cuenca, R. H. (2004) Implementation and verification of the unified Noah land surface model in the WRF model. In *20th Conference on Weather Analysis and Forecasting/16th Conference on Numerical Weather Prediction*. URL: `http://n2t.net/ark:/85065/d7fb523p`.

Thompson, G., Field, P. R., Rasmussen, R. M. and Hall, W. D. (2008) Explicit Forecasts of Winter Precipitation Using an Improved Bulk Microphysics Scheme. Part II: Implementation of a New Snow Parameterization. *Mon. Wea. Rev.*, **136**, 5095–5115.

Tudor, M. and Termonia, P. (2010) Alternative Formulations for Incorporating Lateral Boundary Data into Limited-Area Models. *Mon. Wea. Rev.*, **138**, 2867–2882.

UCAR/NCAR/CISL/TDD (2017) The NCAR Command Language (Version 6.4.0). URL: http://www.ncl.ucar.edu/.

Waldron, K. M., Paegle, J. and Horel, J. D. (1996) Sensitivity of a Spectrally Filtered and Nudged Limited-Area Model to Outer Model Options. *Mon. Wea. Rev.*, **124**, 529–547.

Warner, T. T., Peterson, R. A. and Treadon, R. E. (1997) A Tutorial on Lateral Boundary Conditions as a Basic and Potentially Serious Limitation to Regional Numerical Weather Prediction. *Bull. Amer. Meteor. Soc.*, **78**, 2599–2617.

Xu, K.-M. and Randall, D. A. (1996) A Semiempirical Cloudiness Parameterization for Use in Climate Models. *J. Atmos. Sci.*, **53**, 3084–3102.

XWS Catalogue (cited 2019) Extreme Wind Storms Catalogue. URL: http://www.europeanwindstorms.org/. Copyright Met Office, University of Reading and University of Exeter. Licensed under Creative Commons CC BY 4.0 International Licence: http://creativecommons.org/licenses/by/4.0/deed.en_GB.

TABLE 1 Summary of model settings regarding spatial and temporal parameters and physics

Argument	Value
WRF Version	3.7.1
Forcing data	CFSv2
Spatial Settings	
Domain size	2700 km x 1800 km
Horizontal resolution	$\Delta x = \Delta y = 18$ km
Grid points	150 x 100
Vertical model level	52
Temporal Settings	
Simulation time (incl. spin-up)	36 h
Spin-up time	12 h
LBC update frequency	every 6 hours
Physics	
Microphysics	New Thompson
Radiation	RRTMG
Cumulus parameterisation	Kain-Fritsch
Land surface	Noah LSM
PBL-Scheme	MYNN

TABLE 2 Overview about all performed simulations with their identifier used to address the simulation in the text and a list of key elements characterising the simulation.

Identifier	Characteristics
REF	reference simulation, faces "corner issue", obtained by running WRF with the solid domain in Figure 1, 6 hourly LBC update
REF-South	like "REF" but with a southwards shifted domain to avoid "corner issue", corresponds to dashed domain in Figure 1, 6 hourly LBC update
NUD100km	like "REF" but with spectral nudging of U,V, θ and geopotential height, nudging above 100 km affects all vertical model levels above the planetary boundary layer, 6 hourly LBC update
HalfRelaxZone	like "REF" but with 50% relaxation zone width (2 instead of 4 grid cells), 6 hourly LBC update
2xRelaxZone	like "REF" but with doubled relaxation zone width (8 instead of 4 grid cells), 6 hourly LBC update
CFSv2-3h	like "REF" but with 3-hourly update of the lateral boundary conditions (instead of every 6 hours)
CFSv2-1h	like "REF" but with hourly update of the lateral boundary conditions (instead of every 6 hours)

TABLE 3 Estimated local minimum sea level pressure obtained from the WRF simulations, the CFSv2 forcing data and the XWS catalogue at 1800 UTC 27 October 2013 and 0000 UTC 28 October 2013. Values in **bold** (*italic*) indicate values which are at least 3 hPa lower (higher) than the value of the CFSv2 forcing data.

Identifier	Local minimum sea level pressure (in hPa) at	
	1800 UTC 27 Oct 2013	0000 UTC 28 Oct 2013
REF	*992*	986
REF-South	989	**981**
NUD100km	*991*	985
HalfRelaxZone	990	983
2xRelaxZone	*992*	*987*
CFSv2-3h	987	**981**
CFSv2-1h	**985**	**979**
CFSv2	988	984
XWS	990	983

TABLE 4 Estimated location of local minimum sea level pressure (LMSLP) obtained from the WRF simulations, the CFSv2 forcing data and the XWS catalogue at 1800 UTC 27 October 2013. The great circle distances to XWS (d_{XWS}) and CFSv2 (d_{CFSv2}) locations rounded to closest full 10 km are given as well.

Identifier	**Location of LMSLP (1800 UTC 27 October 2013)**		
	location	d_{CFSv2} [km]	d_{XWS} [km]
REF	49.08°N 10.83°W	30	110
REF-South	49.14°N 9.83°W	50	190
NUD100km	49.68°N 9.68°W	100	220
HalfRelaxZone	49.13°N 10.33°W	20	150
2xRelaxZone	48.06°N 11.10°W	110	120
CFSv2-3h	48.92°N 10.79°W	20	110
CFSv2-1h	48.90°N 11.04°W	40	90
CFSv2	49.0°N 10.5°W	-	130
XWS	48.8°N 12.3°W	130	-

TABLE 5 Estimated location of local minimum sea level pressure (LMSLP) obtained from the WRF simulations, the CFSv2 forcing data and the XWS catalogue at 0000 UTC 28 October 2013. The great circle distances to XWS (d_{XWS}) and CFSv2 (d_{CFSv2}) locations rounded to closest full 10 km are given as well.

Identifier	**Location of LMSLP (0000 UTC 28 October 2013)**		
	location	d_{CFSv2} [km]	d_{XWS} [km]
REF	50.79°N 5.47°W	160	60
REF-South	51.66°N 3.18°W	30	250
NUD100km	51.69°N 3.18°W	30	310
HalfRelaxZone	51.50°N 4.22°W	50	180
2xRelaxZone	51.54°N 2.64°W	60	270
CFSv2-3h	51.69°N 3.45°W	20	230
CFSv2-1h	51.86°N 3.19°W	50	260
CFSv2	51.5°N 3.5°W	-	220
XWS	50.4°N 6.1°W	220	-

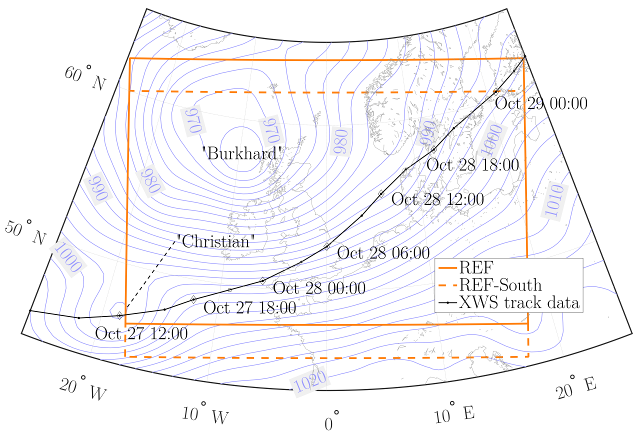

FIGURE 1 Blue: Contours of modelled mean sea level pressure (hPa) obtained from CFSv2 6-h forecast data at 1200 UTC 27 October 2013. Contours are drawn every 2 hPa. The locations of the two low pressure systems "Burkhard" and "Christian" are indicated. Black line: Extract of the storm track "Christian" covering 0600 UTC 27 October 2013 to 0600 UTC 29 October 2013 from the XWS Catalogue (cited 2019). Due to spatial constraints, dates are represented in the short form MMM DD HH:MM. All dates are given in UTC. The hollow data point 'o' is indicating a missing data point at 2100 UTC 27 October 2013 in the data set. Orange: WRF domains "REF" (solid) and "REF-South" (dashed).

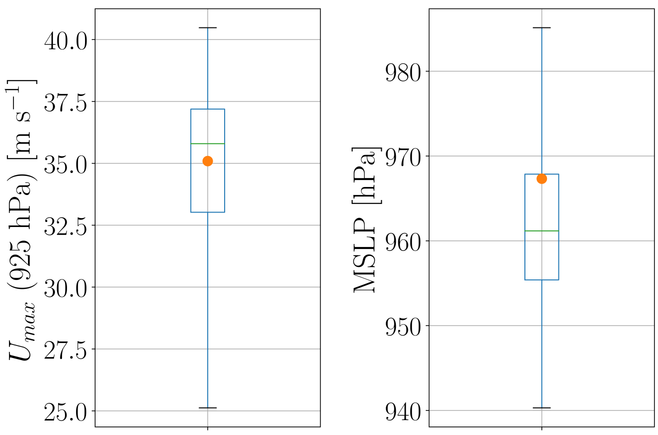

FIGURE 2 Box plots of life-time lowest minimum sea level pressure (MSLP) and life-time highest maximum wind speed (U_{max}) at 925 hPa level determined from all listed storms in the XWS catalogue (52 in total): median values (green), the interquartile range (IQR, blue box) as well as global minimum and maximum (whiskers). The orange dots represent the extreme values of storm “Christian”.

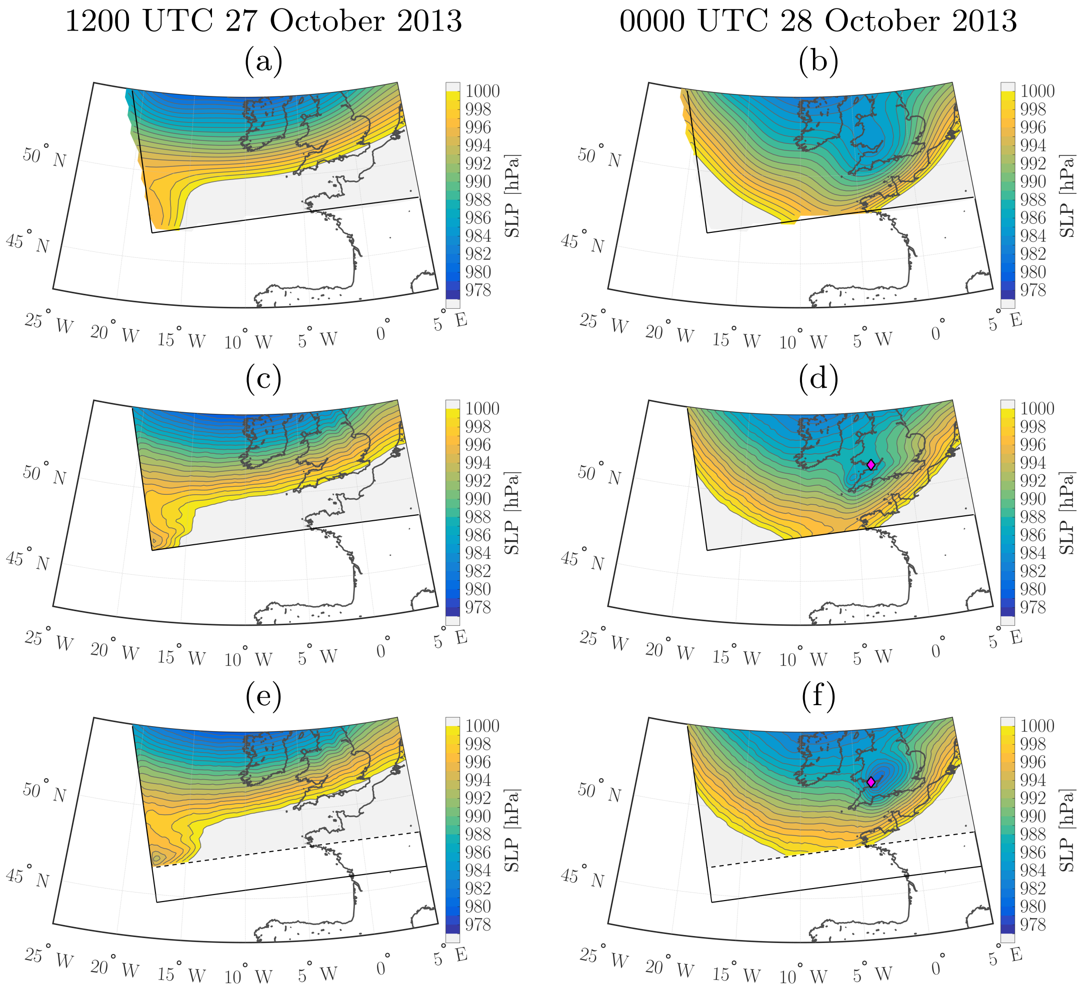

FIGURE 3 Contour plot of modelled sea level pressure field obtained at 1200 UTC 27 October 2013 (left column) and 0000 UTC 28 October 2013 (right column). (a),(b): Sea level pressure field obtained from the CFSv2 forcing data. The black frame indicates the location of the WRF reference domain. (c),(d): Results obtained from "REF". (e),(f): Results obtained from "REF-South". The pink diamond in (d) and (f) marks the position of the minimum sea level pressure determined from CFSv2 data. The dashed line in the bottom row indicates the southern border of "REF" used in the other simulations. Values beyond the given limits are depicted in grey.

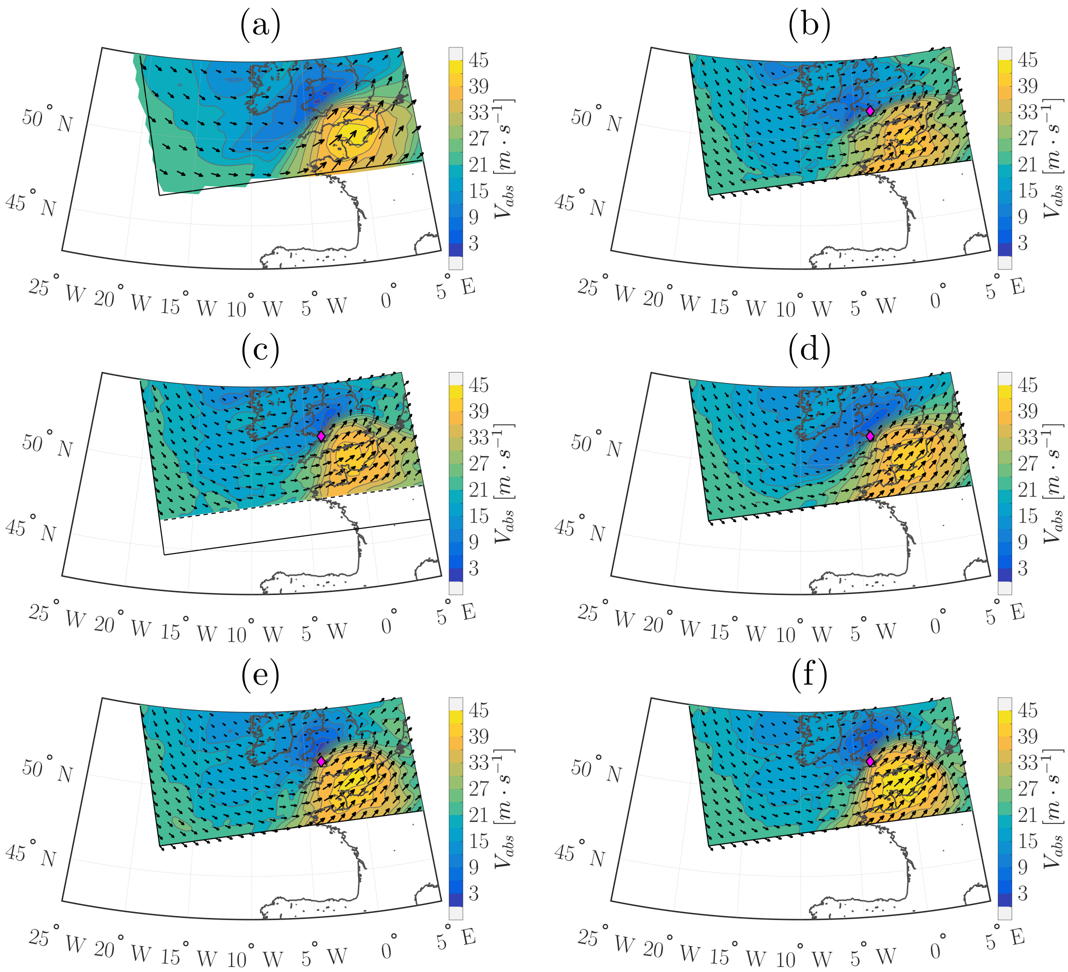

FIGURE 4 Modelled absolute wind speed (contours) and wind direction (vectors) obtained from (a) CFSv2 forcing data in comparison with the WRF results from (b) "REF", (c) "REF-South", (d) "NUD100km", (e) "CFSv2-3h" and (f) "CFSv2-1h". All values are obtained at 850 hPa at 0000 UTC 28 October 2013. The pink diamond indicates the location of the minimum sea level pressure determined in CFSv2. The dashed line in (c) indicates the southern border of "REF" used in the other simulations.

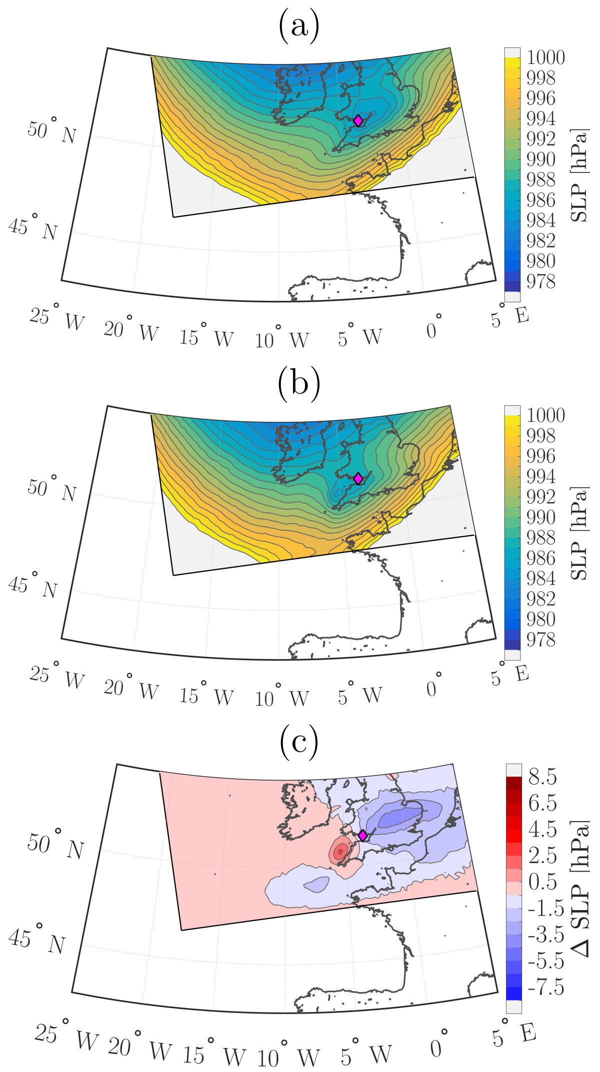

FIGURE 5 Contour plot of modelled sea level pressure field obtained from (a) "NUD100km" and (b) "REF" as well as (c) the difference between the two ("NUD100km" minus "REF"). All fields are determined at 0000 UTC 28 October 2013. The pink diamond indicates the location of the minimum sea level pressure determined in CFSv2. Values beyond the given limits are depicted in grey.

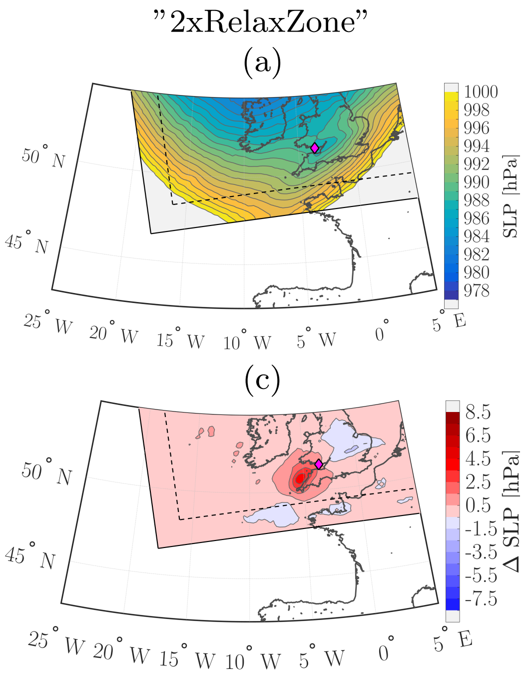

FIGURE 6 Contour plot of modelled sea level pressure determined by (a) "2xRelaxZone" and (b) "HalfRelaxZone" as well as (c) "2xRelaxZone" minus "REF" and (d) "HalfRelaxZone" minus "REF". All fields are determined at 0000 UTC 28 October 2013. Positive ΔSLP indicates higher SLP values in "2xRelaxZone" respectively "HalfRelaxZone". The pink diamond marks the location of the minimum sea level pressure determined in CFSv2. The dashed lines depict the location of the margin of the relaxation zone in "2xRelaxZone" respectively "HalfRelaxZone". Values beyond the given limits are depicted in grey.

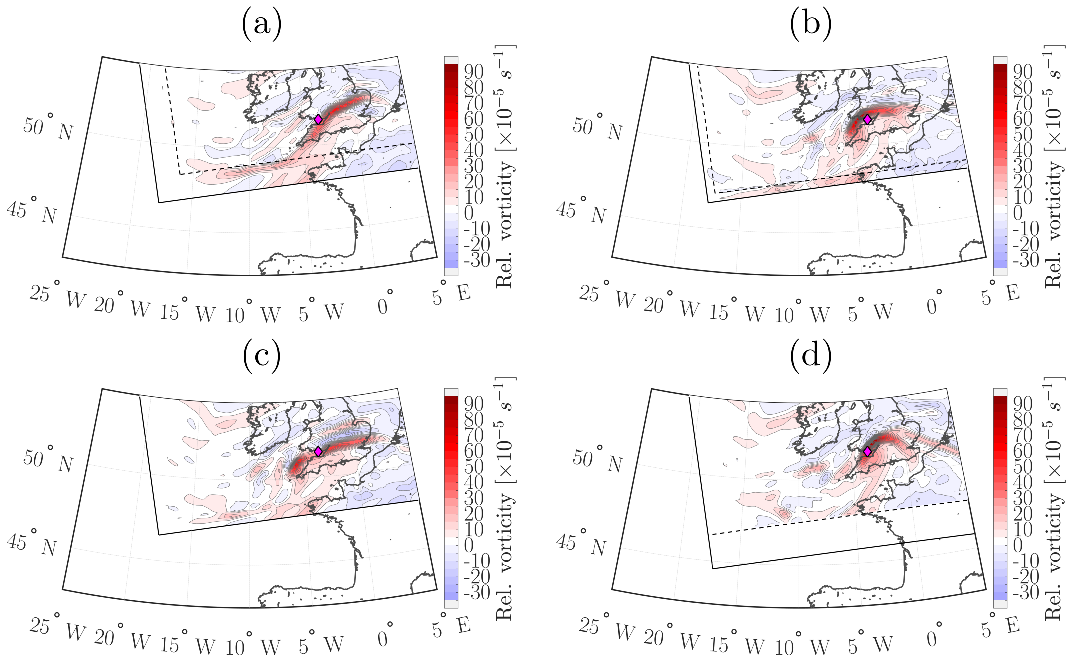

FIGURE 7 Contour plot of modelled relative vorticity at 850 hPa determined by (a) "2xRelaxZone" and (b) "HalfRelaxZone" compared to (c) "REF" and (d) "REF-South". All fields are determined at 0000 UTC 28 October 2013. The pink diamond indicates the location of the minimum sea level pressure determined in CFSv2. The dashed lines in (a),(b) depict the location of the margin of the relaxation zone while the dashed line in (d) marks the southern domain border of "REF" which is used in the other simulations.

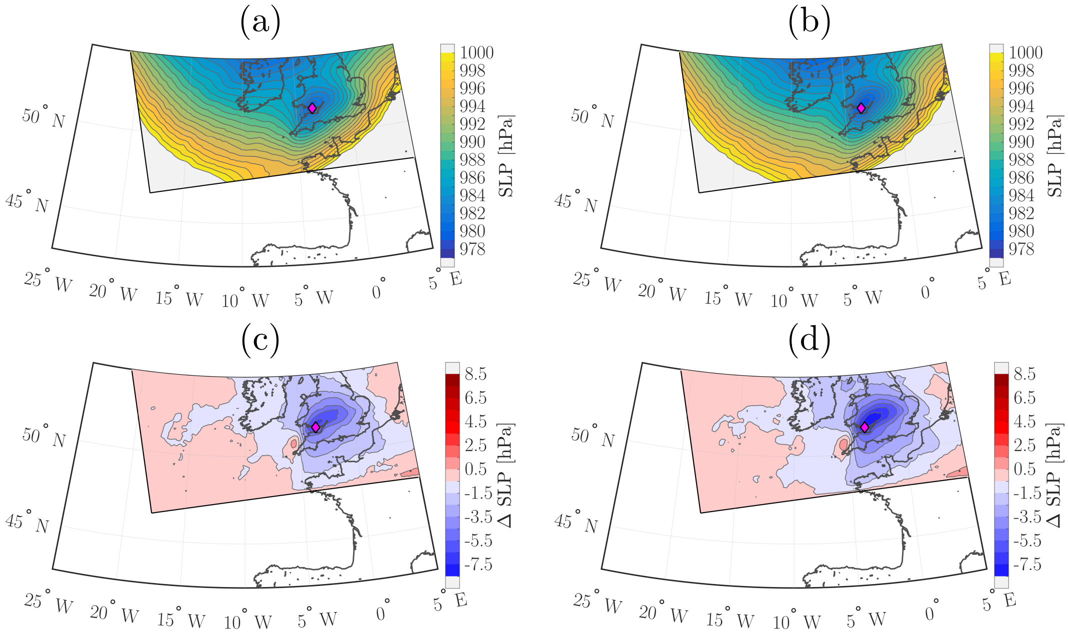

FIGURE 8 Contour plot of modelled SLP obtained from (a) "CFSv2-3h" (update every 3 hours), (b) "CFSv2-1h" (update every hour) and SLP difference between (c) "CFSv2-3h" and "REF" and (d) "CFSv2-1h" and "REF". All fields are determined at 0000 UTC 28 October 2013. The pink diamond marks the location of the minimum sea level pressure determined in CFSv2. Positive ΔSLP indicates higher SLP values in "CFSv2-3h" respectively "CFSv2-1h". Values beyond the given limits are depicted in grey.

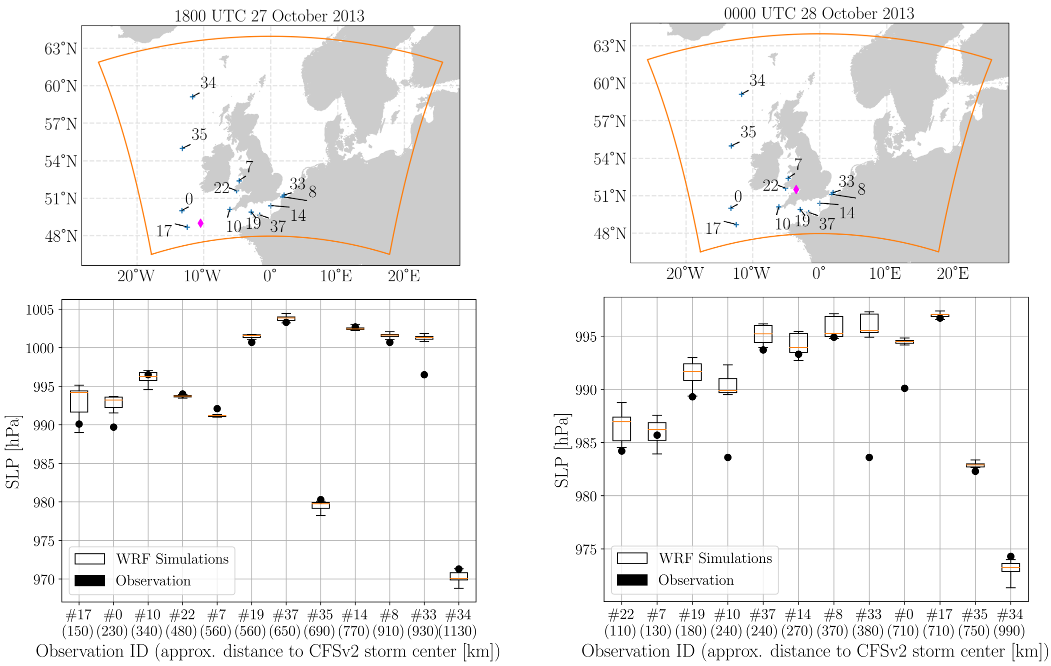

FIGURE 9 Top row: Location of the CFSv2 storm centre (pink diamond) at 1800 UTC 27 October 2013 (left) and 0000 UTC 28 October 2013 (right) in relation to the buoys (blue plus) and the WRF domain (orange frame). Bottom row: Box plot showing median (orange), first and third quartile (black box) and min/max values (whiskers) of SLP estimation of all seven simulations at the list of buoy stations at 1800 UTC 27 October 2013 (left) and 0000 UTC 28 October 2013 (right). The buoys are sorted with increasing distance to the CFSv2 storm centre at that point in time. The black dots depict the measured value for the SLP at the given buoy.

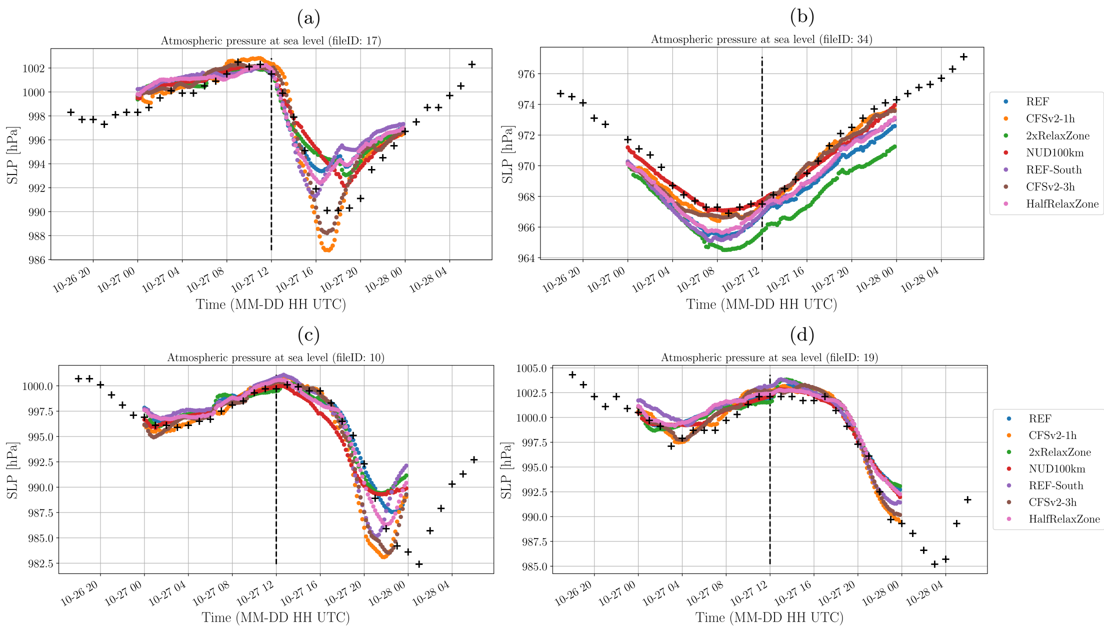

FIGURE 10 Comparison between simulated (dots) and measured (black plus) sea level pressure time series at buoy station (a) #17 , (b) #34, (c) #10 and (d) #19. The dashed line represents the approximate time stamp when the storm centre is visible at the south-west corner of the WRF domain.

APPENDIX B
Investigation of Spatial and Temporal Wind Variability during Open Cellular Convection with the Model For Prediction Across Scales (MPAS) in Comparison with Measurements

The following manuscript is the latest submitted version of:

Imberger, M., Larsén, X. G., Davis, N. **Investigation of Spatial and Temporal Wind Variability during Open Cellular Convection with the Model For Prediction Across Scales (MPAS) in Comparison with Measurements**. Boundary-Layer Meteorology *(accepted with minor revisions)*

Boundary-Layer Meteorology manuscript No.
(will be inserted by the editor)

Investigation of Spatial and Temporal Wind Variability during Open Cellular Convection with the Model For Prediction Across Scales (MPAS) in Comparison with Measurements

Marc Imberger · Xiaoli Guo Larsén · Neil Davis

Received: DD Month YEAR / Accepted: DD Month YEAR

Abstract Open cellular convection (OCC) over, for example, the North Sea is often observed in connection with cold-air outbreaks. It is accompanied by large temporal and spatial fluctuations in wind speed, which affects offshore wind energy in the area. This study uses the global Model for Prediction Across Scales (MPAS), with regional mesh refinement down to convection-permitting scales of 2 km, to simulate an episode of OCC in the North Sea, with a focus on wind variability. Modelled data are combined with satellite retrieved winds and point measurements to investigate the spatial and temporal fluctuations of offshore winds under OCC conditions from a synoptic to mesoscale perspective and to examine MPAS's ability to represent the OCC structures and wind fluctuations. It is shown that MPAS can simulate realistic OCC structures and mesoscale wind speed fluctuations within the limits set by the effective model resolution. Under OCC conditions, significant differences from climatological conditions are found in the spatial wind speed power spectrum and in 10-minute wind speed step changes. The very high horizontal mesh cell spacing in the refinement region of 2 km and the focus on OCC wind variability makes this the first investigation of this kind in MPAS with mesh refinement.

Keywords Convection permitting, Global model, MPAS, Open cells, Wind variability

Marc Imberger (corresponding author)
Wind Energy Department, Technical University of Denmark, Frederiksborgvej 399, 4000 Roskilde, Denmark
E-mail: maim@dtu.dk

Xiaoli Guo Larsén
Wind Energy Department, Technical University of Denmark, Frederiksborgvej 399, 4000 Roskilde, Denmark

Neil Davis
Wind Energy Department, Technical University of Denmark, Frederiksborgvej 399, 4000 Roskilde, Denmark

1 Introduction

Open cellular convection (OCC) is a specific type of mesoscale cellular convection often formed in connection with cold-air outbreaks when cold air is advected over warmer water surfaces (Atkinson and Zhang, 1996). It is characterised by a distinct pattern of convective activity with narrow updraft regions at the cloudy cell borders that are surrounded by weaker and broader downdraft regions in the cell centre (Atkinson and Zhang, 1996; Feingold et al., 2015). While the overall spatial diameters of the cells vary with latitude, they are generally on the order of 20 to 50 km (Bakan and Schwarz, 1992). From an offshore wind energy perspective, the relatively large temporal and spatial fluctuations in wind speed and wind direction, caused by the moving OCC structures, are especially important. Larsén et al. (2017b) found a 5 m s^{-1} spatial variation of the wind speed over 3 km based on Synthetic Aperture Radar (SAR) images for the OCC related to 2006's storm 'Britta'.

OCC can have especially large impacts on regions with a high spatial concentration of turbines, either very large wind farms or wind farm clusters. Due to the close proximity of the turbines in these configurations, the wind fluctuations will cause even larger fluctuations in aggregated power due to the high spatial correlation of the OCC phenomena (Akhmatov et al., 2007; Vincent and Trombe, 2017; Göçmen et al., in press 2020). This has direct consequences on the power system, which needs to balance the fluctuations for example by means of power reserves (Sørensen et al., 2008; Vigueras-Rodríguez et al., 2010).

OCC conditions are common in both the Norwegian and North Sea. Busack et al. (1985)'s inspection of NOAA 6 satellite images over the Norwegian Sea revealed OCC patterns in 111 out of 610 investigated days (1 May 1980 to 31 December 1981). Larsén et al. (2017a)'s North Sea storm climatology study detected OCC in 45% of their 429 investigated storm days. Since the North Sea is currently the main development region for offshore wind energy in Europe (WindEurope, 2020), OCC will have significant effects on wind power for much of Europe. Vincent (2010) and Vincent et al. (2012) found that OCC contributes significantly to the mesoscale variability experienced at the Danish wind farm 'Horns Rev I' by looking at wind speed fluctuations of scales of one hour and larger based on measurements and simulations with the limited area Weather Research and Forecasting model (WRF, Skamarock et al., 2008). Larsén et al. (2013)'s analysis of wind speed measurements during 18 days of OCC presence revealed significant contributions of OCC to wind fluctuations in the spectral gap region between the mesoscale and microscale and Larsén et al. (2019) showed that existing turbulence models underestimate variations in the wind speed in the lower frequencies if the increased variability in the mesoscale range due to OCC is not taken into account.

While previous investigations of OCC effects on wind speed fluctuations are based mainly on measurements and limited area mesoscale models, this study continues the investigation of OCC with a relatively new global circulation model that allows for regional refinement, namely the Model for Prediction Across Scales (MPAS, Skamarock et al., 2012, more details in Section 3.1) and complements the previous investigations from a synoptic to mesoscale perspective. MPAS has the advantage of consistent modelling across the globe, while the local refinement area allows higher resolution in the area of interest. This makes it possible to investigate not only the synoptic-scale frontal system, which drives the open cells, but also the open cell structures themselves without introducing challenges seen in limited area modelling due to the effects of lateral boundary conditions (e.g. Warner et al., 1997; Imberger et al., in press 2020) or sudden resolution jumps between nested domains (Park et al., 2014). MPAS allows the design of smooth transition zones from coarser to finer scales which reduces issues related to the spatial spin-up of small scale structures on inflow boundaries that are observed in limited area models with sharp resolution jumps (Park et al., 2014; Matte et al., 2017). All the above mentioned advantages motivate the use of the global model with regional refinement for this investigation. The methodology of gradual grid refinement in MPAS has already shown encouraging results in idealised simulations and real world applications with mesh refinement at hydrostatic scales (e.g. Ringler et al., 2011; Skamarock et al., 2012; Park et al., 2013, 2014; Hashimoto et al., 2016) and more recently also in MPAS studies involving local mesh refinements to convection-resolving scales (Fowler et al., 2016; Wong and Skamarock, 2016; Pilon et al., 2016; Hagos et al., 2018; Kramer et al., 2018; Huang et al., 2019; Schwartz, 2019; Zhao et al., 2019). Overall, MPAS is a relatively new model and only a limited number of studies have been performed with locally refined simulations down to convection-permitting scales and to the knowledge of the authors, this study is the first investigation of wind variability during OCC in MPAS with regional refinement. The objective of this study is to investigate the potential of MPAS for modelling OCC related spatial and temporal fluctuations of the wind speed with focus on their overall representativeness in the model. Forecasting of individual cells with exact timings is not the focus of this investigation, since it is beyond the expectations for a numerical weather prediction model. An episode of OCC over the North Sea area is simulated, which was selected based on the availability of a wide range of point measurements, cloud pictures and spatial near-surface wind speeds derived from SAR. The measurements are used to both characterise the OCC structures and to evaluate the model's capability to represent OCC and its associated impact on the wind field at the same time. To do so, a global mesh with a base horizontal mesh cell spacing of 55 km and refinement horizontal mesh cell spacing of 2 km (i.e. 55-2 km mesh) is developed. The design of the fine horizontal mesh cell spacing was inspired by the investigation of eight OCC events with the regional mesoscale model WRF in Vincent (2010), which found that a spatial grid spacing of 2 km was required to generate realistic cell patterns and to simulate associated wind fluctuations that agree reasonably well with observations from 'Horns Rev I'. With the fine-scale horizontal mesh cell spacing of 2 km, the mesh has smaller cell spacing in the refinement region than other MPAS meshes currently used in the literature.

The paper is structured as follows: A description of the measurements and the methods is provided in Sect. 2 and Sect. 3, respectively. Results are presented in Sect. 4. A discussion of the results is provided in Sect. 5 and the article finalises with concluding statements in Sect. 6.

2 Measurements

2.1 Satellite Products

The investigated OCC case was observed behind a cold front in December 2010, which was the second event of a period of severe weather affecting the United Kingdom (UK) during the winter season 2010/2011 (Prior and Kendon, 2011). During 16 December 2010, cold air from the arctic region was moving southwards/south-eastwards across the UK and the North Sea region. To provide a synoptic overview, Figure 1a shows the surface analysis chart from UK Met Office at 16 December 2010, 1200 UTC describing the synoptic situation and the location of the frontal zone. Satellite cloud images are used to qualitatively assess the location of the frontal zone and the distribution and size of the convective cells. The images are obtained from the *NERC Satellite Receiving Station, University of Dundee*[1] satellite image archive. Figure 1b shows the cloud picture from the NOAA-19 satellite for 16 December 2010 at 1244 UTC. In this figure, the characteristic hexagonal patterns of open cellular structures (e.g. Agee, 1987) can be seen. The synoptic scale cloud band, associated with the cold front (Fig. 1a), is visible over Denmark and north Germany. Visual inspection of two additional NOAA-19 satellite images over the region (1650 UTC and 1830 UTC) shows that the OCC conditions persist over most of the North Sea area until at least 16 December 2010, 1830 UTC (not shown).

Data from ENVISAT's SAR can be used to retrieve spatial information of the near surface wind speed field over the sea. The retrieval of wind speed information is based on the connection between radar back-scatter and 10 m wind speed via empirical model functions (e.g. Hersbach, 2010; Dagestad et al., 2013). The retrieved wind field used in this investigation covers the area depicted in Fig. 2a. It is obtained from the *Satellite Winds* data base[2]. More details about the specific wind speed retrieval methodology used in the data base can be found in e.g. Section 2 in Badger et al. (2019) and the online documentation[3]. The black frame in Fig. 2a encloses an OCC dominated area, which is used for the spatial spectral analysis described in Sect. 4.3. The timestamp associated with the SAR image snapshot is 16 December 2010, 1018 UTC, approximately 2.5 hours before the cloud image in Fig. 1b is taken.

[1] `http://www.sat.dundee.ac.uk/` (last accessed: Aug. 2019)
[2] `https://satwinds.windenergy.dtu.dk/` (last accessed: July 2019)
[3] `https://satwinds.windenergy.dtu.dk/Info/Methodology` (last accessed: May 2020)

(a)

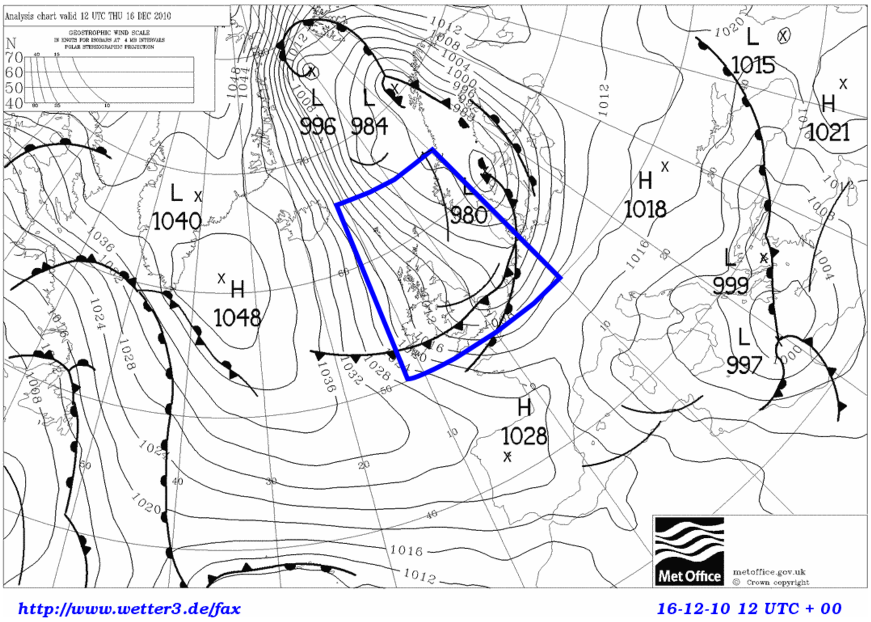

(b)

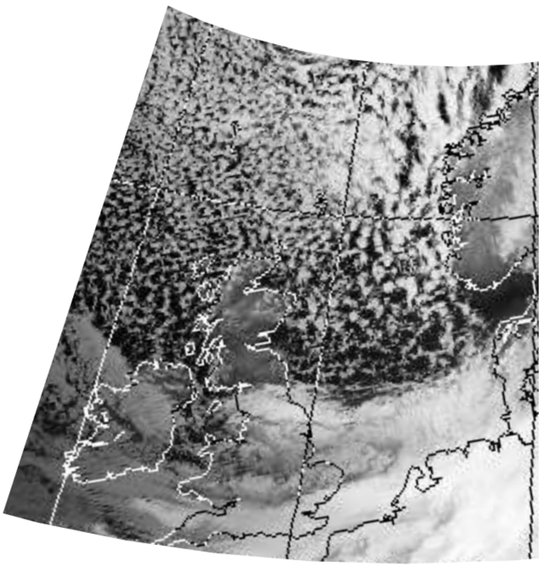

Fig. 1 (a) UK Met Office analysis chart valid at 16 December 2010, 1200 UTC ©Crown Copyright 2010 - Met Office. Source: `http://www1.wetter3.de/archiv_ukmet_dt.html` (last accessed: Feb. 2020). A blue frame is added to the image to indicate the geographic region depicted in (b). (b) Cloud picture from channel 5 of NOAA-19 satellite at 16 December 2010, 1244 UTC. The picture is trimmed to the North Sea area. Source: NERC Satellite Receiving Station, University of Dundee, `http://www.sat.dundee.ac.uk/abin/piccygridhtml/avhrr/2010/12/16/1244+19/ch5.jpg` (last accessed: Aug. 2019).

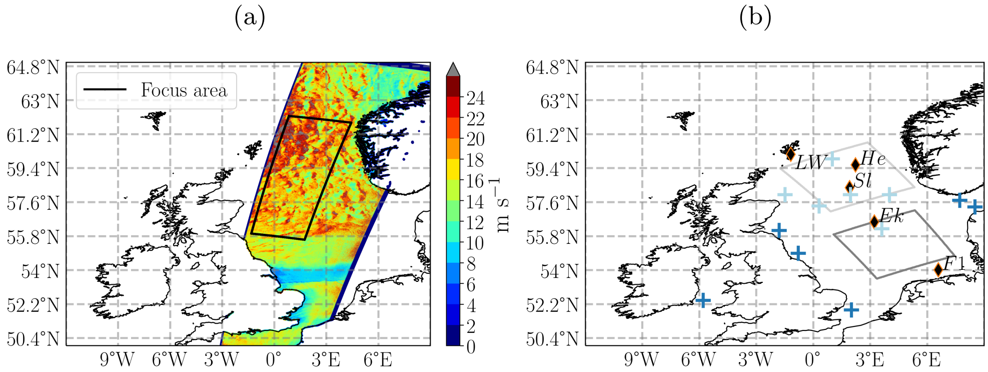

Fig. 2 (a) Retrieved wind speed at 10 m from ENVISAT Synthetic Aperture Radar at 16 December 2010, 1018 UTC. The black frame depicts the focus area for the spatial spectral analysis in Sect. 4.3. (b) Point measurements used within this investigation (black-orange diamonds, abbreviations follow naming convention in Table 1). In addition to measurements, blue plus signs in (b) indicate locations where model results are extracted for the wind speed step change analysis in Sect. 4.2.2. The grey frames in (b) indicate the northern (light grey) and southern (dark grey) region used for the spectral analysis of the vertical wind speed in Sect. 4.1.

2.2 In-situ Measurements

Wind speed and wind direction measurements from four offshore measuring sites ('Heimdal', 'Sleipner-A', 'Ekofisk' and 'Fino 1'), and an atmospheric sounding from Shetland are used for assessing the atmospheric conditions and the comparison with model results. Wind speed and direction data from three offshore oil platforms, 'Heimdal', 'Sleipner-A', and 'Ekofisk' were obtained from the Norwegian Meteorological Institute and are obtained from *NORSK KLIMASERVICESENTER*[4]. We use measurements from 10 m at all three locations, which are available as 20 minute averages every 20 minutes.

'Fino 1' provides a variety of meteorological and ocean observations at different measuring heights, but the wind speed and wind direction at 71 m are the focus of most of our study. The wind speed at 102 m is used for the comparison of wind speed step changes in Sect. 4.2.2. The 'Fino 1' measurements are available as 10 minute statistics (mean and standard deviation) and are obtained from the Federal Maritime and Hydrographic Agency (BSH) FINO data base[5]. The air temperature (at 34 m) and sea surface temperature (SST) were used to study the air-sea temperature difference during the cold air outbreak, which has been shown to be relevant for the formation of OCC structures (e.g. Agee et al., 1973; Bakan and Schwarz, 1992).

The 'Lerwick' sounding from Shetland (station ID 03005) from 16 December 2010, 1200 UTC is used to investigate the vertical profile to understand the large-scale meteorological conditions and validate the MPAS results. The sounding data was obtained from the *University of Wyoming sounding data archive*[6]. The sound-

[4] `https://seklima.met.no/observations/` (last accessed: Sep. 2019)
[5] `http://fino.bsh.de` (last accessed: July 2019)
[6] `http://weather.uwyo.edu/upperair/europe.html` (last accessed: Nov. 2019)

ings at station 03005 are available twice a day at 1200 UTC and 0000 UTC up to a pressure level of 100 hPa.

Table 1 summarises the point measurements together with coordinates, data type and their availability rate while Fig. 2b shows their locations (black-orange diamonds).

Table 1 Name, data type, geographic location and extracted observations from the different point sources. Sites are sorted from north to south. The abbreviations in brackets correspond to the naming in Fig. 2b. For time series data, measuring heights and data coverage of the individual parameters are given in brackets. Data coverage is stated only if it is not 100% within the period of interest.

Name (Abbreviation)	Data type	Location	Observations (height, data coverage)	Availability
Lerwick, 03005 (*LW*)	Vertical profile	60.13°N 1.18°W	Td, T, WS	0000 UTC, 1200 UTC
Heimdal (*He*)	Time series	59.5742°N 2.2273°E	WS (10 m), WD (10 m)	20 min
Sleipner-A (*Sl*)	Time series	58.3711°N 1.9091°E	WS (10 m), WD (10 m)	20 min
Ekofisk (*Ek*)	Time series	56.5453°N 3.2149°E	WS (10 m, 98.1%), WD (10 m, 98.1%)	20 min
Fino 1 (*F1*)	Time series	54.0149°N 6.5876°E	WS (71 m and 102 m), WD (71 m, 95.4%), SST (surface), T (34 m)	10 min†

WS: Wind speed; WD: Wind direction
T: Temperature; Td: Dew point temperature; SST: Sea surface temperature
† SST available every 30 min

3 Methods

3.1 MPAS Model Setup

The atmospheric component of the non-hydrostatic global circulation Model for Prediction Across Scales (MPAS-A, Version 7.0) is used. The discretisation of the globe is based on an unstructured spherical centroidal Voronoi tessellation (Du et al., 1999, 2003). This allows both quasi-uniform discretisation and meshes with local refinement regions that provide a gradual transition to smaller scales. The transition is described through a density function that specifies regions of higher and lower resolution (Ju et al., 2011). This is one major difference to traditional one-way or two-way nesting techniques.

The mesh used in this investigation has a horizontal mesh cell spacing of around 55 km over most of the globe, with a local refinement region centred over the North Sea that has average cell centre distances of approximately 2 km (see Fig. 3a). In total, the mesh consists of a bit more than 9×10^5 cells. To illustrate the nature of the varying spatial horizontal scales of the mesh, Fig. 3b shows a histogram of cell centre distances extracted within the focus area depicted in Fig. 2a. MPAS's vertical discretisation follows a generalised hybrid coordinate system in height-based coordinates as described in Klemp (2011). Fifty-five vertical levels and a model top of 30 km are used. Only the lowest 18 model levels (up to approximately 3 km) were saved, to accommodate a relatively high model output frequency of 10 minutes (storage constraints).

The total model integration time is 24 hours from 16 December 2010, 0000 UTC to 17 December 2010, 0000 UTC, which covers the episode of open cellular convection in the North Sea area described in Sect. 2.1. The model integration time step is 10 s. Initial conditions come from the Climate Forecast System Reanalysis (CFSR) 6-h forecast product (Saha et al., 2010) with a horizontal resolution of 0.5 degrees. Sea surface temperature and sea ice are updated every six hours and are from the same source, but with higher horizontal resolution (approx. 0.3 degrees). The model physics follow the *'convection_permitting'* suite which is summarised in Table 2. The suite contains the scale-aware Grell-Freitas scheme (Grell and Freitas, 2014) which acts as deep convection scheme on regions with coarse cell spacing (above approximately 20 km), while it effectively reduces itself to a shallow convection scheme for decreasing cell spacings below approximately 6 km (Fowler et al., 2016; Skamarock et al., 2018). The modelled wind speed time series at 'Heimdal', 'Sleipner-A', 'Ekofisk' and 'Fino 1' in the early stages of the simulation were used to estimate the model spin-up time needed for the OCC related wind speed fluctuations. Wind speed variability comparable to the point measurements emerge in the modelled time series after around six hours (not shown) at 10 m ('Heimdal', 'Sleipner-A', 'Ekofisk') and 71 m ('Fino 1'). This suggests a minimum model spin-up time of six hours for this event. The spin-up time is removed from the analysis and the remaining 18 hours will be used for the analysis (further referred to also as period of interest).

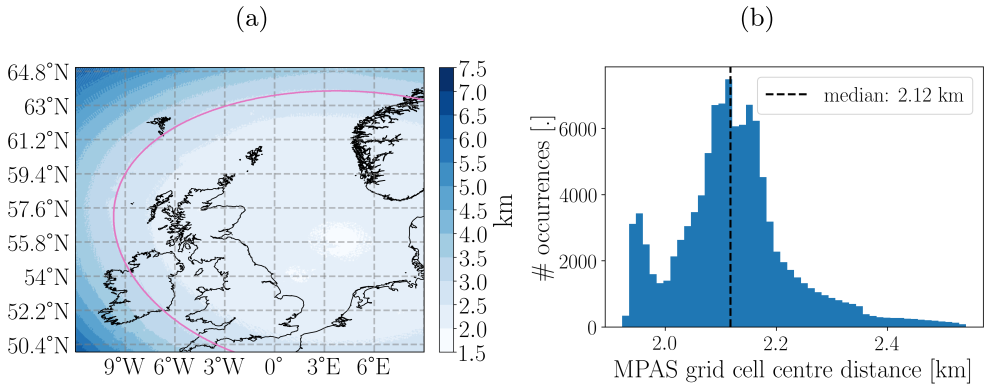

Fig. 3 (a) Approximate MPAS grid cell centre distances based on the average distance between a cell centre to its neighbours within the refinement region. The pink curve indicates the line of approximately 3 km horizontal MPAS grid cell spacing. (b) Histogram of MPAS grid cell centre distances determined at MPAS mesh cell edges within the focus area depicted in Fig. 2a.

Table 2 Summary of the physics schemes in MPAS that are part of the *'convection_permitting'* physics suite. Used abbreviations: MYNN: Mellor–Yamada–Nakanishi–Niino, RRTMG: Rapid Radiative Transfer Model for General Circulation Models.

Parameterisation	Scheme	References
Cumulus	Scale-aware Grell-Freitas	Grell and Freitas (2014)
Microphysics	Thompson non-aerosol aware	Thompson et al. (2008)
Land surface	Noah	Niu et al. (2011), Yang et al. (2011)
Boundary & surface layer	MYNN	Nakanishi and Niino (2009)
Long-/shortwave radiation	RRTMG	Iacono et al. (2008)

3.2 Spatial Power Spectrum Analysis from SAR and MPAS

For the spatial power spectrum analysis of the horizontal wind speed, data within a focus area dominated by OCC (see Fig. 2a, black frame) is examined. The area was chosen in such a way that it (1) includes only areas over water and (2) is located far enough from the border region of the SAR scanning region. This selection minimises the inclusion of fluctuations which are not associated with the OCC structures (e.g. influence of topography). The selection of the focus region contains 387 × 1407 grid points, with data points available every 500 metre. A visual inspection of the wind speed distribution and limits based on the interquartile range are used to classify outliers in the data. Based on this, wind speeds above 27.3 m s^{-1} are declared as outliers and removed. As a first step, each of the 387 data columns are independently detrended by subtracting a linear least-squares fit from the original data within each column. Afterwards, a one-dimensional discrete Fourier transformation for each of the 387 data columns is performed, whereby only data columns with less than 2% missing data are considered. Below that threshold, data gaps are filled via linear interpolation from their neighbouring points. Subsequently, the individual spectra are averaged and a log-smoothing algorithm with 25 points per decade is applied to the averaged spectrum to reduce the noise in the higher frequencies. Then, the final power spectrum is obtained.

To apply the same procedure to the MPAS model results, an interpolation from the native unstructured grid of MPAS to a regular grid with constant spacing is needed. For this purpose, the MPAS model output closest to the timestamp of the SAR data (16 December 2010, 1020 UTC) is interpolated to the regular SAR grid via linear barycentric interpolation using the Earth System Modeling Framework[7] (ESMF, Hill et al. (2004), Version 6.3.0r). Afterwards, points within the focus area are extracted and the same method is applied to the regridded MPAS model output.

For the spatial spectral analysis of the vertical wind speed in Sect. 4.1, modelled vertical wind speeds at the sixth model level (approx. 476 m above sea level) are linear barycentric interpolated via the ESMF routine to two regular grids with constant grid spacing that cover different geographical areas of the North Sea (Fig. 2b, grey domains). Each grid consists of 151 $\times$ 151 points with horizontal grid spacing of 2 km. To obtain the spatial power spectrum, spatial wind speed data on each of the 151 data columns with south-west/north-east orientation are linearly detrended and a one-dimensional Fourier transformation is applied. The obtained spectra are averaged over all 151 data columns with subsequent log-smoothing as described in the previous paragraph. This procedure is performed for each model time step between 16 December 2010, 1300 UTC and the end of the simulation, between which both domains are fully covered by OCC structures, and the obtained power spectra are averaged in time. The resulting average power spectrum builds the foundation of the spectral comparison of the vertical wind speed mentioned in Sect. 4.1.

3.3 Filtering of Wind Speed Time Series

In order to highlight the effects of OCC on wind variability, wind speed time series are filtered by means of two filters (F1 and F2) which are applied as follows: To remove the large-scale effects (low frequency contributions) from the fluctuations attributed to the open cells, all time series (modelled and measured) are high-pass filtered with a 6th-order butterworth filter (F1, backward-forward) with a cut-off frequency equivalent to a cycle duration of 3 h (corresponding to 1/(3 h) or 9.26×10^{-5} Hz). The cycle duration was chosen because it provides a good balance between the inclusion of OCC related mesoscale variability and exclusion of large-scale effects on the variability and is further elaborated in Sect. 5. Similar filtering methods have been applied in Davy et al. (2010) who use band-pass filters as a first step in their calculation of a "variability index" and in Mehrens and von Bremen (2016), who use a Fast Fourier Transformation filter to isolate wind speed fluctuations within certain time scales. In addition to that, an attempt to account for the differences in sampling rate between the model and the data obtained at 'Heimdal', 'Sleipner-A' and 'Ekofisk' was made by applying an additional low-pass filter (F2) to the modelled time series with a cut-off frequency equivalent to a

[7] `https://www.earthsystemcog.org/projects/esmf/` (last accessed: May 2020)

cycle duration of 40 minutes (corresponding to 1/(40 min) or 41.67×10^{-5} Hz) at those locations. This is equivalent to the Nyquist frequency corresponding to the sampling rate at 'Heimdal', 'Sleipner-A' and 'Ekofisk'. The resulting filtered time series build the foundation for the temporal wind speed analysis in Sect. 4.2.1.

3.4 Determination of 10-minute Wind Speed Step Changes

Ten-minute wind speed step changes $\Delta V_{\mathrm{abs,step}}$ are defined as the difference in wind speed magnitude between two consecutive measurements or model outputs at a given 10-minute time step t and its successor $t+1$ (Equ. 1).

$$\Delta V_{\mathrm{abs,step}}(t) = V_{\mathrm{abs,step}}(t+1) - V_{\mathrm{abs,step}}(t) \tag{1}$$

To emphasise the OCC impact, modelled wind speed time series are extracted at 12 randomly selected sites with six locations representing OCC affected sites and six locations representing OCC free sites. The classification was made based on a visual inspection of the time series of the horizontal and vertical wind fields. The exact positions of the 12 sites are marked in Fig. 2b, with OCC affected sites in light blue and OCC free sites in dark blue. For each location, the wind speed time series at 100 m is obtained by linear interpolation from surrounding vertical model levels and extracted. After the removal of the spin-up time, the 10-minute wind speed step changes are calculated following Equ. 1 and the cumulative relative occurrences for the wind speed step change analysis in Sect. 4.2.2 are determined.

4 Results

4.1 Assessment of Open Cellular Structures in Measurements and Model

In order to evaluate the MPAS model capacities in simulating the OCC episode, model results are compared with observations and relations from the literature. While the performance regarding the representation of the wind speed is especially crucial for the wind variability analysis, a qualitative assessment of the atmospheric background conditions driving the open cells is needed as well. For this purpose, the horizontal and vertical wind speed, but also the near surface air-sea temperature difference, and vertical profiles of dew point temperature, absolute temperature and wind speed are investigated.

Fig. 4a,b shows a snapshot (16 December 2010, 1240 UTC) of MPAS modelled vertical velocity at model level 3, which is located around 106 m above sea level. Since the focus lies on the open cells over the sea, values located over land points are omitted. The structure of the modelled vertical velocity shows the characteristic narrow updraft regions (cell borders) and broader downdraft regions (cell centres) described in e.g. Atkinson and Zhang (1996) and Feingold et al. (2015). The structures tend to be smaller in the north (e.g. around 'Heimdal'), becoming larger towards the south (downstream direction). This was further investigated by comparing the spatial power spectrum of the modelled vertical wind speed over an area in the northern North Sea with the spectrum over an area in the southern North Sea (cf. methodology described in Sect. 3.2). The normalised spatial power spectrum obtained from the southern North Sea area shows a higher share

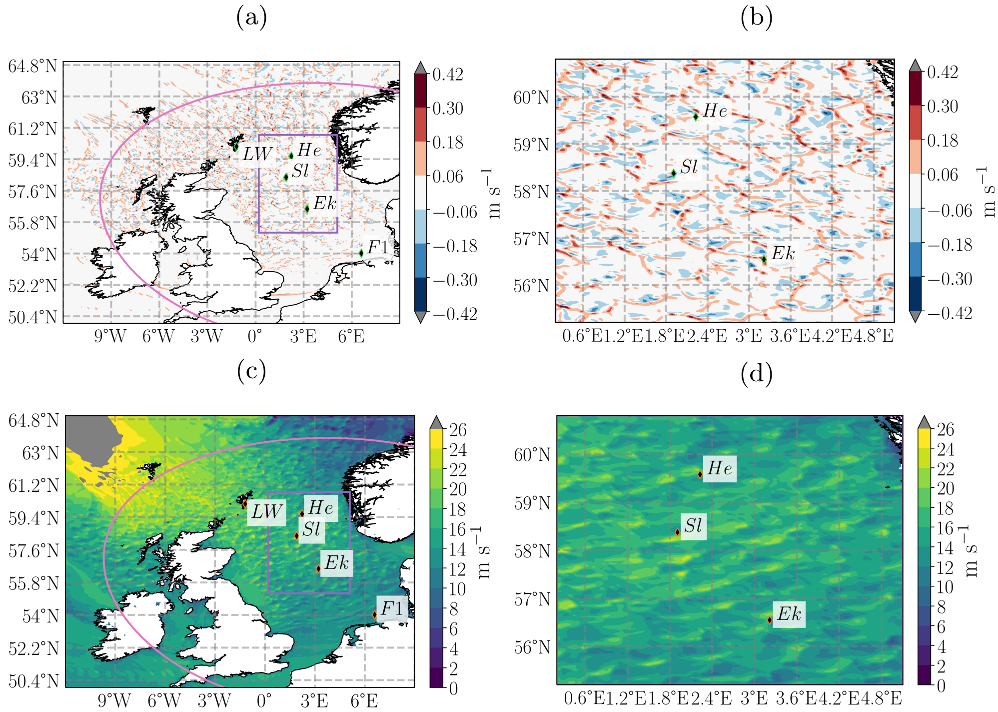

Fig. 4 (a) Vertical velocity over water points at model level 3 (106 m). (b) Zoomed version of (a) around 'Heimdal', 'Sleipner-A' and 'Ekofisk'. (c) Horizontal wind speed over water points at 10 m. (d) Zoomed version of (c) around 'Heimdal', 'Sleipner-A' and 'Ekofisk'. All images show the model output at 16 December 2010, 1240 UTC (snapshot). The geographic area inside the purple lines in (a) and (c) is depicted in (b) and (d), respectively. For orientation purposes, the pink curves in (a) and (c) show the line of approximately 3 km horizontal cell spacing from Fig. 3a.

of larger wavelengths compared to the spectrum obtained in the northern North Sea (not shown) which suggests the presence of larger cell sizes in the south. This also agrees with the observed trend of increasing cell diameters towards lower latitudes in Bakan and Schwarz (1992). Similar structures are visible in the horizontal wind speed at 10 m (Fig. 4c,d) which emphasises the spatial variation of the horizontal wind speed associated with the OCC structures. Visual comparison of the NOAA 19 cloud picture from 16 December 2010, 1244 UTC (Fig. 1b) with closest model output (16 December 2010, 1240 UTC) shows similarities with respect to the overall pattern and cell size distributions (Fig. 4a). In the north/north-west of the Faroe Islands, the cloud image suggests the presence of OCC structures, while MPAS does not show signs of open cell structures in that region. This could be attributed to the gradual refinement region of MPAS (cf. Fig. 3a), which is further discussed in Sect. 5.

To obtain insight into the vertical structure of the atmosphere, model results from the closest data point to the Lerwick sounding station are compared with the sounding observations (Figure 5). Strong agreement with observations is seen for both temperature and wind speed in the vertical profiles. A local peak in high wind speed at around 850 hPa is visible (Fig. 5b) and a closer look at the time series of the modelled horizontal wind speed at 850 hPa centred around 16 December 2010,

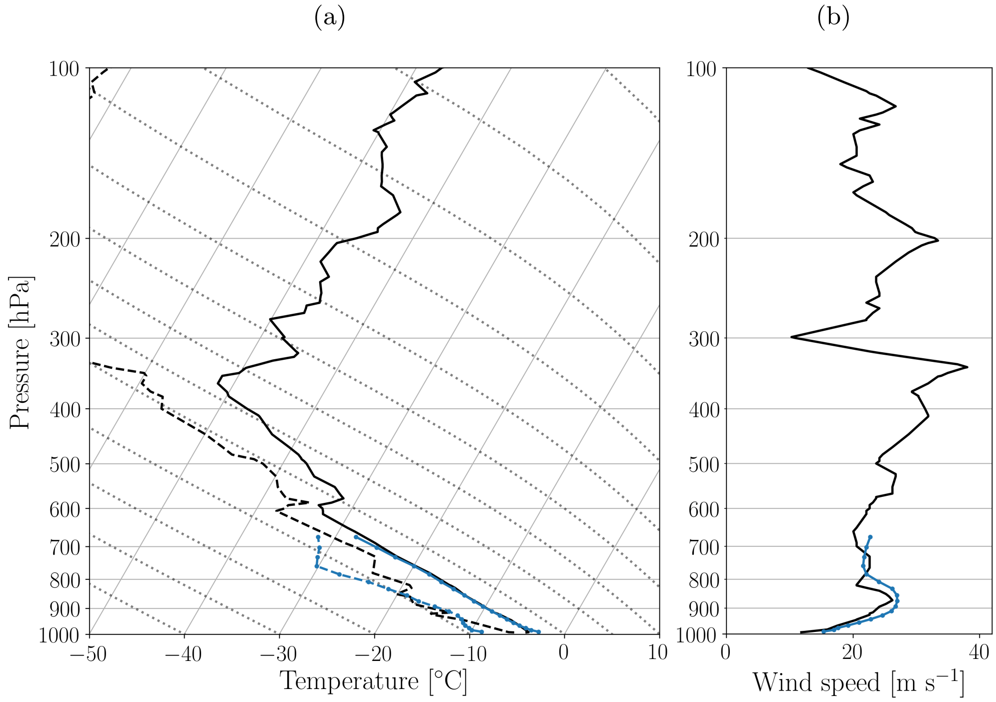

Fig. 5 Comparison between sounding data (black) and modelled vertical profiles (blue) at station 03005 (16 December 2010, 1200 UTC): (a) dew point (dashed line) and absolute temperature (solid line) and (b) wind speed.

1200 UTC suggests that the peak is associated with a passing OCC structure at measuring time. The peak is well captured by the model. Reduced moisture in the model between 850 hPa and 650 hPa is observed, with a deficit of up to -6°C in the dew-point near 750 hPa. However, the modelled profiles 10 minutes before and after 16 December 2010, 1200 UTC do not show this extreme deviation and vertical cross-sections of the dew point temperature parallel to the flow direction (not shown) suggest that the moisture differences are likely related to temporal or spatial displaced cell features in the model. Nevertheless, the strong overall agreement supports confidence in the model results.

For further assessment of the winds, the time series of the modelled wind speed and wind direction are compared with the 10 m measurements at the three oil platforms 'Heimdal', 'Sleipner-A' and 'Ekofisk', and the 71 m measurements at the 'Fino 1' mast (Fig. 6). Although the model results were limited to the period after the initialisation of the OCC event, measurements before and after the simulated period are included to provide additional understanding of the event. Since the dominant flow was from the north/north-west, 360-degrees was added to wind directions below 180-degrees to improve readability. This affects modelled wind directions at 'Heimdal' and 'Sleipner-A'. From the later stages of the cold-air outbreak to the end of the simulated period, both the model and the measurements show wind speed fluctuations related to the presence of open cells. This presence is also supported by the air-sea temperature difference at 'Fino 1' which remains highly negative until the end of the simulation period (not shown). The large-scale trend of decreasing wind speed is captured well by the model at all measuring locations, as is the sharp wind direction shift at 'Fino 1'. On the synoptic scale, the passing of the frontal system (cf. Sect. 1) from north-west to south-east is clearly visible in the sudden change in wind direction between 15 December 2010, 2300 UTC ('Heimdal') and 16 December 2010, 1100 UTC ('Fino 1'). The associated large cold pool also explains the strong similarities in the large scale trend in both wind speed and wind direction at the four measuring locations, even though the sites are several hundreds of kilometres apart. A one-hour time lag is seen between the observed and modelled wind direction change at 'Fino 1', whereby the model determines the wind direction change earlier. After the frontal system passes the region, the wind direction shows higher fluctuations compared to the earlier period (see Fig. 6, right column) with higher uncertainties at 'Fino 1' when the wind speed falls below 5-6 m s^{-1} close to the end of the simulation period after around 16 December 2010, 2300 UTC.

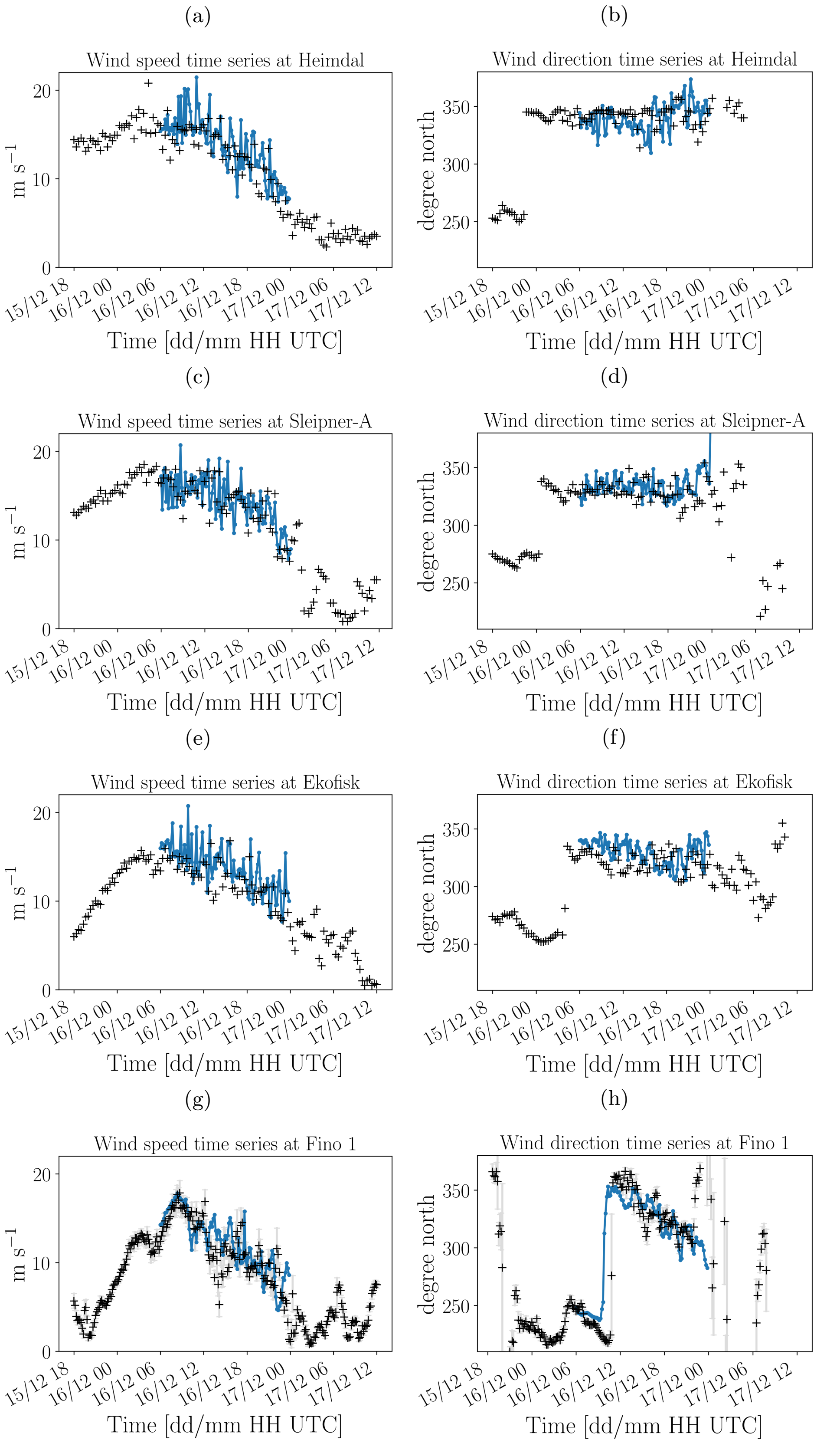

Fig. 6 Comparison of modelled (blue) and observed (black) measures: (a) wind speed at 'Heimdal', (b) wind direction at 'Heimdal', (c) wind speed at 'Sleipner-A', (d) wind direction at 'Sleipner-A', (e) wind speed at 'Ekofisk', (f) wind direction at 'Ekofisk', (g) wind speed at 'Fino 1', (h) wind direction at 'Fino 1'. Measuring heights are 10 m (a-f) and 71 m (g-h). The grey bars in (g), (h) represent the 10-minute mean plus/minus one 10-minute standard deviation.

4.2 Impact of OCC on Wind Speed Fluctuations in Time Domain

In addition to the general trend in the mean wind speed, which was captured reasonably well by the model (cf. Fig. 6), wind variability due to the open cellular structures is investigated in this section. This variability is highly apparent in the fluctuations in the time series in Fig. 6. Two measures are chosen to characterise the wind variability in the time domain, namely the standard deviation (Sect. 4.2.1) and the 10-minute wind speed step change (Sect. 4.2.2), that is the difference between consecutive modelled or measured wind speeds with a time difference of 10-minutes.

4.2.1 Impact Of Open Cells on Standard Deviation of Filtered Time Series

After filtering the wind speed time series following the methodology described in Sect.3.3, the standard deviation of modelled and measured wind speed are calculated within the period of interest (overlapping period between measurements and model without spin-up, 16 December 2010, 0600 UTC to 16 December 2010, 2350 UTC, see also Fig. 6) and used as a measure for the wind speed variability in the relevant scales. The results are given in Table 3. With the exception of 'Sleipner-A', the model and measurements agree well regarding the standard derivation of the wind speed. The absolute value of relative differences is contained within 0.1 m s^{-1} ($< 10\%$) when the effects due to the different sampling rates by additional low-pass filtering are considered. The large deviation at 'Sleipner-A' originates from the poor estimation of the standard deviation in the modelled time series at that location. Its value is overall significantly lower compared to the observations and model results from the three other locations. A closer look at the response of the modelled time series at 'Sleipner-A' to different cut-off frequencies of the low-pass filter F2 between 1/(40 min) and 1/(20 min) revealed that this is partly related to an over-proportional share of very high frequencies in the modelled time series between 1/(40 min) and 1/(20 min) on the total variance. This is not seen to the same extend at 'Heimdal' and 'Ekofisk' (not shown). The currently applied low-pass filter with cut-off frequency of 1/(40 min) removes a large part of those contributions and decreases the modelled total standard deviation at 'Sleipner-A' significantly compared to the unfiltered case (bracketed values for σ_{mod} in Table 3). However, the overall modelled standard deviation at 'Sleipner-A' still remains relatively low compared to 'Heimdal' and 'Ekofisk' even after omitting low-pass filtering. This indicates a more systematic underestimation of the wind speed variability by the model at that location.

Table 3 Standard deviations of the filtered measured (σ_{obs}) and modelled (σ_{mod}) wind speed obtained from values within the period of interest (16 December 2010, 0600 UTC to 16 December 2010, 2350 UTC). The numbers in brackets show the results without additional low-pass filtering of the model results (i.e. deactivated F2) at 'Heimdal', 'Sleipner-A' and 'Ekofisk'.

Location	σ_{obs} [m s^{-1}]	σ_{mod} [m s^{-1}]	σ_{mod} - σ_{obs} [m s^{-1}]	$\frac{\sigma_{\mathrm{mod}}-\sigma_{\mathrm{obs}}}{\sigma_{\mathrm{obs}}}$ [%]
'Heimdal'*	1.31	1.38 (1.76)	0.07 (0.45)	5 (34)
'Sleipner-A'*	1.39	1.07 (1.65)	-0.32 (0.26)	-23 (19)
'Ekofisk'*	1.30	1.26 (1.73)	-0.04 (0.43)	- 3 (33)
'Fino 1'†	1.17	1.26	0.09	8

* evaluated at 10 m
† evaluated at 71 m

4.2.2 Impact of Open Cells on 10-minute Wind Speed Step Changes

While the standard deviation describes the total variability, the analysis of wind speed step changes $\Delta V_{\mathrm{abs,step}}$ is used to characterise the impact of open cells on magnitude changes at the time scale of 10 minutes. The simulated wind speed step changes are extracted and processed as described in Sect. 3.4. They are compared with 10-minute wind speed step changes obtained from Mehrens et al. (2016), which come from a long-term mesoscale simulation over the southern North Sea covering the years 2000-2013 (see Mehrens et al. (2016) for further details). Simulation results are available from model level around 100 m. Due to the relatively long simulation period, Mehrens et al. (2016)'s data set provides a good approximation of mean climatological wind speed step changes for this area. Wind speed step changes were also calculated at 'Fino 1' for the period of OCC presence (16 December 2010, 1300 UTC to 16 December 2010, 2350 UTC) from the wind speed time series available closest to 100 m, that is 102 m. Results are summarised in Fig. 7a. It can be observed that the presence of OCC has large influence on the expected 10-minute wind speed step changes while the cumulative occurrences of sites that are not affected by OCC are in agreement with the climatologically expected wind speed step changes. Sites with OCC conditions show a much flatter cumulative occurrence function, with higher shares of both positive and negative wind speed step changes. There is spread between results from different sites in the same category, as expected, but the general trend shows that moderate to high step changes of $V_{\mathrm{abs,step}}$ with absolute values above to 5 m s^{-1} are observed more often at OCC affected sites than sites which are not affected by OCC. The measurements at 'Fino 1' indicate a slightly steeper curve compared to OCC affected sites, which is caused by the lower mean wind speed at 'Fino 1' ($\bar{V} = 9.7$ m s^{-1}) compared to the other OCC affected sites shown in Fig. 2b ($\bar{V}$ between 15.0 m s^{-1} and 19.5 m s^{-1}). If modelled and measured wind speed step changes are normalised with the local mean wind speed, the behaviour at 'Fino 1' agrees well with the modelled trend at the other OCC affected locations (Fig. 7b). The comparison shows that the climatological representation of wind speed step changes is not valid under OCC conditions and highlights that OCC conditions will result in much larger changes in the wind speed every 10 minutes than what would be expected during average weather conditions.

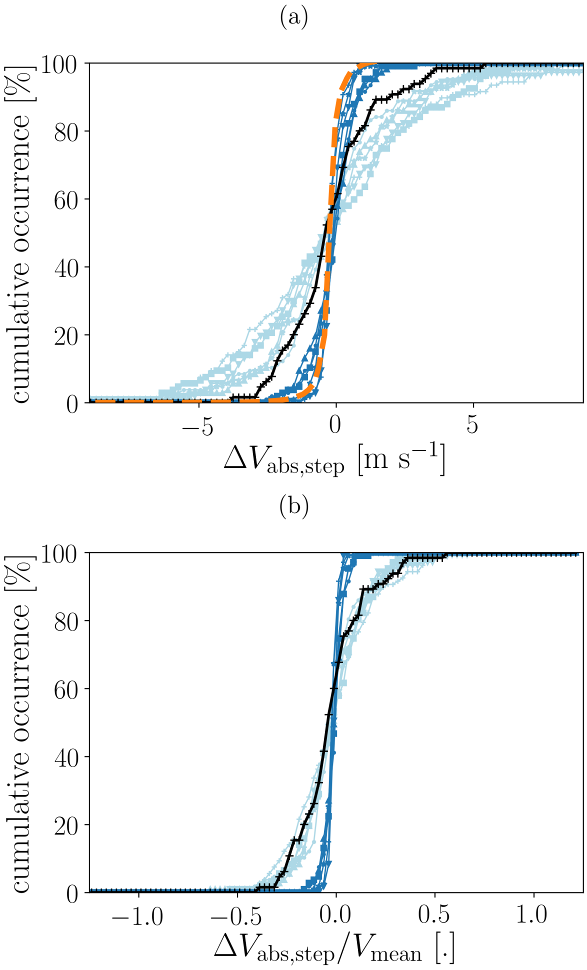

Fig. 7 Cumulative occurrence of (a) absolute 10-minute wind speed step changes $\mathit{\Delta} V_{\mathrm{abs,step}}$ and (b) 10-minute wind speed step changes normalised by the local mean wind speed. Light blue: MPAS output from locations affected by OCC, dark blue: MPAS output from locations unaffected by OCC. The exact positions of the six OCC affected and six OCC unaffected sites are marked in Fig. 2b. Orange: long-term average cumulative occurrence, reconstructed from cumulative sum of the relative occurrences provided in Mehrens et al. (2016), their Fig. 6, black: 'Fino 1' measurements (102 m). Note: Mehrens et al. (2016)'s data could not be normalised due to missing local mean wind speed information.

4.3 Wind fluctuations in Spatial Spectral Space

To determine the impact of the OCC on the spatial variability of the wind, a spatial power spectral analysis is performed. The spatial power spectrum provides a useful tool to relate wind speed fluctuations to the spatial length scales they are associated with. The spatial power spectrum for SAR and MPAS is calculated following the methodology described in Sect. 3.2. Figure 8 depicts the spatial power spectra of the 10 m wind speed obtained from SAR and MPAS in comparison with the measured mean climatological wind speed power spectra from Nastrom and Gage (1985). It can be seen that the wind speed power spectrum increases under

OCC conditions, when compared to the Nastrom and Gage (1985) spectrum, for both measured and modelled spectra. The increased magnitude for wavelengths below approximately 100 km can be connected to the various sizes of open cellular structures seen in the cloud picture (Fig. 1b) and in the modelled vertical and horizontal velocity fields (Fig. 4). The affected scales indicate cell sizes that are slightly larger than those observed in Bakan and Schwarz (1992). The magnitude of the spectrum for very large wavelengths (greater than approximately 150-200 km) has higher uncertainty due to the limited domain size used for the Fourier analysis of the SAR and model data. Quantitatively strong conclusions cannot be made in this range. At smaller wavelengths, the modelled spectra exhibits a sudden decrease in magnitude for wavelengths below approximately 15 km to 20 km, in contrast to the SAR spectra, due to the effective resolution of the numerical model. The effective resolution of MPAS is approximately 6Δx (Skamarock et al., 2014), where Δx is the representative length scale for the minimum cell centre distance. Looking at the distribution of grid cell centre distances within the focus area for the spectral analysis (Fig. 3b), a variety of cell centre distances are present which makes it difficult to sharply define one representative cell centre distance length scale for the analysed region. Based on the range of cell centre distances given in Fig. 3b and the estimator of 6Δx, the effective resolution is on the order of 11.5 km to 15 km, which is only slightly smaller than the observed drop in the wind speed power spectrum. In general, the impact of OCC on the spatial power spectra seen here is consistent with observations in Larsén et al. (2017b), which used the regional Coupled-Ocean-Atmosphere-Wave-Sediment Transport (COAWST) modelling system to investigate an open cell event during 2006's Storm Britta. The decent agreement of the model with the SAR data shows the capability of MPAS to represent the impact of the open cells on the spatial power spectrum for wavelengths larger than the effective resolution.

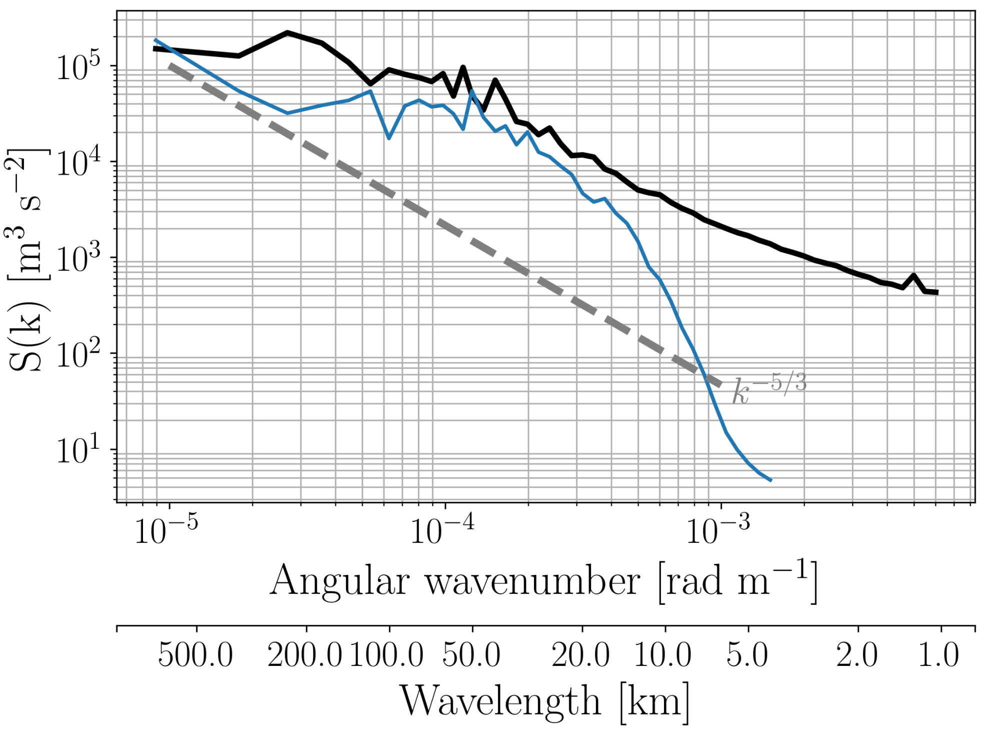

Fig. 8 Spatial power spectra of 10 m wind speed from SAR image (black) and MPAS (blue) during presence of OCC in comparison with the climatological aircraft measurements from Nastrom and Gage (1985) (grey, linear fit is reconstructed from their Fig. 3).

5 Discussion

Within the scope of this investigation, an episode of open cellular convection, associated with a cold-air outbreak, is investigated based on a simulation with the global Model for Prediction Across Scales (MPAS) and a variety of observations. The combination and inter-comparison of point measurements, satellite images, and model results is beneficial for two main reasons. First, it provides a more complete picture of the impacts of OCC conditions with respect to wind energy related parameters. Second, it also makes it possible to frame the capabilities and limitations of simulating OCC conditions using MPAS with a mesh that includes regional refinement down to 2 km grid spacing.

The results show that MPAS is able to capture the significant effects of OCC on several wind energy relevant parameters over a variety of temporal and spatial scales to a high degree. This includes the overall satisfactory representation of the OCC associated higher temporal and spatial fluctuations in the horizontal wind speed (cf. Fig. 6, Fig. 4c,d), the increased 10-minute wind speed step changes (cf. Fig. 7) and the additional energy in the wind speed power spectrum (cf. Fig. 8) between 20 km and 100 km. These scales are larger than current offshore wind farm dimensions, which are on the order of 4-10 km (Borrmann et al., 2018). However, Göçmen et al. (in press 2020) found that the temporal fluctuations induced by the moving cells can be seen in increased power fluctuations in wind farms as small as 'Horns Rev I' (wind farm area of approx. 20 km^2, Borrmann et al., 2018). This includes enhanced turbulence intensity inside the wind farm at temporal scales larger than two minutes (Göçmen et al., in press 2020). However, those scales are beyond the limits of this investigation due to the model's effective resolution, which causes reduced variability in smaller scales. In the current investigation, this was found to affect spatial scales between 15 and 20 km. While a further increase in horizontal cell spacing would move the effective resolution to lower wavelengths, the additional benefits might not balance the large additional increase in computational expenses. The inter-comparison between the MPAS model and measurements also revealed some of its capabilities and limitations for modelling the frontal system and the OCC conditions. Within the model refinement region, modelled horizontal and vertical wind speed (cf. Fig. 4) show that the model is able to create cell patterns that resemble those seen in the cloud picture and the SAR image. A spin-up time of six hours was sufficient to build up smaller scales of the wind speed at the lower levels, when comparing with point measurements. The smooth transition region made it possible to introduce the larger-scale signals more gently, allowing smaller scales to gradually build up in the transition zone, while the atmospheric features propagate through the zone. This results in cells developing close to where the resolution is high enough for them to be generated. Limited area models with traditional nesting methods require larger domains to allow space to spin up finer scale features to develop inside of the high resolution domain (Leduc and Laprise, 2009; Matte et al., 2017). This effect was observed for an OCC event in Vincent (2010), which found that the development of OCC features in the upstream part of the innermost domain is restricted due to the insufficient representation of the OCC structures in the parent domain. The characteristic OCC structures only appeared further inside the domain, after the finer domain built up the missing scales. In this study, a similar effect was only seen to the north of Shetland, which is located relatively far in the transition zone of the refinement region (average cell centre distances around 3.5 km and above, Fig. 3a). While the reduced horizontal mesh cell spacing has an influence on the representation of the smaller-scales in this region due to the effective resolution, the relatively high horizontal wind speeds (cf. Fig. 4c) in the region might also play a role. The fast moving atmospheric structures will pass the transition zone relatively quickly and under the given design of the transition zone, the travel speed could be too quick for the model to build-up smaller scale structure in this region. This suggests that a wider refinement region or a shallower gradient in the horizontal mesh cell spacing between the coarse and fine regions of the mesh could have been beneficial in this region for this particular case.

In the time domain, the investigation of the standard deviation in the wind speed time series (Table 3) showed that model and measurements agree reasonably well in three out of four investigated locations within the considered time scales. High-pass filters were used to minimise the impact of large-scale phenomena like the frontal system on the standard deviation. The chosen cut-off frequency, corresponding to a cycle duration of 3 h, can be associated with spatial scales of around 150 km (assuming Taylor's frozen hypothesis with a mean wind speed of around 14 m s^{-1}). This is larger than the characteristic scales of the open cells (Bakan and Schwarz, 1992) but smaller than scales associated with frontal systems (e.g. Orlanski, 1975), and therefore, provides a justifiable choice for a cycle duration threshold. This places its value between the lower cut-off frequency of the band-pass filter of 1/(2 h) used in Davy et al. (2010) and 1/(6 h) used in the Fast Fourier Transform filter in Mehrens and von Bremen (2016). Naturally, the estimated absolute values of the standard deviations will have some dependency on the cut-off frequency and will be larger the more scales are included. An investigation of four other cut-off frequencies including 1/(2 h) as used in Davy et al. (2010), 1/(4 h), 1/(5 h) and 1/(6 h) as used by Mehrens and von Bremen (2016) showed that the relative differences are not sensitive to the chosen cut-off frequency (not shown). Other impacts, like the effect of different sampling rates (10-minute for 'Fino 1' and model, 20-minute for 'Heimdal', 'Sleipner-A' and 'Ekofisk') and data origin (instantaneous model output in comparison to averaged wind speeds) can only be estimated roughly. The introduction of a low-pass filter, to account for the different sampling rates between the model and measurement data, had the desired effect of bringing them to the same level for comparison. The modelled standard deviations decreased by around 0.4-0.5 m s^{-1} at 'Heimdal' and 'Ekofisk' to 0.6 m s^{-1} at 'Sleipner-A' (cf. Table 3), when the filter was applied. This helped removing some of the higher frequency OCC variation that are averaged out during the 20-minute averaging period of the observations. This is supported by the reasonable agreement between model and observed standard deviations at 'Fino 1' (cf. Table 3), where the model output rate is identical to the measurement data availability. Beyond the above discussed influences, both the model and observations naturally contain other sources of uncertainty which will affect the quantification of the wind speed fluctuations as well.

6 Conclusion

This study presents the investigation of a cold-air outbreak that generated an episode of open cellular convection (OCC) using MPAS with regional grid refinement. With its focus on OCC and the unique mesh design, with fine-scale horizontal mesh cell spacing down to 2 km, this is the first investigation of this kind in MPAS. An inter-comparison of model results and a variety of observations showed that MPAS is able to realistically simulate open cellular convective structures and associated wind speed fluctuations as seen in measurements and literature, given the boundaries set by the effective resolution. The realistic replication and forecasting of OCC wind variability can help to improve estimations of wind power fluctuations of offshore wind farms with positive effects on wind farm operation and scheduling.

Acknowledgements The work in this study is partly supported by the ForskEL/EUDP OffshoreWake (PSO-12521) project. The authors thank NORSK KLIMASERVICESENTER for providing the point measurements at 'Heimdal', 'Sleipner-A' and 'Ekofisk', the Federal Maritime and Hydrographic Agency (BSH) for providing the point measurements at 'Fino 1' and the University of Wyoming sounding data archive for providing the sounding data at Lerwick station. Wind fields from synthetic aperture radar are provided by the Technical University of Denmark, Department of Wind Energy (DTU Wind Energy). The CFSR 6-h forecast products used in this publication are downloaded from UCAR/NCAR Research Data Archive. The first author likes to acknowledge the team behind the python packages *matplotlib* (Hunter, 2007), *MetPy* (May et al., 2008 - 2020) and *cartopy* (Met Office, 2010 - 2015) which are used for the creation of the visual content and also likes to thank Michael Duda (NCAR) for providing the mesh generation code base and support during the mesh generation process.

We would also like to thank the three anonymous reviewers for their helpful remarks and suggestions. The authors have no conflict of interest to declare.

References

Agee EM (1987) Mesoscale cellular convection over the oceans. Dynamics of Atmospheres and Oceans 10(4):317–341, DOI 10.1016/0377-0265(87)90023-6

Agee EM, Chen TS, Dowell KE (1973) A Review of Mesoscale Cellular Convection. Bulletin of the American Meteorological Society 54(10):1004–1012, DOI 10.1175/1520-0477(1973)054⟨1004:aromcc⟩2.0.co;2

Akhmatov V, Rasmussen C, Eriksen PB, Pedersen J (2007) Technical aspects of status and expected future trends for wind power in Denmark. Wind Energy 10(1):31–49, DOI 10.1002/we.206

Atkinson BW, Zhang JW (1996) Mesoscale shallow convection in the atmosphere. Reviews of Geophysics 34(4):403–431, DOI 10.1029/96RG02623

Badger M, Ahsbahs T, Maule P, Karagali I (2019) Inter-calibration of SAR data series for offshore wind resource assessment. Remote Sensing of Environment 232(November 2018):111,316, DOI 10.1016/j.rse.2019.111316

Bakan S, Schwarz E (1992) Cellular convection over the north-eastern Atlantic. International Journal of Climatology 12(4):353–367, DOI 10.1002/joc.3370120404

Borrmann R, Rehfeld K, Wallasch AK, Lüers S (2018) Capacity Densities of European Offshore Wind Farms. Deutsche WindGuard GmbH, Varel, Germany, Tech rep

Busack B, Bakan S, Luthardt H (1985) Surface conditions during mesoscale cellular convection. Contributions To Atmospheric Physics 58(1):4–10

Dagestad KF, Horstmann J, Mouche A, Perrie W, Shen H, Zhang B, Li X, Monaldo F, Pichel W, Lehner S (2013) Wind retrieval from synthetic aperture radar - an overview. In: SAR Oceanography Workshop

Davy RJ, Woods MJ, Russell CJ, Coppin PA (2010) Statistical downscaling of wind variability from meteorological fields. Boundary-Layer Meteorology 135(1):161–175, DOI 10.1007/s10546-009-9462-7

Du Q, Faber V, Gunzburger M (1999) Centroidal Voronoi tessellations: Applications and algorithms. SIAM Review 41(4):637–676, DOI 10.1137/S0036144599352836

Du Q, Gunzburger MD, Ju L (2003) Constrained Centroidal Voronoi Tessellations for Surfaces. SIAM Journal on Scientific Computing 24(5):1488–1506, DOI 10.1137/S1064827501391576

Feingold G, Koren I, Yamaguchi T, Kazil J (2015) On the reversibility of transitions between closed and open cellular convection. Atmospheric Chemistry and Physics 15(13):7351–7367, DOI 10.5194/acp-15-7351-2015

Fowler LD, Skamarock WC, Grell GA, Freitas SR, Duda MG (2016) Analyzing the Grell–Freitas Convection Scheme from Hydrostatic to Nonhydrostatic Scales within a Global Model. Monthly Weather Review 144(6):2285–2306, DOI 10.1175/MWR-D-15-0311.1

Göçmen T, Larsén XG, Imberger M (in press 2020) The effects of open cellular convection on wind farm operation and wakes. Journal of Physics: Conference Series n/a(n/a)

Grell GA, Freitas SR (2014) A scale and aerosol aware stochastic convective parameterization for weather and air quality modeling. Atmospheric Chemistry and Physics 14(10):5233–5250, DOI 10.5194/acp-14-5233-2014

Hagos S, Ruby Leung L, Zhao C, Feng Z, Sakaguchi K (2018) How Do Microphysical Processes Influence Large-Scale Precipitation Variability and Extremes? Geophysical Research Letters 45(3):1661–1667, DOI 10.1002/2017GL076375

Hashimoto A, Done JM, Fowler LD, Bruyère CL (2016) Tropical cyclone activity in nested regional and global grid-refined simulations. Climate Dynamics 47(1-2):497–508, DOI 10.1007/s00382-015-2852-2

Hersbach H (2010) Comparison of C-Band scatterometer CMOD5.N equivalent neutral winds with ECMWF. Journal of Atmospheric and Oceanic Technology 27(4):721–736, DOI 10.1175/2009JTECHO698.1

Hill C, DeLuca C, Balaji, Suarez M, Da Silva A (2004) The architecture of the earth system modeling framework. Computing in Science & Engineering 6(1):18–28, DOI 10.1109/MCISE.2004.1255817

Huang CY, Huang CH, Skamarock WC (2019) Track deflection of typhoon Nesat (2017) as realized by multiresolution simulations of a global model. Monthly Weather Review 147(5):1593–1613, DOI 10.1175/MWR-D-18-0275.1

Hunter JD (2007) Matplotlib: A 2d graphics environment. COMPUTE 9(3):90–95, DOI 10.1109/MCSE.2007.55

Iacono MJ, Delamere JS, Mlawer EJ, Shephard MW, Clough SA, Collins WD (2008) Radiative forcing by long-lived greenhouse gases: Calculations with the aer radiative transfer models. Journal of Geophysical Research: Atmospheres 113(D13), DOI 10.1029/2008JD009944

Imberger M, Larsén XG, Davis N, Du J (in press 2020) Approaches toward improving the modelling of mid-latitude cyclones entering at the lateral boundary corner in the limited area model wrf. Quarterly Journal of the Royal Meteorological Society n/a(n/a), DOI 10.1002/qj.3843

Ju L, Ringler T, Gunzburger M (2011) Voronoi Tessellations and Their Application to Climate and Global Modeling. Lecture Notes in Computational Science and Engineering 80:313–342, DOI 10.1007/978-3-642-11640-7_10

Klemp JB (2011) A Terrain-Following Coordinate with Smoothed Coordinate Surfaces. Monthly Weather Review 139(7):2163–2169, DOI 10.1175/MWR-D-10-05046.1

Kramer M, Heinzeller D, Hartmann H, van den Berg W, Steeneveld GJ (2018) Assessment of MPAS variable resolution simulations in the grey-zone of convection against WRF model results and observations. Climate Dynamics 0(0):1–24, DOI 10.1007/s00382-018-4562-z

Larsén XG, Vincent C, Larsen S (2013) Spectral structure of mesoscale winds over the water. Quarterly Journal of the Royal Meteorological Society 139(672):685–700, DOI 10.1002/qj.2003

Larsén XG, Bolaños R, Du J, Kelly MC, Kofoed-Hansen H, Larsen SE, Karagali I, Badger M, Hahmann AN, Imberger M, Tornfeldt SJ, Jackson S, Volker P, Svenstrup Petersen O, Jenkins A, Graham A (2017a) Extreme winds and waves for offshore turbines: Coupling atmosphere and wave modeling for design and operation in coastal zones. Wind Energy Department, Technical University of Denmark, Roskilde, Denmark, Tech Rep October

Larsén XG, Du J, Bolaños R, Larsen S (2017b) On the impact of wind on the development of wave field during storm Britta. Ocean Dynamics 67(11):1407–

1427, DOI 10.1007/s10236-017-1100-1

Larsén XG, Larsen SE, Petersen EL, Mikkelsen TK (2019) Turbulence Characteristics of Wind-Speed Fluctuations in the Presence of Open Cells: A Case Study. Boundary-Layer Meteorology 171(2):191–212, DOI 10.1007/s10546-019-00425-8

Leduc M, Laprise R (2009) Regional climate model sensitivity to domain size. Climate Dynamics 32(6):833–854, DOI 10.1007/s00382-008-0400-z

Matte D, Laprise R, Thériault JM, Lucas-Picher P (2017) Spatial spin-up of fine scales in a regional climate model simulation driven by low-resolution boundary conditions. Climate Dynamics 49(1-2):563–574, DOI 10.1007/s00382-016-3358-2

May RM, Arms SC, Marsh P, Bruning E, Leeman JR, Goebbert K, Thielen JE, Bruick ZS (2008 - 2020) Metpy: A Python package for meteorological data. DOI 10.5065/D6WW7G29

Mehrens AR, von Bremen L (2016) On the correlation of spatial wind speed and solar irradiance variability above the North Sea. Advances in Science and Research 13:57–61, DOI 10.5194/asr-13-57-2016

Mehrens AR, Hahmann AN, Larsén XG, von Bremen L (2016) Correlation and coherence of mesoscale wind speeds over the sea. Quarterly Journal of the Royal Meteorological Society 142(701):3186–3194, DOI 10.1002/qj.2900

Met Office (2010 - 2015) Cartopy: a cartographic python library with a matplotlib interface. Exeter, Devon

Nakanishi M, Niino H (2009) Development of an improved turbulence closure model for the atmospheric boundary layer. Journal of the Meteorological Society of Japan Ser II 87(5):895–912, DOI 10.2151/jmsj.87.895

Nastrom GD, Gage KS (1985) A climatology of atmospheric wavenumber spectra of wind and temperature observed by commercial aircraft. DOI 10.1175/1520-0469(1985)042⟨0950:ACOAWS⟩2.0.CO;2

Niu GY, Yang ZL, Mitchell KE, Chen F, Ek MB, Barlage M, Kumar A, Manning K, Niyogi D, Rosero E, Tewari M, Xia Y (2011) The community noah land surface model with multiparameterization options (noah-mp): 1. model description and evaluation with local-scale measurements. Journal of Geophysical Research: Atmospheres 116(D12), DOI 10.1029/2010JD015139

Orlanski I (1975) A Rational Subdivision of Scales for Atmospheric Processes. Bulletin of the American Meteorological Society 56(5):527–530

Park SH, Skamarock WC, Klemp JB, Fowler LD, Duda MG (2013) Evaluation of Global Atmospheric Solvers Using Extensions of the Jablonowski and Williamson Baroclinic Wave Test Case. Monthly Weather Review 141(9):3116–3129, DOI 10.1175/MWR-D-12-00096.1

Park Sh, Klemp JB, Skamarock WC (2014) A Comparison of Mesh Refinement in the Global MPAS-A and WRF Models Using an Idealized Normal-Mode Baroclinic Wave Simulation. Monthly Weather Review 142(10):3614–3634, DOI 10.1175/MWR-D-14-00004.1

Pilon R, Zhang C, Dudhia J (2016) Roles of deep and shallow convection and microphysics in the MJO simulated by the model for prediction across scales. Journal of Geophysical Research 121(18):10,575–10,600, DOI 10.1002/2015JD024697

Prior J, Kendon M (2011) The disruptive snowfalls and very low temperatures of late 2010. Weather 66(12):315–321, DOI 10.1002/wea.874

Ringler TD, Jacobsen D, Gunzburger M, Ju L, Duda M, Skamarock W (2011) Exploring a multiresolution modeling approach within the shallow-water equations. Monthly Weather Review 139(11):3348–3368, DOI 10.1175/MWR-D-10-05049.1

Saha S, Moorthi S, Pan HL, Wu X, Wang J, Nadiga S, Tripp P, Kistler R, Woollen J, Behringer D, Liu H, Stokes D, Grumbine R, Gayno G, Wang J, Hou YT, Chuang HY, Juang HMH, Sela J, Iredell M, Treadon R, Kleist D, Van Delst P, Keyser D, Derber J, Ek M, Meng J, Wei H, Yang R, Lord S, van den Dool H, Kumar A, Wang W, Long C, Chelliah M, Xue Y, Huang B, Schemm JK, Ebisuzaki W, Lin R, Xie P, Chen M, Zhou S, Higgins W, Zou CZ, Liu Q, Chen Y, Han Y, Cucurull L, Reynolds RW, Rutledge G, Goldberg M (2010) Ncep climate forecast system reanalysis (cfsr) 6-hourly products, january 1979 to december 2010

Schwartz CS (2019) Medium-Range Convection-Allowing Ensemble Forecasts with a Variable-Resolution Global Model. Monthly Weather Review 147(8):2997–3023, DOI 10.1175/mwr-d-18-0452.1

Skamarock W, Klemp J, Dudhi J, Gill D, Barker D, Duda M, Huang XY, Wang W, Powers J (2008) A Description of the Advanced Research WRF Version 3. Mesoscale and Microscale Meteorology Division, National Center for Atmospheric Research, Boulder, Colorado, USA, Tech Rep June

Skamarock WC, Park SH, Klemp JB, Snyder C (2014) Atmospheric Kinetic Energy Spectra from Global High-Resolution Nonhydrostatic Simulations. Journal of the Atmospheric Sciences 71(11):4369–4381, DOI 10.1175/JAS-D-14-0114.1

Skamarock WC, Duda MG, Ha S, Park SH (2018) Limited-area atmospheric modeling using an unstructured mesh. Monthly Weather Review 146(10):3445–3460, DOI 10.1175/MWR-D-18-0155.1

Skamarock WC, Klemp JB, Duda MG, Fowler LD, Park SH, Ringler TD (2012) A Multiscale Nonhydrostatic Atmospheric Model Using Centroidal Voronoi Tesselations and C-Grid Staggering. MONTHLY WEATHER REVIEW 140(9):3090–3105, DOI {10.1175/MWR-D-11-00215.1}

Sørensen P, Cutululis NA, Vigueras-Rodríguez A, Madsen H, Pinson P, Jensen LE, Hjerrild J, Donovan M (2008) Modelling of power fluctuations from large offshore wind farms. Wind Energy 11(1):29–43, DOI 10.1002/we.246

Thompson G, Field PR, Rasmussen RM, Hall WD (2008) Explicit forecasts of winter precipitation using an improved bulk microphysics scheme. part ii: Implementation of a new snow parameterization. Monthly Weather Review 136(12):5095–5115, DOI 10.1175/2008MWR2387.1

Vigueras-Rodríguez A, Sørensen P, Cutululis NA, Viedma A, Donovan MH (2010) Wind model for low frequency power fluctuations in offshore wind farms. Wind Energy 13(5):471–482, DOI 10.1002/we.368

Vincent CL (2010) Mesoscale wind fluctuations over Danish waters. Risø-phd, Technical University of Denmark. Risø National Laboratory for Sustainable Energy

Vincent CL, Trombe PJ (2017) Forecasting intrahourly variability of wind generation. Elsevier Ltd, DOI 10.1016/B978-0-08-100504-0.00008-1

Vincent CL, Hahmann AN, Kelly MC (2012) Idealized Mesoscale Model Simulations of Open Cellular Convection Over the Sea. Boundary-Layer Meteorology 142(1):103–121, DOI 10.1007/s10546-011-9664-7

Warner TT, Peterson RA, Treadon RE (1997) A Tutorial on Lateral Boundary Conditions as a Basic and Potentially Serious Limitation to Regional Numerical Weather Prediction. Bulletin of the American Meteorological Society 78(11):2599–2617, DOI 10.1175/1520-0477(1997)078⟨2599:ATOLBC⟩2.0.CO;2

WindEurope (2020) Offshore Wind in Europe - Key trends and statistics 2019. WindEurope asbl/vzw, Brussels, Belgium, Tech rep

Wong M, Skamarock WC (2016) Spectral characteristics of convective-scale precipitation observations and forecasts. Monthly Weather Review 144(11):4183–4196, DOI 10.1175/MWR-D-16-0183.1

Yang ZL, Niu GY, Mitchell KE, Chen F, Ek MB, Barlage M, Longuevergne L, Manning K, Niyogi D, Tewari M, Xia Y (2011) The community noah land surface model with multiparameterization options (noah-mp): 2. evaluation over global river basins. Journal of Geophysical Research: Atmospheres 116(D12), DOI 10.1029/2010JD015140

Zhao C, Xu M, Wang Y, Zhang M, Guo J, Hu Z, Leung LR, Duda M, Skamarock W (2019) Modeling extreme precipitation over East China with a global variable-resolution modeling framework (MPASv5.2): impacts of resolution and physics. Geoscientific Model Development 12(7):2707–2726, DOI 10.5194/gmd-12-2707-2019

APPENDIX C
List of Omitted Dissemination Activities and Publication Contributions

The following list contains research work with personal contributions and dissemination activities which were performed during the period of the Ph.D. program but are not included in the thesis.

Journal articles (in preparation):

J1 **Impact of large scale wakes on the balancing and energy markets of Denmark**. Das, K., Kanellas, P., Murcia, J. P., Koivisto, M., Imberger, M., Gea-Bermudez, J., Sørensen, P. E. *In preparation for submission to IEEE TRANSACTIONS ON SUSTAINABLE ENERGY*

Workshop and conference presentations (non peer-reviewed):

W1 **Strength and Challenges in locally refined global MPAS in comparison with WRF - offshore wind farm parameterizations (2019)** [oral presentation]. Imberger, M., Larsén, X. G., Davis, N. *At: NCAS/NCAR WRF Workshop*. Lincoln, United Kingdom.

W2 **Offshore wind farm wakes in global circulation model MPAS compared with WRF and measurements (2019)** [oral presentation]. Imberger, M., Larsén, X.G., Davis, N. *In: European Geosciences Union - General Assembly 2019*. Vienna, Austria.

W3 **Linking calculation of wakes from offshore wind farm cluster to the Danish power integration system (2019)** [Poster]. Larsén, X. G. (speaker), Volker, P., Imberger, M., Fischereit, J., Koivisto, M., Das, K., Kanellas, P., Sørensen, P., Langor, E., Duin, M., Hawkins, S., Maule, P., Ahsbahs, T., Du, J., Hahmann, A., Davis, N., Ott, S., Badger, J. (2019). *At: WindEurope Offshore 2019*. Copenhagen, Denmark.

W4 **Forcing data at WRF lateral boundary corner and its impact on storm intensification – a case study through mid-latitude cyclone Christian (2018)** [oral presentation]. Imberger, M., Larsén, X.G., Du, J., Davis, N. *At: Joint WRF and MPAS Users' Workshop 2018*. Boulder, Colorado, USA.

Conference proceedings (peer-reviewed):

C1 **The Effects of Open Cellular Convection on Wind Farm Operation and Wakes (2020)**. Göçmen, T., Larsén, X. G., Imberger, M. *Accepted in IOP Journal of Physics: Conference Series proceedings for Torque 2020.*

Reports:

R1 **Making the Most of Offshore Wind: Re-Evaluating the Potential of Offshore Wind in the German North Sea (2020)**. In: Agora Energiewende, Agora Verkehrswende, Technical University of Denmark and Max-Planck-Institute for Biogeochemistry (2020): Making the Most of Offshore Wind: Re-Evaluating the Potential of Offshore Wind in the German North Sea. Study commissioned by Agora Energiewende and Agora Verkehrswende. https://www.agora-energiewende.de/fileadmin2/Projekte/2019/Offshore_Potentials/176_A-EW_A-VW_Offshore-Potentials_Publication_WEB.pdf